Creep Properties of Source Rocks Using Indentation: The Role of Organic Matter on Texture and Creep Rates

by

Mirna I. Slim

B. S. Geology, American University of Beirut (1998)
M. S. Geology, Colorado School of Mines (2007)
S.M. Geophysics, Massachusetts Institute of Technology (2013)

Submitted to the Department of Earth, Atmospheric and Planetary Sciences
in partial fulfillment of the requirements for the degree of

Doctor of Philosophy

at the

MASSACHUSETTS INSTITUTE OF TECHNOLOGY

June 2016

Author .....
Department of Earth, Atmospheric and Planetary Sciences
June, 2016

Certified by .....
Franz-Josef Ulm
Professor of Civil and Environmental Engineering
Thesis Supervisor

Accepted by .....
Robert van der Hilst
Schlumberger Professor of Earth and Planetary Sciences, Head of
Department of Earth, Atmospheric and Planetary Sciences

Creep Properties of Source Rocks Using Indentation: The Role of Organic Matter on Texture and Creep Rates

by

Mirna I. Slim

Submitted to the Department of Earth, Atmospheric and Planetary Sciences
on June, 2016, in partial fulfillment of the
requirements for the degree of
Doctor of Philosophy

Abstract

Gas shale formations are source rocks of variable mineralogy with oil and natural gas production potential. Due to their low permeability, these source rocks can be produced only after fracturing. Therefore, understanding and characterizing the time-dependent mechanical properties of these formations are of outmost importance.

This work analyzes the role of organic matter affecting texture and driving creep behavior in source rocks. To isolate the porous organic-rich clay composites, we adopt elaborate methodology that uses the mechanical properties probed with the indentation technique, chemistry obtained from spectroscopy, and chemo-mechanical clustering analysis. We characterize the nanoscale mechanical properties and anisotropy of these composites and show that micromechanical textural modeling depicts the effects of organic maturity on texture and successfully captures and isolates those effects.

Our research reveals that creep in organic-rich shale formations is logarithmic and driven by the porous kerogen phase. The organic matter plays a pivotal role as it affects energy dissipation in the composite with deformations. This conclusion is reached by inspection of (nano- and micro-) indentation creep results, analysis of secondary consolidation by adapting the relevant tools of soil mechanics to nanoindentation, and inspection of changes in packing density of the clay composites with creep deformation. Creep composite modeling reveals that the clay composites lie within two asymptotes defined by textures that relate to the connectivity of the porous kerogen phase.

A comparison of creep microindentation data with triaxial creep tests validates

creep indentation as a means to understand, quantify, and predict creep behavior of source rocks that extends beyond the test duration. Creep microindentation, thus, saves experimentation time and specimen volume. Empirical maturity-dependent scaling relationships between creep rates and both stiffness and hardness are obtained. These relationships are potential additions to petrophysical workflows leading to better fracture planning, which, in turn, reduces the environmental impact of fracturing jobs and production costs.

Thesis Supervisor: Franz-Josef Ulm
Title: Professor of Civil and Environmental Engineering

To a woman with a strong will, beautiful beliefs, and a kind loving heart: To my mom.

Thank you for your love and all you sacrifices, mama.

You mean the world to me.

Acknowledgments

The years I spent at MIT were the longest I have spent in one place other than home. This long journey would not have been successful without the contributions and support of many people I was lucky enough to meet and work with.

First, I would like to express my gratitude to my advisor, Prof. Franz-Josef Ulm. Thanks for the opportunity to be part of your research group and for the support, guidance, motivation, and your patience dealing with a geoscientist. You provided me with an unsurpassed opportunity to broaden my understanding of various topics and research disciplines, improve my research skills, and develop an inquisitive mind. It was a privilege to have known, worked, and learned from you.

I would also like to thank my committee members: Prof. Brian Evans, Prof. Roger Summons, Prof. Taylor Perron, and Dr. Taras Bryndzia. It has been a privilege learning from and working with each and every one of you. Thank you for your guidance, advice, all your comments and revisions of my dissertation, and the constructive discussion during and after my defense. Your contributions made my work better and will only help me expand on my research at MIT and move forward.

Thanks to my sponsors: EAPS, Schlumberger, Shell, and MITei. Your financial support made it possible for me to work in many labs and on three research topics.

My sincere thanks to Prof. Sam Bowring and Prof. Alison Malcolm for their support during my preparation for my general exam and for agreeing to be on my exam committee. Well, you saved the day! Thank you Sam for your encouragement, the nice field trips, and contributions in making many hiking and camping trips possible for my friends and myself to enjoy.

I would like to thank my CSM advisor and mentor, Prof. Neil Hurley, for sug-

gesting and encouraging me to apply to MIT. No need to feel guilty anymore, Neil, it is done.

Thank you Prof. Henri Van Damme, Dr. Roland Pellenq, and Dr. Nicola Ferralis for always being available and welcoming to answer my many questions and improve my understanding of many topics. My sincere thanks to Prof. Jack Germaine and his students, Taylor Nordquist and Dr. Amer Deirieh, for their help and guidance consolidating my first soil samples ever.

Thank you Dr. Shiahn Chen, Dr. Yong Zhang, Dr. Alan Schwartzman, and Patrick Boisvert in the CMSE microscopy and nanotechnology labs. Your knowledge, training, patience, and dedication made my work with electron microscopes and indenters productive, enjoyable, and rewarding.

My sincere thanks to Dr. Ulrich (Uli) Mok for his support and help in the rock mechanics lab in EAPS. Thank you for sharing long hours, days, and sweat working on and helping with the Patterson machine. Thank you Derek Hirst (Jok) for your help in the workshop, drilling and cutting sample plugs and designing tools to make sample preparation go faster and easier.

I would like to thank Dr. Robert Kleinberg for directing me to Prof. Ulm's research group. Thank you Marina Polyakov and Abi Matteson for your help doing experiments and measurements at the Schlumberger Doll Research center. Thanks to Shell Oil and Dr. Calum Macaulay for hosting me at their research facility in 2014.

Thank you Dr. Ronny Hofmann for very constructive and long discussions pertaining to my research and its applicability.

My sincere thanks to all the students and post-docs in Prof. Ulm's research group and the CEE soil mechanics lab for welcoming me to their labs, groups, and offices. Thank you Dr. Konrad Krakowiak, Dr. Christian Hoover, Prof. Sara Abedi,

Prof. Mia Hubler for collaborations, many discussions, help in the X-Shale Hub, and civil "fights" over indenter time. Thank you Hadrien Laubie (my office mate and math consultant!), Siavash Monfared, Prof. Mathieu Vandamme, Dr. Jeremy Berthonneau, Dr. Amael Obliger, Dr. Arghavan Louhghalam, Dr. Alice Dufresne, Dr. Armen Mkrtchyan, David Rosen, Eric Stansifer, Dr. Youssef Mroueh, Dr. Elan Pavlov, Fabian Kozynski, Dr. Murad Abu-Khalaf, Dr. Ahmed Helal, Dina El-Zanfaly, Thomas Petersen, Dr. Amer Deirieh, Farrah Sabouni, and Dr. Muhannad Abuhaikal for answering many questions, entertaining long discussions pertaining to my research and work, checking calculations, sharing scripts and codes, editing sections of my thesis, and helping me prepare my talks and my defense slides. I wish I could have you all with me everywhere I go!

Thank you Dr. Vicki McKenna, Donna Hudson, Roberta Allard, Carol Sprague, Jacqui Taylor, and Sue Turbak for your help, support, and making everything possible when needed.

Thank you Brenda Carbone and Kerin Willis for your quick and long chats, listening, presence, hugs, and smiles. People like you make life away from family bearable.

During my years at MIT, I was lucky to be part of a very vibrant and welcoming graduate community at Sidney-Pacific. I have a lot to thank the SP housemasters, the SP house manager, my SPEC (SPEC10: Amy, Tim, Chelsea, Ian), and the SP trustees for. It was a privilege working with you, serving the SP residents and the MIT graduate community. Thank you Dottie and Roger Mark, Roland and Annette Tang, and Jack and Jean Ahern for opening your hearts and homes to me. Thank you for treating me as a family member. Your love, kindness, presence, constant support, and encouragement made me feel at home far away from home.

Thank you Jacob (Jake) Sobstyl, Sina Moeini Ardakani, Lea Atmani, and Muhan-

nad Abuhaikal for making the night celebrating my graduation so special (I can say no more).

I express my deepest gratitude, love, and thanks to the people that made my life and years at MIT enjoyable and possible. Thank you Farrah, Kendall, Matt, Amy, Tim, Chelsea, Dina, Burcu, Steph, Ozge, Elan, Jit, Dave, Fabian, Jenny, Rachael, Yulia, and Pam. Big hugs to my four heroes: Ahmed, Gabi, Armen, and Sudhish. Thank you all for always being there to provide a shoulder to cry on, jokes to laugh at, and unforgettable moments. Thank you for listening, arguing, helping, procrastinating with me, cooking with and for me, and simply for being there when I needed you. Your friendship is the best thing that happened to me at MIT. This friendship is the best thing (yes, forget about the degree) that I am taking with me from campus.

Lastly, I would like to thank my family for their unconditional love and making me the person I am. Thank you mom and dad for all your sacrifices since I was born. Thank you for your support and strength through good and bad. I learned to be kind, strong, confident, and hopeful because of you. Thank you for helping me know, respect, and love God, who I constantly feel blessed by. Sara and Nassib, you are the best sister and brother I could ever have. You have always been happier and prouder, than myself, of my achievements and successes. I am blessed to have you both in my life. Thank you for introducing Raed and Loubna to the family, and spice life up with the best Nouna and Jado (and the still-unnamed unborn little boy arriving soon) ever. I love you all so much.

Contents

List of Figures

List of Tables

Part I

Introduction, Research Scope, and Objectives

Chapter 1

Introduction

Gas shale formations are source rocks with oil and natural gas production potential. They are referred to as unconventional reservoirs and are competing over production with well-studied conventional (carbonates and sandstones) reservoirs over production in the United States (US). The US Energy Information Administration (EIA) reports increases in total resources due to inclusion of proved and unproved shale reserves worldwide, of 10% and 35% for crude oil, and 48% and 38% for wet natural gas, outside and inside the US, respectively (EIA, 2013). The steady increase in the US proven shale reserves (marketed gas production of 77.3 Bcf/d in November 2014; EIA, 2014) makes gas shale formations a source promising energy sustenance and independence in the US.

The success in shale production is due to two key technological advancements: horizontal drilling and hydraulic fracturing (Koesoemadinata et al., 2011; Rogers, 2011), both of which change the equilibrium stress fields in the formations. Horizontal drilling is advantageous as source rocks usually cover large areas. Hydraulic fracturing (or "fracking"), is a must in low permeability formations such as gas shales.

Fracking operations, however, are not done efficiently. It is reported that only 30% of fracking stages contribute to 70% of production from gas shales (Koesoemadinata et al., 2011). This low efficiency in production return from fracking operations is mainly due to proppant embedment and a decrease in formation pressure, leading to fracture closure and formation deformation. Therefore, a proper mechanical characterization of gas shale formations, assessing their time-dependent properties and relating those to other rock characteristics, is beneficial for better embedment rate predictions and fracking job planning. A reduction of fracking stages for the same production rate within a well reduces the environmental impact of fracking operations and well/field cost.

1.1 Industrial Context

One ultimate quest in geoscience is to obtain rock physics models that resolve and relate reservoir properties (lithology/mineralogy, porosity, kerogen content and maturity) to sonic and seismic data. The difficulty in such a quest stems from the difficulty of quantifying reservoir properties and relating them to very complex and interactive diagenetic processes that transform rocks physically, chemically, and organically. For instance, with burial depth and increase in temperature, deposited sediments compact, pore water gets expelled as long as permeability of sediments/rock allows it, and pore pressure increases. Cementation takes place first at grain contacts. Then, with rising temperature, cementation forms within pore spaces. Also, mineral transformation (e.g., feldspars to clay minerals, smectite to illite) gets accelerated, affecting mineralogy and packing densities. Organic matter matures, generating oil and gas and affecting rock texture. Due to these diagenesis and catagenesis complexities, researchers interested in gas shale formations avoid studying their textural aspect

beyond qualitatively commenting on and interpreting limited observations seen from electron microscopy images. Finding a framework where data acquired at various scales can be related and integrated is always a challenge and concern (Gonzalez et al., 2013). Certain questions recurrently arise. How can geological processes and time-dependent phenomena (e.g., burial and temperature history) affecting diagenesis (cementation, maturation, and microcracking) be reflected in rock physics models?; and, how can measurements at the nano- and microscale be scaled and integrated into such models?, are always echoed. Due to the complexity of diagenesis modifying a rock and of the maturation process, it is often hard to integrate diagenetic effects into workable models. Other challenges that hinder both a proper formation evaluation and the potential production of source rocks are:

1. The conventional petrophysical methods have limited applicability to source rocks. Therefore, correlating mechanical properties to other petrophysical properties is difficult.

2. Due to the difficulty and cost of extracting intact rock samples, laboratory measurements at the macroscale are difficult and scarce.

3. Macroscopic or 'average' property measurements (e.g., on core plugs) are insufficient to fully address heterogeneity and the degree of property variation within organic-rich rocks. They also do not reveal the effects of the various constituents on their mechanical properties.

4. Rock deformation due to drilling, fracking, and production is hard to predict or model.

The motivation of this research, therefore, originates from the above-mentioned industrial challenges along with the desire to find a framework to relate mechanical

properties to organic content, maturity, and texture.

1.2 Research Questions

This research departs from the following points of inquiry:

1. What is the effect of maturity on rock texture?

   Source rocks, like all sedimentary formations, go through diagenetic changes and processes. The presence of organic matter in situ since deposition makes thermal maturity an additional process that affects the host rock. It is documented in literature that maturity changes the distribution of organic matter and the texture of a rock (Zargari et al., 2013). Such a conclusion, however, is based on qualitatively studying or describing SEM images.

2. What is the effect of organic matter on the mechanical properties of source rock?

   Organic matter in source rocks is generated by thermally-induced chain reactions. They have complex structures, compositions, and properties which are different than inorganic crystalline materials (e.g., minerals).

3. Can an experimental approach testing small volumes for a short time be substituted for long-term macroscale experiments?

   One challenge in studying source rocks is to obtain intact specimens to study. This is why conventional experiments at an engineering scale are rare.

1.3 Research Objectives

With the challenges faced by industry understanding and producing gas shale formations and the research questions formulated, our research objectives can be summarized as follows:

1. Characterize time-dependent and time-independent mechanical properties of source rocks at various scales. Our objective behind the mechanical characterization at the nano- and microscale is twofold: 1) the heterogeneity of source rocks makes understanding their mechanical properties at various scales of value. 2) The difficulty and cost of acquiring and preserving intact rock samples for macroscale laboratory testing make such measurements and tests rare. Therefore, we aim to establish a testing approach that uses small gas shale samples.

2. Understand and model the effect of the organic phase maturity on the texture and the time-independent mechanical properties of source rocks. Our objective is to highlight the effect of maturity, if it exists, on texture in a more comprehensive approach than simply collecting and correlating various rock properties. Formations at different maturities are, therefore, tested.

3. Highlight the phase that plays the major role driving creep rates in source rocks. Source rocks contain both organic and inorganic components with remarkably different mechanical properties. Studying the time-dependent properties of these various components will highlight the role assumed by each in response to certain applied load conditions.

4. Compare and validate mechanical measurements obtained from small material

volumes to macroscale test results.

1.4 Hypothesis Testing

With the research objectives presented, we translate research questions into probable hypotheses that we aspire to test and validate using the right methodology, tools, and models. These hypotheses are:

1.4.1 Hypothesis I: Textural models capture kerogen maturity

The burial and temperature history of a formation affect its diagenesis in becoming a lithified rock and a reservoir. They also dictate the maturity of its organic content that, in turn, affects the rock texture and mechanical properties (Zargari et al., 2013). We use microtextural models to describe organic-rich clay composites in mature and immature formations. The validity of the approach is tested based on the capability of such models to capture and isolate the effect of maturity predicting clay particle solid properties and packing densities. A unique set of clay particles' properties is expected in rocks with similar diagenetic history, whereas a spread in such properties indicates different clay mineralogy and/or formations with different burial history (e.g., smectite-to-illite transformation).

1.4.2 Hypothesis II: The Organic phase drives creep behavior in source rocks

The importance of understanding time-dependent viscous behavior of gas shale formations (via creep indentation tests and multiscale creep modeling) brings forward

the role of kerogen, along with porosity, in driving creep behavior. We test this hypothesis both at the organic-rich composite level and at the macroscale.

1.4.3 Hypothesis III: Creep microindentation reflects long-time creep behavior

Three-minute creep microindentation tests can assess the viscoelastic behavior of gas shales at constant load. Small volumes (a few μm^3) of material under the indenter contribute to the mechanical response. The hypothesis is that contact creep moduli obtained from 3-min creep microindentation tests reflect creep behavior of source rock assessed by classical macroscopic means such as triaxial creep testing.

1.5 Research Approach

In order to mechanically characterize the formations at the nano- and microscale, measurement techniques that probe materials' properties and responses at both scales are needed. Similarly, in order to study the role of kerogen maturity on texture and creep rates, microtextural and creep homogenization modeling are done. Our experimental approach aims to isolate organic-rich clay composites and study their mechanical properties. It consists of the following methods and techniques:

1. The indentation test technique is used to probe the mechanical properties of small rock volumes, giving the stiffness and hardness of a homogenized material volume under the indenter tip. In addition to elasticity and hardness, a contact creep modulus is obtained from creep indentation tests. The contact creep modulus describes the creep rates of the material tested.

2. Energy-dispersive x-ray spectroscopy (EDS) is used to study the chemistry of material volumes similar to those tested with indentation.

3. A clustering analysis approach uses, as input, coupled chemo-mechanical results to segregate the different phases in the heterogeneous gas shale formations. Porous organic-rich clay composites are thus isolated.

The modeling approach is to test our various hypotheses. It consists of:

1. Using microtextural models to represent textures in clay composites at different maturity. Texture-based scaling expressions, relating solid particle mechanical properties to structural parameters (packing density and kerogen content), are implemented in a back-analysis approach. The latter uses nanoindentation mechanical data as input to predict the solid particle properties and either the packing density of the clay composite or its organic content. The back-analysis results are used to proof-test Hypothesis I.

2. Creep homogenization modeling propagates the creep behavior and rates of the individual constituents of the clay composites to the macroscale. Creep homogenization results, along with creep nanoindentation and microindentation results, highlight the role of organic matter driving creep behavior (at various scales). Creep experimental and modeling results help test Hypothesis II.

3. Analyzing creep triaxial tests performed by Sone and Zoback (2013) is done to extract a creep modulus of these core plug samples. The extracted creep modulus is then compared to creep microindentation test results. This comparison is proposed as a framework to test Hypothesis III.

1.6 Thesis Structure

The thesis is divided into 5 parts. Part I includes this introductory chapter, which represents the scope of the research and the main objectives.

Part II introduces the material studied, the techniques used to obtain mechanical and chemical data, and the approach used to isolate the clay composites. It includes Chapters 2, 3, 4, and 5. Chapter 2 introduces the various gas shale formations, and summarizes their environments of deposition and the history of the basins where they formed. Also, the porosity, chemistry, organic content, and generation potential of the formations studied are presented. The porosity and volume fractions of the various organic and inorganic phases are calculated at the clay composite level (level I) and at macroscale (level II). Chapter 3 reviews the indentation test technique. Various methods used to extract time-independent mechanical properties (e.g., elasticity, M_o, and hardness, H_o) from an indentation load-depth curve are presented (Stilwell and Tabor, 1961; Pharr et al., 1992; Vlassak and Nix, 1994). Chapter 4 focuses on the chemical characterization at the microscale using energy dispersive x-ray spectroscopy (EDS). The chapter reviews how mechanical results from indentations and chemical results from EDS are coupled to use as input into clustering analysis. Chapter 5 summarizes the model-based clustering analysis and the Bayesian model selection criterion used to isolate porous organic-rich clay composites. The chapter highlights the value of conducting "chemo-mechanical" clustering analysis differentiating the various phases at the composite level.

Part III includes Chapters 6, 7 and 8. Chapter 6 validates the experimental approach detailed in Part II and presents the time-independent mechanical properties of the clay composites acquired by short hold-phase nanoindentation tests. Chapter

7 reviews linear and nonlinear microporomechanics and introduces the microtextural models used to describe the texture of the clay composites. Texture-based fitting expressions relating mechanical properties to structural parameters (packing density and kerogen content) are presented. These are implemented in the back-analysis approach detailed in Chapter 8. The back-analysis results are used to validate Hypothesis I.

Part IV includes Chapters 9 and 10. A review of the theory of linear viscoelasticity and its implementation in creep indentation testing are presented in Chapter 9. Chapter 9 reviews the calculation of the contact creep modulus (an indicator of creep rates) and presents the time-dependent mechanical properties of the clay composites and their constituents. Chapter 10 discusses the creep deformation mechanisms at the composite and particle levels. It presents multiscale creep homogenization modeling, modeling results, and analysis. These results and analysis help test Hypothesis II at the composite level. Finally, the creep microindentation test results are presented and compared to macroscale creep experiments. The comparison provides a framework to test Hypotheses II and III. Chapter 10 finishes by highlighting the potential impact of our creep indentation results and how they can be integrated into petrophysical workflows.

Part V includes Chapter 11, which summarizes the main results and findings of this work, highlights our contributions, and presents recommendations for future work.

Part II

Materials and Methods to Isolate Porous Organic-Rich Clay Composites

Chapter 2

Gas Shale Formations

The objective of this research is to mechanically characterize heterogeneous and anisotropic source rocks and highlight the effect of organic matter content and maturity on mechanical properties and texture. This chapter presents the various gas shale formations studied, summarizing their environment of deposition, chemical compositions (x-ray diffraction data), organic content, and hydrocarbon generation potential or maturity (Rock-Eval data). A multi-scale thought-model is adopted as a mechanical framework to study the source rocks at various scales, mainly the composite level (or level I) and the particle level (or level 0). Volume fractions of the various organic and inorganic phases are calculated at the macroscale level (level II) and level I. Volume fraction calculations are based on hypotheses proposed for porosity distribution in mature and immature formations. This sets the stage for mircrotextural characterization and modeling of the clay composites based on formation maturity in Part III.

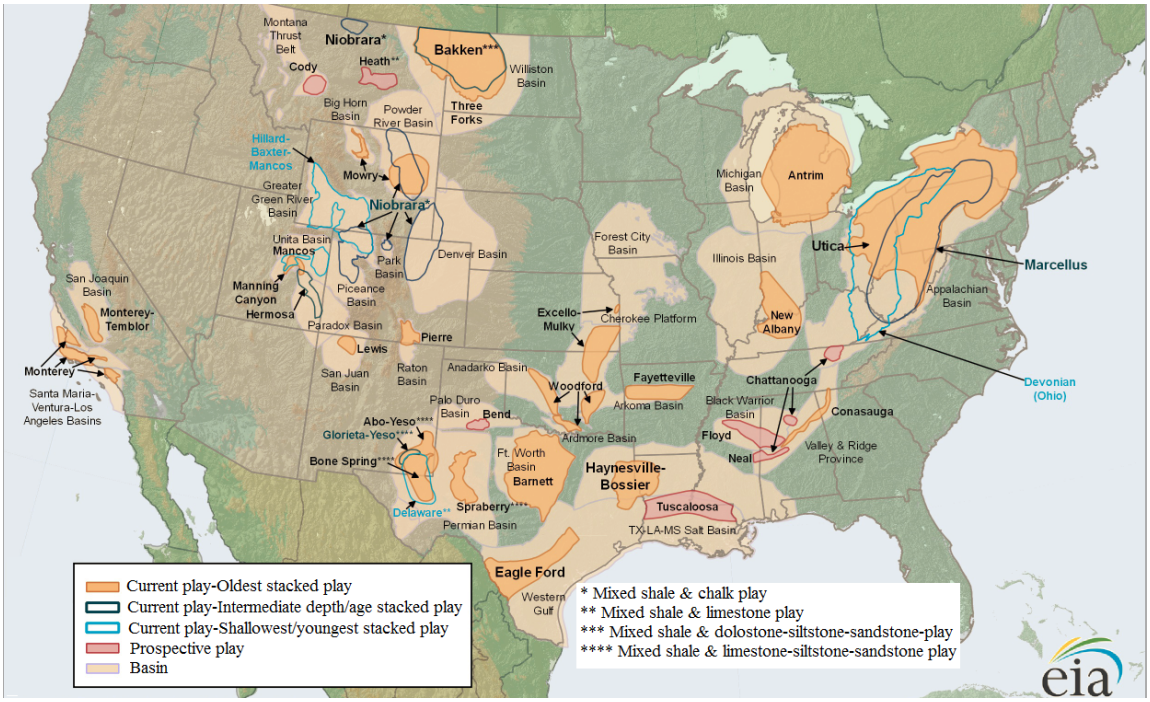

Figure 2-1: Gas shale plays in the US. (modified after US Energy Information Administration. Map is based on data from various published data; updated on April 13, 2015).

2.1 Introduction

In order to address the effect of chemistry, kerogen content, and maturity on the mechanical properties of spatially variable and naturally very heterogeneous source rocks, formations from various producing basins (Figure 2-1), various compositions (argillaceous, siliceous, and carbonaceous; Figure 2-2), and a wide range of organic content and maturity are represented in this work. The source rocks studied are mature Fayetteville, various mature lithofacies of Haynesville, overmature lithofacies of Marcellus, and immature samples from Antrim, Barnett, Marine Type II, and Woodford.

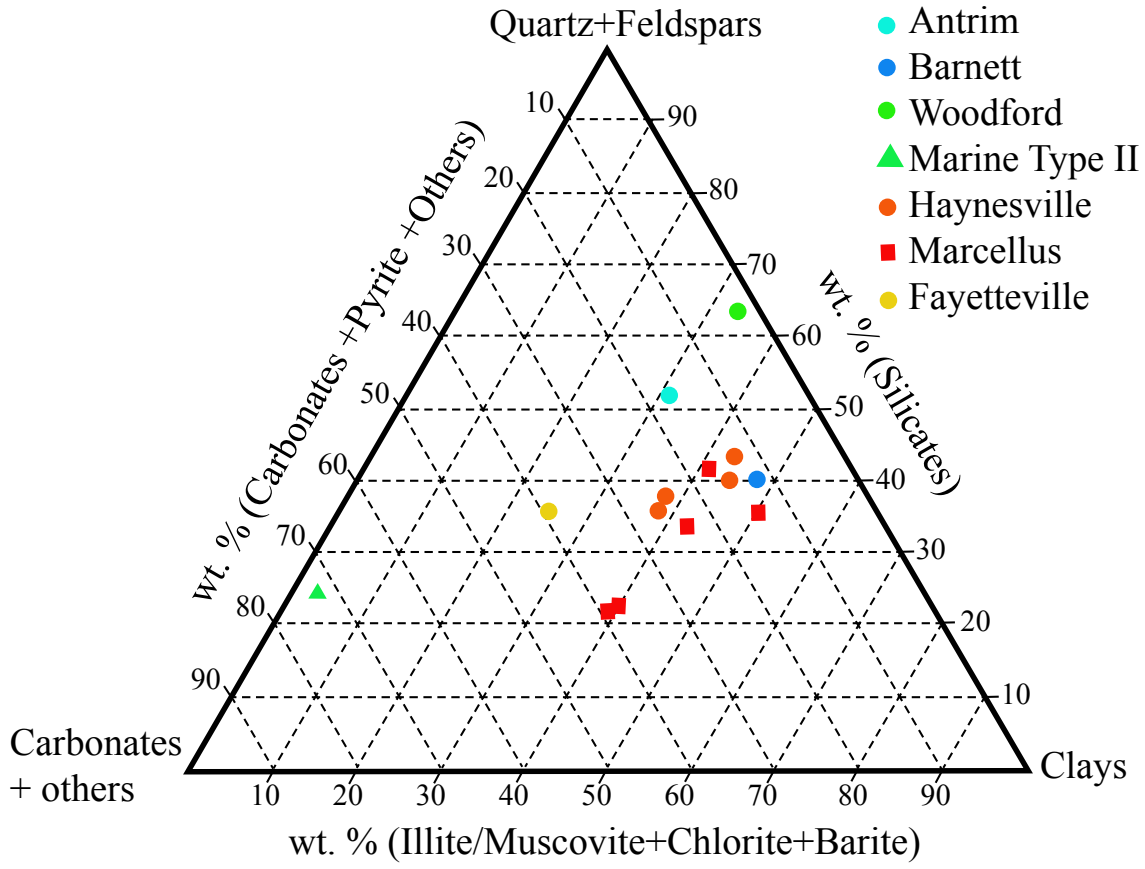

Figure 2-2: A ternary diagram (prepared with CHEMIX trial version: http://www.chemix-chemistry-software.com) showing the chemical composition of the various formations tested in this study. XRD data (Tables 2.1 to 2.7) are recalculated to account for kerogen in the samples' total weight percentages.

One main objective of this work is to highlight the effect of organic matter on the mechanical properties of gas shale formations. To capture the role of the organic phase, we use techniques that allow us to test (Chapters 3 and 4) and isolate (Chapter 5) the porous organic-rich clay composites in the formations. These clay composites constitute the nanoscale or level I of a multi-scale thought-model adopted as a mechanical framework to study the formations at various scales. In this chapter, we focus on highlighting the characteristics of the clay composites and their components. We propose a hypothesis for porosity distribution in gas shale formations based on their maturity and calculate the volume fractions of the various components (organic phase, clay particles, and pores) of the clay composites. These calculations highlight the role and weight of each component in the mechanical behavior of the clay composites and set the stage for the mircrotextural characterization and modeling of clay composites in Part III.

2.2 Gas Shale Formations: Environment of Deposition and Lithology

The exact locations (well names/location and/or counties) of the various source rocks studied are not known. Therefore, summaries of the basin history where each occurs, as well as the geological environment in which each formations was deposited are summarized. Generic lithologic descriptions of the various formations are presented along with x-ray diffraction (XRD) data of the samples studied.

2.2.1 Antrim

Antrim is an organic-rich shale formation of low thermal maturity. It is located in the Michigan Basin, which is an elliptical (250 km in radius and ∼5km deep) intracratonic basin. The Michigan Basin is one (of many) local deep within the long Eastern Interior seaway separating the North America craton on the west from the "Old Red continent, the Avalon terrane microplate, and possibly NW Africa" on the east (Gutschick and Sandberg, 1991). It was formed due to intermittent subsidence throughout the Paleozoic (Howell and Van Der Pluijm, 1990; Martini et al., 1998). Antrim was formed in Late Devonian at the end of the subsidence period and is the result of a 12 m.y. long "episode of slow hemipelagic (continental shelf deposits that accumulate too rapidly to react chemically with seawater) basinal sedimentation" (Gutschick and Sandberg, 1991). Antrim Shale consists of finely laminated, silty, pyritic, and organic-rich black shales interbedded with gray and green shales and carbonate units (Martini et al., 1998). Gutschick and Sandberg (1991) interpret the sedimentary patterns of Antrim to be a distal facies of the Catskill Delta complex of the Appalachian Basin and describe it as containing abundant limestone and dolomite concretions mineralized with various carbonate, sulfide, and sulfate cements. The authors present a detailed review of the four members of Antrim Shale (Figure 3a in Gutschick and Sandberg, 1991); the lower Antrim members, the Norwood and Lachine, have the highest organic content (0.5-24 wt.% TOC) and are the main targets of gas exploitation. The intervening Paxton Member is an interbedded lime mudstone and gray shale unit with lower organic content (0.3-8 wt.%TOC). The silica content (representing microcrystalline quartz and lesser wind-blown silt) ranges from 20 to 41 wt.% in the Lachine and Norwood Members and from 7 to 30 wt.% in the Paxton Member (Gutschick and Sandberg, 1991). The TOC (9.61 wt.%) and quartz

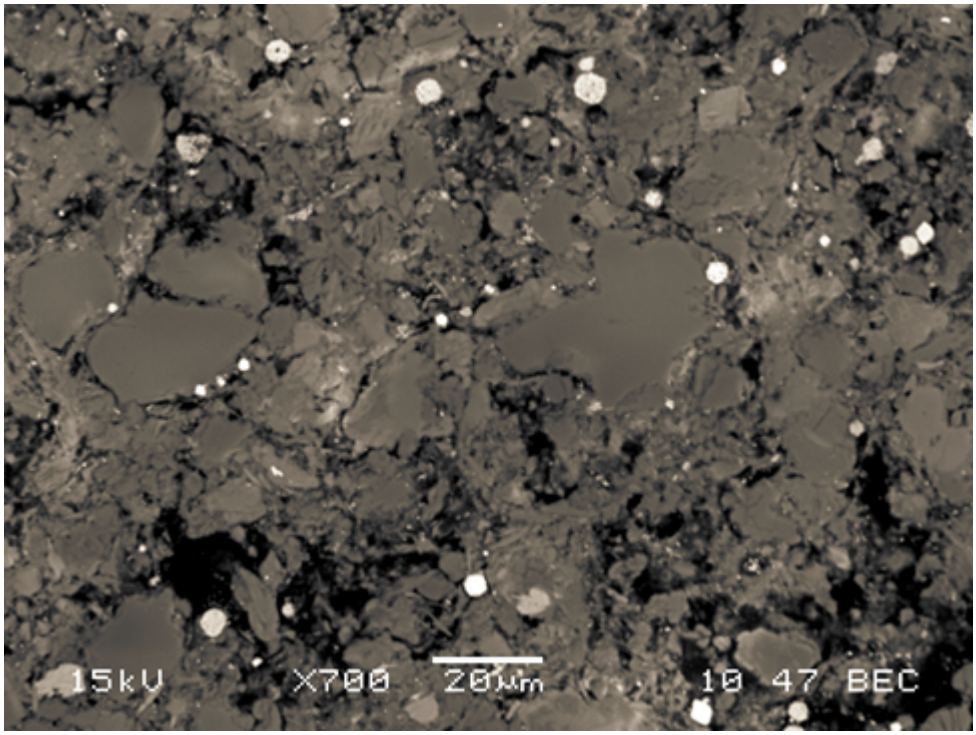

Figure 2-3: A backscatter electron SEM image of an Antrim surface polished perpendicular to the axis of symmetry (Antrim $x_3$cg2)

content (∼41%; Table 2.1) of the Antrim sample studied (Figure 2-3) suggests that it belongs to the lower Antrim members.

Table 2.1: X-ray diffraction results (in wt.%) of the Antrim sample studied; ϕ=porosity.

	Quartz	Albite	Dolomite	Pyrite	Chlorite	Sanidine	Illite +IS	TOC (wt.%)	ϕ (%)
Antrim	40.9	3.5	4.4	3.1	5.8	8.0	25.6	9.61	8.8

2.2.2 Barnett

The Barnett shale is an organic-rich black shale, middle-late Mississippian in age. The production from Barnett is mainly in the Newark East field located in the Fort Worth Basin (Figure 2-1; Montgomery et al. 2005). The Fort Worth Basin is a foreland basing trending N-S in North and Central Texas, covering 1,500 mi^2 (38,900 km^2) with a wedge geometry that deepens to the north. The middle-upper Mississippian strata were deposited during the early phases of subsidence related to the tectonism along the Oklahoma aulacogen (Montgomery et al., 2005) and consist of alternating sequences of shallow-marine limestone (minor dolomite) and black organic-rich siliceous shales. The limestone beds are the result of debris flow sourced from the north. They are abundant in the NE and diminish in the western and southern parts of the Basin (Montgomery et al., 2005). The importance of Barnett comes from the amount of gas formed and stored in it. Estimates of the total in-place Barnett gas resource are 200 trillion cubic feet (tcf) with only 3-40 tcf estimated to be recovered (Montgomery et al., 2005). Secondary cracking of oil into gas and pyrobitumen reflects oil retention in the Barnett system and constitutes the key to the large resources potential of the Barnett Shale gas system (Jarvie et al., 2007). Compared to other gas-shale plays, Barnett is unique in being entirely thermogenic in origin. Production of gas and liquid petroleum comes from greater depths, thus, occurs at high pressures. Montgomery et al. (2005) report that natural fractures do not appear essential for production from the Barnett shale. In some cases, fractures reduce well performance, and they occur filled with carbonate cement near fault zones, making the rock irresponsive to stimulation (Jarvie et al., 2007).

The XRD results of the Barnett samples studied (e.g., Figure 2-4) show low carbonate content (Table 2.2) and indicate that the samples most likely come from

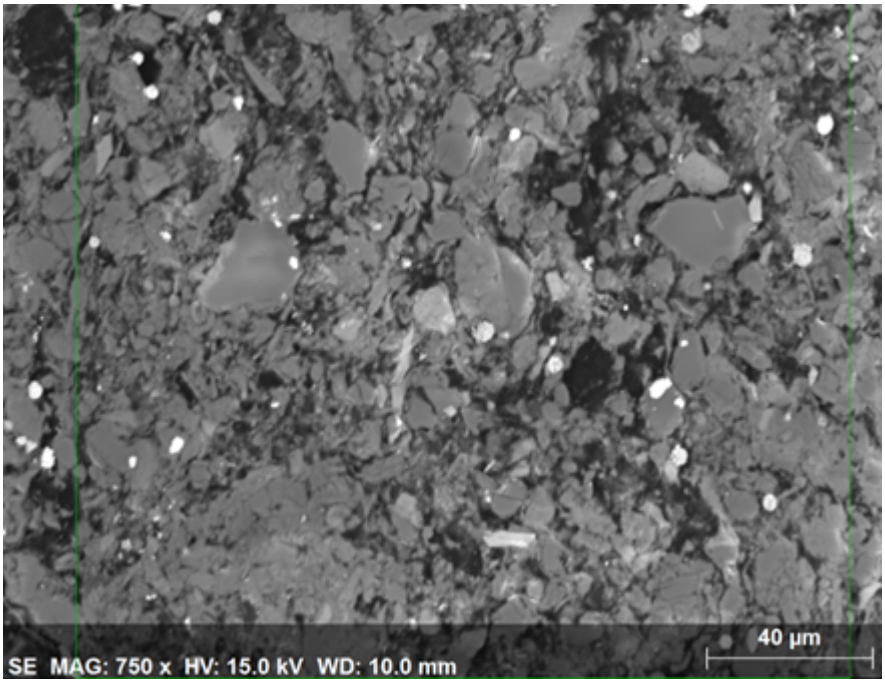

Figure 2-4: A backscatter electron SEM image of Barnett (grid $x_3$cg1 area) showing the texture of the formation (green box delineates the chemicallt analyzed area).

a laminated siliceous mudstone facies (Loucks and Ruppel, 2007).

Table 2.2: X-ray diffraction results (in wt.%) of the Barnett sample studied; ϕ=porosity.

	Quartz	Al-bite	Cal-cite	Py-rite	Chlo-rite	Micro-cline	Gyp-sum	Illite +IS	TOC (wt.%)	ϕ (%)
Barnett	29.7	2.2	2.6	0.5	2.1	3.3	7.8	39.7	12.2	7.3

2.2.3 Haynesville

The Haynesville shale is a post-salt Upper Jurassic source rock. It is the focus of drilling and production activity in NE Texas and NW Louisiana due to its hydrocar-

bon content and high pressure. With other Upper Jurassic strata (siliciclastics and carbonates), Haynesville "records" the early post-rift evolution of the interior Zone rift basins (comprising the East Texas, the North Louisiana, and the Mississippi basins) of the northern Gulf of Mexico Basin (Ewing, 2001). Following rifting, the crust of the interior zone cooled and subsided steadily, allowing space for deposition of sediments above a thick salt layer and fluvial/aeolian siliciclastic of the Norphlet Formation. The sedimentary strata depositing above salt led to salt structures (fault systems, anticlines, and salt diapirs) that later controlled the occurrence of shoal complexes of the shelf edge in Texas and Louisiana (Ewing, 2001). Haynesville was deposited in a restricted lagoon on the subsiding Gulf of Mexico passive margin and became an assemblage of siliciclastics, evaporates, carbonates, and mudstones, representing about 2.5 million years of deposition time (Ewing, 2001). Carbonate and clastic depositional environment dominated during the Lower Haynesville times (Cicero et al., 2010). A dual clastic-carbonate model is proposed for the Haynesville-Bossier shale system; a retrogradational carbonate system (shallow marine platform carbonates and zones of patch reefs) was in place in the East Texas Salt Basin while a progradational clastic system dominated to the east in the North Louisiana and Western Mississippi salt basins (Cicero et al., 2010). During upper Hayneville time, high energy carbonate environment dominated in the west of the East Texas Salt Basin. The Upper Haynesville, as a result, consists of offshore/shelf carbonates grading into condensed shales that expand basinward beyond the continental shelf break (Cicero et al., 2010). The end of Haynesville time is marked by a (second order) flooding surface and cessation of carbonate deposition in most areas. Four Haynesville samples/facies (A2, A5, A6, and A7), very similar in mineralogy, texture (Figure 2-5), and kerogen content (Table 2.3) are studied in this work.

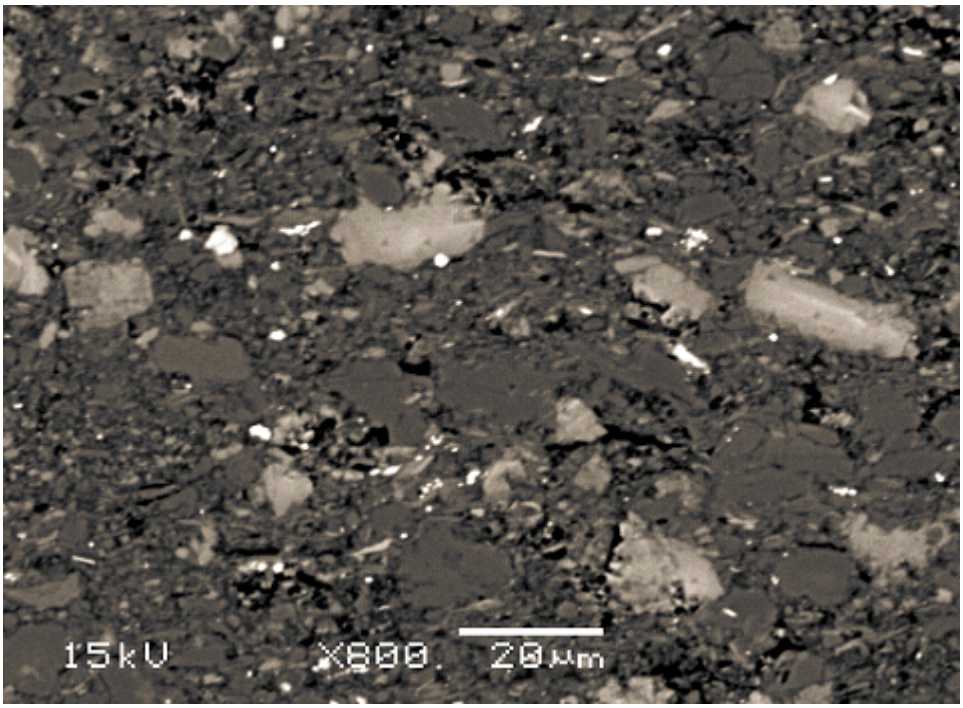

Figure 2-5: An SEM image of Haynesville A7H sample (grid$x_1$cg1 area) showing the texture of the formation.

Table 2.3: X-ray diffraction results (in wt.%) of the Haynesville samples studied; ϕ=porosity. The Haynesville XRD data are courtesy of Shell Oil.

Haynesville	Quartz	Feldspar	Carbonates	Clay	Others	TOC (wt.%)	ϕ (%)
A2H-V	27.0	9.0	22.0	38.0	4.0	3.34	7.4
A5V-H	31.0	9.0	11.0	45.0	5.0	2.57	6.0
A6V-H	32.0	11.0	9.0	43.0	4.0	3.30	7.2
A7V-H	28.0	10.0	12.0	38.0	12.0	3.16	7.6

2.2.4 Marcellus

Marcellus has been studied and produced since the 19^{th} century[1]. The source rock covers an area of 95,000 mi^2 in the Appalachian Basin, which is a foreland basin containing Cambrian to Early Permian sediments. During the Paleozoic, the Appalachian Basin experienced mountain-building episodes, the oldest of which is the Taconic Orogeny (Late Ordovician- Early Silurian), caused by the collision of Laurentia with an oceanic island-arc system (Soeder et al., 2014). The Taconic Orogeny was followed by the Acadian Orogeny (Middle Devonian-Early Mississippian) and Alleghenian Orogeny (Pennsylvanian-Permian). The latter is the result of Laurentia colliding with Gondwana, closing the Rhea Ocean and creating the Appalachian Mountains (Soeder et al., 2014). The orogenic highlands from the first 2 orogenic episodes were the main sediment source of the Marcellus Formation, the lowest stratigraphic unit in the Middle Devonian Hamilton Group. Two schools of thoughts exist among geologists about the environment of deposition of the Marcellus: "the black sea model" or a deep sea environment of deposition in the deepest part of the Appalachian Basin, and the shallow-water environment model (Soeder et al., 2014). There exists more evidence to support the latter model (Soeder et al.'s Figure 4), e.g., the presence of limestone and erosional unconformities below the Marcellus. Marcellus is believed to have been deposited due to a series of transgression and regression eustatic (worldwide changes in sea levels) cycles (Carter et al., 2011) and consists of terrigenous clastics with limestone and calcareous mudstones. It is accepted among stratigraphers that Marcellus contains 3 main members: Union Springs, Cherry Valley, and Oatka Creek members. Crater et al. (2011) summarizes the lithology and log

[1]Refer to Carter et al. (2011) for a summary of the history of exploration, drilling, stimulation and production from Marcellus in Pennsylvania

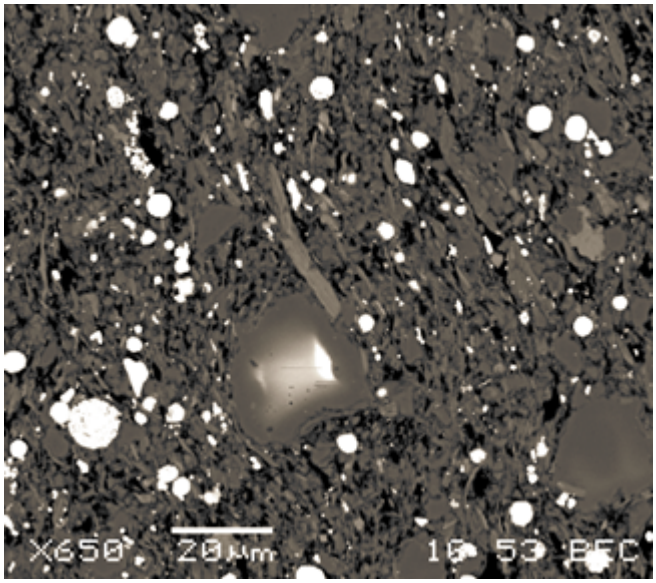

Figure 2-6: A backscatter electron SEM image of Marcellus 108 sample (grid$x_1$cg3 area) showing the texture of the formation and the abundant pyrite (white) content.

signature of the Marcellus members along with typical stratigraphic columns of the Marcellus Shale in New York state and various parts of Pennsylvania. The Marcellus samples studied (Figure 2-6; Table 2.4) come from North Pennsylvania.

2.2.5 Woodford

Woodford Shale is an Upper Devonian-Lower Mississippian source rock. It is one of the most important source rocks in the Anadarko Basin, Oklahoma (Cardott and Lambert, 1985). The Anadarko Basin is a NW trending sedimentary basin of Paleozoic age. It formed at the southern Oklahoma aulacogen that started as an intracratonic rift during Late Precambrian-Early Cambrian (Sullivan, 1985) and then became a failing rift arm of the (pre) Atlantic Ocean (Burke and Dewey, 1973; Keller et al., 1983). Several phases of subsidence (Late Cambrian - Early Mississippian) occurred due to cooling associated with Cambrian crustal thinning (model proposed

Table 2.4: X-ray diffraction results (in wt.%) of the Marcellus samples studied; ϕ=porosity. The Marcellus XRD data are courtesy of Shell Oil.

Marcellus	Quartz	Plagioclase	Calcite	Dolomite	Muscovite	Illite +IS	Chlorite	Anatase	Barite	Siderite	Pyrite	TOC (wt.%)	ϕ (%)
Mar-46	19.7	3.2	30.6	4.4	10.7	23.0	6.2	0.2	0	0.5	1.5	0.49	8.4
Mar-49	18.7	3.5	32.7	3.6	9.6	24.0	5.3	0.1	0	0.7	1.8	1.04	7.9
Mar-108	29.6	6.0	3.1	1.4	10.2	36.3	2.1	0.4	1.5	0.7	8.7	7.68	7.2
Mar-150	29.4	4.8	13.3	2.4	10.0	31.7	0.5	0.4	0	0.4	7.3	7.32	5.9
Mar-151	36.2	5.6	3.0	1.5	9.0	31.8	0.4	0.5	0	0.3	11.7	8.18	6.5

by Garner and Turcotte, 1984), and rate of subsidence slowed down with the lithosphere returning to thermal equilibrium (Garner and Turcotte, 1984).

The Woodford Shale is a carbonaceous and siliceous (gray to black) shale. This composition indicates the transition from carbonate deposition environment in the early Paleozoic to clastic depositional environment toward the end of the era; Woodford lies above a major unconformity. Sullivan (1985) and Walper (1977, in Cardott and Lambert 1985) indicate that the Woodford was deposited in an euxinic (high concentration of hydrogen sulfide and no oxygen) shallow-water epicontinental sea with sediments coming from the east and north east.

The Woodford samples studied (Figure 2-7) are immature facies from a rock outcrop in Oklahoma (Table 2.5). Rock Eval (Section 2.3) done on the sample indicates an immature Woodford facies with a TOC of 4.2 wt.% and a vitrinite reflection, R_o, of 0.65.

Table 2.5: X-ray diffraction results (in wt.%) of the studied Woodford outcrop samples; ϕ=porosity. The Woodford XRD data are acquired by H and M Analytical Services.

	Quartz	Muscovite/ Illite	Albite	Pyrite	Chlorite	TOC (wt.%)	ϕ (%)
Woodford	60.6	30.9	2.8	2.6	3.1	4.2	12.6

2.2.6 Marine Type II

The Marine Type II (MTII) formation is a fossiliferous siliceous carbonate rock rich in apatite (12.6 wt.%) (Table 2.6). Cuttings (Figure 2-8) from a well in Jordan (Middle East) were cleaned and prepared for indentation. No specific location of the well from which the cuttings were collected nor the geologic setting in which the formation

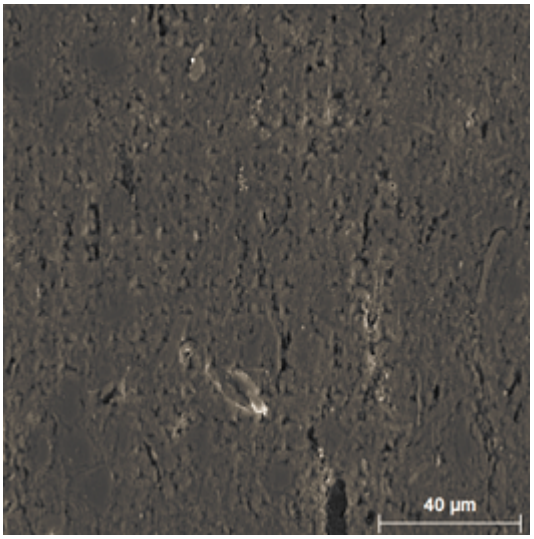

Figure 2-7: A secondary electron SEM image of Woodford showing the texture of the rock in an indented area (grid WoodfA-x_1g1).

formed are available. Pycnometer density measurement of MTII cuttings gave an average density of 1.85-2.094 g./cc. FTIR (Fourier transform infrared spectroscopy) analysis of MTII indicated a kerogen content of 4.71 wt.%.

Table 2.6: X-ray diffraction results (in wt.%) of the studied Marine type II cuttings; ϕ=porosity. The Marine type II XRD data are acquired by H and M Analytical Services.

	Quartz	Cristo-balite	Calcite Dolomite	Illite +IS	Apatite	Others	TOC (wt.%)
Marine Type II	21.2	2.0	53.3 5.8	3.4	12.6	1.7	4.7

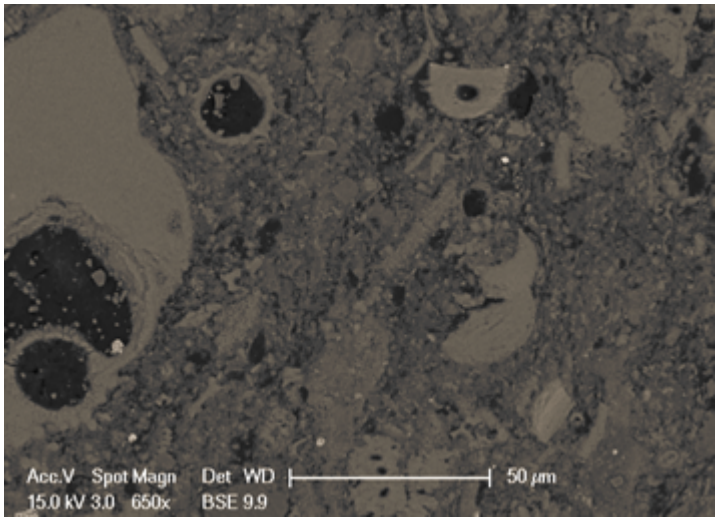

Figure 2-8: An ESEM image of an MTII cutting (grid s1g2) showing the texture and fossil content of the formation.

Table 2.7: X-ray diffraction results (in wt.%) of the studied Fayetteville sample; ϕ=porosity.

	Quartz	Albite	Calcite Dolomite	Pyrite	Halite Chlorite	Illite +IS	Others	TOC (wt.%)	ϕ (%)
Fayetteville	28.8	6.3	22.2 8.9	2.5	3.1 1.2	23.9	2.5	4.92	4

2.2.7 Fayetteville

The Fayetteville Shale (Table 2.7) is a Late Mississippian formation with shaly facies that deposited in a moderately deep stable shelf ($\leq$100 m) gradually shallowing upward into storm-dominating muddy shelf and a shoreface allowing the formation of limestone; Lower Fayetteville facies are made of micritic limestone, indicating a low-energy environment. High-energy limestone (packstones and grainstones) increase upward in the formation (Handford, 1986).

2.3 Hydrocarbon Generation and Rock-Eval

Kerogen, the sedimentary insoluble macromolecular organic matter, is the most abundant organic matter on Earth (Vandenbroucke and Largeau, 2007) and the source of oil and gas. It is usually a mixture of 2 basic categories of organic matter that originate from different plant sources: the vitrinite group (higher land plants with lignin and cellulose in their cell walls) and the liptinite group (Hydrogen-rich plant materials. e.g., spores, resins, wax,. . .) (Dow, 1977). Depositional environment and bacterial reworking affect the composition of kerogen, which is mainly made of carbon, hydrogen, and oxygen with various amounts of sulfur and nitrogen.

Organic matter maturation and oil and gas generation are complex diagenetic processes. They take place under the influence of temperature and involve chain reactions over time (Dow, 1977). Primary thermal cracking of kerogen can be the results of the decomposition of kerogen to gas and bitumen and/or the decomposition of bitumen to oil and gas (Figure 2-9; Jarvie et al. 2007). Natural gas is generated by bacterial methanogenesis, thermal cracking of kerogen, and secondary cracking of oil into gas and pyrobitumen residue (Figure 2-9). To estimate the "generative potential and history" of a source rock, the quantity, quality/type, and maturity of its organic matter must be known. The most accepted classification of source rock kerogen is the van Krevelen classification (Van Krevelen, 1984; Figure 2-10) that describes the thermal evolution of the source rock and the characteristics of the organic matter originally deposited. In order of decreasing petroleum potential (decreasing H/C ratio), kerogen is classified as either Type I (algal), Type II (terrestrial and marine), or Type III (woody terrestrial). Immature gas shale samples, therefore, have high H/C ratios (Table 2.8). This makes Hydrogen a critical component in term of conversion

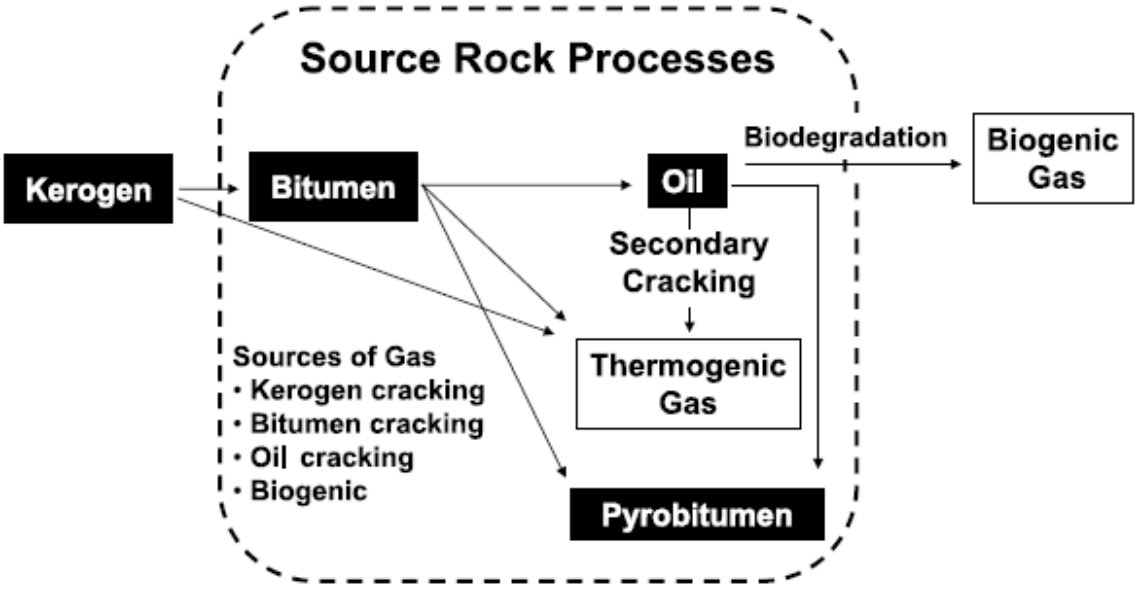

Figure 2-9: Processes that lead to oil and gas generation in source rocks (after Jarvie et al., 2007).

of kerogen to petroleum (Baskin, 1997).

Rock-Eval (Espitalié et al., 1977a,b) is a pyrolysis (thermochemical decomposition of organic material) routine applied by petroleum geochemists to characterize organic matter. Rock Eval is used to assess the amount, quality, and thermal maturity of organic matter in a formation (Baskin, 1997) and to evaluate its potential to generate oil and gas (McCarthy et al., 2011). Vitrinite reflectance is another technique that determines thermal maturity of organic matter; after extracting and concentrating an organic sample (by acid leaching with non-oxidizing acids), the sample is dried, mounted in epoxy, polished, and put in a reflecting microscope to determine its "percent reflectance in oil" or R_o (Dow, 1977). Table 2.8 presents criteria adopted by petroleum geochemists to classify source rocks and their production potential. Table 2.9 summarizes the findings of the Rock-Eval analysis done on the source rocks studied except Marcellus, which is an over-mature formation.

Table 2.8: Source rock Rock-Eval parameters (after Baskin, 1997).

Quantity of Organic Matter

	Organic Matter		**Bitumen**		**Hydrocarbons**
	wt.% TOC	Rock-Eval S_2	wt.% Rock	ppm Rock	ppm Rock
Poor	<0.50	<1.0	<0.05	<500	<300
Fair	0.5-1.0	1.0-5.0	0.05-0.10	500-1000	300-600
Good	1.0-2.0	5.0-10.0	0.10-0.20	1000-2000	600-1200
Very Good	2.0-4.0	10.0-20.0	0.20-0.40	2000-4000	1200-2400
Excellent	>4.0	>20.0	>0.40	>4000	>2400

Quality of Organic Matter

		Hydrogen Index	
	Atomic H/C	**(mg HC/g TOC)**	**Rock-Eval S_2/S_3**
Gas	<0.80	<100	<3
Gas and Oil	0.80-1.0	100-200	3-5
Oil and Gas	1.0-1.2	200-350	5-10
Oil	>1.2	>350	>10

Maturity of Organic Matter

HC Generation	**Maturation**			**Generation**		
Stage	R_o(%)	TAI*	T_{max}(°C)	Bitumen/TOC	mg EOM*/g TOC	Rock-Eval PI
Immature	<0.60	<2.5	<430	<0.05	<50	<0.10
Beginning	0.60	2.5-2.6	430-435	0.05-0.10	50-150	0.10-0.15
Peak	0.90	2.9-3.0	445-450	0.15-0.25	150-250	0.15-0.25
Post	>1.20	>3.2	>460	<0.05	<50	<0.20

*TAI = thermal alteration index. EOM = extractable organic matter.

Table 2.9: Rock Eval analysis of the gas shale formations (measurements performed by GeoMark Research LTD.)

Formation	**TOC** (wt.%)	**S1** (mg HC/g)	**S2** (mg HC/g)	**S3** (mg CO2/g)	T_{max} (°C)	**HI** ($\frac{S2.100}{TOC}$)	**OI** ($\frac{S3.100}{TOC}$)	**Conc.** $\frac{S2}{S3}$ (mgHC/ mgCO2)	**Norm. Oil Content** ($\frac{S1}{TOC}$)	**PI** ($\frac{S1}{S1+S2}$)	($\%R_o$)
Antrim	9.61	6.89	70.11	0.63	441	730	7	111	72	0.09	-
Barnett	12.2	5.39	100.49	0.57	435	824	5	176	44	0.05	-
Eagle Ford	2.85	2.45	1.57	0.22	481	55	8	7	86	0.61	-
Fayetteville	4.92	2.48	0.32	0.34	-	7	7	1	50	0.89	-
Haynesville	3.83	3.84	0.66	0.35	352	17	9	2	100	0.85	-
Woodford	4.42	0.72	25.69	0.36	434	581	8	71	16	0.03	0.65

TOC = total organic carbon in weight percent (wt.%).

S1 = free volatile hydrocarbons (HC) thermally released from a rock sample at 300°C.

S2 = products released during standard Rock Eval procedure between 300-600°C.

S3 = organic CO_2 released between 300-390°C.

T_{max} = temperature at peak evolution of S2.

HI = hydrogen index. HI reflects remaining potential to generate oil and is proportional to amount of hydrogen contained in kerogen (McCarthy et al., 2011).

OI = oxygen index. It is related to the amount of oxygen contained in the kerogen and is useful when tracking kerogen maturation and type (McCarthy et al., 2011).

PI = production index (0.00-1.00). It indicates the free oil content and the evolution of the organic matter (McCarthy et al., 2011)

R_o= vitrinite reflectance (%).

Data in Table 2.9 are used to position the gas shale formations studied on the van Krevelen diagram (Figure 2-10). The total organic carbon (TOC) in the source rocks indicates that they, except for Marcellus 46 and Marcellus 49, are good to excellent source rocks. With low Hydrogen and Oxygen indices, Haynesville and Fayetteville are mature formations. The high hydrogen index, HI (a measurement with ±10% experimental error compared to other reliable measurement such as H/C ratio with only ±0.05% error; Baskin 1997) and low production index (PI) in Antrim, Barnett, and Woodford indicates that they are immature formations.

2.4 Maturity Effect on Kerogen Distribution and Porosity

It is well documented in literature that TOC (Vernik and Landis, 1996) and maturity change the micro-texture of a source rock (Prasad and Mukerji, 2003; Prasad et al., 2009, 2011; Zargari et al., 2011). SEMs images (Zargari et al., 2011) and CT scans (Hubler et al., submitted) show a connected and continuous organic phase in immature formations vs. distributed and isolated organic globules in mature formations. Maturity, therefore, affects the texture of kerogen-bearing phases (Zargari et al., 2011) and that of kerogen by increasing its porosity. Studies relating the development of porosity in organic matter to thermal maturity (Curtis et al., 2012) show that no significant secondary porosity develops in kerogen with vitrinite reflectance, $R_o < 0.90\%$. Secondary porosity starts developing in kerogen with $R_o = 1.3\%$ without necessarily becoming a consistent consequence of thermal maturity; kerogen with $R_o > 2.0\%$ can still have negligible secondary porosity (e.g., Woodford Shale; Curtis et al., 2012), or show various porosities within the same rock (Figure 2-11). The importance of kerogen porosity is highlighted by Prasad et al. (2009). The authors show that better correlations between elastic moduli and density on one hand and sample porosity on the other are obtained when the kerogen content is taken into consideration and added to porosity; and that correlation between velocity and porosity is best if porous kerogen is assumed.

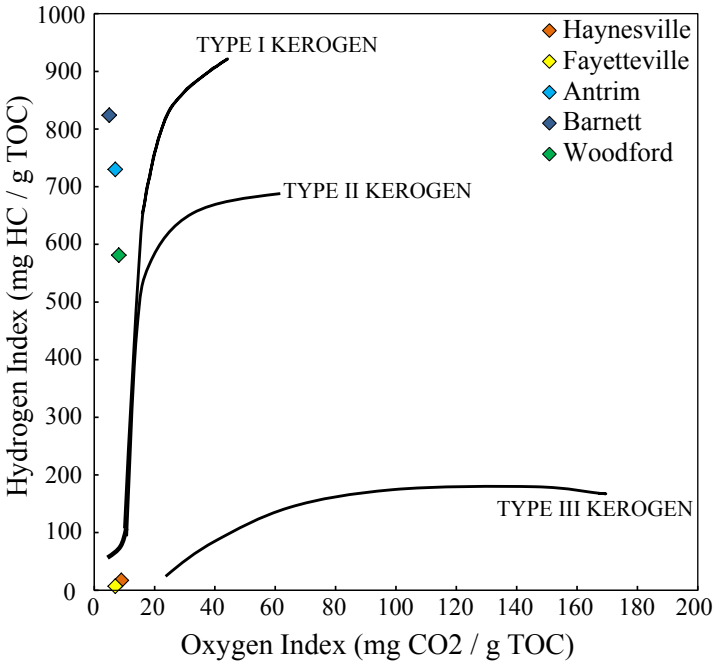

Figure 2-10: Relative positions of the various gas shale formations studied on the van Krevelen classification diagram. Lines representing kerogen types are drawn using the guidelines for HI and OI reported in Table 2.8 (Katz, 1995; Baskin, 1997).

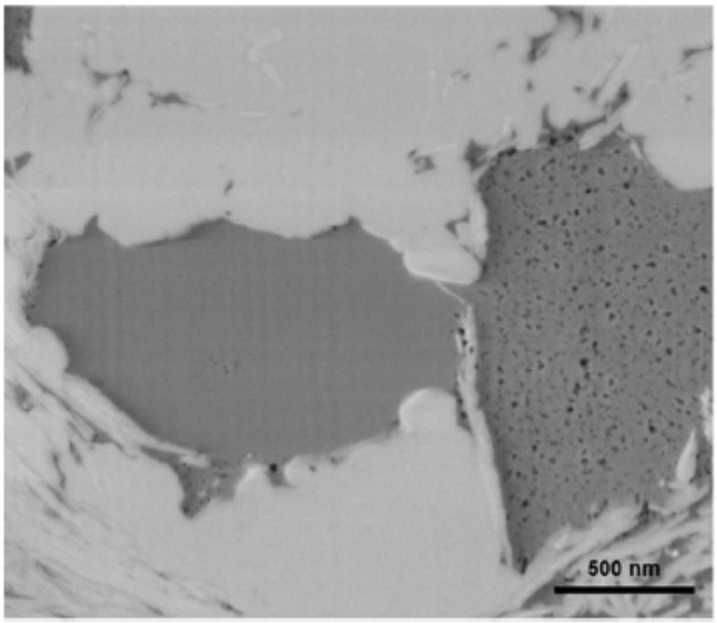

Figure 2-11: A scanning electron microscope (SEM) image of Woodford Shale sample with vitrinite reflectance of 1.4% showing an organic region with no pores (grey left) and one that is highly porous (grey right) (after Curtis et al., 2012).

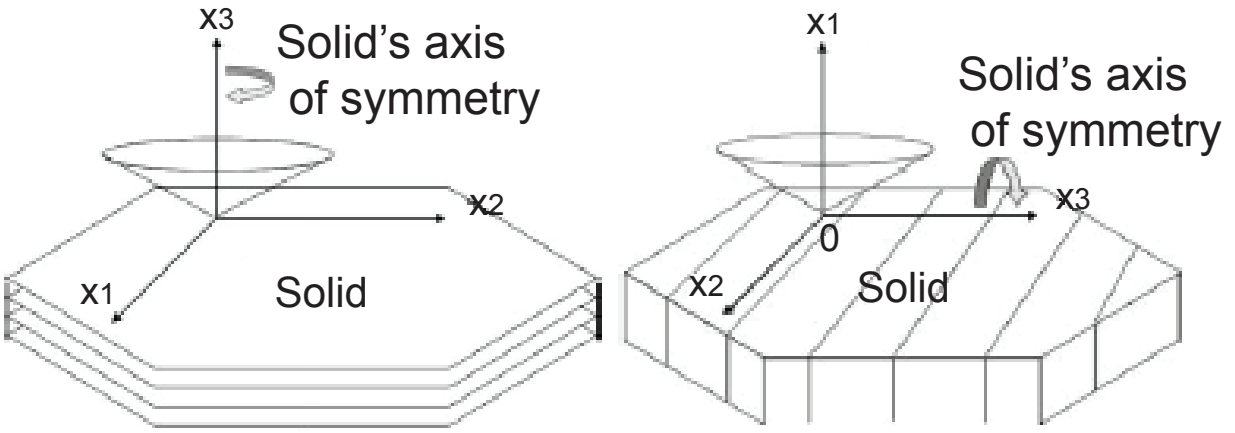

Figure 2-12: s
.A cartoon representing transverse isotropic material in which x_3, the axis of symmetry (left), is perpendicular to bedding planes depicted as sheet. An indenter is pictured as a cone indenting in either the x_3-direction (left) or the x_1-direction (right) (after Delafargue and Ulm, 2004).

2.5 Multiscale Micromechanics Model for Organic-Rich Gas Shales

Gas shale formations are multiphase, transverse isotropic (Figure 2-12), and compositionally very diverse sedimentary rocks; their compositional heterogeneity, submicrometer particle size (Boggs, 2009), low permeability, nanometer pore scale (Loucks et al., 2009; Curtis et al., 2011b,a, 2012), intricate pore structure (Loucks et al., 2009; Keller et al., 2011), and kerogen (at different maturity) content make studying them a challenging task. Understanding gas shale formations calls for proper mechanical models to represent such materials. Early mechanical models for shales were simple empirical correlations between composition (from density logs/measurements) and mechanical behavior and acoustic properties (Minear, 1982; Jones and Wang, 1981) or simplistic 1-D models consisting of layers of kerogen and shale (Vernik and Nur, 1992; Vernik and Landis, 1996). These models, however, lacked integration of kerogen characteristics and properties which are important. The maturity effect on the Young's modulus was reported by Zargari et al. (2013) studying the Bakken formation. Scanning and transmission electron microscope (SEM & TEM) images of gas shale formations shed light on the presence of nanopores, kerogen, kerogen porosity, clay particle shape and

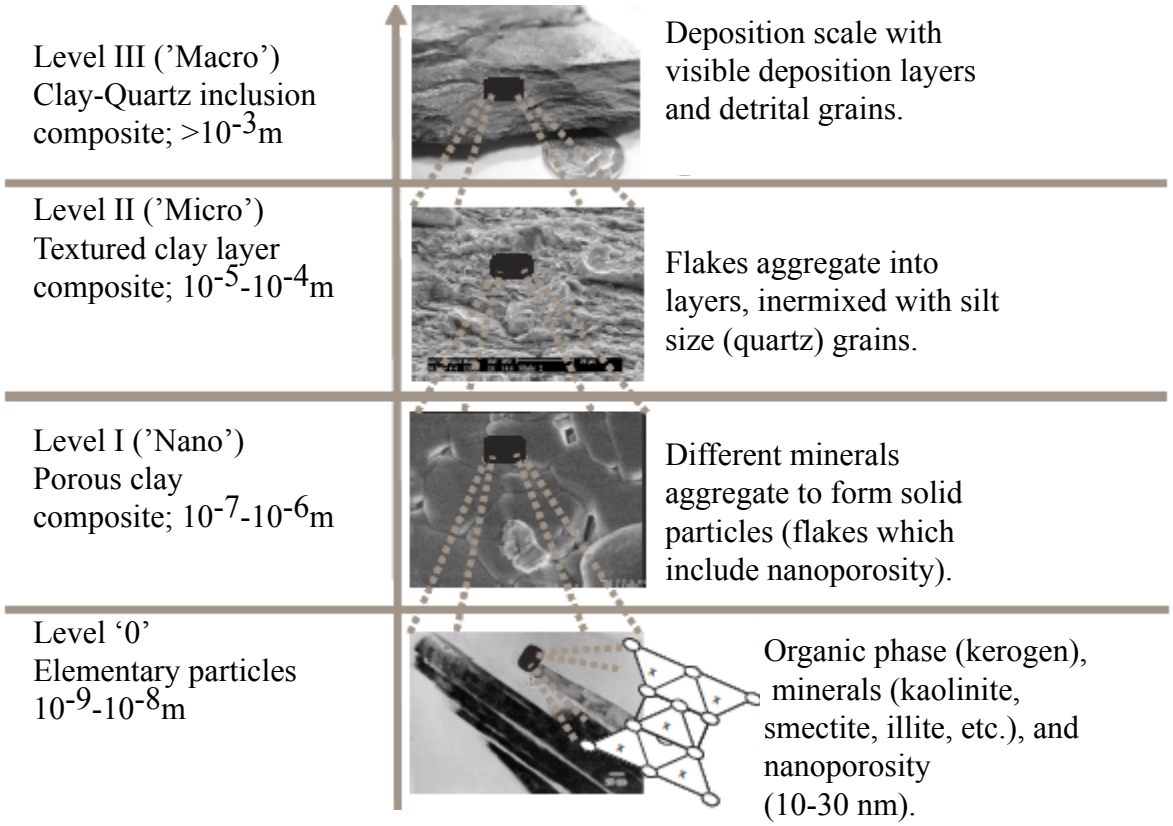

Figure 2-13: A multiscale structural thought-model of shale formations (modified after Ulm et al., 2005a).

orientations, and anisotropy in these rocks (Curtis et al., 2012; Zargari et al., 2013; Vernik and Landis, 1996). A better understanding is needed of the intricate interaction between the mineralogical composition (clay matrix and silt-size inclusions), microstructure (anisotropic clay minerals, nanoporosity, kerogen porosity), and mechanical properties of the various organic and inorganic constituents. This calls for a quantitative description of the anisotropy of gas shales at various scales to present a micromechanics framework to study the material; Ulm et al. (2005a) presented and validated a microstructural thought model for organic-free shales. The model will be adapted to serve as a framework to study organic-rich gas shale formations at the nanoscale (level I; Figure 2-13) and microscale (level II; Figure 2-13). This model consists of the following 4 levels:

2.5.1 Level 0: Elementary Particles

Level 0 is the level above atomic scale and the lowest level of a mechanical representation of a complex microstructure (Ulm et al., 2005b) usually not available for direct mechanical testing. It is the scale of the elementary solid particles (few nanometers) at which the properties of the material tested do not change from one location to another or one formation to another. In this work, the phases of most interest at level 0 are the clay particles and kerogen. Clay particles are the focus of research in clay mineralogy, imaging, and molecular simulation. XRD and electron microscopy imaging show that clay particles (Kaolinite, Illite, smectite) occur in form of platelets with a high aspect ratio (Weber et al., 2014) and exhibit transverse isotropic behavior. The latter is defined by the stiffness tensor C^s_{ij} given in the Voigt's notation as follows:

$$[C]^s_{ij} = \begin{bmatrix} C_{11} & C_{12} & C_{13} & 0 & 0 & 0 \\ C_{12} & C_{11} & C_{13} & 0 & 0 & 0 \\ C_{13} & C_{13} & C_{33} & 0 & 0 & 0 \\ 0 & 0 & 0 & 2C_{66} = C_{11} - C_{12} & 0 & 0 \\ 0 & 0 & 0 & 0 & 2C_{44} & 0 \\ 0 & 0 & 0 & 0 & 0 & 2C_{44} \end{bmatrix} \tag{2.1}$$

within a Cartesian frame of orthonormal basis $[\underline{e}_1, \underline{e}_2, \underline{e}_3]$ of elastic properties, the plane $[\underline{e}_1, \underline{e}_2]$ corresponds to bedding planes, and $\underline{e}_3$ is the direction of the symmetry axis (orthogonal to bedding planes).

2.5.2 Level I: Organic-Rich Porous Clay Composite

Level I is the scale of hundreds of nanometers (500-1000 nm) constituting a composite of clay minerals, pore space, and kerogen. The parameters of importance at this level are the clay mineralogy (reflecting sedimentation, rock burial and diagenetic history), fabric (particle arrangement, anisotropy, and packing density), "physiochemistry" (forces between clay particles, and clay structure and hydration surrounding them; Bennett et al. 1991), and kerogen content and maturity. Defining properties of level I is key to incorporate and

validate the few existing values of elastic properties of level 0, understand the effect of kerogen maturity, and have input in upscaling techniques to predict properties at levels II and III.

2.5.3 Level II: Layered Clay Composite

Level II is a layered and textured matrix of porous clay composites of level I. The structure at this level can range from an ordered sheet structure, wavy flake structure (Figure 2-6), or pressed and crushed sheet structure. Ulm et al. (2005a) show, via scanning electron microscope (SEM) images, the perturbation of the structure/layers when an inclusion is present. The scale of level II is that of (tens) of micrometers, at which the anisotropy of the gas shale formations is clear on SEM image. The prominent shale fabric (anisotropy) at this level is what differentiates level II from level I.

2.5.4 Level III: Porous Clay and Inclusion Composite

Level III is the macroscopic composite (sub-millimeter scale) composed of textured clay composites of level II and inclusions (e.g., quartz, feldspar, calcareous shells, and pyrite). The inclusion size range (sorting) and distribution (localized between clay layers or homogeneously distributed) vary from one gas shale formation to another. At this scale, the gas shale formations are the most studied and measured (acoustic methods and/or exploration petrophysics). It is agreed that at this scale the shale samples behave elastically as transverse isotropic medium (Ulm et al., 2005a).

The various levels described above form a geometric framework to determine the Representative Elementary Volume (REV) at every level. An REV is an infinitesimal volume large enough to describe and statistically represent the material with its local heterogeneities (Dormieux et al., 2006).

2.6 Scale Separability in Clay Composites

As seen in Section 2.5, clay particles are the inorganic elementary particles constituting 'level 0' of the structural thought model (Figure 2-13) we are adopting for the gas shale

formations. The ensemble of clay layers and interlayer-water form clay aggregates. These aggregates, along with porosity and organic matter trapped in them, form the porous organic-rich clay composites in the gas shale formations. The clay composites (level I of the structural thought-model) are the target probed with the nanoindentation technique (Chapter 3) for their elastic and strength properties.

For the structural model to be applicable, its different length scales must satisfy the scale separability condition. That is, the characteristic length scale at one level should be much smaller than the characteristic length scale of the next level. To ensure scale separability between levels 0 and I, the dimensions of the various components (pore volumes, organic matter, and clay particles) of the clay composites are looked at and compared to the volumes of the composite probed with indentation.

Deirieh (2016) used high magnitudes SEM images to study the thicknesses of clay aggregates in high-pressure frozen clay slurries and reconsolidated mudrock samples. He reports thicknesses ranging from 20-400 nm and 200-400 nm in slurries with different pore salinity and reconsolidated mudrock samples, respectively. Also, Ulm and Abousleiman (2006) report clay particle aggregates (matrix material) in shales having a size on the order of 500-1,000 nm. Porosity in source rocks is known to contain macropores (≥ 0.75 μm), micropores (< 0.75 μm) (Loucks et al., 2009; Wang and Reed, 2009), and nanopores (< 100 nm) (Loucks et al., 2009; Curtis et al., 2011b,a, 2012; Kuila and Prasad, 2013; Chalmers et al., 2012). Micropores are usually associated with fossils, fossils fragments, and pyrite. Micropores and nanopores occur mainly in fine-grained matrix materials and organic matter (Loucks et al., 2009). Organic matter occurs in pores situated inside the clay particle aggregates. Kerogen pockets, therefore, are rarely larger than 1-2 μm in size. All constituent of the clay composites are sub-micrometer in size.

Ulm et al. (2010) showed that when an indenter tip reaches a depth h_{max}, material situated on a surface of an average radius $4\times h_{max}$ is activated. In the clay composites (Chapter 6), the depth reached by the indenter tip is $h_{max} =$ 400-650 nm when indenting with a load $P_{max} = 4.8$ mN. The homogenized volumes producing the mechanical responses (Figure 2-14) are half-spheres with 1.6-2.6 μm radius. These homogenized volumes accommodate the composite constituents (clay aggregates, micropores and nanopores, and kerogen pockets),

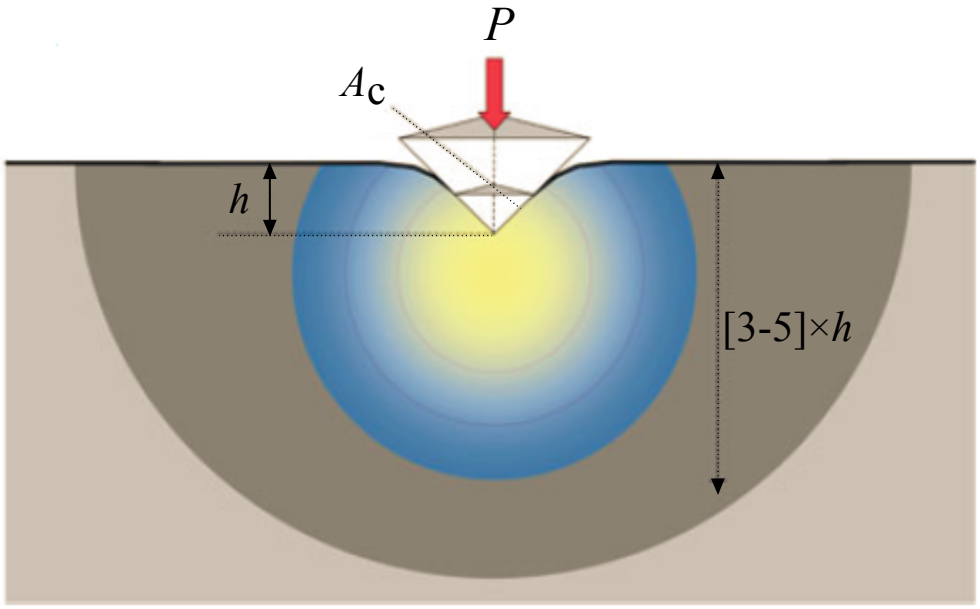

Figure 2-14: A homogenized material volume (grey area) under an indenter tip giving the mechanical response in an indentation tests (modified after Deirieh et al., 2012).

and the scale separability criterion is met.

2.7 Clay Minerals

Clay minerals are the inorganic elementary particles that make up level 0 in the source rocks. Clay minerals are found in sediments, sedimentary rocks, soils, and hydrothermal alterations zones. They are the most abundant minerals in sedimentary rocks, comprising 40% of the rock's mineral content (Weaver and Pollard, 1973). Clay minerals form primarily 1) by reaction of feldspars (tectosilicates minerals: $(Na,K,Ca)Al_{(1-2)}\ Si_{(3-2)}O_8$) and other unstable minerals; 2) mechanical break-down of pre-existing minerals (schists and other metamorphic minerals, quartz, feldspars, and recycled clay minerals); and 3) precipitation from solution (Eslinger and Pevear, 1988). Clay particles are known to group into packed ensembles (e.g., aggregates of illites; Grim, 1939) of tens of nanometers in characteristic length during deposition and diagenetic compaction. They have surfaces with a great affinity to water and other cationic solutions that help form interlayer structures between the clay layers.

Layer silicates are made of silica and brucite/gibbsite sheets. The silica sheets have SiO_4^{4-}

tetrahedra as building blocks (Figure 2-15a) all pointing in the same direction and connected by their three other corners to form hexagonal networks or tetrahedral sheets (Grim, 1939; Weaver and Pollard,1973. Figure 2-15b,c). The brucite and gibbsite sheets are formed of octahedral units (Figure 2-15d) and consist of two planes of hydroxyls ions separated by a plane of Al or Mg octahedrally coordinated to the hydroxyl ions (Figure 2-15e. Weaver and Pollard, 1973; Grim, 1939); only two-thirds of the cation positions are occupied by Al^{3+} in the gibbsite sheets whereas all cation positions are occupied by Mg^{2+} in the brucite sheets (Grim, 1939). As a result, gibbsite dioctahedrals have two cations in a half-a-unit-cell, and brucite trioctahedrals have three cations per half-a-unit-cell (Weaver and Pollard, 1973; Grim, 1939). The classification of clay minerals is based on layer stacking and charge, cation content of the octahedral sheets, interlayer materials, and the tetrahedral-octahedral sheet combinations (1:1 or 2:1 layers) (Eslinger and Pevear, 1988). A 1:1 layer (7 Å thick) consists of 1 tetrahedral sheet and 1 octahedral sheet. The main clay minerals with 1:1 layers are the kaolinite and serpentine groups. A 2:1 layer (10 Å thick) consists of two silica tetrahedral sheets and 1 octahedral sheet, all of which can be determined by XRD. The 2:1 layer clay minerals include the mica and smectite groups.

2.7.1 Illite

Illite is a generic name (after the state of Illinois) proposed by Grim et al. (1937) for the mica-type minerals occurring in argillaceous rocks. Illites make up half of the clay minerals in the Earth's crust (Weaver and Pollard, 1973) and are the major clay minerals in old sedimentary rocks. The Illite structure consists of a 2:1 layers of gibbsite sheets between silica sheets. The general formula of the members of the group is $(OH)_4K_y(Al_4,Fe_4,Mg_4,Mg_6)\ (Si_{8-y},Al_y)O_{20}$. Illite formation has been documented to happen from recrystallization of clay in clay-rich sandstones and shales, direct precipitation from solution on kaolinite or quartz surfaces, and clay transformation in bentonite beds (Meunier and Velde, 2004). There is no evidence for the formation of Illite in deep marine environment; it is accepted that most of the marine Illite are detrital in origin (Meunier and Velde, 2004; Weaver and Pollard, 1973). Both illite and mica are unstable in soils. Sedimentary Illite is formed by diagenetic processes. Weathering

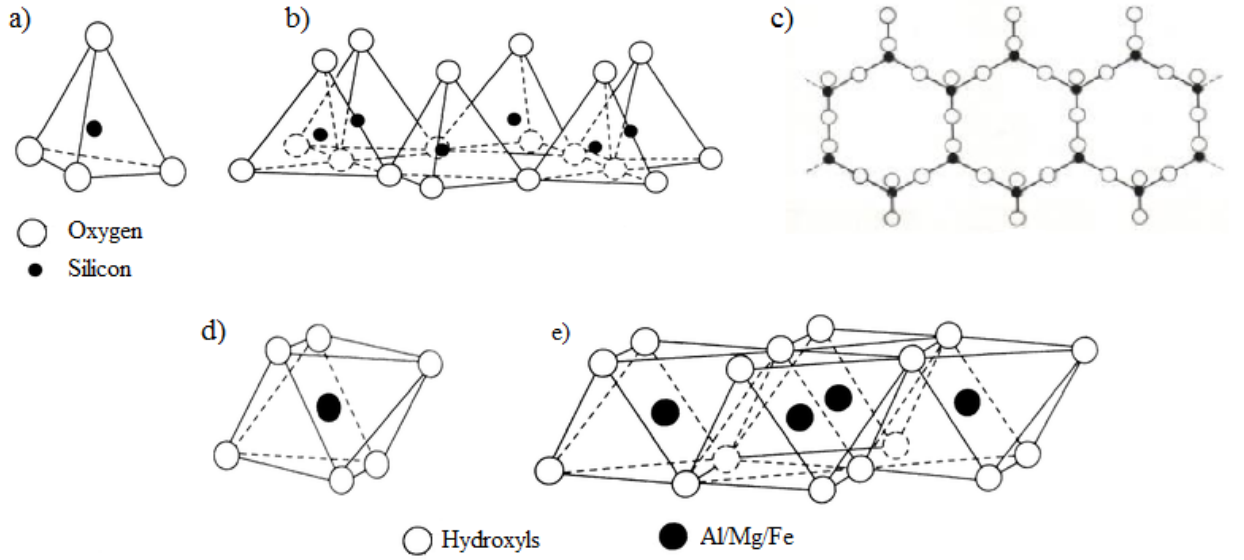

Figure 2-15: The main units constituting clay minerals: a) a silica tetrahedron, b) silica tetrahedra joined in an hexagonal network, c) top view of an extended hexagonal network forming a silica sheet, d) an octahedral unit, and e) octahedral units forming an octahedral sheet with Al, Mg, and Fe being the most likely cations to be found in the sheets (modified after Eslinger and Pevear, 1988).

of K-feldspar is a major process producing illite according to:

$$\text{K-feldspar} + H^+ + Mg \rightarrow \text{illite} + K^+ + Si^{4+} \tag{2.2}$$

Potassium released from K-feldspar weathering is needed in the transformation of pre-existing clay minerals (e.g., smectite) into illite (Meunier and Velde, 2004):

$$\text{Smectite} + K^+ + Al^{3+} \rightarrow \text{illite} + Si^{4+} \tag{2.3}$$

This latter transformation (2.3) takes place in high salinity (high K^+/H^+) waters as K^+ is needed to balance the excess charges when considerable amount of Al^{3+} replaces Si^{4+} in illite. Illite has a pronounced basal cleavage. Illite's flake-shaped grains form aggregates with charged surfaces with attractive forces (Grim, 1939; Hower et al., 1976).

The smectite-to-illite conversion reflects an increase in burial depth. Studies on cuttings from the Gulf Coast indicate a mineral conversion from <20% to 80% illites between 2,000-3,7000 m depth (Hower et al., 1976).

2.7.2 Muscovite

Muscovite is a 2-layer monoclinic dioctahedral clay mineral that belongs to the mica group. Muscovite is a potassium-rich mineral in which aluminum occurs in the octahedral sheets. Its chemical formula is $KAl_3Si_3O_{10}(OH)_2$.

2.7.3 Chlorite

Chlorite is a group of hydrous clay minerals (2:1 and hydroxide sheets) with a wide range of ionic substitution with Al, Mg, and Fe occurring in "widely varied proportions" (Weaver and Pollard, 1973). Tetrahedral sheets in chlorite have net negative charges due to Al substituting Si in the tetrahedral sites. This is balanced by substitution of Al and Fe^{3+} for Mg and Fe^{2+} in the octahedral sheets. A general chemical formula representing clay minerals in the Chlorite Group is $(Mg,Fe)_3(Si, Al)_4O_{10}(OH)_2(Mg, Fe)_3(OH)_6$.

2.7.4 Elastic Properties of Clay Minerals

Elastic properties of clay particles are scarce in literature due to the difficulty of direct measurements on clay crystals. Few studies report plane elastic properties of clay minerals (Woeber et al., 1963; Katahara, 1996; Wang et al., 2001; Prasad et al., 2002a; Vanorio et al., 2003; Ulm et al., 2005a; Mondol et al., 2008) (Table 2.10) with little agreement due to the different methodologies used and the conditions (saturation, source, etc.) of the various minerals studied. Experimentally, direct measurements of the anisotropic elasticity for large muscovite crystals possessing transverse isotropy are reported in Mavko et al. (1998) and reproduced in Table 2.10.

Due to the experimental limitations studying the mechanical properties of clay minerals, the alternative approach is molecular simulations and indentation. Hantal et al. (2014) used molecular simulations to study the elasticity and failure properties of illite. They used two different force fields to determine the elasticity tensor of the mineral (Table 2.10). The indentation technique provides an indentation modulus in which the elastic properties of a solid are condensed (Chapter 3). For a transverse isotropic solid, the indentation modulus in the direction of the axis of symmetry (x_3-direction) is (Delafargue and Ulm, 2004; Bobko

et al., 2011):

Table 2.10: Elastic properties of clay minerals.

	C_{ij} (GPa)					
Mineral	C_{11}	C_{12}	C_{13}	C_{33}	C_{44}	C_{66}
Muscovite[a]	178.0	42.4	14.5	54.9	12.2	-
Muscovite[b]	184.3	48.3	23.8	59.1	16.0	72.4
Illite-ReaxFF[c]	216 ± 5	76 ± 9	29 ± 4	93 ± 1	4.7 ± 0.6	14 ± 2
Illite-ClayFF[c]	292.5 ± 0.5	128.3 ± 0.4	16.7 ± 0.08	48.9 ± 0.1	8.99 ± 0.02	90.1 ± 0.2
Illite[d]	179.9	39.8	14.5	55	11.7	70
Chlorite[d]	181.8	56.8	20.3	106.8	11.4	62.5
Kaolinite[d]	171.5	38.9	27.1	52.6	14.8	66.3
Gas Shales[e]	103.0	41.6	34.1	43.4	7.7	72.3

[a] Direct measurements on muscovite crystal from Mavko et al. (1998).

[b]Vaughan and Guggenheim (1986).

[c] Molecular Simulation from Hantal et al. (2014).

[d]Katahara (1996).

[d]Backanalysis results from sonic measurements from Monfared and Ulm (2015).

$$M_3 = 2\sqrt{\frac{C_{11}C_{33} - C_{13}^2}{C_{11}}\Big(\frac{1}{C_{44}} + \frac{2}{\sqrt{C_{11}C_{33}} + C_{13}}\Big)^{-1}} \tag{2.4}$$

Normal to the axis of symmetry (x_1-direction), the indentation modulus is:

$$M_1 = M_2 = \sqrt{\sqrt{\frac{C_{11}}{C_{33}}}\frac{C_{11}^2 - C_{12}^2}{C_{11}}M_3} \tag{2.5}$$

Elasticity moduli obtained from indentation in the x_1-direction are found to range between 20-100 GPa for different clay minerals and polycrystalline clay samples (data courtesy of Dr. Christian Hoover and Dr. Jeremy Berthonneau).

2.8 Clay Composites: Porosity Distribution and Volume Fractions

In order to use micromechanics textural models (Chapter 7) to describe porous organic-rich clay composites, the XRD results and porosity measurements of the studied samples are

Table 2.11: Mass density of the main minerals in the source rocks studied.

Mineral	Density(g/cm^3)
Albite	2.65
Anatase	3.89
Apatite	3.19
Barite	4.48
Calcite	2.71
Chlorite	2.9
Cristobalite	2.27
Dolomite	2.86
Gypsum	2.32
Halite	2.17
Illite	2.65
K-Feldspar	2.56
Microcline	2.55
Muscovite	2.82
Plagioclase	2.68
Pyrite	5.01
Quartz	2.65
Sanidine	2.52
Siderite	3.96

converted into corresponding composite volumetric fractions. This step helps to understand and model the mechanical behavior of the gas shale rocks and clay composites in terms of the volume fractions of their constituents.

2.8.1 Level II: Volume Fractions

Based on the presented multiscale structural thought-model for organic-rich shales (Section 2.4), the volume fractions at the macroscopic length scale (level II) is $\phi^{II}+\sum_{k=1}^{N} f^i = 1$; where ϕ^{II} is the measured porosity obtained either experimentally by GRI methods (Gas Research Institute Report (GRI-95/0496) on crushed shale analysis method), BET (Brunauer-Emmett-Teller method), or estimated from measuring the volume and mass of a sample. f^i is the volume fraction of phase i in the sample at level II given by:

$$f^i = (1-\phi^{II})\frac{\frac{m_i}{\rho_i}}{\sum_{k=1}^{N}\frac{m_k}{\rho_k}} \tag{2.6}$$

N is the number of all phases (minerals and kerogen) in the formation; m_i is the mass fraction of a phase from XRD results, and ρ_i is the corresponding mass density (Table 2.11).

The inclusion volume fraction is:

$$f^{incl} = (1 - \phi^{II}) \frac{\sum_{j=1}^{R} \frac{m_j}{\rho_j}}{\sum_{k=1}^{N} \frac{m_k}{\rho_k}} \tag{2.7}$$

where R refers to all non-clay inorganics (non-clay minerals) in the samples.

In all formations, kerogen density is assumed to be $\rho_k = 1.2\ g/cm^3$. The choice for this kerogen density is based on values reported in literature. Vernik and Landis (1996) report density range of 1.0-1.4 g/cm^3 for kerogen at different maturity levels. The authors used 1.25 g/cm^3 modeling shale rocks. Similarly, Tissot and Welte (1984, in Gonzalez et al., 2013) report a grain density of kerogen of 1.1-1.4 g/cm^3; whereas Carmichael (1989) reports a kerogen density of 1.3 g/cm^3.

2.8.2 Level I: Volume Fractions

At the indentation level, level I (or mesoscale), the indented volume is composed of an inorganic solid phase (clay particles), organic phase (kerogen), and pore space:

$$\eta_c + \eta_k + \phi^I = 1 \tag{2.8}$$

where η_c and η_k are the volume fractions of clay and kerogen, respectively, in the clay composites. ϕ^I is the porosity at level I, that is the porosity of the clay composite.

Recalling observations in Section 2.4, kerogen maturity affects its texture and connectivity, on one hand, and the texture of the organic-bearing phases, on the other. In mature formations, kerogen occurs as pockets randomly dispersed among clay aggregates (Zargari et al., 2013). In immature formations, the organic phase shows more continuity within the clay layers (Zargari et al., 2013). Therefore, volume fractions of the various constituents in the clay composites are calculated depending on the formation maturity level[2]. In mature

[2]In Chapter 7, the effect of maturity on the clay composite texture is modeled; different textural models are ascribed to clay composites based on the maturity of their organic content.

samples, the porosity is assumed to be evenly distributed among all (organic and inorganic) phases, and kerogen is assumed to be concentrated in the clay composites. Porosity at level I, or mesoscale porosity, is therefore equivalent to the porosity at level II ($\phi^I = \phi^{II}$). With $f_{incl} + f_c + f_k + \phi^{incl} + \phi^c + \phi^k = 1$, the kerogen volume fraction at level I, n_k, is:

$$\eta_k = \frac{f_k}{f_k + f_c + \phi^I} = \frac{f_k}{1 - (f^{incl} + \phi^{incl})} \tag{2.9}$$

where f_c and f_k are volume fraction of clay and kerogen at level II, respectively. $\phi^I = \phi^c + \phi^k$ is the porosity at level I.

The porosity in each phase is obtained using:

$$\phi^i = \frac{f^i}{f_{incl} + f_c + f_k}\phi^{II} \tag{2.10}$$

In immature formations, the clay phase is assumed to contain all the organic matter and porosity. The clay and kerogen volume fractions at level I are obtained using:

$$\eta_{c,k} = \frac{f_{c,k}}{f_k + f_c + \phi^{II}} \tag{2.11}$$

Level I porosity, ϕ^I, is:

$$\phi^I = \frac{\phi^{II}}{f_k + f_c + \phi^{II}} = \frac{\phi^{II}}{1 - f^{incl}} \tag{2.12}$$

Tables 2.12 and 2.13 present porosities and volume fractions of kerogen and clay mineral in the clay composites for the samples studied. The values in the tables are obtained using densities in Table 2.11 and XRD data (Section 2.2). Appendix A contains detailed calculations of level II volumes fractions of all the minerals in the samples as well as level I volume fractions (clay, kerogen and porosities) in the clay composites.

The above assumptions pertaining to porosity distribution assign different weights to different components based on their mechanical behavior in the clay composites. The assumptions will be used (and validated) in Part III in the context of assigning different mechanical effective textures to materials with different maturity.

With the calculated volume fractions in the clay composites, we note that all the gas shale formations have high packing densities (4-9.6 % porosity), and the proposed porosity distribu-

Table 2.12: Porosities and volume fractions of kerogen and clay minerals in the clay composites of immature formations. ϕ^I=level I porosity; ϕ^{II}=level II porosity.

Sample	$n_k(\%)$	$n_c(\%)$	$\phi^{II}(\%)$	$\phi^I(\%)$
Antrim	33.6	49.1	8.8	16.9
Barnett	34.7	53.5	7.3	11.7
Woodford	16.4	57.2	12.6	26.5

Table 2.13: Porosity and volume fractions of kerogen and clay minerals in the clay phases of mature formations. Note that, in mature formations, Level I porosity (ϕ^I) equals Level II porosity (ϕ^{II}).

Sample	$n_k(\%)$	$n_c(\%)$	$\phi^I = \phi^{II}$
A2V-H	15.5	77.2	7.4
A5V-H	10.9	83.1	6.0
A6V-H	13.7	79.11	7.2
A7V-H	14.7	77.7	7.6
Mar46	2.5	89.1	8.4
Mar49	5.3	86.8	7.9
Mar108	25.4	67.4	7.2
Mar150	27.9	66.2	5.9
Mar151	30.5	63.0	6.5
Fayetteville	30.1	65.9	4.0

tions produce higher porosities (less packing) in immature clay composites (Table 2.12) than in mature ones (Table 2.13). This depicts the situation of having a continuous organic phase connecting micropores in immature formations. This is not the case when kerogen occurs in isolated pockets in mature formations. Indeed, we see a good correlation between sample porosity and TOC in the immature formation (Figure 2-16). This correlation is preserved between ϕ^I and TOC in the immature clay composites. No correlation exists between maturity and porosity. This may be due to undetected kerogen nanoporosity with the methods used to measure sample porosity.

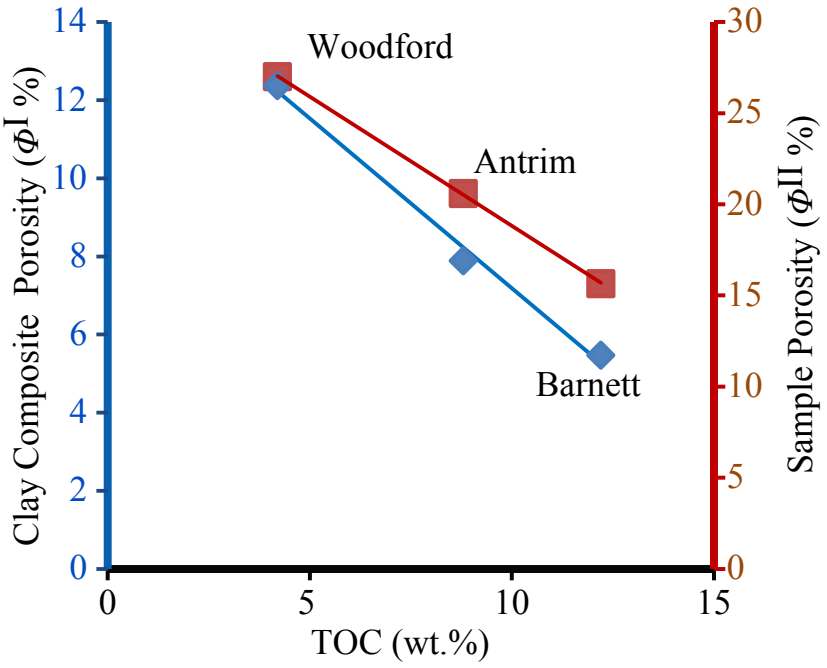

Figure 2-16: TOC vs. porosity (blue = clay composite porosity; red = sample porosity) correlations in immature formations.

2.9 Chapter Summary

Except for a low porosity range, which is an intrinsic property of argillaceous formations, the gas shale formations cover all other depositional and diagenetic aspects that affect the mechanical properties of source rocks. The gas shale formations formed in different basins and depositional environments. They have different mineralogy, and their organic content ranges from poor (0.49 wt. %) to very rich (12.2 wt. %). Also, different maturity levels are represented as immature, mature, and over-mature formations are tested.

A thought-model for shale is used as a mechanical framework to separate and study the gas shale formations at different scales. Two scales are of foremost importance in this work: level 0, the solid particle level, and level I, the porous organic-rich clay composites scale. A review of the dimensions of the various constituents (clay particle aggregates, porosity, and organic phase) of the clay composites demonstrates scale separability between these two

levels, and highlights the volumes that need to be targeted to study the composite mechanical properties. These volumes are equivalent to half-spheres of 1.6-2.6 μm radius, and make the indentation technique (next chapter) a suitable approach to obtain the mechanical properties of the clay composites.

Chapter 3

Elasticity and Strength Properties from Indentation

In Chapter 2, the value of studying source rocks at various scales due to their chemical heterogeneity and textural complexity was highlighted. In this chapter, indentation testing– the first technique in our experimental research approach– is introduced as a means to probe the mechanical properties of small material volumes. Concepts and solutions of the mechanics of contact problem of a probe of certain geometry with a material are reviewed. Contact problem solutions and indentation test analysis give two time-independent mechanical properties: the indentation modulus, M, and hardness, H. The first relates to the elasticity content and the second to strength properties of the indented material. M and H will be coupled with chemical data obtained from spectroscopy (Chapter 4) to isolate, via a statistical analysis approach (Chapter 5), the porous organic-rich clay composites in the formations.

After reviewing the various indenter shapes and the self-similarity of contact problems, solutions to contact problems in isotropic and anisotropic material will be summarized. The aim is to 1) show that the indentation modulus obtained from solutions of the Hertzian contact problem in an isotropic half-space are valid for anisotropic media, 2) emphasize the difficulty of determining the area of contact between indenter and material and the importance of accurately doing so, and 3) present how indentation hardness is determined and related to material strength properties.

3.1 Introduction

To study small volumes of materials and probe their mechanical properties at the sub-micron scale, we use the indentation technique. An indentation test consists of pushing perpendicular to a polished horizontal material surface an indenter (Figure 3-1) of known geometry and mechanical properties at a certain loading or displacement rates (Vlassak and Nix, 1994). Indentation machines (Appendix B) are capable of controlling the load, P, exerted on the material and continuously measuring the depth of indentation, h, of the indenter tip from the flat material surface. The test typically consists of 3 stages (Figure 3-2): a loading phase to reach a maximum load, P_{max}, a hold phase during which load is kept constant, and a continuous unloading phase. The loading and unloading rates and the hold time are all user-specified. In this work, force-controlled nanoindentation tests with maximum force, P_{max}, of 4.8 mN are performed using a Berkovich tip (Figure 3-3d). Microindentation creep tests (Chapter 9) are performed with P_{max} ranging from 12 to 50 mN using the same tip geometry. The choice of P_{max} depends on maximum penetration depth intended during an indentation test and the volume of material to be homogenized under the indenter tip (refer to Section 2.6). In nanoindentation tests, the target is the nanoscale (hundreds of nm) or level I equivalent to the clay composites in gas shale formations. In regular (short hold-time) indentation tests, each stage (loading, hold, unloading) lasts 10 seconds. In creep tests, the hold time is 3-minute long.

Due to the heterogeneity of the gas shale formations studied, the grid indentation technique is followed to cover representative areas of the material surface and acquire a large number of indentations tests that will be treated statistically in Chapter 5. Grid indentation consists of indenting following an $n \times n$ grid, n being the number of columns and rows in the grid. The spacing between indentations depends on P_{max} reached and the maturity of the formation. For instance, 5 μm-spacing and 6 μm-spacing were used indenting mature and immature formations, respectively, with $P_{max} = 4.8$ mN. With higher loads, the spacing between indents increases in order to prevent interference between indented volumes. Every indentation test is checked for a good indenter-material contact at the start of the test and a smooth increase in indentation depth with increasing load. The former ensures that the

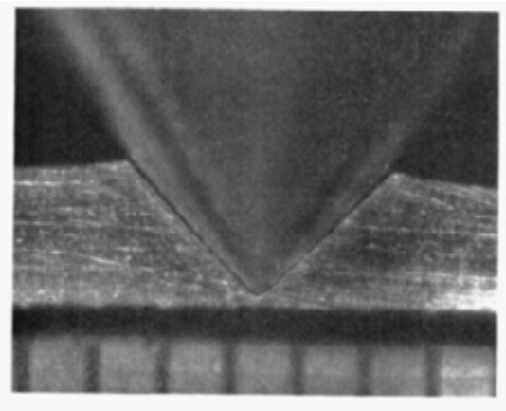

Figure 3-1: Cross-section of an indenter in duralumin showing an indentation with straight edges, each is 1mm in length. Note the conical angle of the indentation impression being slightly larger than that of the indenter (Stilwell and Tabor, 1961).

indenter tip is not falling in a large pore or crack. The latter ensures the absence of a large pore under the sample surface. Hidden pores are indicated as jumps (in depth with negligible change in load) on the loading segment of the test.

3.2 Indenter Geometries

Indenters with variable tip geometries (Figure 3-3; Table 3.1) are used in indentation tests. Flat punch indenters, although not much used today, were important developing the theory of contact problems as the contact area between the indenter and material remains constant during the loading process. Spherical indenter probes are mostly employed for soft materials; they were used by Tabor (1948) to determine material hardness and to show that the elasticity of the material can be studied when dealing with small load magnitudes. Vickers and Berkovich indenters (Figure 3-3d,e) have a suitable (tip) geometry to test smaller volumes of materials but one that generates stress concentrations and leads to plastic deformation even at low load magnitudes (Stilwell and Tabor, 1961).

When two bodies (an indenter and a material half space) come into contact, they interact mechanically at the area of contact, A_c (the area between the indenter tip and the indented material at P_{max}; Figure 3-4). Except when indenting with a flat punch (Figure 3-3a), the projected contact area is usually unknown. It is extrapolated from the depth reached. To illustrate this, consider a Cartesian coordinate system, $O - x_1x_2x_3$, with the origin at the

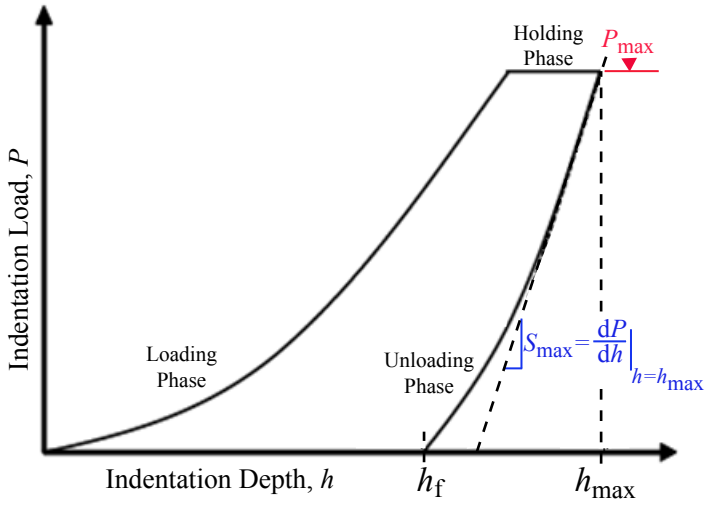

Figure 3-2: Load-displacement curve from a typical indentation test (modified after Vandamme and Ulm, 2006). P_{max} and h_{max} are the maximum load and respective displacement, respectively. h_f is the residual displacement after unloading.

indenter tip, and x_3 being the direction of indentation (i.e. parallel to the depth of the probe). The height, z, of the surface of the probe (Figure 3-4) is a homogeneous function describing the shape of the indenter of degree d (Table 3.2):

$$z(\lambda x_1, \lambda x_2) = \lambda^d z(x_1, x_2), (\lambda > 1) \tag{3.1}$$

For axisymmetric indenters, Equation (3.1) becomes:

$$z(r) = B(\theta) r^d \tag{3.2}$$

$B(\theta)$ (Table 3.2) describes the height of the indenter at a point (θ,r) on a circle of unit radius (Borodich et al., 2003).

Table 3.1: Indenter types and equivalent half-cone angles (Vandamme, 2008).

Indenter Type	Equivalent half-cone angle θ^{eq}
Berkovich, Vickers	70.32°
Cube Corner	42.28°

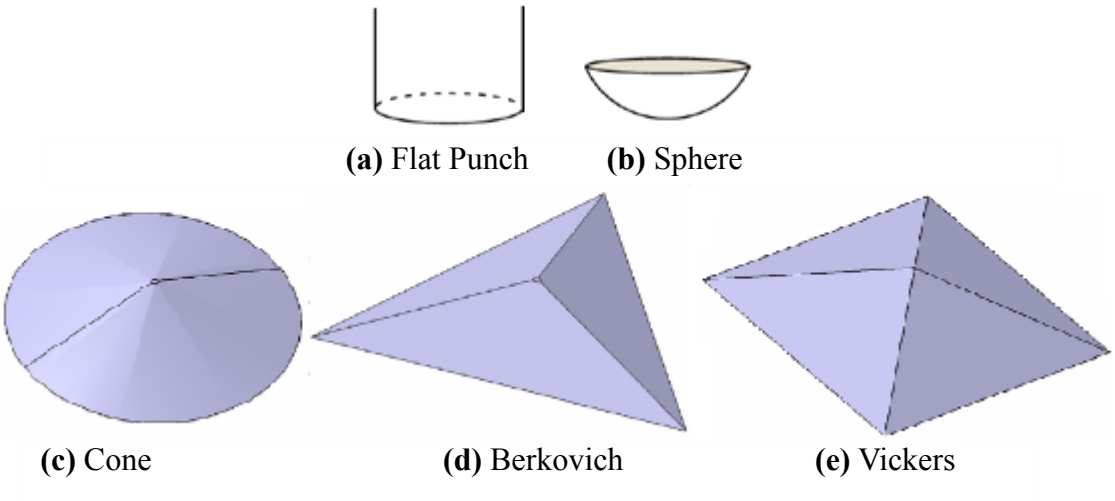

Figure 3-3: Different indenter tip geometries. The Berkovich tip radius is 50-150 nm (Fischer-Cripps, 2007). (a,b are modified after Vandamme, 2008; c,d,e are modified after Sakharova et al., 2009).

Table 3.2: The degree, d, of the homogeneous function describing the shape of the indenter and the proportionality factor, B, for various indenter geometries.

Indenter Type	d	B
Flat Punch	$\rightarrow \infty$	$\frac{1}{a^n}$
Spherical	2	$\frac{1}{2R}$
Conical	1	$\cot(\theta)$
Pyramidal	1	$\cot(\theta^{eq})$

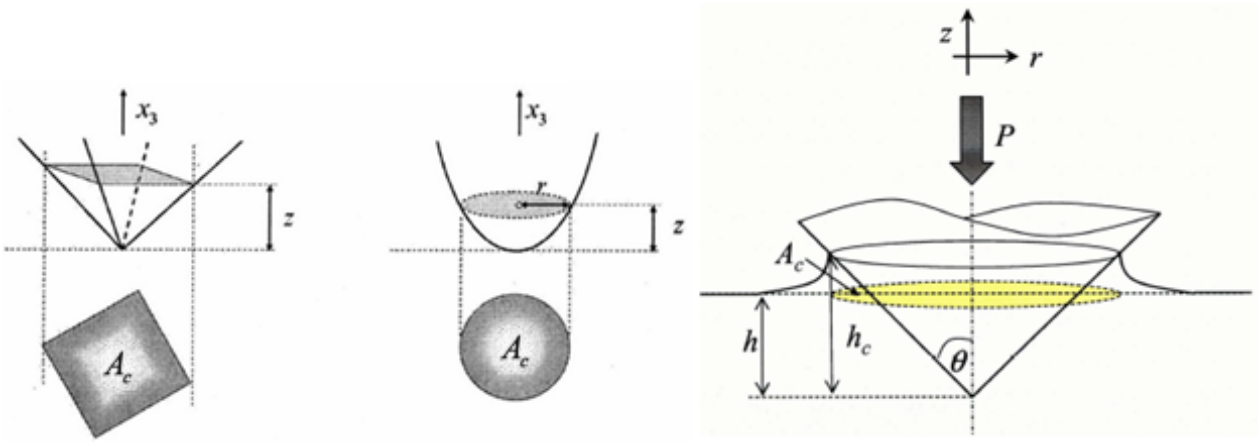

Figure 3-4: Parameters defining the geometry of non-axisymmetric probe (left) and an axisymmetric probe (middle). The indenter geometry (right) shows the half-apex angle, θ, and the rigid indentation depth, h. A_c is the cross-sectional area at an indentation depth corresponding to a probe height, $z = h$ (after Vandamme, 2008).

3.3 Self-Similarity of Indentation Tests

A phenomenon is referred to as self-similar if the "spatial distribution of its properties at various moments of time can be obtained from one another by a similarity transformation" (Barenblatt, 1996). The conditions under which Hertz-type contact problems possess self-similarity are the following (Borodich and Galanov, 2002; Borodich et al., 2003):

- The shape of the indenter probe must be described by a homogeneous function of degree $d \geq 1$ (Equation (3.1)). A flat punch and spherical indenters are geometrically similar. Berkovich, Vickers, and cone indenters are geometrically self-similar.

- The constitutive relations of the indented material must be homogeneous functions with respect to strain (or stress) (Borodich, 1993); that is, the operator of constitutive relations F must scale as:

$$F(\lambda \boldsymbol{\epsilon}) = \lambda^k F(\boldsymbol{\epsilon}) \tag{3.3}$$

  where $\boldsymbol{\epsilon}$ is the strain tensor and k is the degree of the homogeneous constitutive function, F. Equation (3.3) is satisfied by linear or non linear elasticity, since $\boldsymbol{\sigma} = \mathbb{C}(\boldsymbol{\epsilon}) : \boldsymbol{\epsilon}$, and

$$\mathbb{C}(\lambda \boldsymbol{\epsilon}) = \lambda^{k-1} \mathbb{C}(\boldsymbol{\epsilon}) \tag{3.4}$$

where $\mathbb{C}(\boldsymbol{\epsilon})$ is the elastic stiffness tensor. The operator F can also represent elastic or inelastic, isotropic or anisotropic materials (Borodich et al., 2003).

- Loading must be progressive during the contact process (Borodich and Galanov, 2002). Otherwise, the problem is no longer self-similar.

The concept of self-similarity is an important feature of indentation tests as it links indentation data (load and displacement) to material mechanical properties. It implies that the displacement field at any load P can be inferred from the displacement field at a different load P_o (Borodich, 1993):

$$\frac{P}{P_o} = \left(\frac{h}{h_o}\right)^{\frac{2+k(d-1)}{d}} \tag{3.5}$$

This ensures that the indenters have the same cross-sectional area at a given height z, thus, giving expressions relating indentation depths to contact areas (Borodich et al., 2003):

$$\frac{h}{h_o} = \left(\frac{A_c}{(A_c)_o}\right)^{\frac{d}{2}} \tag{3.6}$$

3.4 Solutions to Contact Problems

Solutions to contact problem consist of finding the stress and displacement fields in the (elastic) half-space due to a certain load applied. Most materials deform elastically when the deformation is small. Solutions of contact problems between elastic bodies were developed in the 19^{th} century (Boussinesq, 1885; Hertz, 1882). Love (1939) solved the indenter-material contact problem for both flat and conical indenters. The major contribution of importance in this work, as an axisymmetric indenter is used, is that of Sneddon (1965).

3.4.1 Elastic Isotropic Material: The Galin-Sneddon Solution

Sneddon (1965) solved the Boussinesq problem using Hankel transforms and solving a pair of dual integral equations assuming a contact problem with small perturbations. Sneddon's

problem has the following boundary conditions:

$$\begin{cases} \sigma_{zz}(\rho > a, 0) = 0 \\ \sigma_{\rho z}(0 \leq \rho \leq a, 0) = 0 \\ u_z(0 \leq \rho \leq a, 0, 0) = h - f(\frac{\rho}{a}) \end{cases} \tag{3.7}$$

Expressions for load and penetration depth are then derived (Sneddon, 1965):

$$P = \frac{4G\alpha}{1-\nu} \int_0^1 \frac{x^2 f'(x)}{\sqrt{1-x^2}} dx \tag{3.8}$$

$$h = \int_0^1 \frac{f'(x)}{\sqrt{1-x^2}} dx \tag{3.9}$$

where f is a function defined by the relation $w(\rho) = f(\frac{\rho}{a})$ with $w(\rho)$ being the equation of the punch in polar coordinates (Sneddon, 1965).

Sneddon (1965) also presented simple formulas relating load, indenter depth, and contact area for indenters of various profiles. He showed that the load-displacement relationships are of the form:

$$P = \alpha h^m \tag{3.10}$$

where α and m are constants. m is 1, 2, or 1.5 for flat cylinder, cones, and spherical punch geometries (Table 3.1), respectively, in the limit of small displacements (Oliver and Pharr, 1992). For flat punches, that he used to relate stress and displacement fields to material properties, Sneddon found that:

$$P = \frac{4\mu a}{1-\nu} h \tag{3.11}$$

where a is the radius of the cylindrical punch, μ is the shear modulus, and ν is the Poisson's ratio of the indented material.

Hay et al. (1999) and Vandamme (2008) simplified and summarized Sneddon's findings for an axisymmetric indenters ($z(r) = Br^d$). They showed that:

- A constant depth ratio reflects the self-similarity of the problem from which the contact

depth, h_c, and the contact area, A_c, can be obtained[1]:

$$\frac{h_c}{h} = \frac{1}{\sqrt{\pi}} \frac{\Gamma\left(\frac{d}{2}+\frac{1}{2}\right)}{\Gamma\left(\frac{d}{2}+1\right)} = \frac{2}{\pi} \Rightarrow h = \frac{a\pi}{2\tan\theta} \tag{3.12}$$

where θ is the half-included angle of the indenter. Finite element modeling (Hay et al., 1999) shows that h is independent of boundary conditions.

- A link between the indentation load and depth is obtained:

$$\begin{aligned} P &= \frac{2}{(B\sqrt{\pi})^{\frac{1}{d}}} \frac{E_0}{1-\nu^2} \frac{d}{1+d} \left[\frac{\Gamma(\frac{d}{2}+\frac{1}{2})}{\Gamma(1+\frac{d}{2})}\right]^{\frac{1}{d}} h^{1+\frac{1}{d}} \\ &= \frac{\pi}{2} \frac{E_0}{1-\nu^2} a h_c = \frac{\pi}{2} \frac{E_0}{1-\nu^2} \frac{a^2}{\tan\theta} \\ &= \frac{2}{\pi} \frac{E_0}{1-\nu^2} \tan\theta h^2 \end{aligned} \tag{3.13}$$

where $\Gamma(x) = \int_0^\infty t^{x-1} e^{-t} dt$ is the Euler Gamma function. E_0 is the Young's modulus, ν is the Poisson's ratio of the indented material.

- The stress field in the elastic half-space is:

$$\sigma_{zz}(\rho < a, 0) = \frac{1}{2\tan(\theta)} \frac{E_0}{1-\nu^2} \cosh^{-1}(\frac{a}{\rho}) \tag{3.14}$$

- The displacement field is:

$$u_\rho(\rho < a, 0) = \frac{1-2\nu}{4(1-\nu)\tan\theta} \left[\ln(\frac{\frac{\rho}{a}}{1+\sqrt{1-(\frac{\rho}{a})^2}}) - \frac{1-\sqrt{1-(\frac{\rho}{a})^2}}{(\frac{\rho}{a})^2}\right] \tag{3.15}$$

$$u_z(\rho < a, 0) = \frac{1}{\tan\theta} \left[a \sin^{-1}(\frac{\rho}{a}) + \sqrt{\rho^2 - a^2} - \rho\right] \tag{3.16}$$

Hay et al. (1999) showed, using finite element modeling, that Sneddon's solution overestimates the contact radius by 9%, and consequently, the contact area by 19%. The overestimate is due to the assumption that, in the area of contact, the deformed surface has the same shape

[1]For a Berkovich indenter, d=1. $\Gamma(1) = 0! = 1$, and $\Gamma(\frac{3}{4}) = \frac{\sqrt{\pi}}{2}$.

as that of the indenter. Vandamme (2008) argued that the assumption of small perturbations in the Sneddon's solution is not a valid one and that Equation (3.15) is only valid for incompressible material. For any other material, a correction factor, γ, is needed (Hay et al., 1999; Oliver and Pharr, 2004; Vandamme, 2008). Hay et al. (1999) and Oliver and Pharr (2004) showed that γ is slightly larger than unity, and, for a Berkovich indenter:

$$\gamma(\nu,\theta) = \pi \frac{(\frac{\pi}{4}) + 0.1548\cot\theta\frac{1-2\nu}{4(1-\nu)}}{\frac{\pi}{2} - 0.8312\frac{1-2\nu}{4(1-\nu)}} \tag{3.17}$$

3.4.2 Elastic Anisotropic Material

In anisotropic half-space, the difficulty is in determining the load distribution under the indenter and obtaining the contact area that is no longer circular except when indenting with a cylindrical punch. Vlassak and Nix (1993, 1994) addressed contact problems in anisotropic material and found expressions for the load and displacement fields under indenters of different geometries. Assuming the same load distribution under a flat punch as obtained by Sneddon (1965) in isotropic material, Vlassak and Nix (1993) obtained constant displacement under a flat punch validating the pressure distribution assumption in anisotropic material. The authors obtained the following expressions for load and displacement:

$$P = \iint_S \frac{p_o}{\sqrt{a^2 - (x^2+y^2)}} dxdy = 2\pi p_o a \tag{3.18}$$

and

$$h = \frac{P}{4a} \oint_{|\underline{\xi}|=1} W(\underline{\xi}) ds \tag{3.19}$$

where x and y are the coordinates of a position vector, $\underline{x}$, on the boundary of the half-space. $W(\underline{\xi})$ is the Fourier transform of $w(\underline{x})$, the vertical displacement due to a unit point load applied at the origin and perpendicular to the surface of the half-space (Vlassak and Nix, 1994). $\underline{\xi}$ is a vector (ξ_1, ξ_2). The contact stiffness is given by Vlassak and Nix (1993):

$$S = \frac{dP}{dh} = \frac{2}{\sqrt{\pi}}\sqrt{A_c}\left(\frac{1}{2}\oint_{|\underline{\xi}|=1} W(\underline{\xi}) ds\right)^{-1} \tag{3.20}$$

For a paraboloid indenter penetrating an anisotropic material, the contact area is elliptical with axes a_1 and a_2. The indentation depth and contact stiffness are (Vlassak and Nix, 1993):

$$h = \frac{3P}{8a_1a_2}\oint_{|\underline{\xi}|=1} W(\frac{\xi_1}{a_1},\frac{\xi_2}{a_2})ds = \frac{3P}{8a}\oint_{|\underline{\xi}|=1} W(\frac{\xi_1}{\delta_1},\frac{\xi_2}{\delta_2})ds \tag{3.21}$$

$$S = \frac{dP}{dh} = \frac{2}{\sqrt{\pi}}\sqrt{A_c}\left(\frac{1}{2}\oint_{|\underline{\xi}|=1} W(\frac{\xi_1}{\delta_1},\frac{\xi_2}{\delta_2})ds\right)^{-1} \tag{3.22}$$

with $\delta_1 a_1 = \delta_2 a_2$, and $\delta_1\delta_2 = 1$.

For a three-sided pyramidal indenter modeled as a flat triangular punch, the penetration depth in terms of an unknown pressure distribution, p is (Vlassak and Nix, 1994):

$$h = \iint_S p(\underline{x}')w(\underline{x}-\underline{x}')ds \tag{3.23}$$

$W(\underline{\xi})$ and $W(\frac{\xi_1}{\delta_1},\frac{\xi_2}{\delta_2})$ in the above expressions can be found numerically or analytically depending on the symmetry of the anisotropic half-space (Vlassak and Nix, 1994). Analytical solutions are obtained when indenting parallel to high symmetry directions (e.g., threefold and fourfold rotation axis perpendicular to the half-space surface) as the contact area in this case is circular (Vlassak and Nix, 1994). For higher symmetry, such as transverse isotropy, analytic solutions were presented by Willis (1966). With low symmetry, on the other hand, numerical techniques are used to approximate the eccentricity and orientation of the elliptical contact area (Ciavarella et al., 2001; Bagault et al., 2012) in order to obtain S.

3.5 Time-Independent Properties from Indentation

The indentation modulus, M, and hardness, H, are the properties measured using the indentation technique. M and H are related to the elastic and strength properties of the tested material, respectively, as long as the projected area at maximum load is accurately estimated.

3.5.1 The Indentation Modulus

First introduced by Bulychev et al. (1975) and called the BASh formula, the elastic modulus, M, measured by indentation is obtained from Hert'z contact mechanics in the form:

$$M \stackrel{\text{def}}{=} \frac{\sqrt{\pi}}{2}\frac{S}{\sqrt{A_c}} \tag{3.24}$$

Herein $A_c(=\pi a^2)$ (Figure 3-4). $S = \frac{dP}{dh}$ is the contact stiffness measured from the slope during initial unloading (Figure 3-2).

In elastic isotropic media, S does not depend on the pressure distribution under the indenter, and it is constant for flat, conical and spherical punches (Bulychev et al., 1975). Therefore, Equation (3.24) holds for conical and spherical indenter geometries. Bulychev et al. (1975) argued that no significant deviation from the BASh formula is expected when indenting with a Vickers indenter. This was also confirmed by King (1987) who showed, using finite element calculations, that the deviation from the BASh formula for Vickers and flat ended punches with triangular cross-section is only 1.2 % and 3.4%, respectively. Finally, work by Oliver and Pharr (1992) showed that Equation (3.24) is independent of indenter geometry. The contact area between an indenter and an elastic isotropic half-space is circular simplifying the contact problem in such materials.

In anisotropic media, the difficulty of solving contact problems lies in knowing the pressure distribution under an indenter, determining S, and accurately determining A_c. In their expressions of contact stiffness (Equations (3.20) and (3.22)), Vlassak and Nix (1993) states that the quantities between brackets can be taken as the inverse of the indentation modulus. As mentioned, the symmetry in the anisotropic half-space dictates whether these quantities are obtained analytically or numerically (Vlassak and Nix, 1993, 1994; Willis, 1966). With high symmetry (threefold and fourfold rotation axes; or parallel to the axis of symmetry in transversely isotropic material), the contact area between indenter and material is circular. A_c is determined from the measured indentation depth and an indenter area function (introduced later). Then, the BASh formula is used to obtain the indentation modulus. In the gas shale formations, therefore, M_3 (the indentation modulus obtained when indenting in the x_3-direction parallel to the axis of symmetry) is based on a well-determined circular contact

area. With lower symmetry (e.g., the x_1- or x_2-direction in gas shale formations), the contact area is elliptical. Its eccentricity and orientation depend on the mechanical properties of the anisotropic medium as well as the shape of the indenter (Vlassak and Nix, 1993; Ciavarella et al., 2001). Ciavarella et al. (2001) derived an expression for eccentricity and used it to calculate indentation depths in an anisotropic half-space. Their depths were found very close to depths obtained from an "equivalent isotropic" problem. In such a problem, the first term of the Fourier expansion, h_0, of the surface Green's function (Vlassak and Nix, 1994) is used to obtain the indentation modulus of the medium:

$$M_{eqv} = \frac{1}{\pi h_0} \tag{3.25}$$

Vlassak et al. (2003) also showed that the equivalent isotropic solution, i.e. one that assumes circular contact area, are adequate approximations. The elastic properties of an anisotropic medium can, therefore, be concentrated in an indentation modulus obtained assuming a circular contact area (Ciavarella et al., 2001; Vlassak et al., 2003). The validity of such an approximation calculating M_1 (the indentation modulus obtained indenting parallel to a two-fold symmetry axis) will be evaluated when analyzing the mechanical properties of the clay particles in Part III.

3.5.1.1 Elasticity from the Unloading Phase

Indenting a linear elastic isotropic material, the loading and unloading branches of an indentation test overlap (Figure 3-5), and no indentation impression is seen on the sample surface after unloading. The test is said to have perfect self-similarity. In elasto-plastic materials, no overlap exists between the loading and unloading phases (Figure 3-6), indicating that these phases no longer provide the same information nor depend on the same variables. The questions of whether the unloading curve is still elastic and whether it can be used to obtain the area of contact between the indenter and material needs to be addressed. Tabor (1948) and Stilwell and Tabor (1961) showed that the impression left by an indenter imitates the indenter shape and that the penetration phenomenon, if repeated, is reversible. The authors ascribe these observations to release of elastic stresses revealing that the deformation hap-

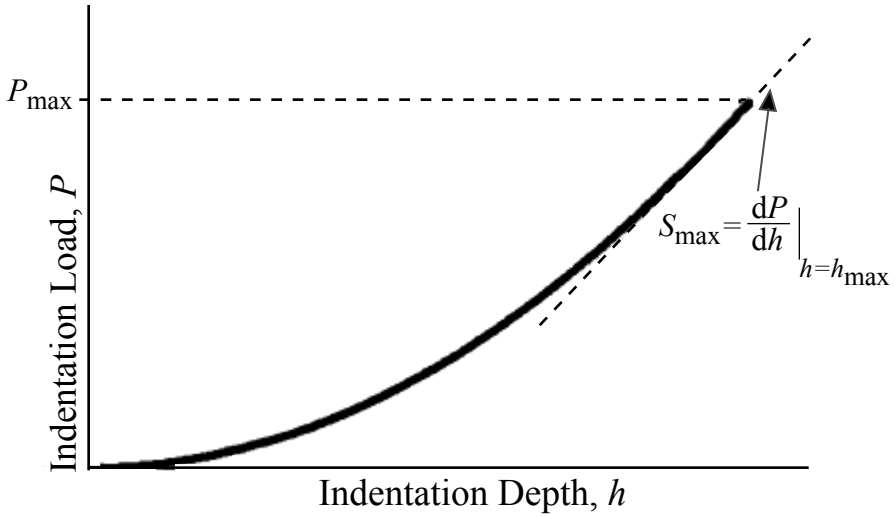

Figure 3-5: Typical indentation load-depth curve in elastic materials. P_{max} and S_{max} are the maximum load reached and contact stiffness at maximum depth, h_{max}, respectively (modified after Vandamme, 2008). No hold time is included in the shown example.

pening at the final unloading phase is elastic. The importance of Tabor's experiments is showing that classical laws of elasticity can be applied to the unloading phase, the recovered displacement (depth recovered due to unloading) can be related to the elastic properties of the material, and the shape of an indentation impression reflects the plastic deformation that has taken place. In additions to Stilwell and Tabor (1961), Doerner and Nix (1986) and Oliver and Pharr (1992) have also shown that the indentation modulus can be determined from the unloading curve even when plastic deformation occurs. Pharr and Bolshakov (2002) showed, via simulation, that plasticity occurs during unloading without affecting the load-displacement behavior. The unloading curves of a multiple-loading cycle indentation test (on Al-alloy) always overlap (Figure 3-7), and the contact between material and indenter during unloading decreases continuously. As a result, the load during the unloading phase is no longer proportional to h^2 only (indenting with a Berkovich tip), but also depends on the ratio $\frac{h}{h_{max}}$ regardless of whether the initial unloading is purely elastic or not.

3.5.1.2 Effective Indenter

Pharr and Bolshakov (2002) addressed the loss of self-similarity of an indentation test when dealing with elasto-plastic materials. They introduced the concept of the effective inden-

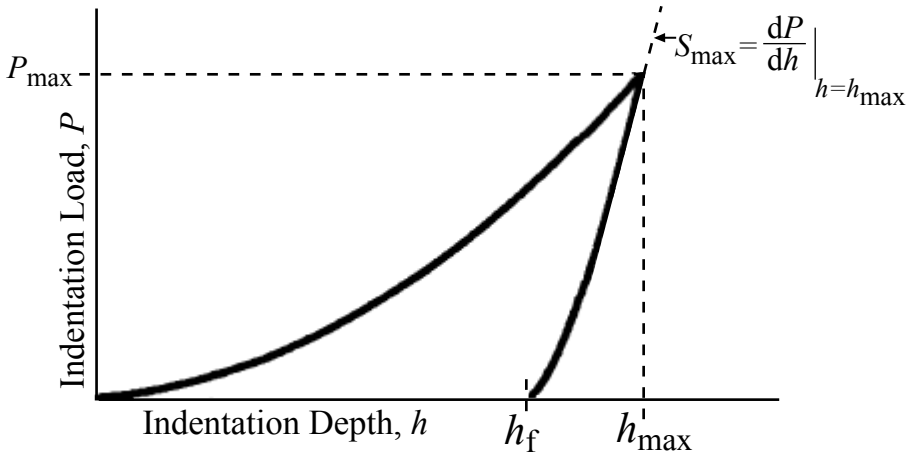

Figure 3-6: Typical indentation load-depth curve in elasto-plastic materials. P_{max} and S_{max} are the maximum load reached and contact stiffness at maximum depth, h_{max}, respectively (modified after Vandamme, 2008). No hold time is included in the indentation test.

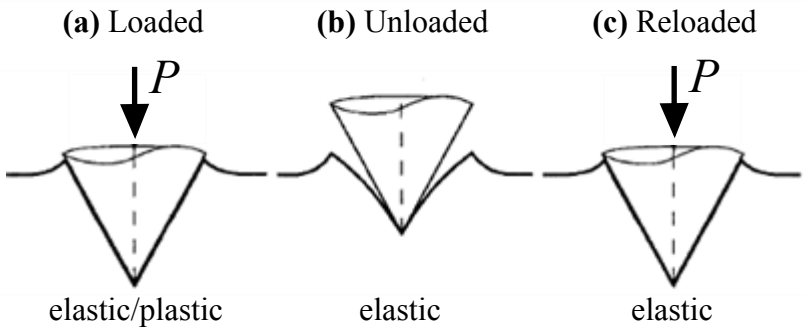

Figure 3-7: Deformation of the indent impression during loading and unloading of a conical indenter. The vertical scale in (b) is exaggerated as the curvature of the impression in soft material is hardly imperceptible (modified after Pharr and Bolshakov, 2002).

ter (an indenter with an "effective shape") whose geometry is unknown but its shape can be determined from the shape of the indentation impression it creates. An effective indenter, also, creates the same specific pressure distribution under an indenter tip during an unloading-reloading cycle in an elasto-plastic material. This rational shifts the dependence of the indentation analysis from the constitutive relationships in the indented material to the geometry of the indenter. For instance, for indentation of fused silica, soda-lime glass, Al, Tg, and sapphire crystals with rigid cones, the unloading phase obeys a power law of the

form (Pharr and Bolshakov, 2002):

$$P = \alpha(h - h_f)^m \tag{3.26}$$

where α and m are fitting parameters that depend on the material indented. The latter ranges between 1.2 and 1.6 and reflects values for an indenter with geometry of that of a parabola. h_f is the residual displacement after unloading. The fact that it is hard to accurately determine the shape and dimension of an indentation impression in elasto-plastic material calls for other approaches to determine the contact area.

3.5.1.3 Oliver-Pharr Method

To obtain the indentation modulus, the contact area at maximum load is needed. This task is not a straightforward one in elasto-plastic material as plasticity in contact mechanics is a complex problem; the constitutive equations are nonlinear and material terms, pertaining to the medium in question, are needed to describe its behavior (Oliver and Pharr, 1992). Analytical solutions, as a result, are hard to obtain, and the plasticity effects are best derived and understood through experiments and finite element modeling. Moreover, unlike the case with elastic material where the depth ratio, $\frac{h_c}{h}$, is obtained by the Galin-Sneddon solutions, the depth ratio is unknown a priori in elasto-plastic materials, and A_c cannot be calculated. A_c can be either tediously approximated from the indentation impression in the material or determined from the shape of the unloading curve. Tabor (1948), Stilwell and Tabor (1961), and Oliver and Pharr (1992) showed that the total amount of recovered displacement can be accurately related to the indentation modulus. Oliver and Pharr (1992) proposed a new methodology that seeks the contact depth, $h_c = h_{max} - h_s$, (h_s is the displacement of the surface at the perimeter of the contact; Figure 3-8) and find A_c as a function of the indenter tip area function, $F(h_c)$. The latter relates the cross-sectional area of an indenter to distance from its tip (Figure 3-8). The area function is obtained by indenting a material of known mechanical properties (e.g., fused quartz) and analyzing the indentation response. For a Berkovich tip, coefficients of a fitting function of the following form are determined to relate

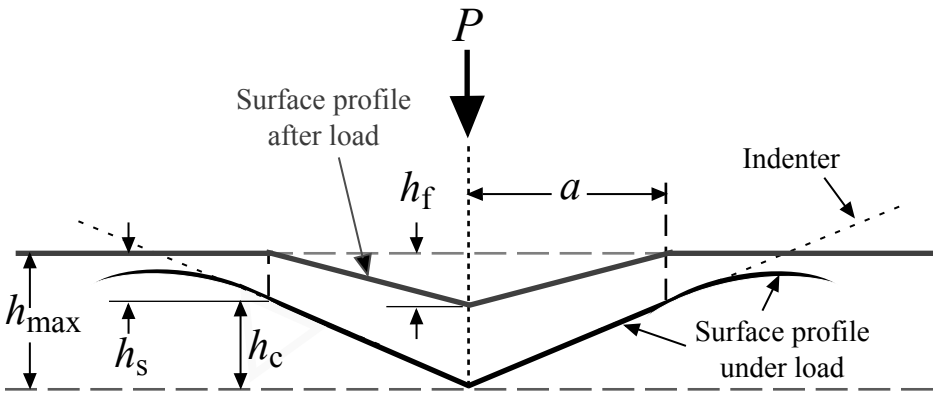

Figure 3-8: Determination of the projected area of contact between an indenter and indented material with the Oliver and Pharr method (after Oliver and Pharr, 1992).

h_c to A_c:

$$A_{h_c} = C_0 h_c^2 + C_1 h_c + C_2 h_c^{\frac{1}{2}} + C_3 h_c^{\frac{1}{4}} + C_4 h_c^{\frac{1}{8}} + C_5 h_c^{\frac{1}{16}} \tag{3.27}$$

Lastly, if the plastic deformation is to be estimated, the impression depths, h_f and h_s (Figure 3-8), are needed. For a conical indenter (Sneddon, 1965),

$$h_s = \frac{\pi - 2}{\pi}(h - h_f) \tag{3.28}$$

$$(h - h_f) = 2\frac{P}{S} \tag{3.29}$$

where $h = h_c + h_s$ is the total depth. For $h = h_{max}$,

$$(h_{max} - h_f) = 2\frac{P_{max}}{S} \tag{3.30}$$

Substituting Equation (3.30) into (3.28), one obtains:

$$h_s = \epsilon \frac{P_{max}}{S} \tag{3.31}$$

where $\epsilon = \frac{2}{\pi}(\pi - 2) = 0.72$ for conical indenters. ϵ equals 1 and 0.75 for flat and paraboloid indenters, respectively (Oliver and Pharr, 1992).

In the case of indenting anisotropic materials, the contact area is elliptical with $A_c = \pi a_1 a_2$

where a_1 and a_2 are semi-axes of the elliptical contact area. For a parabolic indenter, the load is related to the indentation displacement by (Willis, 1966):

$$P = \frac{4Mh^{\frac{3}{2}}}{3\sqrt{k}} \tag{3.32}$$

where k is the curvature of the tip of the indenter. Calculating the stiffness (dP/dh) from Equation (3.32) and using the BASh formula, the indenter displacement is:

$$h = a_1 a_2 k \tag{3.33}$$

The contact depths on the major and minor elliptical axes are $h_{c,1} = \frac{a_1^2}{2}k$ and $h_{c,2} = \frac{a_2^2}{2}k$, respectively. A mean value for h_c can be obtained (Swadener and Pharr, 2001):

$$h_c = \frac{a_1 a_2 k}{2} = \frac{h}{2} \tag{3.34}$$

Using Equations (3.32), (3.33), (3.34), and (3.24), it is found that ϵ =0.75. This is similar to the results obtained by Oliver and Pharr (1992) in elastic and isotropic media. Also, for a conical indenter penetrating an anisotropic half-space, Swadener and Pharr (2001) stated that anisotropic results "must" be reducible to isotropic results. They showed that the self-similarity is satisfied if A_c is proportional to h^2 and h and h_c are linearly related, such that:

$$h = \frac{\pi}{2}\sqrt{a_1 a_2}\, cot\theta \tag{3.35}$$

$$h_c = \sqrt{a_1 a_2}\, cot\theta \tag{3.36}$$

Starting with the following load-depth relationship:

$$P = \frac{M\sqrt{A}}{\sqrt{\pi}}h \tag{3.37}$$

Swadener and Pharr (2001) showed that in an anisotropic medium:

$$h_c = h(1 - \frac{\epsilon}{2}) \tag{3.38}$$

and

$$\epsilon = \frac{2}{\pi}(\pi - 2) \tag{3.39}$$

which is the results obtained by Oliver and Pharr (1992) for conical indenter penetrating isotropic media.

3.5.2 Indentation Hardness

The concept of hardness can be found in publications and work since the 18^{th}. It was used as a means for material mechanical classification and is defined as the average pressure under the indenter tip:

$$H \stackrel{\text{def}}{=} \frac{P}{A_c} \tag{3.40}$$

Tabor (1951) suggested an empirical relation to relate indentation hardness to mechanical properties; for instance, in metals the hardness is related to the uniaxial strength, σ_y, by:

$$\frac{H}{\sigma_y} \simeq 3 \tag{3.41}$$

The two parameters determining H are functions of the stiffness tensor ($\mathbb{C}_{ijkl}$), material cohesion (c), coefficient of friction (μ), indenter geometry (B), and the indentation depth (h):

$$P = f_L(h, M_0, \nu, \mu, c, B) \tag{3.42}$$

and

$$A_c = g(h, M_0, \nu, \mu, c, B) \tag{3.43}$$

Dimensional analysis gives the following dimensionless expressions (Ganneau et al., 2006):

$$\frac{P}{ch^2} = \Pi_P(\nu, \frac{c}{M_0}, \mu, \frac{B}{h^{1-d}}) \tag{3.44}$$

$$\frac{A_c}{h^2} = \Pi_{A_c}(\nu, \frac{c}{M_0}, \mu, \frac{B}{h^{1-d}}) \tag{3.45}$$

Combining Equations (3.44) and (3.45) gives a unique third dimensionless relation relating hardness to cohesion:

$$\frac{H}{c} = \frac{\Pi_P}{\Pi_{A_c}} = \Pi_H(\nu, \frac{c}{M_0}, \mu, \frac{B}{h^{1-d}}) \tag{3.46}$$

The hardness below the indenter tip scales as (Borodich et al., 2003):

$$\frac{H}{H_0} = (\frac{h}{h_0})^{\frac{k(d-1)}{d}} \tag{3.47}$$

where Equations (3.5) and (3.6) have been used to write Equations (3.47). Unlike the rest of the self-similar indenter geometries, however, the hardness obtained with conical indenters ($d = 1, B = \cot\theta$) is not depth-dependent:

$$\frac{H}{c} = \Pi_H(\nu, \frac{c}{M_0}, \mu, \theta) \tag{3.48}$$

3.6 Indentation Machines

Two machines were used to perform the indentation tests: the Hysitron TI 950 TriboIndenter (referred to as the Hysitron) and the Anton Paar Ultra Nanoindentation Tester (UNHT). The specifications of each machine and the various calibrations needed before indentation are summarized in Appendix B.

3.7 Sample Preparation and Polishing

Material indentation is based on a material flat surface model. Therefore, samples need to be polished to minimize surface roughness. Material Samples from core plugs, outcrops, and cuttings were cut into ~0.4-1.5 cm thick specimen and glued onto steel-mounting discs. Surfaces parallel and perpendicular to bedding planes were exposed, polished, and indented. With the rocks being very heterogeneous containing organic and non-organic phases, it was crucial to prepare polished flat surfaces with smooth inclusions while preserving the clay minerals and the organic content. A polishing protocol tested and perfected by Bobko (2008) and Deirieh (2011) was adopted; it starts with lapping the specimen in a cylindrical jig

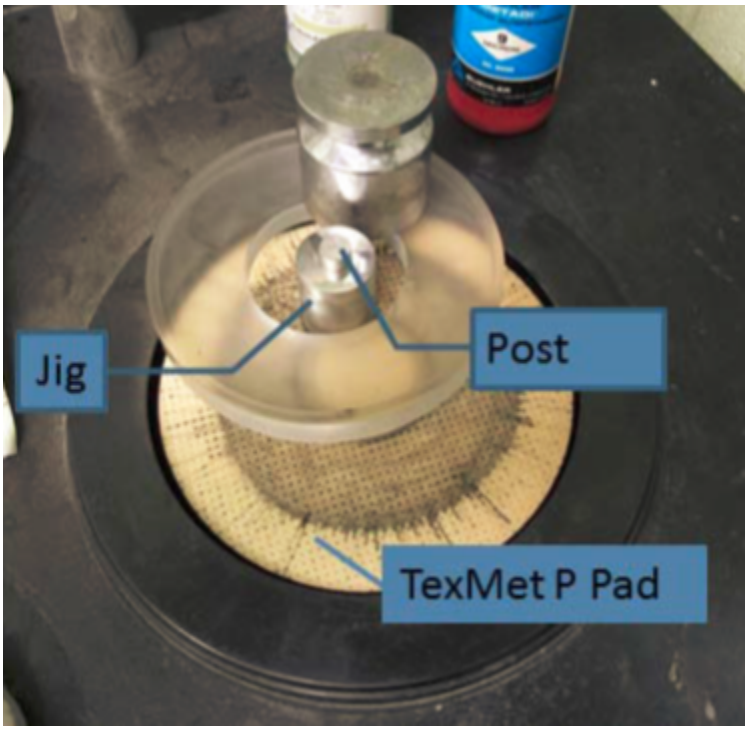

Figure 3-9: Polishing table and equipment used in the 9 μm diamond suspension polishing stage (after Deirieh, 2011).

(Figure 3-9) on a perforated TexMet-P mat (by Buehler) with an oil-based 9 μm diamond suspension solution. The objective of this first polishing stage is to parallel the indentation surface with the mounting plate and smooth any saw marks left on the sample surface after cutting. The duration (usually 30-45 min) of the polishing stage depends on the original inclination and condition of the sample surface. The sample is then submerged in an n-decane solution and put into an ultrasonic bath. The bath, in a fresh n-decane solution, is repeated as necessary to clean all the diamond suspension. Additional polishing stages, interrupted by ultrasonic baths, are then done using alumina pads (by Buehler) with different alumina grit sizes (9 μm, 3 μm, and 1μm). Surface roughness obtained after this polishing protocol was tested by Deirieh (2011) using Atomic Force Microscopy (AFM); the root mean square (RMS) roughness of polished samples was found to range between 10 and 30 nm. Using similar polishing protocols on Boston Blue Clay and other shale formations, Bobko (2008) measured a surface roughness of 150-200 nm. An additional polishing step with 0.5 μm alumina grit pads was done on some samples indented with the UNHT. Finally, we note that it was much easier to obtain a mirror finish polishing surfaces perpendicular to bedding

planes than parallel to them. This is due to the fissile nature of some of the tested formations causing splitting along bedding planes exposing fresh rough surfaces and to plucking-out of clay aggregates increasing surface roughness and increasing apparent porosity.

3.8 Chapter Summary

The indentation technique is used to localize stresses and probe the mechanical properties of small homogenized material volumes (level I) under the indenter tip. The mechanics of contact problems and the self-similarity aspect of the indentation test allow finding the load and depth distributions under the indenter tip and relate load to depth for various indenter tip geometries and material with various mechanical properties. We showed that solutions obtained for elastic isotropic materials can be applied to elastic anisotropic ones.

Two mechanical properties are obtained from indentation tests: the indentation modulus (M) that relates to the elasticity content, and hardness (H) that relates to strength properties of the indented material. The stiffness of indented material (S) and the contact area (A_c) between the indenter and material are the two important parameters needed to obtain $H = \frac{P}{A_c}$ and M, using the BASH formula ($M = \frac{\sqrt{\pi}}{2}\frac{S}{\sqrt{A_c}}$), which is valid for all tip geometries. The stiffness is the slope of the initial part of the unloading curve and represents elastic behavior even in elasto-plastic materials. The area is obtained from the calculated penetration contact depth $h_c = h_{max} - \epsilon\frac{P_{max}}{S}$ and the indenter tip area function using the Oliver-Pharr method. The hardness from indentation is related to the cohesion of the medium indented.

The indentation mechanical results depend on an accurate determination of A_c. A_c has a circular shape when indenting parallel to a high-symmetry direction. In our case, this is parallel to the material axis of symmetry or the x_3-direction. M_3, therefore, is an accurate measurement of stiffness. The elliptical A_c in low-symmetry directions (i.e. parallel to the formation bedding plane) is approximated to a circle and is used to calculate M_1. The validity of this area shape approximation, when indenting in the x_1-direction, will be revisited in Part III analyzing indentation results.

With the elastic and strength properties of the material indented in hand, the objective is then to use M and H to isolate nanoindentation tests performed on porous organic-rich

clay composites in every grid area. Due to the chemical heterogeneity of source rocks, a chemical description of the indented volumes is crucial; microscale chemical analysis, using energy-dispersive spectroscopy, is reviewed next.

Chapter 4

Energy-Dispersive X-Ray Spectroscopy

The second pillar of our experimental approach consists of obtaining the chemistry of the material volumes, under the indenter tip, from which the homogenized mechanical responses are obtained. To meet that objective, the Energy Dispersive X-ray Spectrometry (EDS) is used. EDS is a capability of scanning electron microscopes (SEMs), equipped with spectrometers, to detect characteristic x-rays generated from the interaction of beam electrons with the specimen atoms. The beam voltage used when acquiring EDS maps is chosen so that the volumes generating the characteristic x-rays are the same as those giving homogenized mechanical responses with indentation. Once EDS maps are acquired, chemical averages in areas coinciding with and including indentation impressions are calculated. This coupling of chemical data with the nanoindentation mechanical results will be used as input to clustering analysis (Chapter 5) to reveal the various chemo-mechanical phases in the grid areas and isolate the porous organic-rich clay composites.

4.1 Scanning Electron Microscopes and Beam-Sample Interaction

The objective of the chemical analysis is to have the chemistry of the material volumes from which the homogenized mechanical responses are obtained. Therefore, using petrographical microscopes to study chemistry and deduce the mineralogy is not feasible. SEMs are used

instead. SEMs are microscopes that provide high magnitudes and high resolution images by having a high energy beam of electrons interact with the surface of a specimen. When equipped with spectrometers to detect the outputs of the beam-specimen interactions, SEMs provide chemical spectra of the various chemical elements in a specimen.

4.1.1 Electron-Material Interaction

In an SEM, rock samples are bombarded with electrons produced by an electron source/gun and accelerated through a potential of 2 to $\geq$30 kV (Potts, 1992). The potential that accelerate the electrons is called the acceleration voltage and is held constant in order to produce electrons of the same energy. An electron accelerated through a potential of x kV has an energy of x keV (Potts, 1992). The electron beam is focused at a point ($\sim$1 μm in diameter) by a series of electromagnetic lenses (Severin, 2004). The negatively charged gun electrons enter the material and interact (elastically and inelastically) with the electric fields of the atoms present (Figure 4-1). Upon interaction, the electrons get deflected and change their momentum and/or energy.

4.1.2 Elastic Scattering

Elastic scattering happens when the beam electrons enter the electron clouds of atoms, get deflected, and transfer all their energy to the sample atom electrons; as a result, scattered and backscattered electrons (BSE) leave the sample with the same energies as the incident electrons (Figure 4-1). Backscattered electrons are important in SEM imaging.

4.1.3 Inelastic Scattering

Inelastic scattering happens when the beam of electron decelerates due to interactions with sample atoms producing electrons and photons with the same energy as that lost by the incident electrons. The first products of inelastic scattering are loosely-bound outer shell electrons (Figure 4-1) or secondary electrons (SE). Like BSEs, SE are also important for imaging. Auger electrons and x-rays are other byproducts of inelastic electron-sample interactions. They are low-energy electrons that come from inner shells of atoms on, or just below,

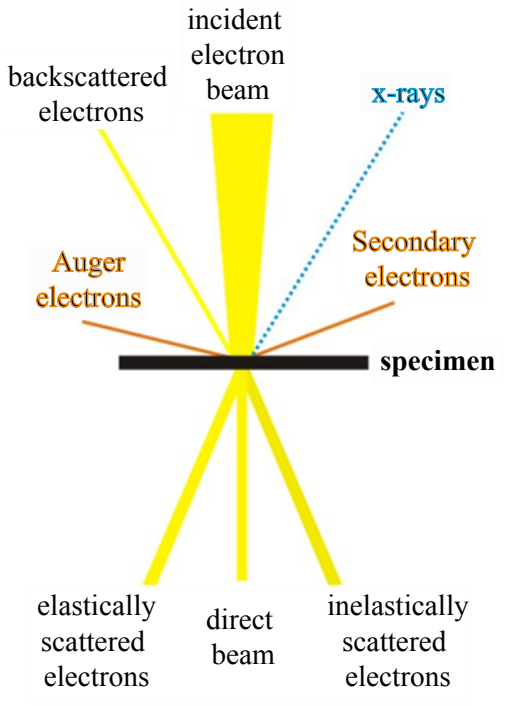

Figure 4-1: A schematic showing results of interactions between an SEM beam of electrons and material atoms (after http://www.microscopy.ethz.ch accessed in February 2015).

the sample surface (Khursheed, 2011). Auger emission is one form of spectroscopy used to determine the composition of surface layers of a sample (Leng, 2009). X-rays are photons of electromagnetic radiation with wavelengths ranging from 0.1-100 Å (Russ, 1984). One type of X-ray produced by inelastic interaction is the "Bremsstrahlung" X- rays (also called breaking radiations) affected by the acceleration voltage and atomic number. They form the major portion of the background that can complicate the identification and quantification of the second type of X-ray of interest in EDS, the characteristics X-ray (Severin, 2004).

Characteristic X-rays are generated when the beam electrons interact with the inner-shell electrons of atoms in the specimen, knocking the shell electron from its energy shell and exciting the atom (Severin, 2004; Russ, 1984). The atom, ionized and in an excited state, returns to its normal state by refilling the vacancy in the inner energy shell by an outer shell electron (Figure 4-2) generating a characteristic x-ray. The energy of the characteristic x-ray is the difference in energy between the two energy shells that have exchanged electrons (Reed, 2005). Characteristic x-rays are so called as they characterize chemical elements and

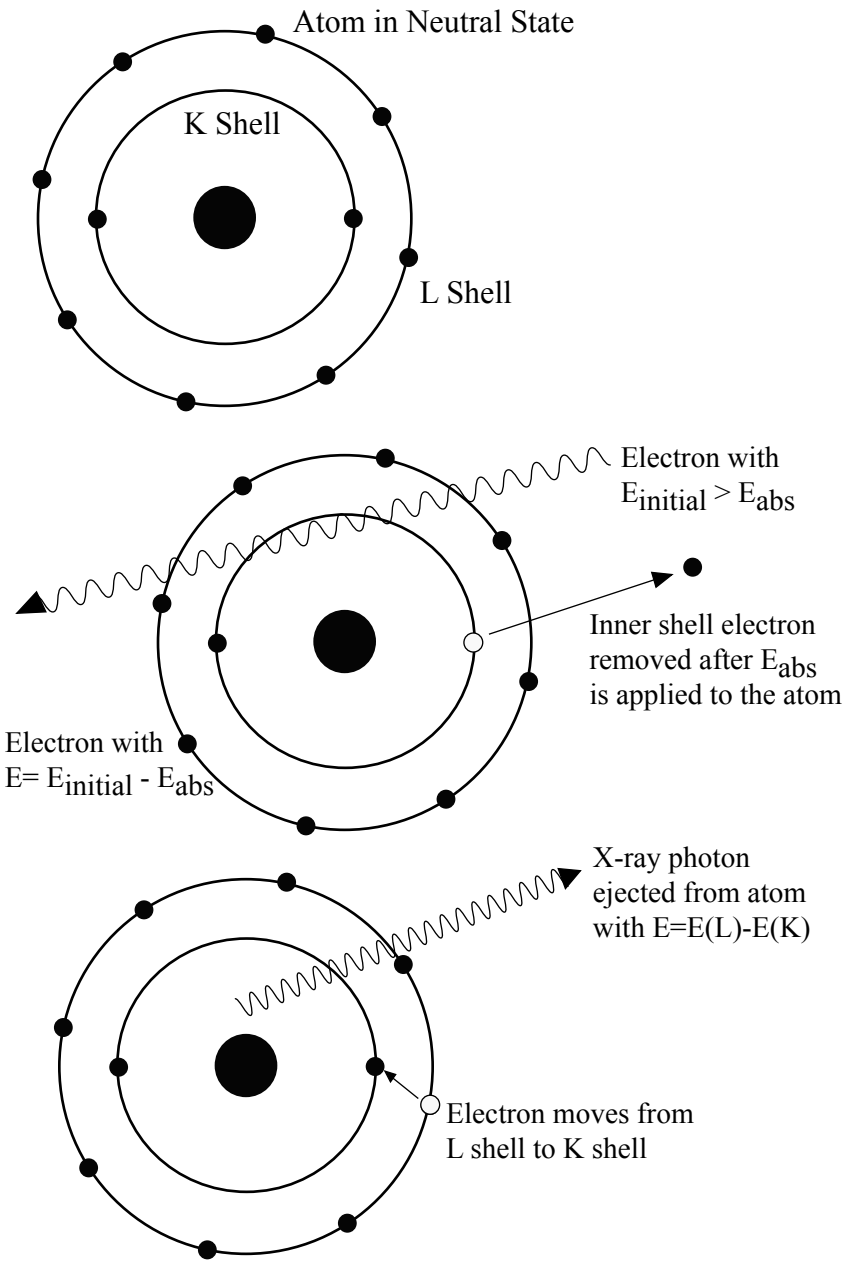

Figure 4-2: Generation of x-rays in an excited atom (after Severin, 2004). "X-rays lines" are identified by a letter (K, L, or M) indicating the shell containing the electron vacancy.

depend on their atomic numbers; Moseley's law (Moseley, 1913) relates the wavelength of the characteristic x-ray to the atomic number of the chemical elements:

$$\lambda = \frac{B}{(Z-\sigma)^2} \tag{4.1}$$

where Z is the atomic number; B and σ are constants that depend on specific shells. The ability of an atom to generate characteristic x-rays (vs. Auger electrons) depends on the fluorescent yield, which is a parameter that reflects the effectiveness of generating characteristic x-rays. The fluorescent yield increases with increasing Z. As Z decreases, the probability of Auger electrons generation increases (Russ, 1984) rendering the EDS technique disadvantageous when detecting light elements[1]. The lightest element that can be detected with EDS is Oxygen (Z=8).

4.2 X-Ray Spectroscopy

X-ray spectrometry is a technique for chemical analysis of bulk specimens. X-ray spectrometers are widely available and very common in SEMs today. Two main types of x-ray spectrometers (Potts, 1992) exist depending on one of two main techniques used in spectroscopy: the Wave Dispersive X-ray Spectroscopy (WDS) and EDS. After detecting characteristic x-rays and measure their intensities, the intensities are compared to "standards" (samples of known composition) containing known values of the elements of interest by means of calibrations curves (Russ, 1984). Such a comparison allows the conversion of intensities into mass concentrations.

4.2.1 Wave Dispersive Spectroscopy

WDS is a quantitative technique that classifies x-rays based on their wavelengths. A WD spectrometer measures the intensity of x-rays using the Bragg's diffraction phenomenon. The latter allows the classification of x-rays based on their wavelengths and the capability of certain crystalline material to strongly diffract x-rays (Potts, 1992). WDS provides a good

[1]Light elements have denser electron clouds per volume than heavy element leading to higher x-ray excitation and high stopping power (Potts, 1992).

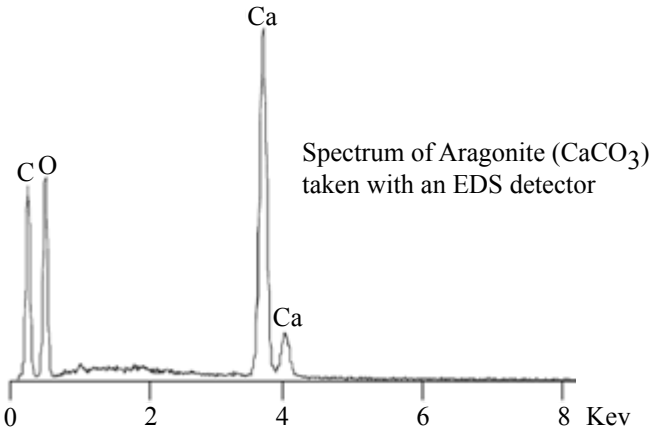

Figure 4-3: An aragonite spectrum taken with an EDS detector (modified after Severin, 2004).

.

resolution, and a WD system can measure simultaneously as many elements as the number of detectors it contains. The need to chemically analyze tens of indentation grid areas and the heterogeneity of gas shale formations require multiple WDS passes (over hundreds on indentation tests) even with SEMs with three or four detectors. This aspect of WDS makes the technique expensive and time consuming.

4.2.2 Energy Dispersive Spectroscopy

EDS is also a technique that classifies x-rays based on their intensities. An ED spectrometer uses a solid state "lithium drifted silicon detector" and is able to handle low count rates. An advantage that an EDS spectrometer has is its ability to detect x-rays of all energies and, thus, record complete elemental spectra (Figure 4-3) in one session. EDS started as a qualitative chemical analysis technique using ED detectors of poor resolution and restricted to a much lower maximum count rates than the WD detectors. This limitation used to cause element spectra to overlap. However, the introduction of "high performance pulse processing amplifiers" and sophisticated computer algorithms made it possible to deconvolute overlaps and interference in the ED spectra (Potts, 1992) and identify various chemical elements. EDS, therefore, became a semi-quantitative technique very useful for detecting multiple elements present in a specimen.

4.2.2.1 Effect of sample topography

One advantage of EDS is that it gives relatively good results on "irregular" (not perfectly flat) surfaces and heterogeneous material (Russ, 1984). However, on a very rough surface, the generated intensities of characteristic x-rays vary with tilt because of backscattering effects caused by the x-ray take-off angle. Also, rough topography affects imaging showing dark areas shadowed from the detector and bright ones tilted sharply toward it (Russ, 1984).

4.2.2.2 Excited Volume

The excited volume is the volume of material where collisions and interactions happen between the beam electrons and the sample atoms. The beam in an SEM can be as small as 20 Å giving high resolution images (e.g., SE images). However, EDS mapping is done with a beam spot size ~ 1 μm in radius. Despite focusing the beam on a small surface area, the beam spread in three dimensions (Severin, 2004), and x-rays are produced from the much larger excited volumes in the specimen. The depth below the surface reached by the beam electron (x in μm) and the distance across the excited volume (y in μm) depend on both the density of the sample, ρ, and the acceleration voltage (KV) used (Figure 4-4) as follows:

$$x = \frac{0.1 E_0^{1.5}}{\rho} \tag{4.2}$$

$$y = \frac{0.077 E_0^{1.5}}{\rho} \tag{4.3}$$

With EDS as a technique of choice for chemical analysis, the aim is to be consistent with the volumes probed by indentation (mechanical analysis) and those excited with EDS (chemical analysis). Deirieh et al. (2012) provided a Monte Carlo simulation (reproduced in this study; Figure 4-5) of the electron trajectories inside the material during spectroscopy measurements. The simulation shows that, using a 15 KV beam with shale material with an average density of 2.55 g/cc, an interaction volume of $\sim 2\mu$m deep is probed. Severin (2004) also reports pear-shaped interaction volumes of 2 μm deep and 2 μm across for typical silicate rocks. With similar volumes homogenized under the indenter tip (Section 2.6)

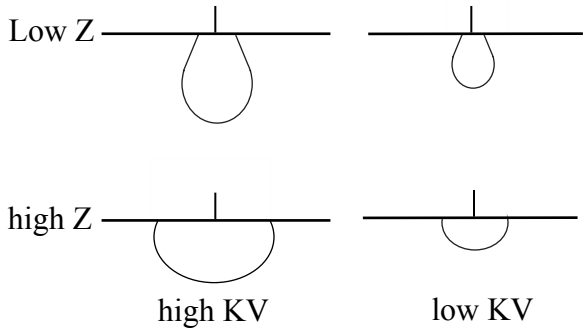

Figure 4-4: Excited volume variation with atomic number and acceleration voltage (after Russ, 1984).

and contributing to EDS, The EDS measures average compositions of the porous mineral composites, that is the compositions of level I.

4.3 EDS X-Ray Mapping

In addition to measuring intensity spectra to identify chemical elements and minerals (Figure 4-3), EDS produces x-ray intensity maps. In x-ray mapping, the beam of electrons scans a sample surface in a rectangular raster fashion, and x-ray intensities of various chemical elements (identified by their characteristic x-rays) are recorded for each pixel. Elemental maps (Figure 4-6), thus, provide spatial distributions of specific chemical elements.

In this work, an SEM JEOL-JSM-5910 (unless otherwise specified), operated with an acceleration voltage of 15 KV and a working distance (distance between the detector and sample surface) of 10 mm, was used to acquire the EDS maps. The beam spot size used varied depending on several factors: the status of the electron gun filament, the current strength of the lenses, the shape of the lenses (they are never perfectly circular), the aperture used, and the condition of the detectors (detector gain and signal-to-noise ratio). The SEM was operated in a way to ensure a spot size large enough to allow for good x-ray count rates, but small enough to achieve good imaging and analysis resolutions while avoiding charging (especially when analyzing immature formations) and migration. The duration of an EDS acquisition varied between 45-75 minutes.

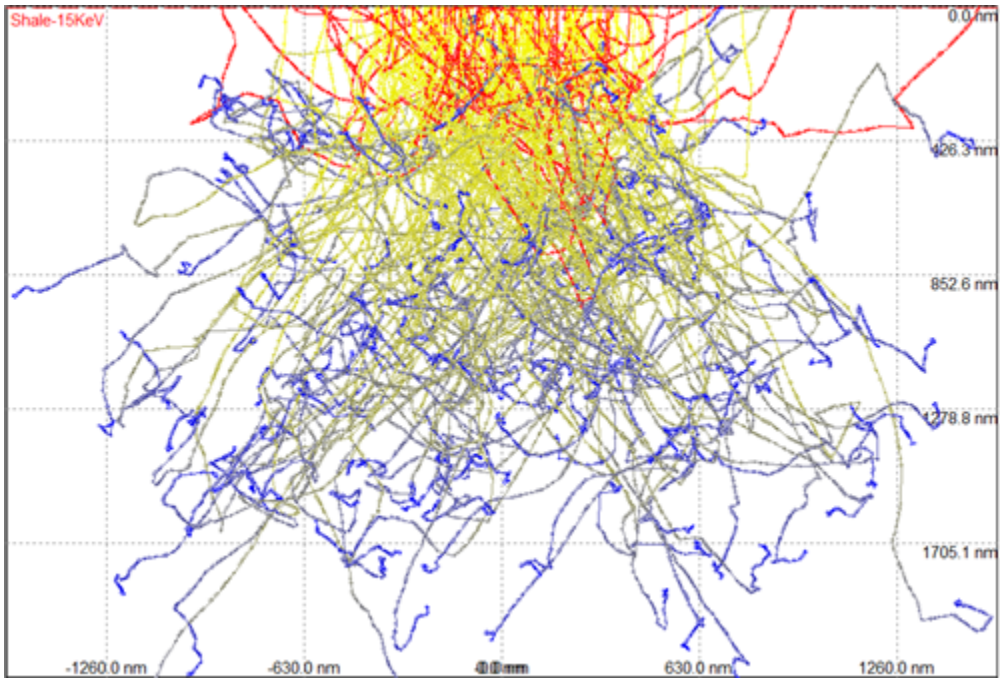

Figure 4-5: A Monte Carlo simulation (run on CASINO v2.4.8.1) of the electron trajectories in a shale sample with density of 2.55 g/cm^3. The simulation was run with an acceleration voltage of 15 KV. Red = trajectories of backscattered electrons; Yellow and blue = trajectories of electrons with low and high energies, respectively.

4.3.1 Chemical Averaging at Indentation

The advantage of EDS mapping is that it allows the chemical analysis of the indented volumes and the acquisition of a large number of elemental maps. Once acquired over an indentation grid (e.g., Figure 4-7), EDS elemental maps (Figure 4-6) are cropped to frame the indentation grid (area inside red contour in Figure 4-7), and X-ray intensities are averaged in a 1 μm radius circular area around every indentation test. The schematic in Figure 4-8 illustrates the areas (red circles) where chemical averaging is done around the indentation impressions (blue triangles). Features in Figure 4-8 are not drawn to scale as indentation impressions can vary in dimension/widths (Figure 4-6) depending on the final depth reached at maximum load. The latter in turn depends on the mechanical properties of the material indented.

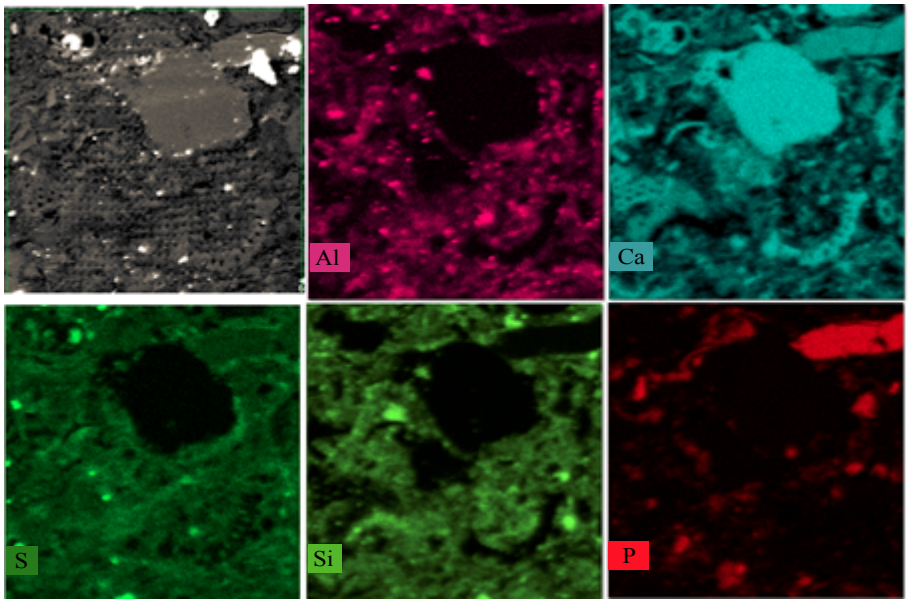

Figure 4-6: A backscatter SEM image (upper left) of the indentation grid (S1G2) performed on a MTII cutting showing the area where the EDS mapping is done. The colored maps are EDS maps of different chemical elements.

4.3.2 Chemo-Mechanical Coupling of Data

Averaging the x-ray intensities around every indentation test allows transforming every EDS elemental map (e.g., Figure 4-9a) into an average intensity map (Figure 4-9b). Averaged EDS maps are coarsely pixelated $n \times n$ maps, with $n \times n$ being the total number of pixels, coinciding with the coordinates of the indentation tests in a grid. Indentation tests with bad indenter-material contact, large pore volume at or under the surface, and/or microcrack generated during the test (depth jump with no increase in load seen in the loading phase of an indentation test) are eliminated from the EDS intensity maps (dark blue pixels in Figure 4-9c). With the chemical averaging at every indentation test, mechanical and chemical data are coupled and ready to be statistically analyzed to reveal the various clusters, or the chemo-mechanical phases, in the formations.

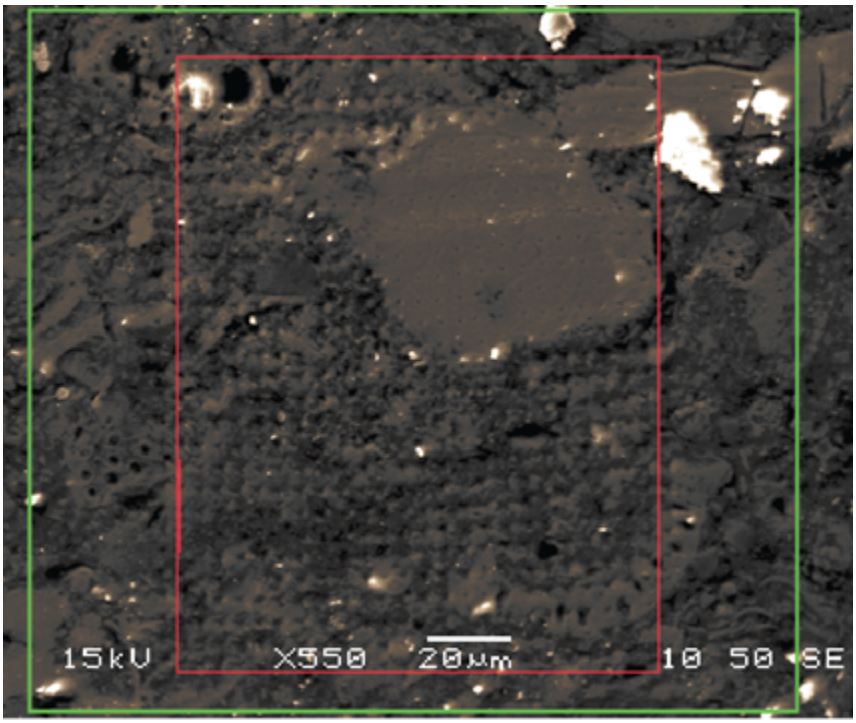

Figure 4-7: An SEM image acquired with the SE detector of grid S1G2 from a Marine Type II cutting. The image was acquired with a 15 KV acceleration voltage and 10 mm of working distance. The green contour delineates the area of the EDS elemental maps. The red contour frames the indentation grid.

4.4 Chapter Summary

In this chapter, the physics of SEM beam electrons interactions with sample atoms and characteristics x-rays generation are reviewed. The semi-quantitative EDS technique produces x-ray elemental intensity maps of the same areas where indentation grids were performed. The material volumes that interact with the electron beam to generate the intensity maps are of the same dimensions as those homogenized under the indenter tip to give mechanical properties. With the indentation tests and EDS probing the same material volumes, chemo-mechanical data coupling is feasible. Data coupling is done averaging chemistry around every indentation test. The coupled chemo-mechanical data is used as input into clustering analysis discussed in the next chapter.

Figure 4-8: A schematic showing a 5×5 indentation grids. Blue triangles depict indentation impressions obtained indenting with a Berkovich tip. The spacing between indentations varies depending on P_{max} and maturity of the formations; 5 μm-spacing and 6 μm-spacing were used indenting mature and immature formations, respectively, with P_{max} = 4.8mN. Red circles simulate 1μm-radius areas around indentation tests where x-ray intensities are averaged. The triangles, triangle spacing, and circles areas are not drawn to scale.

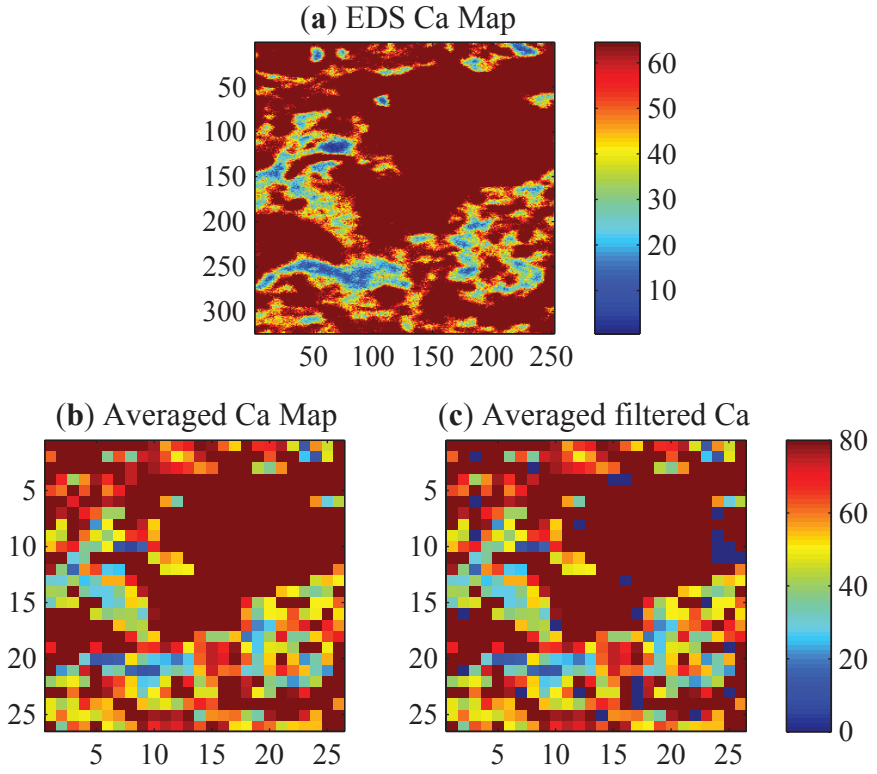

Figure 4-9: (a) EDS Ca intensity map from grid S1g2 of Marine type II. (b) Chemical averaging done in 1 μm radius circular areas centered at the indentation points. (c) Average intensity map with pixels (dark blue), corresponding to rejected indentation tests, removed. The scale bars represent x-ray intensity reflecting counts per second.

Chapter 5

Clustering Analysis

In this chapter, we review clustering analysis, the last technique in the proposed methodology to isolate the clay composites. Clustering analysis is a tool to reveal and determine the "intrinsic structure" of a data set when no information other than observed values describing the data are available (Fraley and Raftery, 1998). We use MCLUST, which is an R-software package that implements a hierarchical clustering and Expectation-Maximization algorithms for parametrized Gaussian mixture models. Coupled chemo-mechanical data sets (Chapters 3 and 4) are fed into the clustering algorithm to differentiate the various chemo-mechanical phases in the gas shale formations and isolate the clay composites. We emphasize the importance of coupling chemistry to mechanical data for better clustering results in the heterogeneous source rocks.

5.1 Introduction

Available indentation studies of source rocks either use literature values or threshold to differentiate the various chemical phases. These studies either ascribe weak mechanical properties to clay aggregates and organic matter (Mba et al., 2010), are not statistically representative (Mba et al., 2010; Ahmadov et al., 2009) acquiring only tens of indentations in very heterogeneous material, or use tedious methods to locate the organic phase in the rocks (Ahmadov et al., 2009). In this work, we use clustering analysis to differentiate the different chemo-mechanical phases in the rocks.

Clustering analysis helps partition data in a multidimensional space into meaningful (sub)groups. Points belonging to the same group have a natural relationship to one another while those belonging to different groups do not show such a relationship (Dubes and Jain, 1976). Many hierarchical and relocation approaches exist with different clustering methods. Hierarchical approaches are based on computing distances between points to check their similarities or dissimilarities (e.g., nearest-neighbor approach). They start by introducing a sequence of partitions, each corresponding to a certain number of clusters, and proceed in either an "agglomerative" or "divisive" way. Agglomerative methods merge groups or clusters, so they can start with as many groups as the number of data points (maximum number of iterative stages) and be computationally expensive. Divisive methods divide groups at each stage (Fraley and Raftery, 1998). Relocation approaches start with an initial user-specified data partition and proceed with iteratively relocating observations among various clusters (Fraley and Raftery, 1998). The most common relocation method is the k-mean method that divides a set of n observations into k clusters ($k \leq n$) and tries to minimize sums of squares within the clusters (Binder, 1978; Fraley and Raftery, 1998).

5.2 Model-Based Clustering Approaches

Unlike hierarchical and relocation approaches, a model-based clustering approach assumes that the data comes from a mixture of an unknown number of probability normal (Gaussian) distributions (Fraley and Raftery, 1998, 1999, 2002b). Given p-dimensional observations $x = (x_1, x_2, \ldots, x_n)$, $f_k(x_i \mid \theta_k)$ is defined as the density of an observation x_i from (say) the k^{th} cluster; with θ_k being the corresponding parameter (e.g., mean vector μ_k or the center of the distribution) (Fraley and Raftery, 1998, 2002a):

$$f_k(x_i \mid \mu_k, \Sigma_k) = \frac{\exp\{-\frac{1}{2}(x_i - \mu_k)^T \Sigma_k^{-1}(x_i - \mu_k)\}}{\sqrt{(2\pi)^p det(\Sigma_k)}} \tag{5.1}$$

With the assumption of a data set with a mixture of Gaussian distributions, the sought-after parameters in Equation (5.1) reduce to only μ_k and Σ_k. Σ_k is a covariance matrix that determines the cluster's geometric characteristics. It is parametrized in terms of its

eigenvalue decomposition:

$$\Sigma_k = \lambda_k D_k A_k D_k^T \tag{5.2}$$

where λ_k, the first eigenvalue of Σ_k, is an associated constant of proportionality that governs the volume/size of the cluster in the p-space. D_k is the orthogonal matrix of eigenvectors that controls the orientation of the k^{th} component of the mixture. A_k is a diagonal matrix with elements proportional to the eigenvalues and controlling the shape of the cluster (Banfield and Raftery, 1993; Fraley and Raftery, 1998). Various model options with various combinations of the above parameters are available in MCLUST (Fraley and Raftery, 1999, 2002b). For instance, in one-dimension, there are only two models: equal and varying variance models (Fraley and Raftery, 2002a). In higher dimension, models become more complex with clusters with varying shapes, sizes, and orientations. For instance, clusters can be spherical of the same size ($\Sigma_k = \lambda I$), constant with the same geometry ($\Sigma_k = \Sigma$), or unrestricted where each cluster can have a different geometry (Fraley and Raftery, 2002b).

With the models changing according to the dimension of the input/observations, the ultimate objective behind using clustering analysis is to isolate clay composites with minimum contamination from other chemical phases and work with the simplest model possible (i.e., one that requires the lowest number of input parameters). In this work, we couple mechanical (M and H[1] obtained from indentation.) and chemical data (mainly Si and Al, and, to a lesser extent, S, Ca, and/or Mg) to use as input for clustering analysis. The choice of the chemical input depends on 1) the chemical heterogeneity of the formation tested (types of inclusions and the carbonate and sulfur contents; XRD data in Chapter 2), and 2) obtaining the minimum number of clusters possible (optimally $\leq$5). On every data set, clustering was done with different chemical element combinations. Very often, it was seen that adding chemical elements other than Si and Al does not change the clustering results much nor complicate the model obtained. Adding chemical elements helps differentiate inclusions types (quartz, apatite, carbonate grains, pyrite framboids) and/or produce more mixture phases/clusters. Occasionally, clustering results with more than seven clusters were obtained indicating very complex models. These clustering scenarios were rejected unless obtained using the minimum

[1]In case of creep indentations (discussed in Part IV), the contact creep modulus, C, is also added as part of the mechanical input into the clustering algorithm.

required input (e.g., M, H, Al, and Si).

5.2.1 Maximum Likelihood

In statistics, a likelihood function is a function of the parameters of a statistical model. It "tends to be the most sensitive criterion of the deviation of the model parameters from true values" (Akaike, 1974). With the maximum likelihood (ML) approach (Dempster et al., 1977), the estimation of a d-dimensional parameter vector, θ, for a given density, $f_k(x_i \mid \theta_k)$, of the random vector, x_i, is $\hat{\theta}$. The main purpose of estimating the parameters of $f_k(x_i \mid \theta_k)$ is to base the decision on $f_k(x_i \mid \hat{\theta}_k)$ (Akaike, 1998). The estimate is provided by the solution of the likelihood equation or its log:

$$\frac{\partial L(\theta)}{\partial \theta} = 0; \quad \frac{\partial \log(L(\theta))}{\partial \theta} = 0 \tag{5.3}$$

where $L(\theta) = \Pi_{(i-1)}^{n} f(x_i, \theta)$ is the likelihood function for θ formed under the assumption that the observations in a data set are independent events. As the objective of the ML estimation is to find estimates of θ, a sequence of roots, or local maxima, in the interior of the parameter space of the likelihood equation is defined. The sought-after sequence is obtained taking $\hat{\theta}$ to be the root that globally maximizes $L(\theta)$. $\hat{\theta}$ is, thus, called the maximum likelihood estimator (MLE) (McLachlan and Peel, 2000).

In order to describe the use of the concept of maximum likelihood in formulating a model and obtaining its parameters, a model of a composite of G clusters is assumed. The model has a random vector of density, $f(x)$, given by:

$$f(x) = \Sigma_{k=1}^{G} p_k f_k(x_i \mid \mu_k, \Sigma_k) \tag{5.4}$$

with p_k being the mixing proportions for all k $(0 < p_k < 1; \Sigma_k p_k = 1)$. The model is usually formulated in one of two ways. The first is the classification likelihood approach that maximizes the likelihood over the mixture parameters and the identifying labels (γ_i) of the mixture components (Banfield and Raftery, 1993; Celeux and Govaert, 1995; Fraley and

Raftery, 1998):

$$\mathcal{L}_c(\theta_1, \ldots, \theta_G; \gamma_1, \ldots, \gamma_G \mid x) = \Pi_{i=1}^{n} f_{\gamma_i}(x_i \mid \theta_{\gamma i}) \tag{5.5}$$

where γ_i are discrete values that label the classification ($\gamma_i = k$ if x_i belongs to the k^{th} cluster). The classification likelihood approach has several limitations detailed in Banfield and Raftery (1993). The second way the model can be formulated is by the mixture likelihood approach that maximizes the likelihood over all the mixture parameters (i.e., the mixture proportions, clusters' mean vector, and covariance matrices; Celeux and Govaert 1995; Fraley and Raftery 1998):

$$\mathcal{L}_M(\theta_1, \ldots, \theta_G; \tau_1, \ldots, \tau_G \mid x) = \Pi_{i=1}^{n} \Sigma_{k=1}^{G} \tau_k f_k(x_i \mid \theta_k) \tag{5.6}$$

where $\tau_k (\tau_k \geq 0)$ is the probability that an observation belongs to the k^{th} cluster and $\Sigma_{k=1}^{G} \tau_k = 1$.

5.2.2 Expectation-Maximization (EM) Algorithms

The Expectation-Maximization (EM) algorithms (Dempster et al., 1977; McLachlan and Peel, 2000) are iterative relocation methods for clustering via mixture models. They are the general approach used for the maximum likelihood fitting (McLachlan and Peel, 2000) for problems in which the data is viewed as consisting of n observations recoverable from (y_i, z_i); where y_i is observed/measured data while z_i is missing data. The density of an observation, x_i, given z_i is:

$$\Pi_{k=1}^{G} f_k(x_i, \theta_k)^{z_{ik}} = \left\{ \begin{array}{l} 1 \text{ if } x_{\mathrm{i}} \text{ belongs to cluster k} \\ 0 \text{ otherwise} \end{array} \right\} \tag{5.7}$$

As a result, the complete data log likelihood function becomes (Fraley and Raftery, 1998):

$$\mathcal{L}(\theta_k, \tau_k, z_{ik} \mid x) = \Sigma_{i=1}^{n} \Sigma_{k=1}^{G} z_{ik} [\log \tau_k f_k(x_i \mid \theta_k)] \tag{5.8}$$

The quantity $\hat{z}_{ik}$ is the conditional expectation of z_{ik} given observation x_i and parameter values. The value z_{ik}^* of $\hat{z}_{ik}$ at a maximum of Equation (5.6) is the conditional probability that an observation i belongs to group k. The classification of an observation x_i is taken to be $\{j \mid z_{ik}^* = max_k z_{ik}^*\}$ (Fraley and Raftery, 1998).

The EM algorithm starts with an initial set of parameters and iterates between 2 steps; the expectation step (E-step) and the maximization step (M-step). In the E-step, the conditional expectation of the complete data likelihood (Equation (5.8)), given the observed data and initial parameters, is computed by:

$$\hat{z}_{ik} \longleftarrow \frac{\hat{\tau}_k f_k(x_i \mid \hat{\mu}_k, \hat{\Sigma}_k)}{\Sigma_{j=1}^{G} \hat{\tau}_j f_i(x_i \mid \hat{\mu}_j, \hat{\Sigma}_j)} \tag{5.9}$$

The M-step, detailed in (Celeux and Govaert, 1995), consists of determining the parameters that maximize the expected likelihood in terms of the parameters (τ_k, θ_k) using the $\hat{z}_{ik}$ found in the E-step. "Estimates of the means $(\hat{\mu}_k)$ and probability $(\hat{\tau}_k)$ have closed-form expressions involving the data $(\hat{z}_{ik})$ obtained from the E-step":

$$\frac{n_k}{n} \rightarrow \hat{\tau}_k; \quad \frac{\Sigma_{i=1}^{n} \hat{z}_{ik} x_i}{n_k} \rightarrow \hat{\mu}_k; \quad \Sigma_{i=1}^{n} \hat{z}_{ik} \equiv n_k \tag{5.10}$$

The EM iteration converges to a local maximum of the observed data likelihood. This approach was found to hold in practice and to give good results. The limitations of the EM algorithms is that it can be computationally expensive to reach convergence. Also, the number of conditional probabilities calculated/iterated can reach the number of components in the mixture (Fraley and Raftery, 1998, 2002b).

5.3 Bayesian Model Selection

The selection of a clustering technique and the number of clusters determined can give many statistical models for the same set of observations. The task becomes one of considering and comparing a set of potential models and choosing a model with appropriate dimensionality (e.g., degree of a polynomial in a regression problem or number of step in Markov chain) that fits a set of observations (Schwarz, 1978). The ML approach (section 5.2.1) leads to the choice of the highest possible dimension.

One approach to model selection is to calculate the Bayes factor, B_{10} (Kass and Raftery, 1995), which is the ratio of posterior to prior odds (ratio of the integrated likelihoods) of

one model, M_0, against another, M_1. Given a set of data $x = (x_1, \ldots, x_n)$, the Bayes factor is obtained without favoring one model a priori by (Schwarz, 1978; Biernacki and Govaert, 1999; Kass and Raftery, 1995):

$$B_{10} = \frac{P(x \mid M_1)}{P(x \mid M_0)} \tag{5.11}$$

with

$$P(x \mid M_j) = \int P(x \mid \theta_j, M_j) P(\theta_j \mid M_j) d\theta_j \tag{5.12}$$

where $P(x \mid M_j)$ is the integrated likelihood of the data for model M_j. θ_j are the parameters of model M_j and $P(\theta_j \mid M_j)$ is its prior density. A way to obtain the integrated likelihood (Equation (5.12)) using the EM algorithm is to use the Bayesian Information Criterion (BIC):

$$BIC \equiv 2 \log P(x \mid M_j) + constant \approx 2\mathcal{L}_M(x, \hat{\theta}) - m \log(n) \tag{5.13}$$

where $\mathcal{L}_M(x, \hat{\theta})$ is the maximized mixture likelihood for the model (Schwarz, 1978; Fraley and Raftery, 1998), m_M is the number of independent parameters to be estimated in the model, and n is the number of observations.

The BIC approximation is valid for a large number of observations as the fit of a mixture model can only improve as more terms are added. However, the likelihood assessment, $\mathcal{L}_M$, alone is not enough to deduce whether or not a model is a good one. A term is, therefore, added to the likelihood to "penalize" for the complexity of the model chosen (Fraley and Raftery, 1998; Wagenmakers and Farrell, 2004). The importance of the penalizing term is that it helps rejecting models with too many clusters that increase the number of parameters in the model. A large BIC reflects a strong evidence for the model.

5.4 Chemo-Mechanical Clustering Analysis in Gas Shales

The goal of performing chemo-mechanical clustering analysis is to 1) produce the various clusters/phases in the data set from every indentation grid, 2) contour the various chemical phases that exist in an indentation area, and 3) extract indentations performed in porous organic-rich clay composites.

In the clustering analysis, we use the MCLUST software package (Fraley and Raftery,

1999, 2002a) that implements the EM algorithms for parametrized Gaussian mixture models as well as the Bayesian model selection criterion. The package reads input data from simple text files. In the following section, examples of clustering analysis results of experimental data from gas shale formations are reviewed. The advantage of adding chemistry to mechanical properties for better clustering and phase identification is emphasized.

We note that chemo-mechanical clustering analysis was run on almost all the areas where indentation grids were acquired. Clustering analysis with only mechanical data was performed in few cases where the indentation grid could not be defined (seen in full) due to surface condition (charging and migration and/or conductive coating covering indentation impressions) and/or sample texture (unclear indentation impressions).

5.4.1 Chemical Phase Segregation

Clustering analysis using coupled chemo-mechanical data provides a semi-quantitative chemical description of every cluster/phase in a grid. The approach is advantageous over conducting the clustering analysis using only mechanical data. The latter only produces clusters with different mechanical properties and is adequate in formations with high clay content, simple lithology, and/or texture. To illustrate the advantage to chemo-mechanical clustering over mechanical clustering, we compare grid data analyzed with both approaches. Figure 5-1 shows the results of clustering analysis done with mechanical data (M and H) revealing three phases with different mechanical properties in the grid area. Without any chemical data attached to the clusters, the interpretation of what the various phases are is a simple speculation based on XRD data from a macrosample. For instance, phases in Figure 5-1 would be interpreted as a clayey matrix phase (black squares), an inclusion (quartz grains and/or calcite shells) phase (green diamonds), and a mixture phase (red triangles). The mixture phase is the result of the indenter falling on boundaries between different phases, say a grain boundary embedded in a clayey matrix. Clustering analysis adding Si and Al to the same mechanical data set of Figure 5-1 helps produce the Si/Al ratio that indicates clay mineralogy (e.g., green phase in Figure 5-2). Comparing Figures 5-1 and 5-2, we see fewer points in the clay phase (Phase 2) of Figure 5-2 than Phase 1 of Figure 5-1. The results indicate stricter clustering when coupling chemistry to mechanical data producing the purest

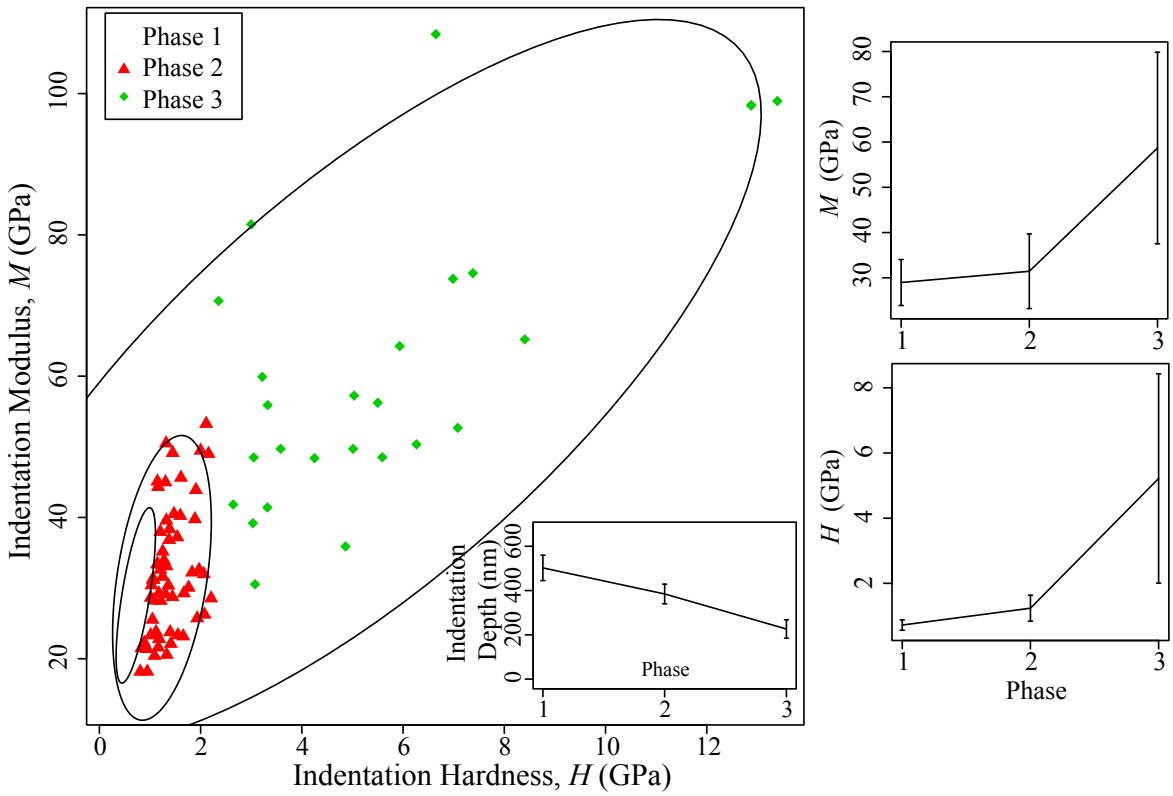

Figure 5-1: Results of clustering analysis using only mechanical data M and H on a Marcellus sample (Mar108-x_1g1). Three mechanically different phases are identified. Values of M and H are average values (in GPa) in each cluster. Error bar indicates one standard deviation from the mean. The Inset shows the depths of indentation in each cluster.

possible clay composites.

One concern running clustering analysis with multiple chemical elements is how complex the clustering model becomes. In general, clustering analysis using M, H, Si and Al is adequate in many formations (Haynesville, Antrim, Barnett, Fayetteville; Work courtesy of Dr. Sara Abedi). However, due to the abundance of carbonates (reaching 36 wt.%) and pyrite (reaching 12 wt.%) in some Marcellus facies, and with Marine Type II (MTII) being a carbonate formation, adding S, Ca and/or Mg to clustering proves valuable. This addition highlights tests in pyrite-rich areas, differentiates different types of inclusions (e.g., sand grains vs. apatite grains), and occasionally differentiates different clay composites contaminated with other phases (e.g., Ca-rich or Si-rich clay composites). For instance, clay composites isolated in MTII (containing $<$ 4 wt.% clay content) and Woodford (containing 60.6 wt.% quartz) are, respectively, contaminated with carbonates and (amorphous) quartz.

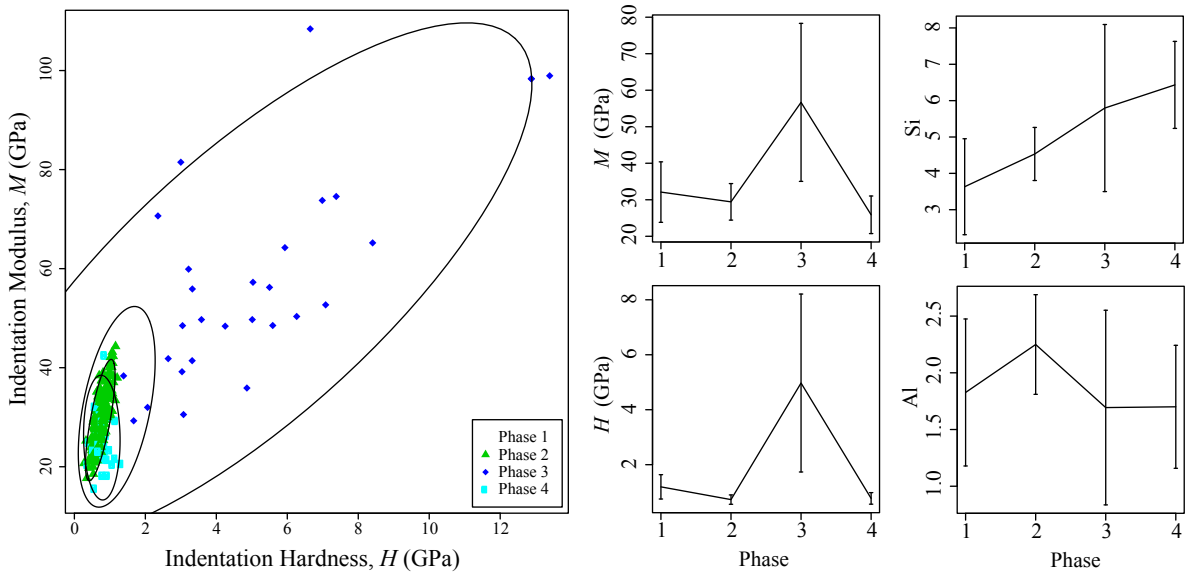

Figure 5-2: Results of clustering analysis done with coupled chemo-mechanical data (M, H, Si and Al) of Mar108x_1g1 (same sample seen in Figure 5-1). Four different phases are identified. Values of M and H are average values (in GPa) in every cluster. Values of Si and Al are average count rates. Error bar indicates one standard deviation from the mean.

The following example from Marine Type II is presented to show that chemo-mechanical clustering does not render a clustering model more complex. Clustering analysis using mechanical data (M and H; Figure 5-3) reveals five mechanically-different clusters. The fact that the formation is chemically and texturally complex (porous shells and shell fragments; Figure 2-8) calls for coupling few chemical elements to the mechanical data. In this example, Si and Al are needed to identify the low clay content. Ca, P, and S are added because MTII is a carbonate rock and to capture the apatite ($\sim$ 13 wt. %) and sulfur content of the formation. The chemo-mechanical clustering in MTII using the five chemical elements (Si, Al, Ca, S, P) (Figure 5-4) produce a total of six clusters, thus adding only one cluster to those obtained from mechanical clustering (Figure 5-3).

In addition to the chemical description of every phase in a grid area, chemo-mechanical clustering helps differentiate chemically-different phases with similar mechanical properties and/or chemically-similar phases with different mechanical properties. This differentiation is illustrated in Figure 5-5 (right) that indicates the presence of two Ca-rich phases with different mechanical properties. The first (orange phase in Figure 5-5) is mechanically stronger, representing a well-preserved carbonate shell, whereas the second (green phase in Figure 5-5)

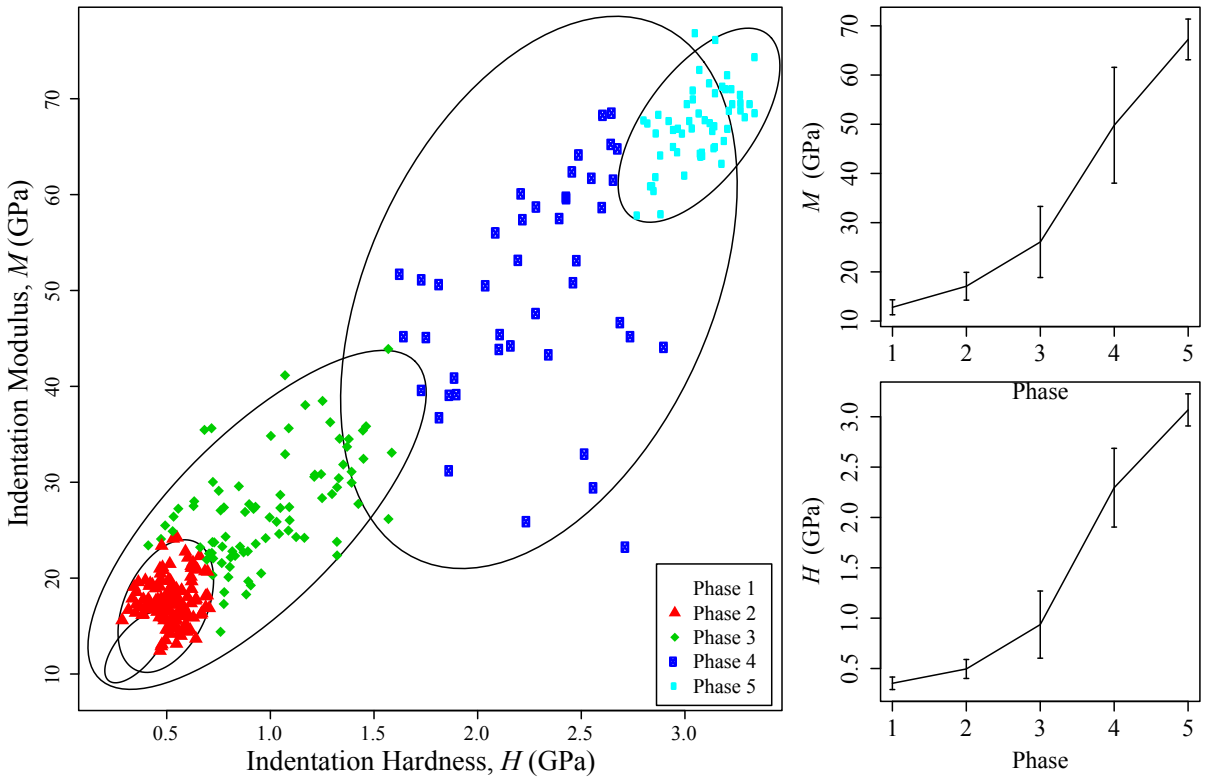

Figure 5-3: Results of clustering analysis using only mechanical data M and H from Marine Type II (MTII-S1G2). Five different mechanical phases are identified. Values of M and H are average values (in GPa) from all points in a cluster. Error bar indicates one standard deviation from the mean.

indicates highly porous shell fragments.

5.5 Chapter Summary

Model-based clustering analysis implements maximum likelihood functions, an expectation-maximization algorithm, and Bayesian model selection assuming that the data sets are mixtures of unknown number of Gaussian distributions. The complexity of the clustering model is related to the number of parameters used as input. In addition to mechanical properties (M and H), the clustering analysis algorithm is run using the least number of chemical elements needed to represent the mineralogical heterogeneity in a formation. We have shown that clustering analysis using coupled chemo-mechanical data provides a chemical descriptions of the various clusters produced and isolates the purest possible organic-rich clay composites

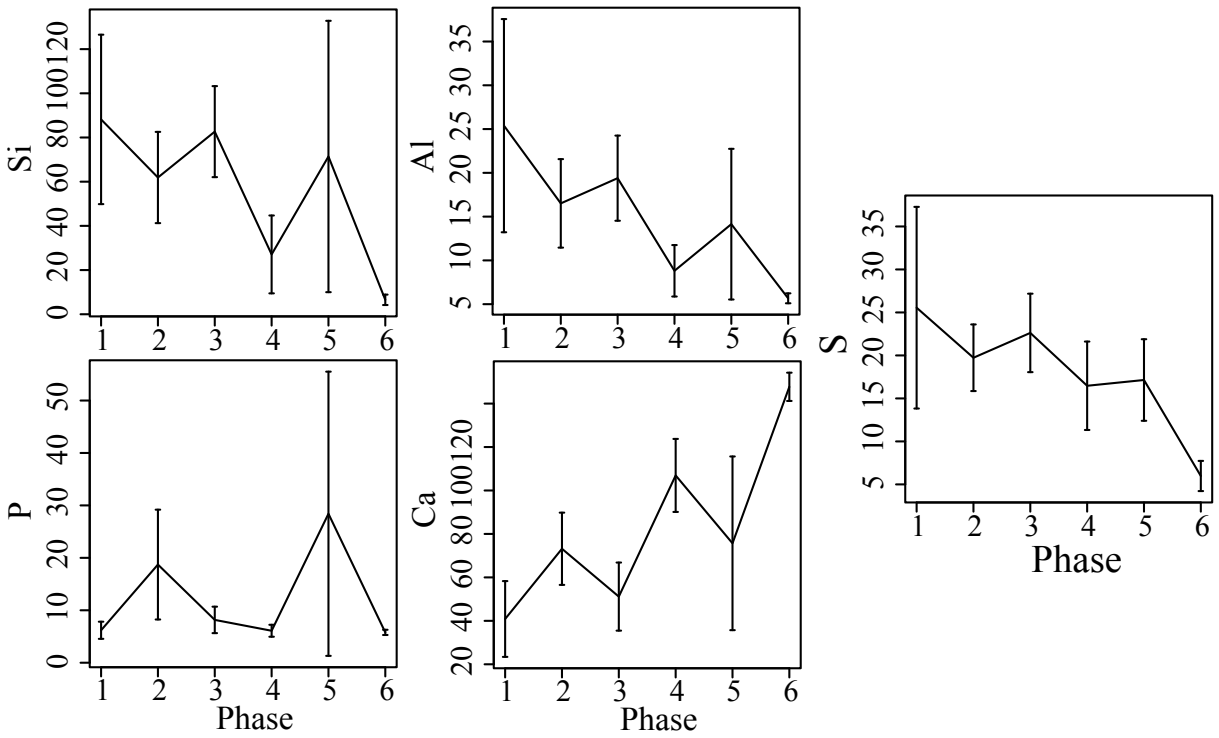

Figure 5-4: The five chemical elements used, in addition to M and H, in the chemo-mechanical clustering analysis of MTII-S1G2. Values of chemical elements are average count rates. Error bar indicates one standard deviation from the mean. Clusters and Mechanical data are seen on the next page.

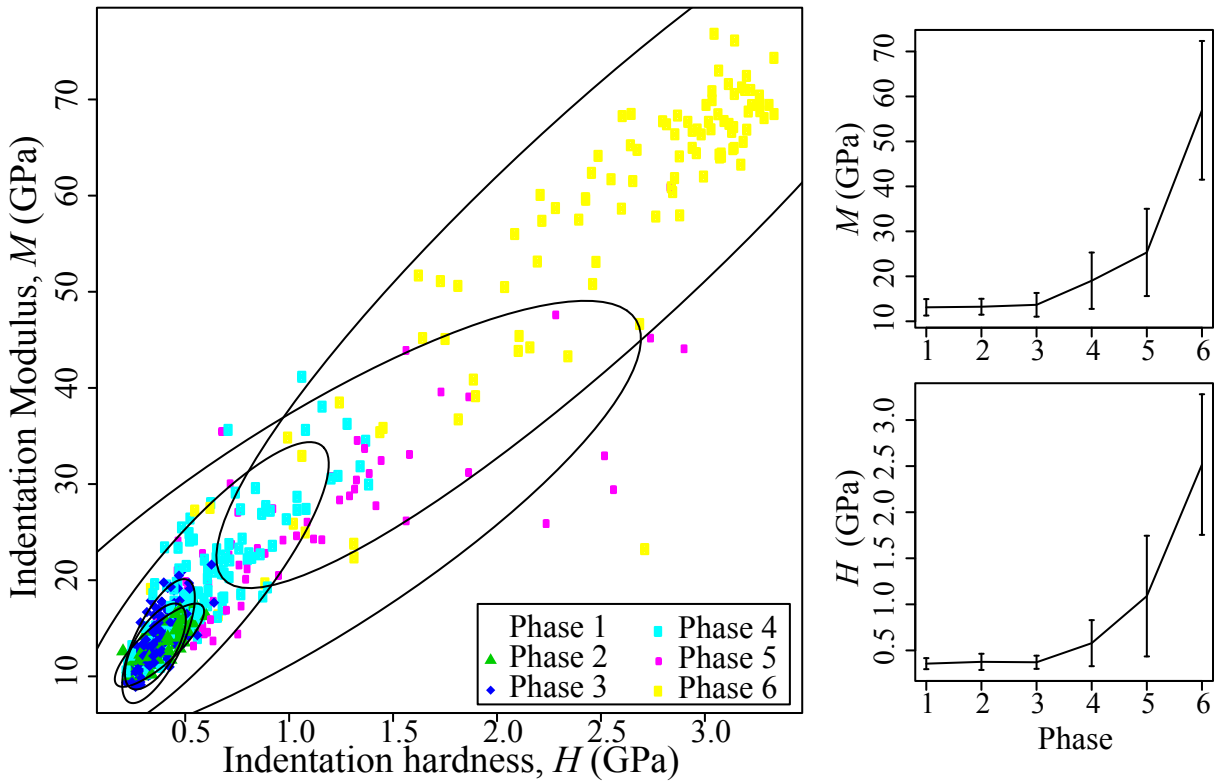

Figure 5-4: (Cnt'd) Clustering analysis results using coupled chemo-mechanical data of MTII-S1G2. Values of M and H are average values (in GPa) in a cluster. Error bar indicates one standard deviation from the mean.

from every grid area. Validating the clustering analysis results, interpreting and understanding the mechanical properties of the isolated organic-rich clay composites, and using these properties in textural modeling are the focal topics in Part III.

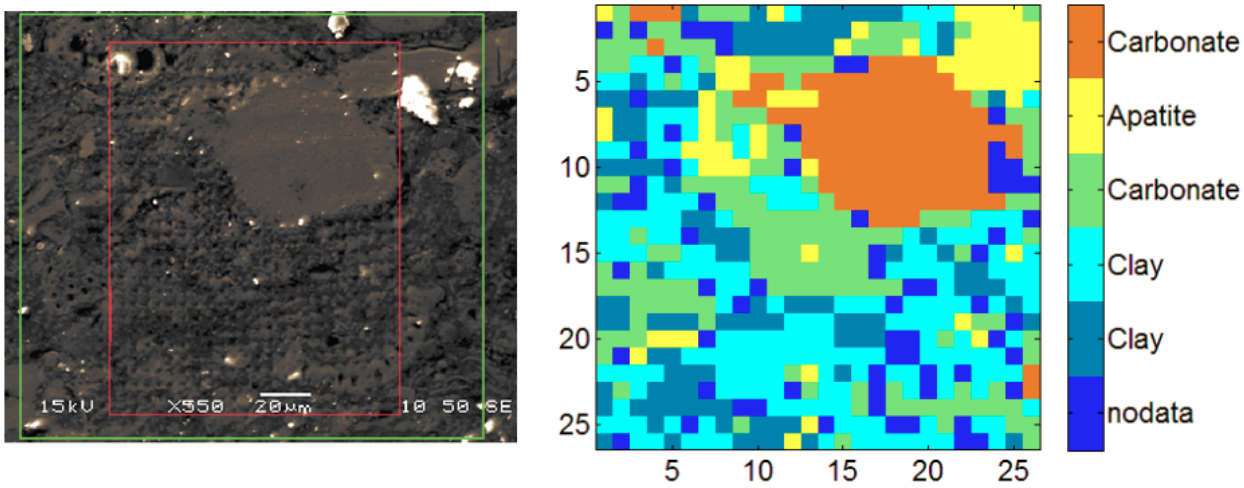

Figure 5-5: A phase map (right) obtained interpreting chemo-mechanical clustering results (Figure 5-4) of grid S1G2 (left) indented on Marine Type II sample. Note the apatite grain (yellow phase) identified and the presence of two carbonate rich phases: a large carbonate shell (orange phase) and carbonate-rich fragments/matrix (green phase).

Part III

Time-Independent Mechanical Properties and Textural Modeling

Chapter 6

Time-Independent Mechanical Properties of Organic-Rich Clay Composites

An experimental and statistical approach was undertaken in Part II to isolate the organic-rich clay composites in every formation. In part III, we study the time-dependent mechanical properties of the clay composites and the role of organic matter affecting these mechanical properties as well as the composites' texture.

In this chapter, we validate the experimental approach and highlight the success of the clustering analysis algorithm isolating the clay composites in the heterogeneous formations. The time-independent mechanical properties (M_o and H_o) of the clay composites are summarized and discussed to better understand 1) any correlation between stiffness and hardness, 2) mechanical anisotropy at the microscale, and 3) the effect of composite packing density and organic content. M_o and H_o represent instantaneous elastic moduli and hardness obtained from nanoindentation tests done with $P_{max} = 4.8$ mN and hold-time phase duration of 10 s. Experimental work of Dr. Sara Abedi testing Haynesville, Fayetteville, Antrim, and Barnett formations is used to complement tests done, as part of this thesis, on over-mature Marcellus and immature Woodford[1].

[1]Except for results from Marine Type II and Woodford, the results and findings listed in this chapter were published. We refer the reader to: Abedi, S., Slim, M., Hofmann, R., Bryndzia, T., and Ulm, F.-J.. 2015. Nanochemo-mechanical signature of organic-rich shales: a coupled indentation–EDX analysis. Acta Geotechnica, 1-14.

6.1 Clustering Analysis: Validity of Results

Several nanoindentation grids are performed on each sample for a good statistical representation of the mechanical properties of the various chemical phases. The clay composites are isolated with clustering analysis after coupling mechanical data (M_o and H_o) with EDS intensities of the most abundant chemical elements in the formations (e.g., Si, Al, S, and/or Ca). The clay composites in Haynesville, Fayetteville, Antrim and Barnett are isolated using clustering with M_o, H_o, Si, and Al as input (results courtesy of Dr. Sara Abedi). Due to the abundance of carbonates (reaching 36 wt.%) and pyrite (reaching 12 wt.%) in some Marcellus facies and apatite in Marine Type II, S, Ca, P, and/or Mg are also added as input in the clustering analysis in these formations.

The clusters interpreted as clay composites are those with the lowest hardness and stiffness, and an Si/Al ratio $\leq$2 indicating either a 1:1 or 2:1 clay structure. These criterion were adequate to differentiate the clay composites in every nanoindentation grid performed in all the formations. The clay composites in Woodford show high Si/Al ratios (Si/Al $\geq$4) ascribed to the presence of fine-grained amorphous quartz. We recall that Woodford is 60.6 wt. % quartz not all of which occur in the form of inclusions (sand grains).

As seen in Chapter 5, clusters obtained with clustering analysis are based on parameterizing the covariance matrix (Equation (5.2)) of the (coupled) variables (M, H, Si, Al, ...) at every indentation location. The covariance matrix generalizes the notion of variance (or standard deviation) in high-dimensional spaces, determines the volume, shape, and orientation of each cluster, and reflect whether 2 variables co-vary. Clusters drawn in the M-H space (e.g., Figure 5-2) use the M_o-H_o covariance matrix and indicate, from their elliptical shape and orientation, a relationship between M_o and H_o. Figure 6-1 shows mechanical data of the clay composites isolated with clustering analysis from various grids performed on Marcellus 108. The overlapping data sets indicate the similarity in shape, volume, and orientation of the clay composite clusters obtained from different grids taken in random areas. Such a similarity attests to the success of the clustering analysis isolating the clay composites within every grid area. The Marcellus data, also, reveal a power scaling relationship of the form $M_o = A \times H_o^{\alpha}$ between the nanoindentation elastic modulus and hardness from individual

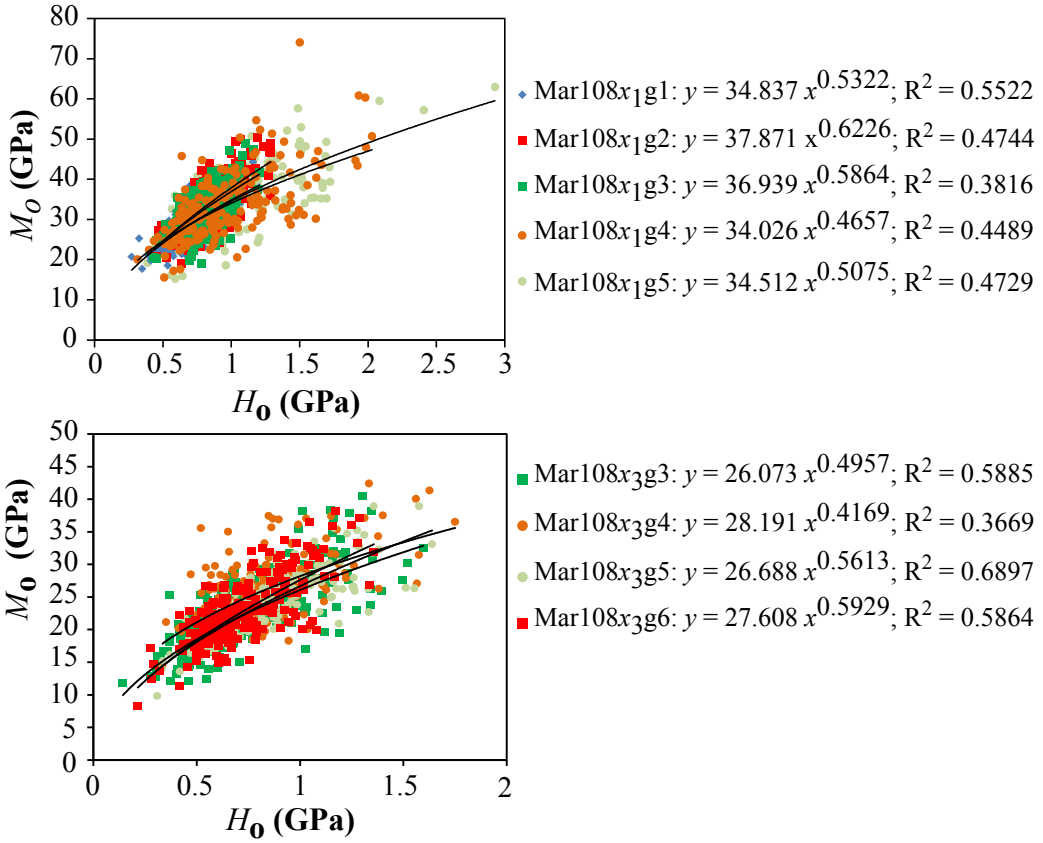

Figure 6-1: The power-law relationship between M_o and H_o in the clay composites isolated with clustering analysis in the grids performed on Marcellus 108 (Mar108) in both x_1- and x_3-directions. Note the similarity in the clusters' shapes, volumes, and orientations. Slight variations in the fits reflect localized heterogeneity in the clay composites.

nanoindentation tests penetration clay composites in a grid area. Like Marcellus 108, Marcellus 46, Marcellus 151, and Woodford data (Tables 6.1-6.3) also show consistent power scaling between M_o and H_o. Variations in the power fit parameters (A and α) in Marcellus 46, which is an organic-poor sample, indicate localized heterogeneity within the clay composites and/or contamination of the clay composites by other chemical phases.

Table 6.1: The parameters of the power fits ($M_o = A \times H_o^{\alpha}$) relating M_o and H_o of the clay composites obtained indenting the Marcellus facies parallel to their bedding planes (x_1-direction). Indentation data are from 10 s hold-time nanoindentation tests done with $P_{max} =$ 4.8 mN.

Sample	Grid	# of Indents	A	α	R^2
Mar46x_1	g0*	120	43.27	0.4055	0.6726
Mar46x_1	g1	155	27.196	0.5038	0.8564
Mar46x_1	g2	144	33.03	0.3350	0.4696
Mar46x_1	g3	116	42.33	0.2824	0.4227
Mar46x_1	g4	75	43.615	0.3461	0.4838
Mar46x_1	g5	197	34.282	0.6301	0.6825
Mar46x_1	All	807	34.588	0.5089	0.6445
Mar108x_1	g1	239	34.837	0.5322	0.5522
Mar108x_1	g2	136	37.871	0.6226	0.4744
Mar108x_1	g3	175	36.939	0.5864	0.3816
Mar108x_1	g4	200	34.026	0.4657	0.4489
Mar108x_1	g5	178	34.512	0.5075	0.4729
Mar108x_1	All	928	35.17	0.5104	0.4892
Mar151x_1	g1	245	29.424	0.4804	0.5145
Mar151x_1	g2	201	29.727	0.4941	0.4726
Mar151x_1	g3	240	29.674	0.5124	0.592
Mar151x_1	g4	172	29.272	0.536	0.588
Mar151x_1	All	858	29.517	0.5058	0.5516

*Data courtesy of Dr. S. Abedi.

Table 6.2: The parameters of the power fits ($M_o = A \times H_o^{\alpha}$) relating M_o and H_o of the clay composites obtained indenting the Marcellus facies perpendicular to their bedding planes (x_3-direction). Data are from 10 s hold-time nanoindentation tests done with $P_{max} = 4.8$ mN.

Sample	Grid	# of Indents	A	α	R^2
Mar46x_3	g1	84	32.867	0.2926	0.5923
Mar46x_3	g2	87	31.949	0.4333	0.4298
Mar46x_3	g3	76	38.571	0.3093	0.4326
Mar46x_3	g4	121	38.493	0.3516	0.6397
Mar46x_3	All	368	35.837	0.3316	0.5081
Mar108x_3	g3	315	26.073	0.4957	0.5885
Mar108x_3	g4	193	28.191	0.4169	0.3669
Mar108x_3	g5	206	26.688	0.5613	0.6897
Mar108x_3	g6	231	27.608	0.5929	0.5864
Mar108x_3	All	1217	26.874	0.4943	0.6278
Mar151x_3	g1	117	26.403	0.5539	0.5875
Mar151x_3	g2	206	25.739	0.5197	0.4805
Mar151x_3	g3	210	24.894	0.5068	0.5715
Mar151x_3	g4	255	26.015	0.4545	0.629
Mar151x_3	All	788	25.639	0.4795	0.5674

Table 6.3: The parameters of the power fits ($M_o = A \times H_o^{\alpha}$) relating M_o and H_o of the clay composites obtained indenting the Woodford samples parallel (x_1-direction) and perpendicular (x_3-direction) to their bedding planes. Data are from 10 s hold-time nanoindentation tests done with $P_{max} = 4.8$ mN.

Sample	Grid	# of Indents	A	α	R^2
Woodford Ax_1	g1	223	27.507	0.5386	0.4778
Woodford Ax_1	g2	230	25.538	0.4446	0.5378
Woodford Ax_1	g3	277	24.13	0.4291	0.5331
Woodford Bx_1	g1	278	24.14	0.4301	0.3347
Woodford Bx_1	g2	294	24.308	0.3590	0.5331
Woodford Bx_1	All	1302	24.92	0.4336	0.4595
Woodford Ax_3	g1	281	21.171	0.395	0.568
Woodford Ax_3	g2	235	21.618	0.5292	0.5767
Woodford Ax_3	g3	241	19.349	0.4223	0.3375
Woodford Bx_3	g1	340	19.922	0.4009	0.6488
Woodford Bx_3	g2	246	20.712	0.4225	0.4639
Woodford Bx_3	g3	356	21.197	0.4552	0.6286
Woodford Bx_3	All	1699	20.668	0.4377	0.5905

6.2 Clay Composites Mechanical Properties: Results and Discussion

With the clay composites isolated in every grid, the mean values and standard deviation of M_o and H_o, assuming normal distribution, in each cluster are calculated. Data are reported in Tables 6.4-6.6 and plotted in Figure 6-2, which is informative in many ways.

6.2.1 Stiffness and Hardness of Clay Composites

The mechanical data from nanoindentation (Figure 6-2) show that mature formations are stiffer and harder than immature ones. This is ascribed to an increase in organic matter stiffness with maturity (Mba et al., 2010; Prasad et al., 2011; Zargari et al., 2011; Bousige et al., 2016).

Despite the different mineralogy (Figure 2-2), maturity (Table 2.9), total organic content (TOC = 0.49-12.2 wt.%), and porosities (ϕ = 4.0-12.6%) of the formations studied, a power

Table 6.4: Indentation mechanical properties (M_o, H_o) of the clay composites in the mature Marcellus facies. The data are obtained from 10 s hold-time nanoindentation tests done with $P_{max} = 4.8$ mN in x_1- and x_3-directions. h_{max} is the maximum depth reached by the indenter tip (μ = mean values; σ = standard deviation).

		# of	H_o (GPa)		M_o (GPa)		h_{max} (nm)	
Sample	Grid	Indents	μ	σ	μ	σ	μ	σ
Mar46x_1	g0*	120	1.05	0.41	43.58	8.74	432.02	92.07
Mar46x_1	g1	155	0.93	0.34	25.76	5.87	477.49	129.95
Mar46x_1	g2	144	2.03	0.57	41.70	6.32	317.64	49.22
Mar46x_1	g3	116	2.30	0.66	53.37	7.32	290.55	46.09
Mar46x_1	g4	75	1.71	0.81	51.97	13.88	358.96	117.99
Mar46x_1	g5	197	2.28	0.39	57.59	7.36	284.63	23.76
Mar49x_1	g0*	-	1.88	0.60	50.94	9.01	-	-
Mar108x_1	g1	239	0.73	0.17	29.42	5.07	500.31	59.32
Mar108x_1	g2	136	0.86	0.18	34.69	6.63	458.61	48.88
Mar108x_1	g3	175	0.82	0.15	33.02	5.76	469.22	44.22
Mar108x_1	g4	200	0.95	0.34	33.21	8.28	456.27	72.50
Mar108x_1	g5	178	1.04	0.36	35.21	8.10	434.48	66.31
Mar150x_1	g0*	-	0.73	0.15	29.10	5.55	-	-
Mar151x_1	g1	245	1.05	0.37	30.03	6.61	429.92	63.78
Mar151x_1	g2	201	1.04	0.30	30.27	5.96	426.51	52.48
Mar151x_1	g3	240	1.00	0.40	29.50	7.39	444.82	78.16
Mar151x_1	g4	172	0.97	0.31	28.75	6.39	444.89	70.07
Mar46x_3	g1	84	2.38	1.22	41.65	7.81	312.04	64.93
Mar46x_3	g2	87	2.23	0.89	45.31	12.09	312.92	75.35
Mar46x_3	g3	76	3.50	1.86	56.16	14.43	263.69	65.58
Mar46x_3	g4	121	1.83	0.90	46.75	12.96	362.99	199.52
Mar108x_3	g3	315	0.71	0.25	21.90	5.04	500.31	81.00
Mar108x_3	g4	193	0.82	0.24	25.98	5.21	479.06	62.64
Mar108x_3	g5	206	0.83	0.25	23.86	4.71	482.87	69.35
Mar108x_3	g6	231	0.73	0.20	22.85	5.04	510.90	73.41
Mar151x_3	g1	117	0.83	0.25	23.77	5.35	480.31	70.27
Mar151x_3	g2	206	0.93	0.32	24.91	6.40	458.45	70.37
Mar151x_3	g3	210	0.88	0.30	23.29	5.41	480.64	89.21
Mar151x_3	g4	255	0.75	0.29	22.71	5.68	524.67	134.21

*Data courtesy of Dr. S. Abedi.

Table 6.5: Mechanical properties (M_o, H_o) of the clay composites in mature Haynesville (A#V) facies and Fayetteville. Data are obtained from 10 s hold-time nanoindentation tests done with P_{max} = 4.8 mN in x_1- and x_3-directions. Data courtesy of Dr. S. Abedi (μ = mean values; σ = standard deviation).

		# of	H_o (GPa)		M_o (GPa)	
Sample	Grid	Indents	μ	σ	μ	σ
A5Vx_1	g0a	89	0.65	0.20	30.58	7.09
A5Vx_1	g0b	155	0.62	0.14	30.20	5.43
A5Vx_1	g0	225	0.90	0.17	31.60	4.51
A6Vx_1	g0a	-	0.79	0.33	28.36	6.89
A6Vx_1	g0b	67	1.20	0.20	37.79	5.00
A6Vx_1	g0	161	0.95	0.20	34.90	6.14
A7Vx_1	g0	179	0.62	0.25	29.94	7.05
A7Vx_1	g0	157	0.86	0.23	32.24	6.56
A2Vx_3	g0a	75	0.5	0.19	23.11	6.17
A2Vx_3	g0b	149	0.49	0.26	22.32	6.42
A2Vx_3	g0c	165	0.79	0.18	24.33	4.12
A2Vx_3	g0d	108	0.51	0.22	24.02	6.54
A5Vx_3	g0	-	0.59	0.26	22.85	7.75
A6Vx_3	g0b	157	0.38	0.15	20.2	5.61
A6Vx_3	g0	197	0.52	0.2	20.17	5.43
A7Vx_3	g0b	246	0.53	0.23	20.94	5.92
A7Vx_3	g0	244	0.55	0.24	19.28	4.84
Fayetteville x1	g0a	-	0.96	0.21	31.99	5.91
Fayetteville x1	g0b	-	0.87	0.18	30.27	6.05

Table 6.6: Indentation mechanical properties (M_o, H_o) of the clay composites in the immature Antrim, Barnett, and Woodford samples. Data are obtained from 10 s hold-time nanoindentation tests done with $P_{max} = 4.8$ mN in x_1- and x_3- direction. h_{max} is the maximum depth reached by the indenter tip in the clay composite (μ = mean values; σ = standard deviation).

		# of	H_o (GPa)		M_o (GPa)		h_{max} (nm)	
Sample	Grid	Indents	μ	σ	μ	σ	μ	σ
Antrimx_1	g0a*	356	0.64	0.13	21.60	5.33	-	-
Antrimx_1	g0b*		0.60	0.10	20.49	3.58	-	-
Antrimx_3	g0a*	325	0.47	0.11	13.49	3.06	-	-
Antrimx_3	g0b*		0.49	0.12	11.16	2.4	-	-
Barnettx_1	g0a*	342	0.54	0.09	18.99	4.56	-	-
Barnettx_1	g0b*		0.50	0.08	16.19	3.07	-	-
Barnettx_3	g0a*	217	0.47	0.08	11.78	2.45	-	-
Barnettx_3	g0b*		0.51	0.08	12.97	1.87	-	-
WoodfordAx_1	g1	223	0.79	0.46	22.37	6.10	517.61	110.44
WoodfordAx_1	g2	230	0.59	0.21	20.09	4.11	563.79	92.05
WoodfordAx_1	g3	277	0.63	0.23	19.68	4.14	550.74	90.34
WoodfordBx_1	g1	278	0.53	0.16	18.31	3.60	596.03	88.54
WoodfordBx_1	g2	294	0.63	0.22	20.58	4.36	552.43	88.47
WoodfordAx_3	g1	281	0.71	0.27	18.32	3.75	541.26	94.91
WoodfordAx_3	g2	235	0.58	0.16	16.20	3.17	582.09	80.82
WoodfordAx_3	g3	241	0.53	0.14	14.86	2.74	607.31	74.26
WoodfordBx_3	g1	340	0.63	0.32	16.31	3.85	577.99	117.66
WoodfordBx_3	g2	246	0.44	0.11	14.69	2.31	641.05	75.78
WoodfordBx_3	g3	356	0.61	0.29	16.77	4.42	579.51	114.88

*Data courtesy of Dr. S. Abedi.

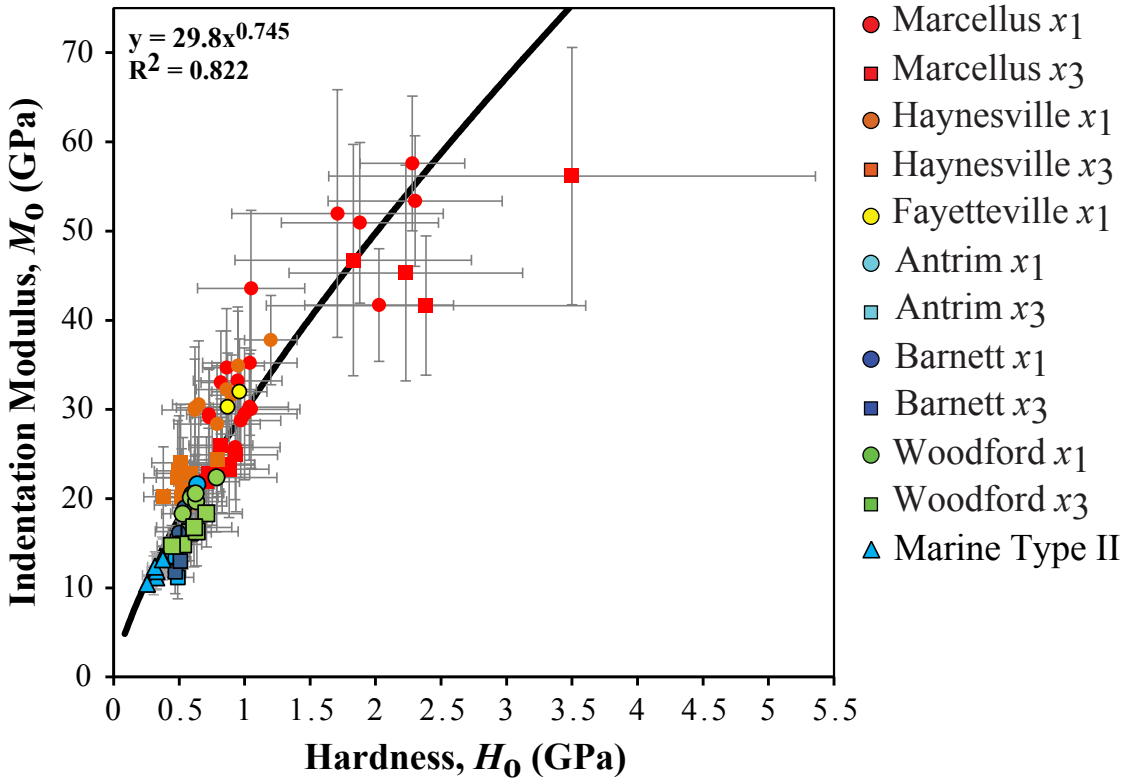

Figure 6-2: Mean mechanical properties of the clay composites (M_o vs. H_o) from overmature (Marcellus), mature (Haynesville and Fayetteville) and immature (Antrim, Barnett, and Woodford) formations. Haynesville, Fayetteville, Antrim, and Barnett data are courtesy of Dr. S. Abedi.

scaling relationship -as seen in individual grids- exists between grid mean stiffness and hardness. Such an M_o-H_o scaling relationships seems to be a universal functional relationship within the clay composites. It reflects a dependence between the mechanical properties (M_o and H_o) on one hand and the collective rock characteristics (microtexture, organic content and maturity, and clay volume fraction) on the other.

6.2.2 Anisotropy of the Clay Composites

The clay composites exhibit distinct anisotropy in stiffness (M_o), but to a much lesser extent, in hardness (H_o). The values in the x_1-direction (nanoindentations parallel to bedding plane; X1-fit in Figure 6-3) are typically higher than values in x_3-direction (nanoindentations perpendicular to bedding planes; X3-fit in Figure 6-3). Like source rocks (this work; Holt et al.,

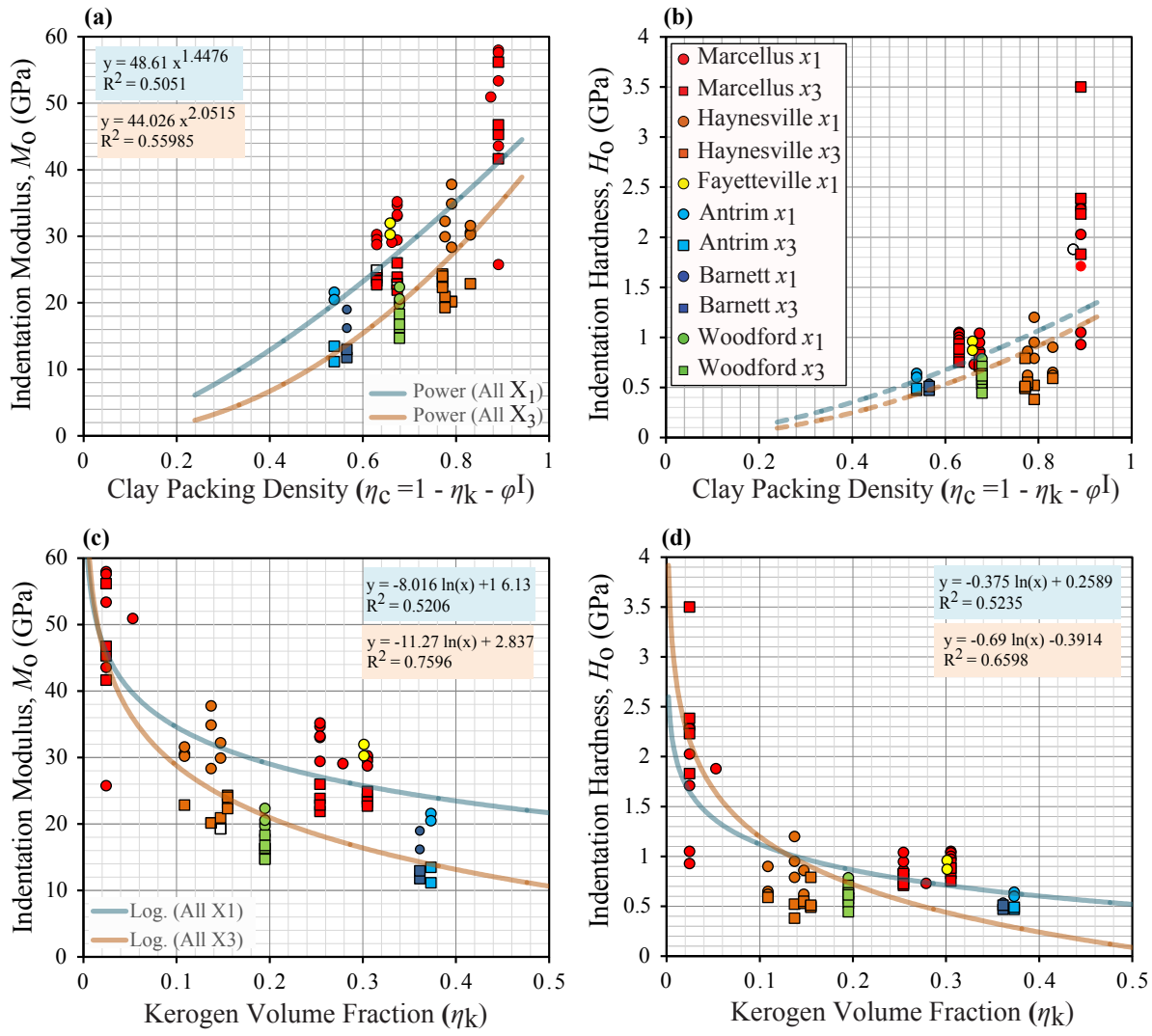

Figure 6-3: Relationships between nanoindentation mechanical properties (M_o, H_o) and (a,b) clay packing density and (c,d) kerogen volume fraction. Kerogen volume fraction, η_k, is calculated from TOC assuming ρ_k=1.2 g/cc and using Equation (2.6): $\eta_k = (1-\phi)\frac{m_k/\rho_k}{\Sigma_{i=1}^{N}(m_i/\rho_i)}$. All parameters are defined in the text.

2011; Lucier et al., 2011; Harris et al., 2011; Sondergeld and Rai, 2011), organic-free shale formations also exhibit elastic anisotropy (Ulm and Abousleiman, 2006; Bobko and Ulm, 2008; Deirieh, 2011) at the composite level (level I). This mechanical anisotropy is ascribed to texture and packing density of clay aggregates, diagenetic smectite-to-illite transformations (Vernik and Landis, 1996; Vernik and Liu, 1997), changes in organics matter texture with compaction and maturity, and microcrack development (Vernik and Landis, 1996). Stiffness anisotropy (Figure 6-3 a,c) is affected by both packing density and TOC, with the latter becoming a more important factor at high TOC. Nanoindentation hardness (H_o), that relates to cohesion and friction of the clay particles (Bobko et al., 2011), is found to be slightly affected by the clay packing (Figure 6-3b) and strongly affected by TOC (Figure 6-3d) when the latter constitutes more than 10% of the clay composite volume.

6.2.3 Ductility of Clay Composites

Another observation from the experimental data is ductility, which is the ratio of the elasticity modulus and hardness (M_o/H_o). Ductility is inversely proportional to the elastic strain limit of a material. In other words, a material with high ductility has a low elastic strain limit and deforms plastically. For elastic material, M_o/H_o only depends on the indenter geometry. For instance, for a Berkovich tip (with an equivalent half-cone angle $\theta = 70.32°$), $M_o/H_o = 2\tan\theta = 5.59$ (Constantinides and Ulm, 2007). M_o/H_o values from the clay composites range between 21-49 and 16-53 in the in x_1- and x_3-directions, respectively. These ranges indicate a deviation from elastic behavior (an observation that is further investigated in Part III, studying time-dependent mechanical properties and creep deformation mechanisms) and match, in order of magnitude, ductility of clay minerals (vermiculite, phlogopite, muscovite, talc, and pyrophyllite) obtained by Berthonneau et al. (in preparation) using indentations with loads ranging between 1.3-6.0 mN (Table 6.7). Berthonneau's results also reflect plasticity in the clay mineral.

To study the effect of clay volume fraction and organic content on the mechanical properties, assumptions about porosity and organic matter distributions are made. In a first approach, porosity in each sample is assumed to be equally distributed among all phases

Table 6.7: Elasticity and hardness properties of clay minerals obtained by indenting clay minerals using 1.3-6.0 mN loads (Berthonneau et al., in preparation).

(GPa)	Nanoindentation				
	Muscovite	Phlogopite	Vermiculite	Talc	Pyrophyllite
m_1	97.9± 8.7	62.1± 6.6	17.7± 1.9	25.5± 4.2	26.2± 4.7
m_3	66.7± 3.5	42.5± 0.8	4.6±0.2	20.0± 2.5	31.5±5.3
h_1	4.44± 0.61	1.86± 0.32	0.43±0.05	0.46± 0.1	0.52±0.14
h_3	6.5± 0.52	5.69± 0.18	0.43±0.02	1.43± 0.3	1.57±0.41
m_1/h_1	22.0± 3.6	33.4± 6.8	41.2± 6.5	55.4± 15.1	50.4± 16.3
m_3/h_3	10.3± 1.0	7.5± 0.3	10.7± 0.7	14.0± 3.4	20.1± 6.2

(inorganic inclusion, clay aggregates, and organic phase)[2]. Kerogen, on the other hand, is assumed to only occur in the clay composite and to have a constant density ($\rho_k = 1.2$ g/cc) regardless of its maturity. The volume fraction of kerogen, η_k, is obtained using Equation (2.6)[3]. In the clay composites, the clay packing density, η_c, equals to:

$$\eta_c = 1 - (\phi + \eta_k) \tag{6.1}$$

where ϕ is the sample porosity. Plotted against clay packing density (Figure 6-4a) and kerogen content (Figure 6-4b), ductility shows some expected correlation with both η_k and η_c: ductility is low when the clay packing density is low (<60%) or very high (>80%). The expected decrease of ductility with increasing packing density indicates concentrated stresses at particle contacts leading to brittle behavior (dilation) in highly brittle systems (Hantal et al., 2014). Decreasing ductility with decreasing packing density, on the other hand, indicates high yield strain and low yield strength. In relation to TOC, an expected increase in ductility is seen with increasing TOC (Figure 6-4b) until the effect of (low) clay packing density becomes dominant counteracting the effect of organic matter. Increasing ductility due to kerogen is expected to be more prominent in immature formations that have less stiff organic matter.

[2]Such an assumption is taken as a first approach to calculate volume fractions of the various constituents of the clay composites. In later presentation in this part (Chapter 8), different porosity distributions pertaining to formation maturity will be proposed.

[3]$\eta_k = (1-\phi)\frac{m_k/\rho_k}{\Sigma_{i=1}^{N}(m_i/\rho_i)}$; where N is the number of all (inorganic and organic) phases.

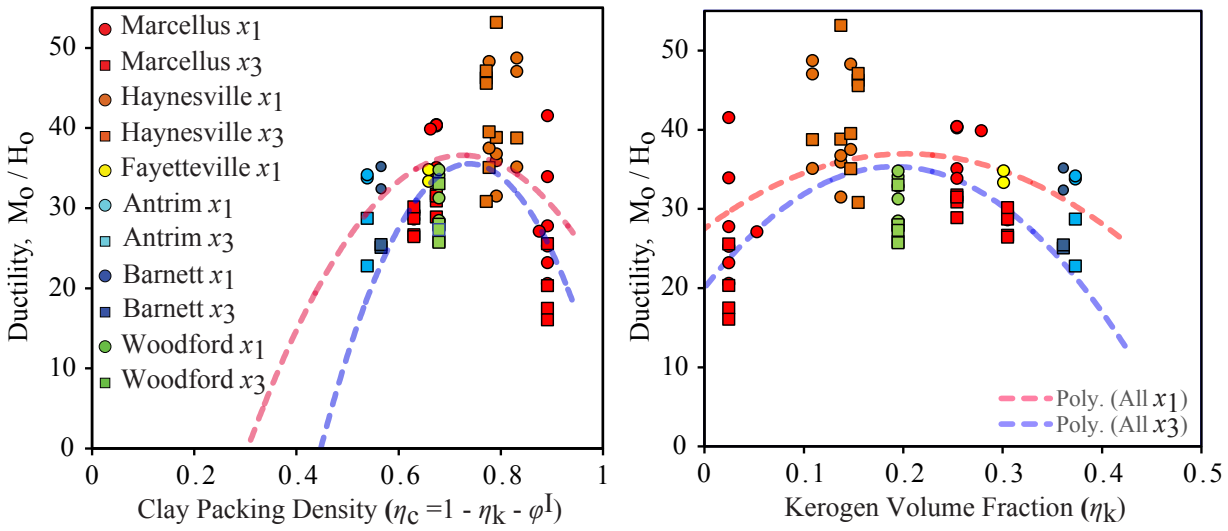

Figure 6-4: Ductility vs. a) clay packing density, η_c, and b) kerogen volume fraction, η_k. η_k is calculated from TOC assuming ρ_k=1.2 g/cc and using Equation (2.6): $\eta_k = (1-\phi)\frac{m_k/\rho_k}{\Sigma_{i=1}^{N} m_i/\rho_i}$. All parameters are defined in the text. Polynomial fits are indicated with dashed lines to follow the effect of η_c and η_k on ductility.

6.3 Chapter Summary

Mechanical properties of the clay composites isolated in each grid show similar clusters in terms of shapes, volumes, and orientations in the M-H space. Such similarity in the clustering results reveals the (repeatable) success of the clustering algorithm isolating clay composites in different (grid) areas within the same specimen as well as in the various formations. The chemo-mechanical clustering, therefore, is a successful approach to differentiate various geo-chemo-mechanical phases in the highly heterogeneous source rocks.

A power scaling relationship of the form $M_0 \sim H_0^{\alpha}$ ($\alpha < 1$) exists between the nanoindentation elasticity modulus, M_0, and hardness, H_0. This power scaling relationship between M_0 and H_0 is consistent within clay composites in individual grids and as well as using all the grids' M_o and H_o mean values. Such a consistency suggests a universal relationship between elasticity and hardness and indicates a concurrent-influence of packing density and TOC determining the mechanical properties of clay composites. Our experimental data also show an increase in stiffness with increasing clay packing density and a role of TOC affecting stiffness anisotropy and strength at the microscale. Ductility ($\frac{M_0}{H_0}$), reflects a deviation from elastic

behavior and the onset of plastic deformation even with short hold-time nanoindentation tests. Ductility decreases with increasing clay packing density and increases with high kerogen content until the effect of (low) clay packing density becomes dominant counteracting the effect of kerogen. This latter observation seems to be the results of low yield strength of systems with low packing densities.

The success isolating the clay composites and the clear dependence of their stiffness, hardness, and ductility on TOC and packing density call for a more in-depth investigation and an understanding of these composites' mechanical properties. A review of the elasticity and hardness homogenization theories is discussed next.

Chapter 7

Elasticity and Strength Homogenization in Porous Media

In this chapter, we review the framework of upscaling operations for elasticity and strength properties in porous media. The linear homogenization theory of elastic properties is reviewed to derive the strain concentration tensor and homogeneous elasticity tensor. Two morphologies that approximate the interaction of pore space in porous media are presented: the matrix-inclusion morphology and the self-consistent scheme. The first assumes a continuous load-bearing solid phase playing the role of a matrix. The second is a disordered morphology in which no one phase plays the role of a matrix. To study hardness, the yield design and limit analysis are introduced as concepts and tools used in nonlinear strength homogenization. We also review the effective strain rate approach and the yield design approach. The former is used to derive strength criteria and dissipation capacities at levels 0 (solid particle level) and I (porous composite level). The latter is used to develop solutions that relate particle strength properties and composite microstructure (packing density) to indentation hardness measurements.

7.1 Elements of Continuum Mechanics and Homogenization Theory

Working with heterogeneous and complex materials such as gas shales, tools and techniques are needed to mechanically represent the material and predict its responses to applied stresses or strains. Microporomechanics is a "continuum approach" used to scale physical quantities from the microscale to the macroscale, devising upscaling rules (Dormieux et al., 2006). Such an approach can be based on averaging techniques used on a representative elementary volume of the material (Dormieux et al., 2006).

7.1.1 Representative Elementary Volume

The concept of a representative elementary volume (REV) is a critical element of a continuum approach as it ensures scale separability. An REV, by definition, is an infinitesimal volume, in a 3D material, large enough to describe and statistically represent the material with all its local heterogeneities. Denoting by d the dimension of a local homogeneity in a material, l the REV length dimension, and L the characteristic length of the material, differential calculus tools can be used for continuum description if the following condition is fulfilled (Zaoui, 2002; Dormieux et al., 2006):

$$d_o \ll d \ll l \ll L \tag{7.1}$$

where d_o is the lower bound length under which continuum mechanics is no longer valid. The REV length dimension, l, must be smaller than the load fluctuation length, λ.

The following section summarizes the discussions of Zaoui (2002) and Dormieux et al. (2006) of localization and homogenization steps in micromechanics.

7.1.2 Scale Separability in the Clay Composites

An indentation test probes a volume of homogenized material under the indenter tip. Ulm et al. (2010) showed that if an indentation probe reaches a depth h_{max}, material situated on a surface of an average radius $4\times h_{max}$ is activated. In the clay composites isolated in Chapter

6, the indentation depth h_{max} = 400-650 nm when indenting with P_{max} = 4.8 mN (Tables 6.4 and 6.6). The homogenized volumes, therefore, are a half-spheres of 1.6-2.6 μm radius surrounding the indenter tip. The dimensions of the various constituents of the clay composites were reviewed in Chapter 2; we recall that clay particle aggregates have a submicrometer size (Ulm and Abousleiman, 2006; Deirieh, 2016), micropores (<0.75 μm) and nanopores (<100 nm) are dominant, and organic pockets occur within the clay particle aggregates (Loucks et al., 2009; Wang and Reed, 2009; Chalmers et al., 2012). These dimensions make us conclude that the scale separability criterion between levels 0 (clay particles and kerogen) and I (clay composites) is met in the gas shale formations.

7.1.3 Localization

Gas shales are heterogeneous at every scale. Their textural parameters are usually not available or are hard to get. An REV, therefore, needs to be established at every scale. The geometry and mechanical properties of the REV must be obtained along with a morphology describing the spatial distribution of the phases in it. Morphological descriptors are usually "texture functions, correlation functions (e.g., the lattice orientation in the case of polycrystal), volume fractions of various phases, and particle shapes and distribution," (Zaoui, 2002). In such complex systems, statistical approaches are usually undertaken specifying the various mechanical phases, determining their geometries and mechanical characteristics, and adopting statistical descriptors of their morphologies. Practically, it is impossible to determine the morphology of a phase, even statistically. The behavior of an REV (or an equivalent homogeneous medium, EHM) is difficult to obtain without assumptions and approximations using a localization step. Localization consists of mechanically modeling the interactions of the various phases and deriving local strain ($\boldsymbol{\epsilon}(\underline{z})$) and local stress ($\boldsymbol{\sigma}(\underline{z})$) fields, knowing the macro fields ($\mathbf{E}$ and $\boldsymbol{\Sigma}$). To simplify the problem, the bounds of the overall mechanical properties are usually defined considering approaches that incorporate admissible strain or stress fields and obey either a displacement or tension boundary condition on the REV. The problem can be further simplified if homogeneous stress or strain boundary conditions are assumed. In the case of a stress boundary condition assumed on dV, the boundary of the REV, the traction on the boundary is (Zaoui, 2002; Hellmich et al., 2004; Dormieux et al.,

2006):

$$T^d = \boldsymbol{\Sigma}(\underline{x}) \cdot \underline{n}(\underline{x}) \tag{7.2}$$

where $\boldsymbol{\Sigma}$ is a known macroscopic stress tensor, and $\underline{n}(\underline{x})$ is the unit outward normal at the boundary. Such a simplification is a valid approximation as long as the requirement of scale separability (Equation (7.1)) is met. The macroscopic stress tensor is equal to the volume average of the stress, $\langle \boldsymbol{\sigma} \rangle_V$, in the REV:

$$\boldsymbol{\Sigma} = \langle \boldsymbol{\sigma} \rangle_V = \frac{1}{V} \int_V \boldsymbol{\sigma}(\underline{z}) dV \tag{7.3}$$

If a homogeneous strain boundary condition is assumed on dV, the displacement at the boundary is given by:

$$\underline{\xi}^d = \mathbf{E}(\underline{x}) \cdot \underline{n} \tag{7.4}$$

and the macroscopic strain tensor is given by the compatibility requirement between micro- and macrostrain:

$$\mathbf{E} = \langle \boldsymbol{\epsilon} \rangle_V = \frac{1}{\mid V \mid} \int_V \boldsymbol{\epsilon}(\underline{z}) dV \tag{7.5}$$

Dealing with homogeneous boundary conditions, the Hill Lemma applies. It shows that the average strain energy density due to externally supplied work to a heterogeneous material satisfies the following (Dormieux et al., 2006):

$$\langle \boldsymbol{\sigma} : \boldsymbol{\epsilon} \rangle = \langle \boldsymbol{\sigma} \rangle : \langle \boldsymbol{\epsilon} \rangle = \boldsymbol{\Sigma} : \mathbf{E} \tag{7.6}$$

In linear elasticity, the macroscopic stress and strain are related to microscopic ones by fourth rank concentration tensors (Zaoui, 2002; Dormieux et al., 2006):

$$\boldsymbol{\sigma}(\underline{z}) = \mathbb{B} : \boldsymbol{\Sigma} \tag{7.7}$$

$$\boldsymbol{\epsilon}(\underline{z}) = \mathbb{A} : \mathbf{E} \tag{7.8}$$

where $\mathbb{A}$ and $\mathbb{B}$ are fourth rank strain and stress concentration tensors, respectively, with $\langle \mathbb{A} \rangle = \langle \mathbb{B} \rangle = \mathbb{I}$; $\mathbb{I}$ being the fourth order symmetric unit tensor.

7.1.4 Strain Concentration Tensor: Eshelby's Problem

The Eshelby inclusion solution (Eshelby, 1957) provides an estimate of the concentration tensors. It solves for the strain field in an ellipsoidal inhomogeneity in an infinite homogeneous matrix and gives changes in the elastic properties of a material when ellipsoidal inhomogeneities are introduced into it (Nemat-Nasser and Hori, 1993). The problem is presented by the following set of equations assuming an inhomogeneity (or a pore phase), (Ω^I), embedded in an infinite solid domain, Ω^s, subjected to a uniform strain boundary condition (Dormieux et al., 2006):

$$\begin{cases} \text{div}\boldsymbol{\sigma} = 0 \\ \boldsymbol{\sigma}(\underline{z}) = \mathbb{C}(\underline{z}) : \boldsymbol{\varepsilon}(\underline{z}),\ with\ \mathbb{C}(\underline{z}) = \begin{cases} \mathbb{C}^I = 0\ for\ \underline{z} \in \Omega^I \\ \mathbb{C}^s\ for\ \underline{z} \in \Omega^s \end{cases} \\ \underline{\xi}(\underline{z}) = \mathbf{E} \cdot \underline{z}\ when\ \underline{z} \to \infty \end{cases} \tag{7.9}$$

where $\mathbf{E}$ is the uniform strain tensor at infinity. Given the contrast in elasticity between an inclusion and a matrix ($\delta\mathbb{C} = \mathbb{C}^I - \mathbb{C}^s$), the linear elastic stress-strain relation is rewritten in the form:

$$\boldsymbol{\sigma} = \mathbb{C}^s : \boldsymbol{\varepsilon} + \boldsymbol{\sigma}^p(\underline{z}) \tag{7.10}$$

where $\boldsymbol{\sigma}^p(\underline{z}) = \delta\mathbb{C} : \varepsilon\chi_I(\underline{z})$ is the fictitious stress. It is non-zero only in the inclusion, I, and captures the deviation from the homogeneous situation induced by the addition of the inhomogeneity or inclusion. χ_I is the characteristic function of the inclusion domain[1]. By assuming that $\boldsymbol{\sigma}^p(\underline{z}) = \boldsymbol{\sigma}^I\chi_I(\underline{z})$ (where $\boldsymbol{\sigma}^I = \delta\mathbb{C} : \varepsilon$) is constant within I, Eshelby's inclusion problem can be re-written as (Dormieux et al., 2006):

[1] $\underline{grad}\chi_I = -\underline{n}\delta_{\partial I}$ where $\delta_{\partial I}$ is the Dirac distribution associated with the boundary of the inclusion (Dormieux et al., 2006).

$$\begin{cases} \text{div}\boldsymbol{\sigma} = 0 \\ \boldsymbol{\sigma}(\underline{z}) = \mathbb{C}^s : \boldsymbol{\varepsilon}(\underline{z}) + \boldsymbol{\sigma}^I \chi_I(\underline{z}) = \mathbb{C}^s : \boldsymbol{\varepsilon} + \delta\mathbb{C} : \boldsymbol{\varepsilon}\chi_I(\underline{z}) \\ \underline{\xi}(\underline{z}) = \mathbf{E}^\infty \cdot \underline{z} \, when \; \underline{z} \to \infty \end{cases} \tag{7.11}$$

The solution to the problem (Equation (7.11)) is given by (Dormieux et al., 2006):

$$\boldsymbol{\varepsilon}(\underline{z}) = -\mathbb{P}(\underline{z}) : \boldsymbol{\sigma}^I + \mathbf{E}^\infty \tag{7.12}$$

where $\mathbb{P}$ is the Hill tensor that characterizes the interactions between particles and depends on the morphology of the inclusion and the elasticity of the medium (Dormieux et al., 2006; Ortega et al., 2007). Having a uniform strain tensor throughout the inclusion, $\boldsymbol{\sigma}^I$ can be written as:

$$\boldsymbol{\sigma}^I = (\mathbb{I} + \delta\mathbb{C} : \mathbb{P})^{-1} : \delta\mathbb{C} : \mathbf{E}^\infty \tag{7.13}$$

where $\boldsymbol{\sigma}^I = \delta\mathbb{C} : \boldsymbol{\varepsilon}^I$ and $\boldsymbol{\varepsilon}^I = -\mathbb{P} : \boldsymbol{\sigma}^I + \mathbf{E}^\infty$ have been used. The strain tensor is (Hellmich et al., 2004; Dormieux et al., 2006):

$$\boldsymbol{\varepsilon}^I = (\mathbb{I} + \mathbb{P} : \delta\mathbb{C})^{-1} : \mathbf{E}^\infty \tag{7.14}$$

Equation (7.14) is valid for an empty porous medium in which $\delta\mathbb{C} = -\mathbb{C}^s$. The Eshelby tensor, $\mathbb{S} = \mathbb{P} : \mathbb{C}^s$, can be introduced into Equation (7.14) to obtain a link between micro- and macrostrain:

$$\boldsymbol{\varepsilon}^I = (\mathbb{I} - \mathbb{S})^{-1} : \mathbf{E}^\infty \tag{7.15}$$

where $(\mathbb{I}-\mathbb{S})^{-1}$ is the strain concentration tensor averaged over the pore space,$\langle \mathbb{A}(z) \rangle_{V_\phi} \equiv \mathbb{A}_I$.

Obtaining the Hill tensor involves finding the displacement field of the problem in Equation (7.11). In the case where $\mathbf{E}^\infty = 0$, Equation (7.11) gives:

$$\text{div}(\mathbb{C}^s : \boldsymbol{\varepsilon}) + \boldsymbol{\sigma}^I \cdot \underline{grad}\chi_I = \text{div}(\mathbb{C}^s : \boldsymbol{\varepsilon}) - \boldsymbol{\sigma}^I \cdot \underline{n}\delta_{\partial I} = 0 \tag{7.16}$$

where $\delta_{\partial I}$ is the Dirac distribution associated with the boundary of I. The solution of the

problem in Equation (7.16) requires using the Green function concept. This concept finds the elementary displacement field solution, $\underline{\xi}^{(p)}$, in an infinite homogeneous elastic continuum (with stiffness $\mathbb{C}^s$) induced by a unit force $\underline{f} = \delta_0(\underline{z})\underline{e}_p$ located at the origin and parallel to $\underline{e}_p$ (Dormieux et al., 2006):

$$\mathrm{div}(\mathbb{C}^s : \mathbf{grad}\underline{\xi}^{(p)}) + \delta_0(\underline{z})\underline{e}_p = 0 \tag{7.17}$$

The second-order Green tensor, $\mathbf{G}$, is defined by $\mathbf{G} \cdot \underline{e}_p = \underline{\xi}^{(p)}$ with components satisfying

$$C^s_{ijkl} G_{kp,jl} + \delta_{ip}\delta_0(\underline{z})\underline{e}_p = 0 \tag{7.18}$$

Using the principle of superposition, the displacement induced at point $\underline{z}$ by a unit point load at $\underline{z}'$, is

$$\underline{\xi}(\underline{z}) = -\int_{\partial I} \boldsymbol{G}(\underline{z} - \underline{z}') \cdot \boldsymbol{\sigma}^I \cdot \underline{n}(\underline{z}') dS_{z'} \tag{7.19}$$

that is,

$$\xi_i(\underline{z}) = -\int_{\partial I} G_{il}(\underline{z} - \underline{z}') n_k(\underline{z}') dS_{z'} \sigma^I_{lk} \tag{7.20}$$

Using the divergence theorem, Equation (7.20) becomes

$$\xi_i(\underline{z}) = -\int_{\partial I} \frac{\partial}{\partial z'_k} G_{il}(\underline{z} - \underline{z}') dV_{z'} \sigma^I_{lk} = \frac{\partial}{\partial z_k}\left(\int_{\partial I} G_{il}(\underline{z} - \underline{z}') dV_{z'} \right) \sigma^I_{lk} \tag{7.21}$$

With the strain tensor being

$$\varepsilon_{ij}(\underline{z}) = \left(\frac{\partial^2}{\partial z_j \partial z_k} \left(\int_{\partial I} G_{il}(\underline{z} - \underline{z}') dV_{z'} \right) \right)_{(ij)} \sigma^I_{lk} \tag{7.22}$$

The symmetry of $\boldsymbol{\sigma}^I$ gives the following:

$$\boldsymbol{\varepsilon}(\underline{z}) = -\mathbb{P}(\underline{z}) : \boldsymbol{\sigma}^I \tag{7.23}$$

where the Hill tensor components are (Dormieux et al., 2006)

$$P_{ijkl}(\underline{z}) = -\left(\frac{\partial^2}{\partial z_j \partial z_k}\left(\int_I G_{il}(\underline{z}-\underline{z}')dV_{z'}\right)\right)_{(ij),(kl)} \tag{7.24}$$

For $\mathbf{E}^\infty \neq 0$, the complete solution for the problem is Equation (7.12).

If the inclusions are spheres in an isotropic medium, then,

$$\mathbb{C}^s = 3k^s\mathbb{J} + 2\mu^s\mathbb{K} \tag{7.25}$$

where k^s and μ^s are the bulk and shear moduli of the matrix, respectively. In this case, the Hill and Eshelby tensors[2] are given by:

$$\mathbb{P} = \frac{\alpha}{3k^s+4\mu^s}\mathbb{J} + \frac{\beta}{2\mu^s}\mathbb{K} \quad and \quad \mathbb{S} = \alpha\mathbb{J} + \beta\mathbb{K} \tag{7.26}$$

with $\alpha = \dfrac{3k^s}{3k^s+4\mu^s}$ and $\beta = \dfrac{6(k^s+2\mu^s)}{5(3k^s+4\mu^s)}$ for the dilute scheme. We note that the dilute approximation neglects interactions between inclusions. To use Eshelby's solution of a constant strain within the inclusion and account for inclusion interactions, the average strain in a homogeneous material surrounding inclusions is needed. It is obtained using the homogenization theory.

7.1.5 Linear Homogenization of Elastic Properties

Macroscopic constitutive laws characterize the deformation of an REV due to the application of external forces and establish relationships between macroscopic forces and macroscopic strains (Dormieux et al., 2006). Rather than deriving the mechanical response of a material by solving a boundary value problem (BVP), averaging microstress and strain values over the REV is obtained using the homogenization theory. Homogenization is the final step when upscaling mechanical properties. It accounts for microstructural inhomogeneity and replaces a complex heterogeneous material by a homogeneous one that behaves, mechanically, in the same way at the macroscopic scale (Zaoui, 2002; Ortega, 2010). Appropriate expressions for

[2] $\mathbb{J} = \frac{1}{3}\mathbf{I}\bigotimes\mathbf{I}$ *and* $\mathbb{K} = \mathbb{I} - \mathbb{J}; \mathbb{J}:\mathbb{J} = \mathbb{J}; \mathbb{K}:\mathbb{K} = \mathbb{K}; \mathbb{K}:\mathbb{J} = \mathbb{J}:\mathbb{K} = 0.$

the macroscopic strain $\mathbf{E}$ (or $\mathbf{\Sigma}$) associated with microscopic strain field $\boldsymbol{\epsilon}(\underline{z})$ (or $\boldsymbol{\sigma}(\underline{z})$) when the REV is loaded with a macroscopic stress $\mathbf{\Sigma}$ (or strain $\mathbf{E}$) are determined (Zaoui, 2002).

In linear elasticity, local constitutive equations are given by Hooke's law:

$$\boldsymbol{\sigma}(\underline{z}) = \mathbb{C}^r(\underline{z}) : \boldsymbol{\varepsilon}(\underline{z}) \tag{7.27}$$

$$\boldsymbol{\varepsilon}(\underline{z}) = \mathbb{S}^r(\underline{z}) : \boldsymbol{\sigma}(\underline{z}) \tag{7.28}$$

where $\mathbb{C}^r$ and $\mathbb{S}^r$ are the stiffness and compliance tensors, respectively, of a phase, r. Using Equations (7.7) and (7.8), in linear elasticity, Equations (7.27) and (7.28) become:

$$\boldsymbol{\sigma}(\underline{z}) = \mathbb{C}^r(\underline{z}) : \boldsymbol{\varepsilon}(\underline{z}) = \mathbb{C}^r(\underline{z}) : \mathbb{A}(\underline{z}) : \mathbf{E} \tag{7.29}$$

$$\boldsymbol{\varepsilon}(\underline{z}) = \mathbb{S}^r(\underline{z}) : \boldsymbol{\sigma}(\underline{z}) = \mathbb{S}^r(\underline{z}) : \mathbb{B}(\underline{z}) : \mathbf{\Sigma} \tag{7.30}$$

Then, using Equations (7.3), (7.5), (7.29), and (7.30) one can write:

$$\mathbf{E} = \overline{\boldsymbol{\varepsilon}} = \overline{\mathbb{A} : \mathbf{E}} = \overline{\mathbb{A}} : \mathbf{E} \tag{7.31}$$

Equation (7.31) holds for any macroscopic strain tensor. Thus,

$$\overline{\mathbb{A}} = \mathbb{I} = (1-\phi)\langle \mathbb{A}(\underline{z}) \rangle_{V_s} + \phi \langle \mathbb{A}(\underline{z}) \rangle_{V_\phi} \tag{7.32}$$

Also,

$$\mathbf{\Sigma} = \overline{\mathbb{C} : \mathbb{A} : \mathbf{E}} = \mathbb{C}^{hom} : \mathbf{E} \tag{7.33}$$

where $\mathbb{C}^{hom} = \overline{\mathbb{C} : \mathbb{A}}$.

To make use of Eshelby's solution while taking interactions among inclusions into account, the average strain in the homogeneous material surrounding the inclusion ($\mathbf{E} = \langle \boldsymbol{\varepsilon}(\underline{z}) \rangle$) is considered. Revisiting the inclusion strain in Equation (7.14), one can write

$$\boldsymbol{\varepsilon}^I = (\mathbb{I} + \mathbb{S} : \mathbb{C}^{s^{-1}} : \delta\mathbb{C})^{-1} : \mathbf{E}^\infty = (\mathbb{I} + \mathbb{S} : (\mathbb{C}^{s^{-1}} : \mathbb{C}^I - \mathbb{I}))^{-1} : \mathbf{E}^\infty \tag{7.34}$$

The strain localization condition concentrating the macroscopic strain at infinity, $\mathbf{E}^{\infty}$, into the inclusion phase is

$$\mathbb{A}^I = (\mathbb{I} + \mathbb{S} : (\mathbb{C}^{s^{-1}} : \mathbb{C}^I - \mathbb{I}))^{-1} \tag{7.35}$$

In the case of an empty porous material, the inclusion domain is the pore volumes with $\mathbb{C}^I = 0$. The strain concentration tensor averaged over the pore space is

$$\langle \mathbb{A}(\underline{z}) \rangle_{V_\phi} \equiv \mathbb{A}^I = (\mathbb{I} - \mathbb{S})^{-1} \tag{7.36}$$

Equation (7.34) reduces to (7.15), and $\mathbb{C}^{hom}$ becomes

$$\mathbb{C}^{hom} = (1 - \phi)\mathbb{C}^s : \mathbb{A}^s = \mathbb{C}^s : (\mathbb{I} - \phi\overline{\mathbb{A}}^p) \tag{7.37}$$

When the compatibility of the micro- and macrostrains is used, the average strain concentration tensor of the matrix requires:

$$\mathbf{E}^{\infty} = \langle \boldsymbol{\varepsilon}(\underline{z}) \rangle_V = (1 - \phi)\langle \boldsymbol{\varepsilon}(\underline{z}) \rangle_{V_s} + \phi \langle \boldsymbol{\varepsilon}(\underline{z}) \rangle_{V_\phi} \tag{7.38}$$

Based on an approach detailed in Dormieux et al. (2006), one way to capture the interaction between pores consists of changing the strain boundary condition at infinity to $\mathbf{E}_0 \cdot (\underline{z})$. This change continues to meet the micro-macro strain compatibility requirement ($\overline{\varepsilon} = \mathbf{E}$). As in the dilute scheme, the uniform strain in an inclusion is taken as an average strain $\overline{\boldsymbol{\varepsilon}}^p$ in the pore space:

$$\overline{\boldsymbol{\varepsilon}}^p = \boldsymbol{\varepsilon}^I = (\mathbb{I} + \mathbb{P} : \delta\mathbb{C})^{-1} : \mathbf{E}_0 \tag{7.39}$$

The average strain $\overline{\boldsymbol{\varepsilon}}^s$ in the solid phase of the REV equals the average strain in the homogeneous continuum surrounding the pores:

$$\overline{\boldsymbol{\varepsilon}}^s = \mathbf{E}_0 \tag{7.40}$$

To relate $\mathbf{E}_0$ and $\mathbf{E}$, the strain average condition, $\overline{\boldsymbol{\varepsilon}} = \mathbf{E}$, is used, and one can write (Dormieux

et al., 2006):

$$\phi\overline{\boldsymbol{\varepsilon}}^{p} + (1-\phi)\overline{\boldsymbol{\varepsilon}}^{s} = \mathbf{E} \tag{7.41}$$

Using Equations (7.39) and (7.41), one obtains:

$$\mathbf{E}_0 = \Big((1-\phi)\mathbb{I} + \phi(\mathbb{I} + \mathbb{P} : \delta\mathbb{C})^{-1}\Big)^{-1} : \mathbf{E} \tag{7.42}$$

The average strain concentration tensor in the pore space is estimated:

$$\overline{\mathbb{A}}^{p} = (\mathbb{I} + \mathbb{P} : \delta\mathbb{C})^{-1} : \Big((1-\phi)\mathbb{I} + \phi(\mathbb{I} + \mathbb{P} : \delta\mathbb{C})^{-1}\Big)^{-1} \tag{7.43}$$

A different form of Equation (7.43) is

$$\overline{\mathbb{A}}^{p} = \Big(\mathbb{I} + \mathbb{S} : (\mathbb{C}^{0^{-1}} : \mathbb{C}^{I} - \mathbb{I})\Big)^{-1} : \Big\langle \Big(\mathbb{I} + \mathbb{S} : \Big(\mathbb{C}^{0^{-1}} : \mathbb{C}^{r} - \mathbb{I}\Big)\Big)^{-1} \Big\rangle_{\Omega}^{-1} \tag{7.44}$$

where $\mathbb{C}^r = (\mathbb{C}^0, \mathbb{C}^I)$ in (Ω^0,Ω^I). $\mathbb{C}^0$ is the reference stiffness of the surrounding medium; $\mathbb{C}^0$ depends on the morphology ascribed to the porous composite.

Using Equation (7.8), the strain concentration tensor has the following general expression in porous media (Hellmich et al., 2004; Dormieux et al., 2006):

$$\mathbb{A}^{r} = [\mathbb{I} + \mathbb{P}_r : (\mathbb{C}^r - \mathbb{C}^0)]^{-1} : \{\sum_{s} \eta^s [\mathbb{I} + \mathbb{P}_s : (\mathbb{C}^s - \mathbb{C}^0)]^{-1}\}^{-1} \tag{7.45}$$

where $\mathbb{I}$ and $\mathbb{P}_r$ are the fourth order unit and Hill tensor, respectively. $\mathbb{C}^r$ and η^r are the stiffness tensor and packing density, respectively, of phase r in the REV ($r = p, s$).

The homogenized stiffness tensor, if Equation (7.33) is used, can be expressed as (Zaoui, 2002; Hellmich et al., 2004; Dormieux et al., 2006):

$$\mathbb{C}^{hom} = \langle \mathbb{C}^r(\underline{z}) : \mathbb{A}^r(\underline{z}) \rangle_V = \sum_{r} \eta^r \mathbb{C}^r \mathbb{A}^r \tag{7.46}$$

where $\mathbb{C}^r$, η^r, and $\mathbb{A}^r$ are the stiffness tensor, packing density, and strain concentration tensor, respectively, of phase r. Employing Equations (7.45), Equation (7.46) becomes (Zaoui, 2002;

Hellmich et al., 2004):

$$\mathbb{C}^{hom} = \langle \mathbb{C}^r [\mathbb{I} + \mathbb{P}_r : (\mathbb{C}^r - \mathbb{C}^0)]^{-1} \rangle : \langle [\mathbb{I} + \mathbb{P}_r : (\mathbb{C}^r - \mathbb{C}^0)]^{-1} \rangle^{-1} \tag{7.47}$$

Two approximations morphologies for porous media can be used to obtain the strain concentration tensor and the stiffness tensor of the homogeneous continuum. These are the matrix-inclusion morphology and the self-consistent morphology.

7.1.5.1 Matrix-Inclusion Morphology

A matrix-inclusion morphology (or Mori-Tanaka; MT) (Mori and Tanaka, 1973; Benveniste, 1987, Figure 7-1) is one in which the solid phase plays the role of the load-bearing matrix, that is, $\mathbb{C}^0 = \mathbb{C}^{mat} = \mathbb{C}^s$ in Equation (7.47). For such a morphology, Equation (7.44) becomes:

$$\mathbb{A}^{p,MT} = \left(\mathbb{I} + \mathbb{S} : (\mathbb{C}^{s^{-1}} : \mathbb{C}^I - \mathbb{I}) \right)^{-1} : \left\langle \left(\mathbb{I} + \mathbb{S} : \left(\mathbb{C}^{s^{-1}} : \mathbb{C}^r - \mathbb{I} \right) \right)^{-1} \right\rangle_{\Omega}^{-1} \tag{7.48}$$

In a porous medium with a matrix-inclusion morphology ($\mathbb{C}^0 = \mathbb{C}^s$), $\mathbb{C}^I = 0$ and Equation (7.48) reduces to:

$$\mathbb{A}^{p,MT} = (\mathbb{I} - \mathbb{S})^{-1} : \left((1-\phi)\mathbb{I} + \phi(\mathbb{I} - \mathbb{S})^{-1} \right)^{-1} \tag{7.49}$$

The stiffness tensor is obtained using Equation (7.45) in Equation (7.37) (Dormieux et al., 2006):

$$\mathbb{C}^{MT} = (1-\phi)\mathbb{C}^s : \left((1-\phi)\mathbb{I} + \phi(\mathbb{I} - \mathbb{S})^{-1} \right)^{-1} \tag{7.50}$$

We note that a porous material with a matrix-inclusion morphology has a continuous solid phase for any packing density, and the percolation threshold is $0 < \eta_0 < 1$.

7.1.5.2 Granular (Self-Consistent) Morphology

The granular, or self-consistent (SC), morphology (Hershey and Dahlgren, 1954; Hill, 1965; Budiansky, 1965, Figure 7-1) is one in which no one phase plays the role of a matrix. It is a disordered morphology where each phase (pore and solid) reacts as if it is embedded in

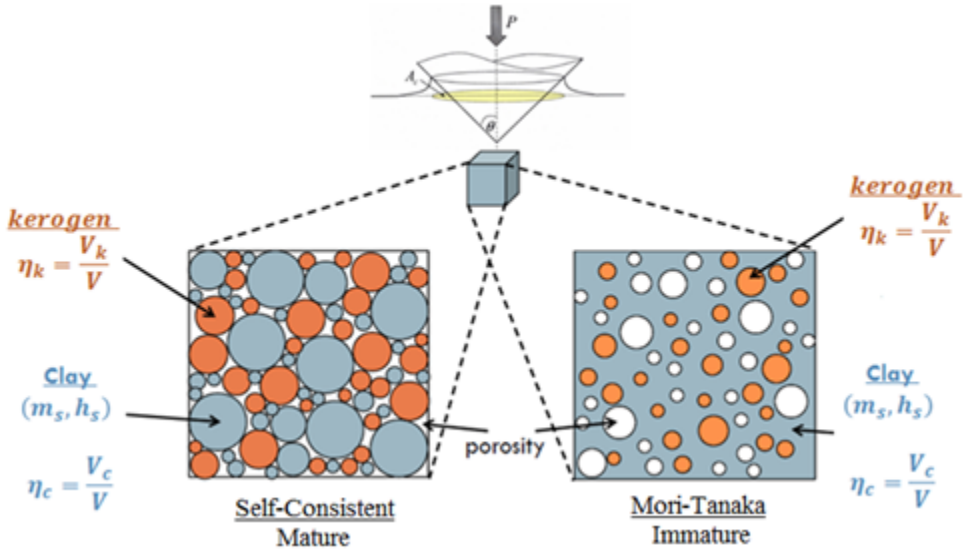

Figure 7-1: A cartoon depicting the texture of porous organic-rich clay composite in mature (left) and immature (right) formations. (Adapted from Cariou et al. (2008) and modified from a figure courtesy of Dr. Sara Abedi).

a homogeneous medium (Dormieux et al., 2006). This disorder translates into $\mathbb{C}^0 = \mathbb{C}^{hom}$ in Equation (7.47). The strain concentration tensor and the stiffness tensor are (Dormieux et al., 2006)

$$\overline{\mathbb{A}}^{p,SC} = \left(\mathbb{I} + \mathbb{S} : (\mathbb{C}^{hom^{-1}} : \mathbb{C}^I - \mathbb{I})\right)^{-1} : \left\langle \left(\mathbb{I} + \mathbb{S} : \left(\mathbb{C}^{hom^{-1}} : \mathbb{C}^r - \mathbb{I}\right)\right)^{-1} \right\rangle_\Omega^{-1} \tag{7.51}$$

and

$$\mathbb{C}^{SC} = \left\langle \mathbb{C}^r : \left(\mathbb{I} + \mathbb{P} : \left(\mathbb{C}^r - \mathbb{C}^{SC}\right)\right)^{-1} \right\rangle_\Omega : \left\langle \left(\mathbb{I} + \mathbb{P} : \left(\mathbb{C}^r - \mathbb{C}^{SC}\right)\right)^{-1} \right\rangle_\Omega^{-1} \tag{7.52}$$

Making use of the fact that the Hill tensor is identical for all the phases in a self-consistent scheme, one can re-write Equation (7.52) as:

$$\left\langle \left(\mathbb{C}^r - \mathbb{C}^{SC}\right) : \left(\mathbb{I} + \mathbb{P} : \left(\mathbb{C}^r - \mathbb{C}^{SC}\right)\right)^{-1} \right\rangle_\Omega = 0 \tag{7.53}$$

Noting that the second term in Equation (7.53) is $\mathbb{I}$, Equation (7.52) can be further simplified to:

$$\mathbb{C}^{SC} = \left\langle \mathbb{C}^r : \left(\mathbb{I} + \mathbb{P} : \left(\mathbb{C}^r - \mathbb{C}^{SC}\right)\right)^{-1} \right\rangle_\Omega \tag{7.54}$$

The composite material in the SC scheme has a solid percolation threshold, $\eta_0 = \frac{1}{2}$, below which the solid is unstable.

The two morphologies described above will be revisited in Chapter 8 relating solid properties of clay particles to nanoindentation data (M and H).

7.2 Strength Homogenization

The strength properties of a material can be obtained from determining the yield strength at the onset of plastic deformation in macroscopic tests. An alternative approach to strength determination is strength homogenization. Strength homogenization consists of finding the macroscopic strength domain of an REV of a heterogeneous material by knowing the microscopic strength domains of its various constituents. The next section reviews yield criteria and various approaches that determine microscopic and macroscopic strength domains. Also, the elements of strength homogenization of porous materials are summarized along with criteria that relate strength domains to material strength properties. The objective is to show three points: 1) the solid particles in the clay composites can be modeled as cohesive frictionless material; 2) porous composites follow a Drucker-Prager criterion; and 3) strength properties are isotropic and independent of homogenization schemes. The section also presents scaling relationships between solid particle strength properties and indentation hardness.

7.2.1 Yield Criteria

Strength homogenization and upscaling can be approached by studying the yield design theory or the theory of plastic limit analysis. The yield design theory focuses on irreversible material behavior after plastic collapse. Plastic yield analysis is based on two underlying ideas. First, plastic collapse occurs when the material, subjected to external loading, can no longer develop stress fields statically compatible with loading and plastically admissible with the strength of the constitutive material. In other words, the material structure can no longer sustain any additional load in form of stresses that satisfy equilibrium and do not exceed material strength. Second, the work rate supplied to the material can no longer be stored as recoverable energy. As a result, the work supplied is entirely and instantaneously

dissipated as heat through plastic yielding (Ulm and Coussy, 2003).

Plastic models describe irreversible plastic behavior and have a plasticity criterion and a flow rule as elements (Ulm and Coussy, 2003). A plasticity criterion is a generalized strength criterion that defines the elasticity domain (D_E) of the material and the onset of plastic deformation (Ulm and Coussy, 2003). The material strength domain is defined as the "maximum strength on all possible material planes on which a stress vector reaches the material strength" (Ulm and Coussy, 2003). For instance, for a 1D think model with a friction element depicting the friction strength k of a material, plastic deformation takes place when the stress reaches friction strength (Ulm and Coussy, 2003):

$$\sigma \in D_E : f(\sigma) = |\sigma| - k \leq 0 \tag{7.55}$$

Upon reaching friction strength, $f = 0$, the loading stress is on the boundary of the elastic domain. While plastic deformation is taking place, $df = 0$. This can be expressed by the consistency condition (Ulm and Coussy, 2003):

$$f(\sigma + d\sigma) = f(\sigma) + \frac{\partial f}{\partial \sigma} d\sigma = 0 \Longleftrightarrow df = 0 \tag{7.56}$$

Moreover, the yield design or the flow rule defines how plastic deformation occurs by setting the kinematics of the deformation (Ulm and Coussy, 2003):

$$d\varepsilon^p = d\lambda \, \text{sign}(\sigma) = d\lambda \frac{\partial f}{\partial \sigma}; \;\; f \leq 0; d\lambda \geq 0; d\lambda f = 0 \tag{7.57}$$

where $d\lambda$ is the plastic multiplier expressing the intensity of the plastic flow ($d\lambda = |d\varepsilon^p|$). The three conditions represent the plastic loading-unloading conditions and are called the Kuhn-Tucker conditions.

The occurrence of plastic deformation is not related to a time scale but only to the stress history and is assumed to happen instantaneously. The normality rule of plastic flow states that plastic deformation takes place in the direction of the applied load (sign(σ)) and normal to the loading surface (sign(σ) = $\partial f / \partial \sigma$).

7.2.1.1 Elements of Yield Design

The two elements of yield design are a statically admissible stress field and a kinematically admissible velocity field. A statically admissible stress field in a material domain Ω is one that satisfies the equation of motion and the symmetry condition:

$$\begin{cases} div\boldsymbol{\sigma} = 0 \quad \text{(ignoring externally applied load density)} \\ \boldsymbol{\sigma} = {}^{t}\boldsymbol{\sigma} \\ \underline{T}^{d} = \boldsymbol{\sigma} \cdot \underline{n} \end{cases} \tag{7.58}$$

where $\partial\Omega$ is the boundary of the material domain, and T^d is a prescribed boundary condition on $\partial\Omega_{T^d}$ ($\partial\Omega_{T^d} \in \partial\Omega$).

A kinematically admissible velocity field is one that is kinematically compatible with boundary conditions and with the kinematics of a plastic flow in the structure bulk and/or along plastic slippage planes (Ulm and Coussy, 2003).

Given the two elements of yield design, there are two approaches to define the strength domain of a solid phase within a heterogeneous REV: the direct approach and the dual one. The first explores statically and plastically admissible stress states and gives a lower bound of the dissipation capacity. The second explores kinematically compatible velocity fields and gives an upper bound of the dissipation capacity.

7.2.1.2 The Direct Stress-Strength Approach

A microscopic stress field $\boldsymbol{\sigma}(\underline{z})$ defined in an REV is statically compatible with a given macroscopic stress state $\boldsymbol{\Sigma}$ if:

$$\begin{cases} div\boldsymbol{\sigma} = 0 \\ \boldsymbol{\Sigma} = \overline{\boldsymbol{\sigma}} \\ \forall \underline{z} \in \Omega^{p},\ \boldsymbol{\sigma}^{p} = 0 \end{cases} \tag{7.59}$$

where $\boldsymbol{\sigma}^p$ is the stress in the pore space. In the above case, the heterogeneous REV is subjected to a regular traction on its boundary ∂V oriented by the outward normal, $\underline{n}$, given

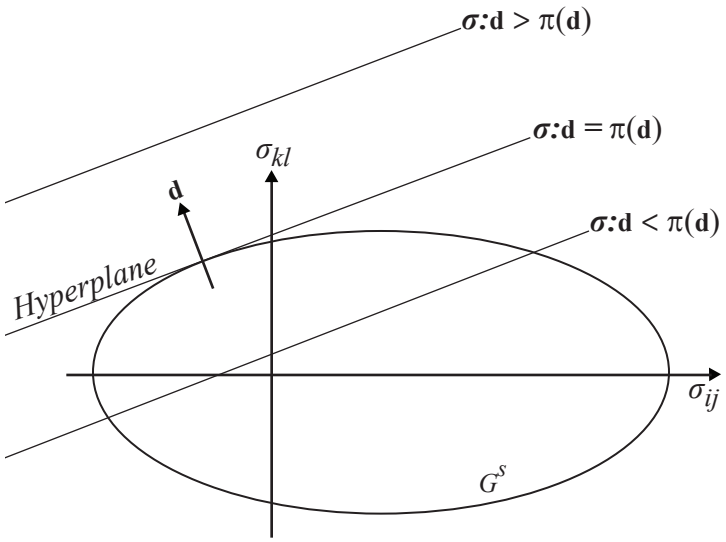

Figure 7-2: An elliptical strength domain, G^s, and a geometrical interpretation of the support function as hyperplanes in the stress space. The hyperplane $(\mathbf{d})$ corresponding to $\pi(\mathbf{d}) = \boldsymbol{\sigma} : \mathbf{d}$ is tangent to the boundary ∂G^s of the strength domain (modified after Dormieux et al., 2006).

by:

$$\forall\, \underline{x} \in \partial V : \underline{t}(\underline{x}) = \boldsymbol{\Sigma} \cdot \underline{n}(\underline{x}) \tag{7.60}$$

The direct approach consists of defining a convex set G^s (Figure 7-2) of strength-compatible stress states admissible to the D_E of the solid phase. This convex set can be expressed in the form of a strength criterion or a scalar loading function, $f^s(\boldsymbol{\sigma})$, such that (Ulm and Coussy, 2003; Dormieux et al., 2006):

$$G^s = \{\boldsymbol{\sigma}, f^s(\boldsymbol{\sigma}) \leqslant 0\} \tag{7.61}$$

The zero-stress state is assumed to be strength-compatible, and the boundary of G^s is characterized by the condition $f^s(\boldsymbol{\sigma}) = 0$.

7.2.1.3 The Dual Approach

The dual approach (Dormieux et al., 2006) is based on the premise that the material, at plastic collapse, can no longer store external work as recoverable elastic energy. As a result, the supplied work is dissipated as heat. After the use of the Hill Lemma (Equation (7.6))

along with Equation (7.60), the external work rate applied to the REV is (Ulm and Coussy, 2003):

$$\delta W = \frac{1}{|V|}\int_{\partial V} \underline{t}(\underline{z}) \cdot \underline{v}(\underline{z}) da = \overline{\boldsymbol{\sigma}(\underline{z}) : \boldsymbol{d}(\underline{z})} = \boldsymbol{\Sigma} : \boldsymbol{D} \tag{7.62}$$

where $\boldsymbol{\Sigma}$ is the macroscopic stress tensor and the volume average of the microscopic stress field; and $\underline{v}(\underline{z})$ is the kinematically admissible microscopic velocity field[3] related to the microscopic strain rate field, $\mathbf{d}$, at failure by:

$$\mathbf{d} = \mathbf{d}(\underline{v}(\underline{z})) = \frac{1}{2}(\mathrm{grad}\underline{v} + {}^{t}\mathrm{grad}\underline{v}) \tag{7.63}$$

$\mathbf{D}$ is the macroscopic strain rate field:

$$\mathbf{D} = \overline{\mathbf{d}(\underline{z})} = \frac{1}{2|V|}\int_{\partial V} (\underline{v} \otimes \underline{n} + \underline{n} \otimes \underline{v}) da \tag{7.64}$$

For the dissipated work rate to be finite, the dual approach introduces a homogeneous support function of degree one:

$$\pi(\mathbf{d}) = \sup_{\boldsymbol{\sigma} \in G^s} (\boldsymbol{\sigma} : \mathbf{d}) \tag{7.65}$$

Thus,

$$(\forall t \in \mathbb{R}^+)\, \pi(t\mathbf{d}) = t\pi(\mathbf{d}) \tag{7.66}$$

The dual definition of solid strength takes the form (Dormieux et al., 2006):

$$\boldsymbol{\sigma} \in G^s \leftrightarrow (\forall\, \mathbf{d})\ \boldsymbol{\sigma} : \mathbf{d} \leq \pi(\mathbf{d}) \tag{7.67}$$

Relationship (7.67) implies that, at the solid particle level (level 0), the support function $\pi(\mathbf{d})$ represents the maximum plastic dissipation capacity that the material can undergo, recalling that the zero stress state is strength-compatible ($\pi(\mathbf{d}) \geq 0$). Also, with the boundary of the stress domain, ∂G^s, equivalent to $f(\boldsymbol{\sigma}) = 0$, the stress at the boundary of the domain maximizes the work rate, and $\boldsymbol{\sigma} : \mathbf{d} = \pi(\mathbf{d})$. We note that $\boldsymbol{\sigma} : \mathbf{d} = \pi(\mathbf{d})$ defines a hyperplane $\mathcal{H}(\mathbf{d})$ in the stress space. The hyperplane is tangent to the boundary ∂G^s at the point $\boldsymbol{\sigma}$,

[3] $\underline{v}$ needs to satisfy a zero-velocity boundary condition. This condition is met since the problem has a stress boundary condition.

at which the normal to the boundary is parallel to $\mathbf{d}$ (Figure 7-2). At the boundary ∂G^s, $\boldsymbol{\sigma}$ and $\mathbf{d}$ are linked:

$$\boldsymbol{\sigma} = \frac{\partial \pi}{\partial \mathbf{d}}(\mathbf{d}) \tag{7.68}$$

7.2.1.4 Strength-Compatible Macroscopic Strength States

A macroscopic stress is compatible with material strength if the microscopic stress field exists and satisfies the conditions in (7.59). The set of strength-compatible macroscopic stress states is G^{hom} (Dormieux et al., 2006):

$$G^{hom} = \{\boldsymbol{\Sigma}, \exists\, \boldsymbol{\sigma} \text{ s.a. with } \boldsymbol{\Sigma}, (\forall \underline{z} \in \Omega^s)\, \boldsymbol{\sigma}(\underline{z}) \in G^s\}$$

For a given macroscopic strain rate tensor $\mathbf{D}$, a set of kinematically admissible microscopic velocity fields $\underline{v}(\underline{z})$ satisfies the following boundary conditions:

$$\mathcal{V}(\boldsymbol{D}) = \{\underline{v}, (\forall \underline{z} \in \partial\Omega)\, \underline{v}(\underline{z}) = \boldsymbol{D} \cdot \underline{z}\} \tag{7.69}$$

The Hill Lemma gives (Dormieux et al., 2006)

$$\boldsymbol{\Sigma} : \boldsymbol{D} = \overline{\boldsymbol{\sigma} : \boldsymbol{d}} = (1-\phi)\overline{\boldsymbol{\sigma} : \boldsymbol{d}}^s \tag{7.70}$$

where s stands for solid, and ϕ is the pore fraction in the material.

Using the definition of the support function (Equation (7.65)), Equation (7.70) gives (Barthélémy and Dormieux, 2004; Dormieux et al., 2006)

$$\boldsymbol{\Sigma} : \boldsymbol{D} \leq \overline{\pi(\boldsymbol{d})} \tag{7.71}$$

Barthélémy and Dormieux (2004) argue that the above equation must be satisfied for any kinematically admissible velocity field. Therefore,

$$\boldsymbol{\Sigma} : \boldsymbol{D} \leq \Pi^{hom}(\boldsymbol{D}) \tag{7.72}$$

and $\Pi^{hom}(\boldsymbol{D})$ can be interpreted as the support function of G^{hom}.

Given Equation (7.72), G^{hom} is located in a half-space bounded by the hyperplane $\boldsymbol{\Sigma} : \boldsymbol{D} = \Pi^{hom}(\boldsymbol{D})$. Belonging to both the hyperplane and G^{hom}, $\boldsymbol{\Sigma}$ is located on the boundary ∂G^{hom} of G^{hom} at a point where the normal to ∂G^{hom} is parallel to $\boldsymbol{D}$ (Barthélémy and Dormieux, 2004; Dormieux et al., 2006). Therefore, $\boldsymbol{\Sigma}$ satisfies the dual definition of the strength domain of cohesive-frictional porous material:

$$\Pi^{hom}(\boldsymbol{D}) = \sup_{\boldsymbol{\Sigma} \in G^{hom}} \boldsymbol{\Sigma} : \boldsymbol{D} \geq 0 \tag{7.73}$$

In order to determine the macroscopic stress solution, the solution to the yield design is formulated:

$$\boldsymbol{\Sigma} : \boldsymbol{D} = \Pi^{hom}(\boldsymbol{D}); \ \boldsymbol{\Sigma} = \frac{\partial \Pi^{hom}}{\partial \boldsymbol{D}} \tag{7.74}$$

The problem becomes one of finding estimates or bounds to $\Pi^{hom}(\boldsymbol{D})$. This is done using limit analysis.

7.2.2 Limit Analysis

Limit analysis is a means to determine the load-bearing capacity of a material. Limit theorems provide estimates of the energy dissipated upon plastic collapse. The lower limit theorem explores the compatibility between static equilibrium and material strength. It states that if no compatibility between a statically admissible stress field ($f(\boldsymbol{\sigma'}) \leq 0$) and the kinematics of plastic flow is evoked, the dissipation associated with $\boldsymbol{\sigma'}$ is a lower bound of the actual dissipation rate. The upper limit theorem explores kinematically admissible velocity fields related to strain rate through Equation (7.63) and to a stress field $\boldsymbol{\sigma}$ through a plastic flow rule specified by the normality rule of ideal plasticity (Ulm and Coussy, 2003):

$$\boldsymbol{d} \overset{\text{def}}{=} \boldsymbol{d}^{pl} = \dot{\lambda} \frac{\partial f}{\partial \boldsymbol{\sigma}}; \dot{\lambda} \geq 0; f \leq 0; \dot{\lambda} f = 0 \tag{7.75}$$

Evoking the principle of maximum plastic work[4], the plastic work realized by $\boldsymbol{\sigma} : \boldsymbol{d}^{pl}$ is

[4]During plastic evolution, the dissipation of the (plastic) work provided as heat is given by:

$$d\mathcal{D} = dW^p = \boldsymbol{\sigma} : d\varepsilon^p \geq 0$$

greater than or equal to the plastic work realized by any other stress (e.g., $\boldsymbol{\sigma'}$) not associated with $\boldsymbol{d}^{pl}$. Therefore, the maximum available plastic work rate the material can locally dissipate depends only on $\boldsymbol{d}^{pl}$, and

$$\forall \boldsymbol{\sigma'} \in G^s; \boldsymbol{\sigma'} : \boldsymbol{d}^{pl} \leq \sup_{\boldsymbol{\sigma} \in G^s} \boldsymbol{\sigma} : \boldsymbol{d}^{pl} = \pi(\boldsymbol{d}^{pl} = \dot{\lambda} \frac{\partial f}{\partial \boldsymbol{\sigma}}(\boldsymbol{\sigma})) \tag{7.76}$$

In order to find the strain rate during plastic collapse, let $\mathcal{K}(\boldsymbol{D})$ be a set of velocity fields such that:

$$\mathcal{K}(\boldsymbol{D}) = \{\underline{v}^*(\underline{z}) \,|\overline{\boldsymbol{d}(\underline{v}^*)} = \boldsymbol{D}\} \tag{7.77}$$

For any velocity field belonging to $\mathcal{K}(\boldsymbol{D})$, the following is true:

$$\delta W = \overline{\boldsymbol{\sigma} : \boldsymbol{d}(\underline{v}^*)} = \boldsymbol{\Sigma} : \boldsymbol{D} \leq \overline{\pi(\boldsymbol{d}(\underline{v}^*), \underline{z})} \tag{7.78}$$

However, if $\boldsymbol{\Sigma}$ is the macroscopic stress solution to the yield design problem and $\underline{v}(\underline{z})$ is the associated velocity field solution to the problem, then,

$$\delta W = \overline{\boldsymbol{\sigma} : \boldsymbol{d}(\underline{v})} = \boldsymbol{\Sigma} : \boldsymbol{D} = \overline{\pi(\boldsymbol{d}(\underline{v}), \underline{z})} = \Pi^{hom}(\boldsymbol{D}) \tag{7.79}$$

From the above two equations and the upper limit theorem, one can see that $\Pi^{hom}(\boldsymbol{D})$ provides an upper bound estimate of the actual dissipation capacity that the REV can afford. Therefore (Barthélémy and Dormieux, 2004; Dormieux et al., 2006):

$$\Pi^{hom}(\boldsymbol{D}) = \inf_{\underline{v}^* \in \mathcal{K}(\boldsymbol{D})} \overline{\pi(\boldsymbol{d}^* = \boldsymbol{d}(\underline{v}^*, \underline{z}))} \tag{7.80}$$

Gathier (2008) indicated that the problem in (7.80) is a variational problem. Gathier's variational approach to solve the problem is summarized next.

When compared to the plastic work provided by any other plastically admissible stress $\boldsymbol{\sigma'}$ within or on the boundary of the elasticity domain ($f(\boldsymbol{\sigma'}) \leq 0$), the stress $\boldsymbol{\sigma}$ associated with $d\varepsilon^p$ provokes the maximum dissipation (Ulm and Coussy, 2003):

$$\forall f(\boldsymbol{\sigma}) = 0; f(\boldsymbol{\sigma'}) \leq 0; (\boldsymbol{\sigma} - \boldsymbol{\sigma'}) : d\varepsilon^p \geq 0$$

.

7.2.3 Variational Approach

When solving elasticity problems with small perturbations, formulations of a well-posed problem are attempted. The unknowns in such problem are six stress components ($\sigma_{ij}; i,j = 1,2,3$), six strain components (ε_{ij}), and three displacement components (ξ_i). The problem is formulated with three equilibrium equations ($\mathrm{div}\boldsymbol{\sigma} = 0$) and six strain-displacements equations ($\boldsymbol{\varepsilon} = \frac{1}{2}(\mathbf{grad}\underline{\xi} + {}^t\mathbf{grad}\underline{\xi})$). With more unknowns than equations, more material laws are needed to provide relationships and links between stresses and strains. For instance, the elastic potential ($\psi(\boldsymbol{\varepsilon})$) can be used to link stress to strain by the following equation of state (Ulm and Coussy, 2003):

$$\boldsymbol{\sigma} = \boldsymbol{\sigma}(\boldsymbol{\varepsilon}) = \frac{\partial \psi(\boldsymbol{\varepsilon})}{\partial \boldsymbol{\sigma}} \tag{7.81}$$

Variational methods are used to find solutions or bounds to an elastic problem by using the theorem of virtual work. The theorem states that, in the absence of inertia forces, the work done by external forces, $\mathcal{W}_{ext}$, equals to the internal work or internal strain energy, $\mathcal{W}_{int}$. The application of the theorem with statically admissible stress field and a kinematically admissible displacement field gives a lower and an upper bounds of the exact solution, respectively. An exact solution is obtained when we simultaneously consider a statically admissible stress field and a kinematically admissible displacement field. In a problem where the boundary condition is split between a prescribed displacement boundary condition and a prescribed traction boundary condition ($\partial\Omega = \partial\Omega_{\underline{\xi}^d} \cup \partial\Omega_{\underline{T}^d}$), the external work can be separated between work due to prescribed body and surface forces ($\Phi(\underline{\xi})$), and work due to prescribed displacement ($\Phi^*(\boldsymbol{\sigma})$) (Ulm and Coussy, 2003):

$$\Phi(\underline{\xi}) = \int_\Omega \underline{\xi} \cdot (\rho \underline{f}) d\Omega + \int_{\partial\Omega_{\underline{T}^d}} \underline{\xi} \cdot \underline{T}^d da \tag{7.82}$$

$$\Phi^*(\boldsymbol{\sigma}) = \int_{\partial\Omega_{\underline{\xi}^d}} \underline{\xi}^d \cdot \underline{T} da = \int_{\partial\Omega_{\underline{\xi}^d}} \underline{\xi}^d \cdot (\boldsymbol{\sigma} \cdot \underline{n}) da \tag{7.83}$$

Therefore, one can write (Ulm and Coussy, 2003):

$$\underbrace{\Phi(\underline{\xi}) + \Phi^*(\boldsymbol{\sigma})}_{\mathcal{W}_{\text{ext}}} = \underbrace{\int_\Omega \boldsymbol{\sigma} : \boldsymbol{\varepsilon} d\Omega}_{\mathcal{W}_{\text{int}}} \tag{7.84}$$

Furthermore, for elastic behavior, the energy potential can be separated into energy potentials associated with strain and stress as follows:

$$\boldsymbol{\sigma} : \boldsymbol{\varepsilon} = \psi(\boldsymbol{\varepsilon}) + \psi^*(\boldsymbol{\sigma}) \tag{7.85}$$

On the right side of Equation (7.85), the first term is the Helmholtz free energy volume density, and the second term is the complementary elastic energy. Integrating Equation (7.85) yields:

$$\mathcal{W}_{int} = \int_\Omega \boldsymbol{\sigma} : \boldsymbol{\varepsilon} d\Omega = W(\boldsymbol{\varepsilon}) + W(\boldsymbol{\sigma}) \tag{7.86}$$

The theorem of virtual work can be written in the form (Ulm and Coussy, 2003):

$$\underbrace{W(\boldsymbol{\varepsilon}) - \Phi(\underline{\xi})}_{\varepsilon_{pot}(\underline{\xi})} + \underbrace{W^*(\boldsymbol{\sigma}) - \Phi^*(\boldsymbol{\sigma})}_{\varepsilon_{com}(\boldsymbol{\sigma})} = 0 \tag{7.87}$$

and used as a means to upscale micromechanical behavior of a heterogeneous system to the macroscopic level/REV where the material appears homogeneous. This is done by using homogenization theories (e.g., Equations (7.3) and (7.5)). For instance, in an REV composed of i phases, a homogenization problem requires solving the following:

$$\begin{cases} \text{div}\boldsymbol{\sigma} = 0 & \text{in} V \quad (7.88a) \\ \boldsymbol{\sigma}(\underline{z}) = \dfrac{\partial \pi_i}{\partial \boldsymbol{d}}(\boldsymbol{d}(\underline{z})) & \text{in} V_i \quad (7.88b) \\ \boldsymbol{d} = \dfrac{1}{2}(\mathbf{grad}\underline{v} + {}^t\mathbf{grad}\underline{v}) & \text{in} V \quad (7.88c) \\ \underline{v} = \boldsymbol{D} \cdot \underline{z} & \text{on} \partial V \quad (7.88d) \end{cases}$$

Dormieux et al. (2006) noted that problem (7.88) appears as an elastic one if $\boldsymbol{d}$ is replaced

by the strain $\boldsymbol{\varepsilon}$, and $\pi(\boldsymbol{d})$ by a strain energy function $\omega(\boldsymbol{\varepsilon})$. The difference is that $\pi(\boldsymbol{d})$ is a homogeneous function of degree 1 whereas $\psi(\boldsymbol{\varepsilon})$ is a quadratic function given by (Dormieux et al., 2006):

$$\psi(\boldsymbol{\varepsilon}) = \frac{1}{2}\boldsymbol{\varepsilon} : \mathbb{C} : \boldsymbol{\varepsilon} \tag{7.89}$$

Two approaches can be followed to solve the nonlinear problem (7.88), both of which have much in common and agree for cohesive-frictionless materials. The first approach is that of Ponte Castañeda (1992, 2002) adapted by Gathier (2008) for shales. It replaces the nonlinear problem by a linear one depicting an equivalent heterogeneous linear comparison composite (LCC) having $\mathbb{C}$ as a stiffness tensor. With such a replacement, the linear homogenization theory can be used. The second approach is the effective strain rate approach (Suquet, 1997; Dormieux et al., 2006) adapted by Cariou et al. (2008) to relate the strength properties of the solid in a porous medium to indentation hardness.

7.2.4 Nonlinear Strength Homogenization: Effective Strain Rate Approach

The objective of strength homogenization is to find the yield function $f(\boldsymbol{\Sigma})$ and the corresponding dissipation function, $\Pi^{hom}(\boldsymbol{D})$, in a porous material made of a (cohesive-frictional) solid phase and empty pores. One approach to estimate the dissipation capacity is to substitute for the rigid-plastic behavior of the solid (second equation in problem (7.88)) a "fictitious" viscous behavior described by the following viscous constitutive law:

$$\boldsymbol{\sigma}(\underline{z}) = \frac{\partial \pi_i}{\partial \boldsymbol{d}}(\boldsymbol{d}(\underline{z})) = \mathbb{C}(\underline{z}) : \boldsymbol{d}(\underline{z}) \begin{cases} \mathbb{C}(\underline{z}) = \mathbb{C}^s(\boldsymbol{d}(\underline{z})) & \text{in}\Omega^s \\ \mathbb{C}(\underline{z}) = 0 & \text{in}\Omega^p \end{cases} \tag{7.90}$$

The above equation captures the heterogeneity of $\mathbb{C}^s(\boldsymbol{d}(\underline{z}))$ and its dependence on loading. It also reveals the key to homogenization following the effective strain rate approach; that is, to find an appropriate microscopic strain rate field that develops within the solid at plastic

collapse, such that (Dormieux et al., 2006):

$$\forall \underline{z} \in \Omega^s \ \mathbb{C}(\underline{z}) = \mathbb{C}^s(\boldsymbol{d}(\underline{z})) \approx \mathbb{C}^s(\boldsymbol{d}^r) \tag{7.91}$$

where:

$$\boldsymbol{d}^r = \overline{\boldsymbol{d}(\underline{z})}^s \tag{7.92}$$

The next step is the secant formulation (Suquet, 1997; Dormieux et al., 2006) in which quadratic averages are used to estimate strain rates. It is assumed that the strength of the solid depends on the mean ($\sigma_m = \frac{1}{3}tr(\boldsymbol{\sigma})$) and deviatoric ($\boldsymbol{s}$) stresses, recalling that the invariants of the stress tensors are $I_1 = tr\boldsymbol{\sigma}$ and $J_2 = \dfrac{1}{2}\boldsymbol{s} : \boldsymbol{s}$. Equivalently, the dissipation function depends on the invariants of the strain rate tensor $\boldsymbol{d} = \boldsymbol{\delta} + \frac{1}{3}d_v\mathbf{1}$, which are $I_1^{'} = tr(\boldsymbol{d}) = d_v$ and $J_2^{'} = \frac{1}{2}tr(\boldsymbol{\delta}\cdot\boldsymbol{\delta}) = d_d^2$, where d_v and d_d are the volumetric and deviatoric strain rate tensors, respectively. The state equation then is (Dormieux et al., 2006):

$$\boldsymbol{\sigma} = \frac{\partial \pi^s}{\partial I_1^{'}}(I_1^{'}, J_2^{'})\mathbf{1} + \frac{\partial \pi^s}{\partial J_2^{'}}(I_1^{'}, J_2^{'})\boldsymbol{\delta} = \mathbb{C}^s(\boldsymbol{d}) : \boldsymbol{d} \tag{7.93}$$

If the behavior of the porous material is isotropic or assumed so, the secant stiffness tensor is given by:

$$\mathbb{C}^s(\boldsymbol{d}) = 3k^s(I_1^{'}, J_2^{'})\mathbb{J} + 2\mu^s(I_1^{'}, J_2^{'})\mathbb{K} \text{ with } \begin{cases} k^s(I_1^{'}, J_2^{'}) = \dfrac{1}{I_1^{'}}\dfrac{\partial \pi^s}{\partial I_1^{'}}(I_1^{'}, J_2^{'}) \\ 2\mu^s(I_1^{'}, J_2^{'}) = \dfrac{\partial \pi^s}{\partial J_2^{'}}(I_1^{'}, J_2^{'}) \end{cases} \tag{7.94}$$

where k^s and μ^s are the secant bulk and shear moduli, respectively.

7.3 Strength Homogenization of Shale

The application of yield design solutions in indentation hardness analysis was developed by Gathier (2008) and Cariou et al. (2008) to relate indentation hardness to material strength properties. Such an application is based on the "premise that the material, in response to an applied (indentation) load, has exhausted its capacity to store supplied work into

recoverable energy," and behaves in a rigid plastic way. The hardness, therefore, relates only to the strength properties (cohesion and friction of the solid) of the indented material. The following sections summarize work by Dormieux et al. (2006), Cariou et al. (2008), and Gathier (2008).

7.3.1 Level 0 Strength Criteria

Few criteria exist to describe the strength behavior of solid particles (clay particles in our case).

7.3.1.1 Mohr-Coulomb and Drucker-Prager Plasticity

The Mohr-Coulomb (MC) criterion and Drucker-Prager (DP) criterion are yield criteria that describe material bulk frictional behavior. Both imply that the maximum shear stress a material can support depends on confining pressure (Kaliszky, 1989). The MC criterion is:

$$f(\underline{T} = \boldsymbol{\sigma}.\underline{n}) = \mid T_t \mid + \mu T_n - C \leq 0 \tag{7.95}$$

where T_t and T_n are the tangential shear stress and the normal stress, respectively, acting on a material surface oriented by unit outward normal $\underline{n}$. C is the MC cohesion, and $\mu = \tan\varphi$ is the MC friction coefficient. Expressed in terms of principal stresses ($\sigma_I \geq \sigma_{II} \geq \sigma_{III}$), the MC criterion reads as:

$$f(\boldsymbol{\sigma}) = \sigma_I - \sigma_{III} + (\sigma_I + \sigma_{III})\sin(\varphi) - 2c\cos\varphi \leq 0 \tag{7.96}$$

The limitation of using the MC criterion is that it does not take the intermediate stress, σ_{II}, into account, implying that σ_{II} does not influence failure. The criterion also does not describe a stress state inside the failure envelope (Figure 7-3). Schweiger (1994) stated that the MC criterion is not very realistic in 2D and 3D as it gives (computational) problems due to a non-smooth failure surface. To overcome the shortcomings of the MC criterion, the

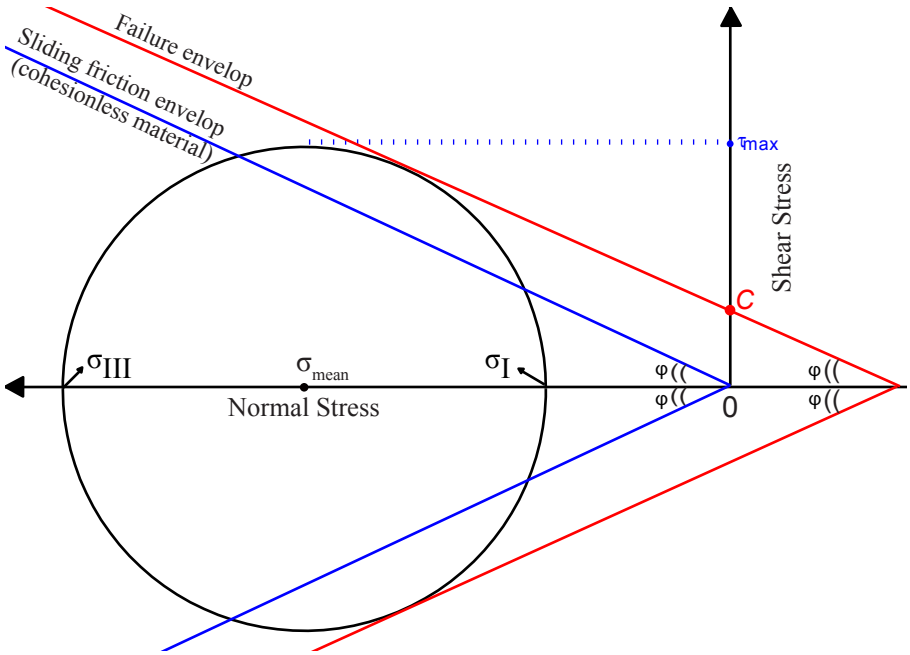

Figure 7-3: A Mohr circle defined by most tensile (σ_I) and most compressive (σ_{III}) principal stresses. The MC failure envelope (red) is drawn to indicate cohesion at failure, C, and the internal friction angle, φ. For cohesionless material, the failure envelope coincides with the origin (indicating zero tensile strength) and becomes the sliding friction envelope (blue). For frictionless material following the Tresca criterion (not depicted in the figure), $\varphi = 0$, and the yield is represented by 2 parallel lines at $c = \boldsymbol{\tau}_0$, which is the yield shear stress in pure shear state (σ_{mean} = mean stress and $\boldsymbol{\tau}_{max}$ = maximum shear stress).

DP criterion is considered. It is viewed as the MC criterion on the deviatoric stress plane[5] (Figure 7-4) and given by:

$$f(\boldsymbol{\sigma}) = \sqrt{J_2} + \alpha\sigma_m - c \leq 0 \tag{7.97}$$

where J_2 is the second invariant ($J_2 = \dfrac{\sigma_d^2}{2}$), α is the friction coefficient, and c is the cohesion. The mean stress is $\sigma_m = \frac{1}{3}tr(\boldsymbol{\sigma}) = \frac{1}{3}(\sigma_I + \sigma_{II} + \sigma_{III})$. The magnitude of the shear stress is $\sigma_d = \sqrt{tr(\mathbf{s}.\mathbf{s})}$ where $\mathbf{s}$ is the stress deviator ($\mathbf{s} = \boldsymbol{\sigma} - \sigma_m\mathbf{1}$).

The DP criterion provides a better approximation to relate material strength properties to stress (Schweiger, 1994). In addition to Schweiger's arguments favoring the DP criterion (Schweiger, 1994) and based on the work of Fritsch et al. (2007), Gathier (2008) shows that the DP criterion represents a distinct weakness of the intercrystalline interfaces at smaller

[5]In the principal stress space, any stress state can be decomposed into a volumetric component given by the length $\frac{1}{\sqrt{3}}(\sigma_I + \sigma_{II} + \sigma_{III})$ and a deviatoric component within the deviatoric or π-plane (Figure 7-4). The deviatoric plane is defined by the mean stress and the shear stress magnitude and is perpendicular to the hydrostatic line where $\sigma_I = \sigma_{II} = \sigma_{III}$.

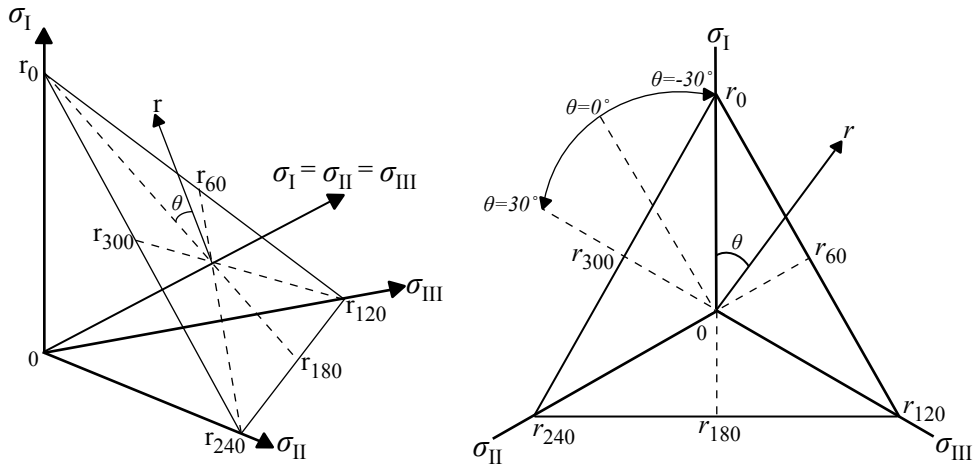

Figure 7-4: The principal stress space and the π-plane. θ is the Lode angle, an invariant of the stress deviator tensor defined as $\theta = -\frac{1}{3}\sin^{-1}(\frac{3\sqrt{3}}{2}\frac{J_3}{J_2^{3/2}})$, with $J_2 = \frac{\sigma_d^2}{2}$ and $J_3 = (\sigma_I - \sigma_m)(\sigma_{II} - \sigma_m)(\sigma_{III} - \sigma_m)$. If $\sigma_I > \sigma_{II} > \sigma_{III}$ is assumed, then θ gives the location of σ_{II} between $\boldsymbol{\sigma}_I$ and σ_{III}. θ equals -30° and 30° in conventional triaxial compression and extension tests, respectively. r ($r = \sqrt{J_2}$) is the radial coordinate in a polar coordinate system (modified after Pei, 2008).

scales. Hence, the criterion can be used to describe the strength domain of the polycrystal clay particles at level 0, and the dual definition of the strength domain is written as (Salençon, 1983 in Cariou et al., 2008):

$$\boldsymbol{\sigma} \in G_s(\underline{z}) \Leftrightarrow \begin{cases} f(\boldsymbol{\sigma}) = \sqrt{J_2} + \alpha_s \sigma_m - c_s \leq 0 \\ \pi^s(\boldsymbol{d}) = \text{stat}(\boldsymbol{\sigma} : \boldsymbol{d}) = \begin{cases} \dfrac{c_s}{\alpha_s} I_1' & \text{if } I_1' \geq 2\alpha\sqrt{J_2'} \\ \infty \text{ else} \end{cases} \end{cases} \tag{7.98}$$

7.3.1.2 Von-Mises Plasticity

The Von-Mises criteria is a shear strength criterion on a slippage plane oriented by its outward normal $\underline{n}$. It reads:

$$\boldsymbol{\sigma} \in D_E \longleftrightarrow f(\boldsymbol{\sigma}) = |\underline{t} \cdot \underline{T}(\underline{n})| - k \leq 0 \tag{7.99}$$

where $\underline{t}$ is the tangent vector on the slippage or deviator plane, k is the shear stress threshold defining shear strength on a specific slippage plane, and $\underline{n}$ is the orientation of the hydrostatic

axis:

$$\underline{n} = \frac{\sqrt{3}}{3}(\underline{u}_I + \underline{u}_{II} + \underline{u}_{III}) \tag{7.100}$$

where $\underline{u}_J (J = I, II, III)$ are the principal stress directions.

In terms of the stress and strain rate tensor invariants, the Von-Mises yield criterion and dissipation function read:

$$\boldsymbol{\sigma} \in G^S \longleftrightarrow f(\boldsymbol{\sigma}) = \sqrt{J_2} - c_s \leq 0 \tag{7.101}$$

and

$$\pi^s(\boldsymbol{d}) = \text{stat}(\boldsymbol{\sigma} : \boldsymbol{d}) = \begin{cases} 2c_s\sqrt{J_2'} \; if d_v = 0 \\ \infty \text{ else} \end{cases} \tag{7.102}$$

Evoking the Hill Lemma that provides a link between the microscopic and macroscopic dissipation capacities, Cariou et al. (2008) reports the following macroscopic dissipation capacity for cohesive porous material:

$$\Pi(\boldsymbol{D}) = \boldsymbol{\Sigma} : \boldsymbol{D} = \overline{\boldsymbol{\sigma} : \boldsymbol{d}} = \eta\overline{\pi^s(\boldsymbol{d})}^s = 2c^s\overline{\sqrt{J_2'}}^s \tag{7.103}$$

Due to the high packing density of gas shale formations, the solid phase (level 0) is assumed to be a cohesive frictionless solid obeying the Von-Mises strength criterion. Works by Gathier (2008) and Cariou et al. (2008) justify the assumption. Gathier (2008), through his scaling modeling, investigated the dependence of solid strength properties on the packing density of the material. He found that α_s decreases with packing density, and as $\eta \longrightarrow 1, \alpha_s \longrightarrow 0$. Also, in their work on level I strength homogenization, Cariou et al. (2008) validated an upper bound approach to obtain the yield design solution, that is, to give the actual dissipation capacity of the material below the indenter tip. The authors concluded that using a "pure Von-Mises" solid in zero-to-low porosity predicts hardness-to-strength values in "excellent" agreement with other analyses in the literature such as the analysis of Cheng and Cheng (2004).

7.3.2 Level I Strength Criterion

Barthélémy and Dormieux (2004) and Dormieux et al. (2006) employed the effective strain rate approach for strength homogenization. They showed that level I strength homogenization of a porous material follows the elliptical DP strength model. Starting with a material made of solids that obey the DP strength criterion (Equation (7.98)), the macroscopic dissipation capacity, for an associated flow rule $I_1' = 2\alpha\sqrt{J_2'} \geq 0$, is:

$$\Pi^{hom}(\boldsymbol{D}) = 2\eta c_s \sqrt{\overline{J_2'}^s} = c_s(\sqrt{(\mathscr{A} D_v)^2 + (2\mathscr{B} D_d)^2} - \mathscr{C} D_v) \geq 0 \tag{7.104}$$

where

$$\mathscr{A}^2 = \frac{\eta^3 \mathscr{K}}{(\eta - \mathscr{K}\alpha^2)^2}; \mathscr{B}^2 = \frac{\eta^2 \mathscr{M}}{(\eta - \mathscr{K}\alpha^2)}; \mathscr{C} = \frac{\alpha\eta\mathscr{K}}{(\eta - \mathscr{K}\alpha^2)} \tag{7.105}$$

$\mathscr{K}$ and $\mathscr{M}$ are pore morphology factors that account for the incompressibility condition of the Von-Mises plasticity model[6] given by:

$$\mathscr{K}(\eta, \eta_0) = \lim_{k^s \to \infty} \frac{\partial k^{hom}}{\partial \mu^s}; \quad \mathscr{M}(\eta, \eta_0) = \lim_{k^s \to \infty} \frac{\partial \mu^{hom}}{\partial \mu^s} \tag{7.106}$$

Pore morphology affects the strength homogenization criterion. The pore morphology factors $\mathscr{K}$ and $\mathscr{M}$ are part of the effective strain rate tensor we seek. Consequently, they are part of the nonlinear strength homogenization approach based on second-order strain rate averages, assuming isotropic strength behavior. In this work, phases making level I (both pore volumes and solid particles) are assumed to have isotropic (spherical) shapes. Ortega et al. (2010) showed that modeling clay particles with spherical morphology but transverse isotropic elasticity yields accurate predictions of the anisotropy of clay composites measured by indentation. Therefore, with spherical pore shapes and isotropic strength behavior, the pore morphology factors depend on the elastic properties of the solid phase (k^{hom} and μ^{hom}), the friction coefficient (α_s), and the packing density of the medium ($\eta = 1 - \phi$). This brings us back to the two limit cases, the matrix-inclusion and the self-consistent morphologies. The pertaining pore morphology factors of these morphologies are:

[6] Refer to Dormieux et al. (2006) andCariou et al. (2008).

$$\mathcal{K}_{MT} = \frac{k^{hom}}{\mu} = \mathcal{K}_I(\frac{k}{\mu} = \frac{1}{\alpha_s^2}, \eta, \eta_0 = 0) = \frac{4\eta}{3(1-\eta) + 4\alpha_s^2} \tag{7.107a}$$

$$\mathcal{M}_{MT} = \frac{\mu^{hom}}{\mu} = \mathcal{M}_I(\frac{k}{\mu} = \frac{1}{\alpha_s^2}, \eta, \eta_0 = 0) = \frac{\eta(9 + 8\alpha_s^2)}{15 - 6\eta + (20 - 12\eta)\alpha_s^2} \tag{7.107b}$$

$$\mathcal{K}_{SC} = \mathcal{K}_I(\frac{k}{\mu} = \frac{1}{\alpha_s^2}, \eta, \eta_0 = 0.5) = \frac{4\eta\mathcal{M}_{SC}}{4\alpha_s^2\mathcal{M}_{SC} + 3(1-\eta)} \tag{7.108}$$

$$\mathcal{M}_{SC} = \mathcal{M}(\frac{k}{\mu} = \frac{1}{\alpha_s^2}, \eta, \eta_0 = 0.5) = \frac{1}{2} - \frac{5}{4}(1-\eta) - \frac{3}{16\alpha_s^2}(2+\eta) + ...$$
$$\frac{1}{16\alpha_s^2}\sqrt{144(\alpha_s^4 - \alpha_s^2) - 480\alpha_s^4\eta + 400\alpha_s^4\eta^2 + 408\alpha_s^2\eta - 120\alpha_s^2\eta^2 + 9(2+\eta)^2} \tag{7.109}$$

with $\mathcal{K}_{SC} = \mathcal{M}_{SC} = 0$ at the percolation threshold.

If a Von-Mises solid is assumed ($\alpha_s = 0$), the pore morphology factors (Equations (7.107)-(7.109)) reduce to

$$\mathcal{K}_{MT} = \mathcal{K}(\eta, \eta_0 = 0) = \frac{4\eta}{3(1-\eta)} \tag{7.110a}$$

$$\mathcal{M}_{MT} = \mathcal{M}(\eta, \eta_0 = 0) = \frac{3\eta}{5 - 2\eta} \tag{7.110b}$$

and

$$\mathcal{K}_{SC} = \mathcal{K}(\eta, \eta_0 = 1/2) = \frac{4\eta(2\eta - 1)}{(1-\eta)(2+\eta)} \tag{7.111a}$$

$$\mathcal{M}_{MT} = \mathcal{M}(\eta, \eta_0 = 1/2) = 3\frac{(2\eta - 1)}{2 + \eta} \tag{7.111b}$$

Cariou et al. (2008) showed that the above pore morphology factors, which hold for Von-Mises (incompressible) solids, remain a good approximation for cohesive-frictional materials. The macroscopic elliptical strength criterion is then given by

$$f(\Sigma_m, \Sigma_d) = \left(\frac{\Sigma_m/c_s + \mathscr{C}}{\mathscr{A}}\right)^2 \left(\frac{\Sigma_d/c_s}{\mathscr{B}}\right)^2 - 1 = 0 \tag{7.112}$$

The strength criterion is centered at $(\Sigma_m = c_s\mathscr{C}, \Sigma_d = 0)$ and is a close ellipse as long as

$\mathscr{B}^2 > 0$.

7.3.3 Yield Design and Multi-Scale Indentation Analysis

An indentation test gives access to the strength properties of the homogenized porous composite from, which the strength properties of the solid phase are extracted. Using multiscale yield design, Cariou et al. (2008) and Gathier (2008) developed a solution that incorporates the properties of the solid (c_S and α_s), the packing density ($\eta = 1-\phi$), and the microstructure as follows:

$$\frac{H}{h_s} = \Pi_H(\theta, \alpha_s, \eta, \eta_0) \tag{7.113}$$

where $h_s = h_s(c_s, \alpha_s) = lim_{\eta \to 1} H$ is the solid hardness that depends only on the solid properties. In other words, the asymptotic value is independent of the linear homogenization scheme. In order to relate h_s to the solid cohesion, c_s, solutions from finite element discretization of the material domain (using the "Limit Analysis Solver" of Borges et al., 1996) were used (Vandamme, 2008; Gathier, 2008; Vandamme et al., 2010), assuming loading with a conical indenter with the equivalent half-cone angle of a Berkovich. The discreet simulation results were fitted with a continuous function of the form:

$$\frac{h_s}{c_s} = \Pi_H(\alpha_s, \theta = 70.32^\circ) = A(1 + B\alpha_s + (C\alpha_s)^3 + (D\alpha_s)^{10}) \tag{7.114}$$

$$\begin{cases} A = 4.7644 & B = 2.5934 \\ C = 2.1860 & D = 1.6777 \end{cases}$$

With the assumption that the material is a frictionless solid, Equation (7.114) simplifies to:

$$h_s = 4.7644\, c_s \tag{7.115}$$

To find bounds for H and deduce an expression for the scaling relationship Π_H, Cariou et al. (2008) used the limit analysis theorems. They first determined the external work, δW,

provided by an indenter to a rigid plastic material in the absence of surfaces of discontinuity:

$$\delta W = P\dot{h} = \int_{A_c} \underline{T}(\underline{n}) \cdot \underline{U} da = \int_{\Omega} \boldsymbol{\Sigma} : \mathbf{D}(\underline{U})\, d\Omega \tag{7.116}$$

where P is the indentation load, A_c is the indenter-material contact area, $\underline{T}(\underline{n})$ is the stress vector on the contact area oriented by the unit normal $\underline{n}$, and $\dot{h}$ is the rate of penetration of the probe into the indented half-space Ω. The macrostress, $\boldsymbol{\Sigma}$, is a statically admissible stress field satisfying equilibrium; $\mathbf{D}$ is the strain rate field; and $\underline{U}(\underline{x})$ is the kinematically admissible macroscopic velocity, satisfying the following boundary conditions[7]:

$$\begin{cases} \underline{U}(\underline{x}).\underline{n} = -\dot{h}\sin\theta \text{ inside the area of contact} \\ \underline{U}(\underline{x}).\underline{n} \to 0 \text{ for } \underline{x} \to \infty \end{cases} \tag{7.117}$$

Cariou et al. (2008), then, determined P at plastic collapse after numerically estimating the macroscopic stress field. For $\dot{h} = 1$,

$$H = \frac{P}{A_c} = \frac{1}{A_c} \int_{\Omega} \boldsymbol{\Sigma} : \mathbf{D}\, d\Omega \tag{7.118}$$

The lower (H^-) and upper (H^+) bounds for H are found to be:

$$H^- \leq H = \frac{1}{A_c} \sup_{f(\boldsymbol{\Sigma}' s.a.) \leq 0} \int_{\Omega} \boldsymbol{\Sigma}' : \boldsymbol{D} d\Omega \tag{7.119}$$

and

$$H = \frac{1}{A_c} \inf_{\underline{U}' k.a} \int_{\Omega} \Pi(\boldsymbol{D}') d\Omega \leq H^+ \tag{7.120}$$

The dimensionless expression for hardness, Π_H^I (Equation (7.113)), depends on the packing density η, the homogenization scheme via the percolation threshold η_0, and the solid's

[7]The first boundary condition implies that the frictionless contact condition at the indenter-material contact permits a tangential slip without dissipation. Also, the yield design solution $P\dot{h}$ is proportional to $\dot{h}$ which is a dummy variable that can be set equal to one.

friction coefficient α_s as follows:

$$\Pi_H^I(\alpha_s, \eta, \eta_0) = \Pi_1(\eta, \eta_0) + \alpha_s(1-\eta)\Pi_2(\alpha_s, \eta, \eta_0) \tag{7.121}$$

In the case of frictionless cohesive solids and for the case of granular morphology (self-consistent scheme), Equation (7.121) reads (Bobko, 2008; Gathier, 2008):

$$\Pi_H^{SC}(\eta, \eta_0 = 1/2) = \frac{\sqrt{2(2\eta-1)} - (2\eta-1)}{\sqrt{2}-1}\Big(1 + a(1-\eta) + b(1-\eta)^2 + c(1-\eta)^3\Big) \tag{7.122}$$

For the Mori-Tanaka morphology, Π_H^I reads (Gathier, 2008):

$$\Pi_H^{MT}(\eta) = \eta\Big(1 + d(1-\eta) + e(1-\eta)^2 + f(1-\eta)^3\eta^3\Big) \tag{7.123}$$

with

$$\begin{cases} a = -5.3678 \quad b = 12.1933 \quad c = -10.3071 \\ d = -1.2078 \quad e = 0.4907 \quad f = -1.7257 \end{cases}$$

For the yield design solution to be valid, the loading rate in an indentation test should be "infinitely" fast so that neither the elastic nor viscous properties affect the hardness-strength relations (Vandamme, 2008). This condition is met in our indentation protocol.

7.4 Chapter Summary

This chapter reviews the elements of continuum mechanics along with elasticity and strength homogenization theories. From the elastic homogenization theory, the strain concentration tensor ($\mathbb{A}^r$) and the homogenized stiffness tensor in porous media ($\mathbb{C}^{hom}$) are obtained:

$$\mathbb{A}^r = [\mathbb{I} + \mathbb{P}_r : (\mathbb{C}^r - \mathbb{C}^0)]^{-1} : \{\sum_s \eta^s [\mathbb{I} + \mathbb{P}_s : (\mathbb{C}^s - \mathbb{C}^0)]^{-1}\}^{-1}$$

$$\mathbb{C}^{hom} = \langle \mathbb{C}^r(\underline{z}) : \mathbb{A}^r(\underline{z}) \rangle_V = \sum_r \eta^r \mathbb{C}^r \mathbb{A}^r$$

The linear elasticity homogenization is done assuming 1) a solid phase (clay particles) with a transverse isotropic elasticity and 2) phases with isotropic (spherical) shapes. Therefore, the elastic models contain anisotropy at level 0. The nonlinear strength homogenization approach is based on second-order strain rate averages. It assumes isotropic strength behavior, and the clay particles are taken to be frictionless-cohesive solids obeying the Von-Mises strength criterion. Strength homogenization gives Π_H, which relates the particle strength properties, h_s, to H as follows:

$$\frac{H}{h_s(c_s)} = \Pi_H(\eta, \eta_0)$$

The scaling expressions (Π_M and Π_H) relate the indentation modulus and hardness of the clay composites (M_o and H_o of level 1; Chapter 6) to the composites' microstructure (packing density) and solid phase properties (m_s and h_s of level 0). These expressions depend on the role assumed by the solid phase in the porous composites. Two approximation morphologies describe such a role and account for pore interaction in porous media. In the matrix-inclusion morphology, the solid phase plays the role of a matrix. There is no solid percolation threshold, and $\mathbb{C}^0 = \mathbb{C}^s$. In the self-consistent morphology, no one phase assumes the role of a matrix. The percolation threshold is $\eta_0 = 1/2$, and $\mathbb{C}^0 = \mathbb{C}^{hom}$.

The homogenization approaches and expressions derived in this chapter will be implemented in micromechanical textural modeling and in the back-analysis approach discussed in Chapter 8.

Chapter 8

Thermal Maturity and Micromechanical Modeling of Clay Composites

It is well known that burial and temperature history affect diagenesis and the maturity of organic matter in a formation. With maturity, the distribution and continuity of the organic phase change. Organic matter occurs in immature source rocks as a continuous network of water-saturated bitumen that expands between bedding planes and into micropores. With maturity and primary migration, the organic matter becomes isolated and randomly dispersed. This chapter models the observed maturity-dependent microtexture using micromechanical textural models. Our hypothesis (referred to as Hypothesis I) states that a matrix-inclusion morphology describes clay composites in immature formations, and a granular morphology describes those in mature formations. The former adopts clay minerals as a load-bearing matrix. The latter presents the material as a polycrystal with no one component assuming the role of a matrix.

Morphology-dependent hardness and stiffness scaling relationships (discussed in Chapter 7) are used to relate indentation responses in clay composites to microstructure (packing density) and the solid properties of clay particles. We present a “back-analysis" approach that implements these scaling relationships. Hypothesis I is tested based on the success (or failure) of the textural models to a) capture and isolate the effects of organic matter predicting the clay solid properties, b) reveal anisotropy of stiffness properties and isotropy of strength properties, and c) predict local (within indentation grid areas) packing density

and/or kerogen volume fractions in the homogenized clay composites[1].

8.1 Introduction

Many available techniques and tools have been used to study the microstructure of gas shale formations. Neutron scattering is used to map and characterize pore features as small as 3 nm (Jin et al., 2011). Transmission and scanning electron microscopes (TEM and SEM) are used to study texture, pore structure, size, and distribution within clay aggregates (Chalmers et al., 2012). SEMs and TEMs are also used to study organic matter porosity, relating it to thermal maturity (Curtis et al., 2012). Given its ease of use, x-ray diffraction is used to study mineral preferred (crystallographic) orientations. Such studies reveal the effects of clay mineralogy (Ho et al., 1999) and inclusion content (Sintubin, 1994) on rock fabric and macroscale mechanical anisotropy (Lonardelli et al., 2007). Confocal laser scanning has also been used to identify the organic parts in a rock to study their mechanical properties (Ahmadov et al., 2009). Heterogeneity in mechanical properties can be assessed by atomic force acoustic microscopy (AFAM) (Prasad et al., 2002a,b; Ahmadov et al., 2009) and indentation. The latter technique has been used to study organic-free shale formations (Constantinides et al., 2006; Bobko and Ulm, 2008; Bobko, 2008; Deirieh, 2011), minerals (Zhang et al., 2010; Broz et al., 2006; Berthonneau et al., in preparation), gas shale formations (Ahmadov et al., 2009; Mba et al., 2010; Zargari et al., 2011), and naturally matured and pyrolyzed gas shale samples (Zargari et al., 2011).

Indentation studies of source rocks available have three main drawbacks. First, they either use literature values or thresholds to differentiate the various chemical phases, ascribing weak mechanical data to clay aggregates and organic matter (Mba et al., 2010). Second, they are not statistically representative (Mba et al., 2010; Ahmadov et al., 2009), acquiring only tens of indentations in very heterogeneous materials. Third, they use tedious methods to locate organic parts in the rocks (Ahmadov et al., 2009). Our approach, the focus of this chapter, uses micromechanical textural models to study the texture and microstructure

[1]The results and findings listed in this chapter were submitted for publication. We refer the reader to: Abedi, S., Slim, M., and Ulm, F.-J.(in review). Nano-Mechanics of Organic Rich Shales: The Role of Thermal Maturity and Organic Matter Content.

of clay composites based on the maturity of their organic phase. The advantages of such an approach, if validated, are multifold. The approach helps model the texture of very heterogeneous geomaterials and provides a link between their textures, microstructures and mechanical properties that are more comprehensible than simple correlation. The approach can also be used to predict properties challenging to obtain experimentally such as clay particle solid properties, porosity, organic content, and ductility.

8.2 Research Hypothesis I: Maturity-Dependent Morphology

As discussed in Chapter 2, the volume, texture, and connectivity of organic matter change with maturity. Our hypothesis is that different microtextural models describe porous organic-rich clay composites based on the maturity of the their organic content. A self-consistent morphology (SC; Section 7.1.5.2) describes clay composites in mature formations, while a matrix-inclusion morphology (MT; Section 7.1.5.1) describes those in immature formations. The choice of modeling mature gas shales as polycrystalline material with a granular nature is justified by intuitively thinking of mature organic matter, which has expelled oil and gas, as disperse and stiff. The mature formations are, therefore, more texturally heterogeneous (Prasad et al., 2009, 2011; Zargari et al., 2013). We recall that the SC scheme has a solid percolation threshold, $\eta_0 = \frac{1}{2}$, below which the solid is unstable. The hypothesis of modeling immature formations with the MT morphology is supported by textural observations from SEM images (Prasad et al., 2009, 2011; Zargari et al., 2013) and phase correlation studies from CT scans at the nanoscale (Hubler et al., submitted). These studies show connected textures in immature source rocks.

8.3 Textural Modeling Assumptions

8.3.1 Maturity-Dependent Porosity Distribution

The following distribution of porosity and kerogen in the clay composites is proposed based on maturity. In mature formations, porosity is assumed to be evenly distributed among all phases (inclusions, clay phase, and organic matter). The porosity of the clay composites (level I porosity, ϕ^I) is the same as the sample porosity (level II porosity, ϕ^{II}). Kerogen is assumed to occur only in the clay composites, and its volume fraction (η_k) is obtained using Equation (2.9).

In immature formations, all porosity and kerogen are assumed to occur in the clay composites. Equations in Section 2.8 are used to calculate the organic content, η_k $\left(\eta_k = \dfrac{f_k}{1 - f^{incl}}\right)$, and porosity, ϕ^I $\left(\phi^I = \dfrac{\phi^{II}}{1 - f^{incl}}\right)$.

8.3.2 Kerogen Stiffness

In the microtextural modeling, we assume that the organic phase (kerogen) does not contribute to the effective elasticity of the rock. Thus, $\mathbb{C}^k = \mathbb{C}^p = 0$ (k, p stand for kerogen and porosity, respectively). This assumption is justified by 1) the low stiffness of organic matter (Zeszotarski et al., 2004; Ahmadov et al., 2009) being one order of magnitude less than that of a crystalline solid phase, and 2) the tendency of the stiffness of the clay composite to approach that of the solid phase at high packing density ($m_s = \lim_{\eta \longrightarrow 1} M$; M is the indentation modulus, and m_s is the elasticity of the solid/clay particle).

8.3.3 Particle Morphology

In our textural models, the various phases (clay particles, pores, and kerogen) are assumed to have an isotropic (spherical) shape. The clay particles are assumed to have transverse isotropic elasticity and isotropic strength behavior. These assumptions are based on work by Ortega et al. (2010), who showed that modeling clay particles with spherical morphology but transverse isotropic elasticity yields accurate predictions of the (level I) anisotropy of clay

composites measured by indentation. This approach dictates the form of the Hill tensor that characterizes the interaction of the different phases in the clay composites.

8.4 Link between Indentation Response and Microstructure

The two mechanical properties extracted from an indentation test (M_o and H_o; Chapter 6) are mechanical properties of a homogenized volume of porous material under the indenter tip. Micromechanical textural models (Sections 7.1.5.2 and 7.1.5.1) relate such homogenized responses to material solid properties (m_s and h_s) and microstructure (η) via the scaling relationships introduced in Chapter 7. In a dimensionless form, the homogenized response reflects the isotropy of the strength behavior and the anisotropy of the elastic one, such that (Ulm et al., 2007):

$$\frac{H_o}{h_s(c_s)} = \Pi_H(\eta_s, \eta_k, \eta_o) \tag{8.1}$$

$$\frac{M_o}{m_s} = \Pi_M(\frac{c_{ijkl}}{m_s}, \eta_s, \eta_k, \eta_0) \tag{8.2}$$

Recalling that $\eta_c + \eta_k + \phi = 1$ and with no stiffness assumed for the organic phase, the dimensionless expressions for hardness, Π_H, can be restated in terms of η_k and ϕ. For the case of granular morphology (the self-consistent scheme), applicable to mature samples, Equation (7.122) becomes (Bobko, 2008; Gathier, 2008):

$$\Pi_H^{SC} = \frac{\sqrt{2(1-2(\phi+\eta_k))} - (1-2(\phi+\eta_k))}{\sqrt{2}-1}\Big(1 + a(\phi+\eta_k) + b(\phi+\eta_k)^2 + c(\phi+\eta_k)^3\Big) \tag{8.3}$$

whereas for the Mori-Tanaka morphology, applicable to immature samples, Equations (7.123) reads (Gathier, 2008):

$$\Pi_H^{MT} = (1-\phi-\eta_k)\Big(1 + d(\phi+\eta_k) + e(\phi+\eta_k)^2 + f(\phi+\eta_k)(1-\phi-\eta_k)^3\Big) \tag{8.4}$$

with:

$$\begin{cases} a = -5.3678 \quad b = 12.1933 \quad c = -10.3071 \\ d = -1.2078 \quad e = 0.4907 \quad f = -1.7257 \end{cases}$$

For the elastically anisotropic composite, the homogenized elastic response $\mathbb{C}^{hom}$ (Equation (7.46)) depends on the expression of the strain concentration tensor, $\mathbb{A}^r$, of each phase (Equation (7.45)) in the composite. $\mathbb{A}^r$ is a function of $\mathbb{C}^0$ that, in turn, depends on the morphology chosen for the porous medium (e.g., $\mathbb{C}^0 = \mathbb{C}^{hom}$ in mature formations and $\mathbb{C}^0 = \mathbb{C}^s$ in immature ones). The scaling relationships of the elasticity moduli are power functions that relate Π_M to the solid packing density (Ulm et al., 2007; Bobko, 2008). They produce the stiffness tensor of a transversely isotropic material (e.g., inorganic solid phase in the clay composites) solving for the non-zero entries of the Hill concentration tensor[2]. For a granular morphology (mature formations), however, the elastic moduli scaling relationship, $\Pi_M^{SC}(\frac{C_{ijkl}}{m_s}, \eta_s, \eta_k, \eta_0 = 0.5)$, can be approximated by a linear scaling of the form (Ulm et al., 2007; Bobko and Ulm, 2008; Bobko, 2008):

$$\frac{M}{m_s} = \Pi_M^{SC} \approx 2\eta - 1 \tag{8.5}$$

8.5 Back-Analysis Approach

The mechanical properties extracted from nanoindentation tests describe the elasticity and strength properties of the porous clay composites using the scaling relationships presented in Section 8.4. An inverse approach can be employed to use the indentation measurements ($M_{1,3}$ and $H_{1,3}$) to obtain clay particle solid properties ($m_{s,1}$, $m_{s,3}$, and h_s) and either the packing density of the clay composites or its organic content.

8.5.1 Back-Analysis Approach Algorithm

The inverse or back-analysis approach (Bobko et al., 2011) employs multiple ($N = 10s - 100s$) indentation tests acquired in every indentation grid and assumes the following:

[2]Expressions for these line integrals are listed in Ortega et al. (2007).

- The back-analysis approach neglects the strength and stiffness properties of kerogen. Also, the solid properties of the inorganic phase (clay particles) ($m_{s,1}, m_{s,3}, \text{and}\, h_s$) are assumed to be constant in every grid. The clay particle solid properties are the first three unknowns in the problem.

- The microstructure in the homogenized volume under the indenter tip can vary from one indentation test to another. The varying local packing densities or porosities ($N \times \phi_i$; with $i = 1...N$ = number of indents) add another N unknowns to look for.

- The model can be constrained with either the porosity of the clay composite, ϕ^I (Refer to Section 2.8), to predict the organic content or the volume fraction of the organic phase, η_k, to predict the composite porosity. In this chapter, we use the back-analysis approach to predict the organic content of the clay composites. Therefore, η_k is another unknown to find.

- The indentation moduli (M_1^i or M_3^i) and the indentation hardness (H_1^i or H_3^i) are measured composite (level I) properties. They are the $2 \times N$ known variables in the problem.

With $(2N + 1)$ knowns and $(N + 4)$ unknowns to solve for, a highly over-determined system of equations can be formulated. For a large N, the back-analysis approach is feasible. It is formulated as a minimization algorithm implemented using the non-linear least squares solver ("lsqnonlin" function) in Matlab (Bobko et al., 2011; Abedi et al., in preparation). The error to be minimized at each point is:

$$S_i = \left(\frac{M^{i,mod}(\eta_i, m_{s,j}) - M_j^i}{M_{0,j}} \right)^2 + \left(\frac{H^{i,mod}(\eta_i, c_s) - H_j^i}{H_{0,j}} \right)^2 \tag{8.6}$$

where i is the number of indentation tests in a grid. Subscript $j = 1, 3$ for indentations parallel and normal, respectively, to the depositional bedding planes (i.e., normal and parallel, respectively, to the elastic axis of symmetry). $M_{0,j}$ and $H_{0,j}$ are normalization factors typically chosen as the mean values of the indentation modulus and hardness in a grid. With each indentation test being an independent statistical event, the minimization problem is

(Bobko et al., 2011):

$$\min_{m_s,h_s,\eta_i} \sum_i S_i^2 \tag{8.7}$$

8.5.1.1 Statistical Analysis of Back-Analysis Results

The clay composites are highly heterogeneous in terms of mineralogy, texture, organic content and maturity. Therefore, it is important to investigate the optimum data set size needed for the back-analysis algorithm to converge to a unique set of solid properties (m_s and h_s) and η_k. The investigation helps us understand any scatter seen in the back-analysis results within the same sample. Toward that end, a population of $N = 928$ nanoindentation tests penetrating clay composites in Marcellus 108 indented in the x_1-direction was acquired. This test population combines mechanical responses from five nanoindentation grids performed on random areas on the mechanically polished surface of Marcellus 108. From the population, samples of various sizes, n ($n \sim 10\%\ N, 20\%\ N$,..., $80\%\ N$), are randomly drawn (without replacement). The back-analysis is then run on each drawn sample. The objective behind this sampling exercise is to address the following questions:

1. Is there a scatter in the solid properties (m_s and h_s) obtained from different nanoindentation grids on the same sample surface? If so, is the scatter due to various grid sizes, variability in the chemical phase itself (clay mineralogy and texture), or both?

2. How many data points are needed in the clay phase? In other words, what is a representative sample size that reflects the variability of the phase and gives the "true" means of the solid properties within the limits of the mean-field modeling approach?

3. What is the error introduced when fewer data points than needed to represent the phase variability and its solid properties are available? How far from the true means of the solid properties and what standard deviation/error do we expect when the back-analysis is done on samples with sizes $n \ll N$?

The random sampling process described was repeated tens of times (Table 8.1) for each sample size to obtain sizable distributions of mean values of the solid properties. Knowing

Table 8.1: Mean and standard deviation of the distributions of solid properties values, porosity, and η_k obtained from the back-analysis approach on samples of variable sizes (n).

Mar108x_1

n = Sample Size	# of Samples	m_s (GPa)		h_s (GPa)		ϕ (%)		η_k(%)	
		μ	σ	μ	σ	μ	σ	μ	σ
100	230	66.72	9.89	3.03	0.59	7.4	3.1	16.3	3.1
200	117	71.36	7.62	3.29	0.44	7.6	2.3	17.8	2.3
300	118	71.76	6.53	3.32	0.37	7.8	1.9	17.7	1.9
400	185	69.93	5.45	3.26	0.29	7.9	1.6	17.2	1.6
500	80	71.77	5.05	3.33	0.29	8.1	1.8	17.5	1.8
600	66	71.90	3.99	3.35	0.23	8.2	1.2	17.4	1.2
700	150*	71.19	2.83	3.31	0.17	8.4	0.9	17.1	0.9
800	60	71.65	1.68	3.34	0.09	8.6	0.6	17.0	0.6
900	10	71.08	0.43	3.30	0.02	8.7	0.1	16.8	0.1
$N = 928$	1	71.86	-	3.29	-	8.7	-	16.7	-

*More simulations than needed were run for n=700 to confirm convergence to mean values; (n= Sample size; N= population size = 928 nanoindentation tests).

that the micromechanics models are based on the principle of ergodicity[3], the convergence criteria for the mean and standard deviation followed for obtaining the solid properties are:

$$| 1 - \frac{\mu_j}{\mu_{j-1}} | \leq 1\% \tag{8.8}$$

$$| 1 - \frac{\sigma_j}{\sigma_{j-1}} | \leq 5\% \tag{8.9}$$

where μ_j and σ_j are the means and standard deviations from simulations 1 to j.

Sampling results show that it takes fewer simulations (draws) to fulfill the mean convergence criterion (Equation (8.8)) than the standard deviation one (Equation (8.9)). Still, even when few simulations were needed to fulfill the mean convergence criterion (e.g., $\backsim$24 simulations with $n = 100$), enough simulations were conducted to build a representative distribution of mean values ($f_n(\mu_n, \sigma_n, n)$) for every n. The confidence in the μ_n and σ_n obtained for each sample size is reflected in the uniformity (mainly, the decrease in the amplitude and increase in the wavelengths of the curves in Figures 8-1 to 8-3). The number of samples needed to

[3]The principle of ergodicity implies that, in an upscaling procedure, fluctuations are neglected.

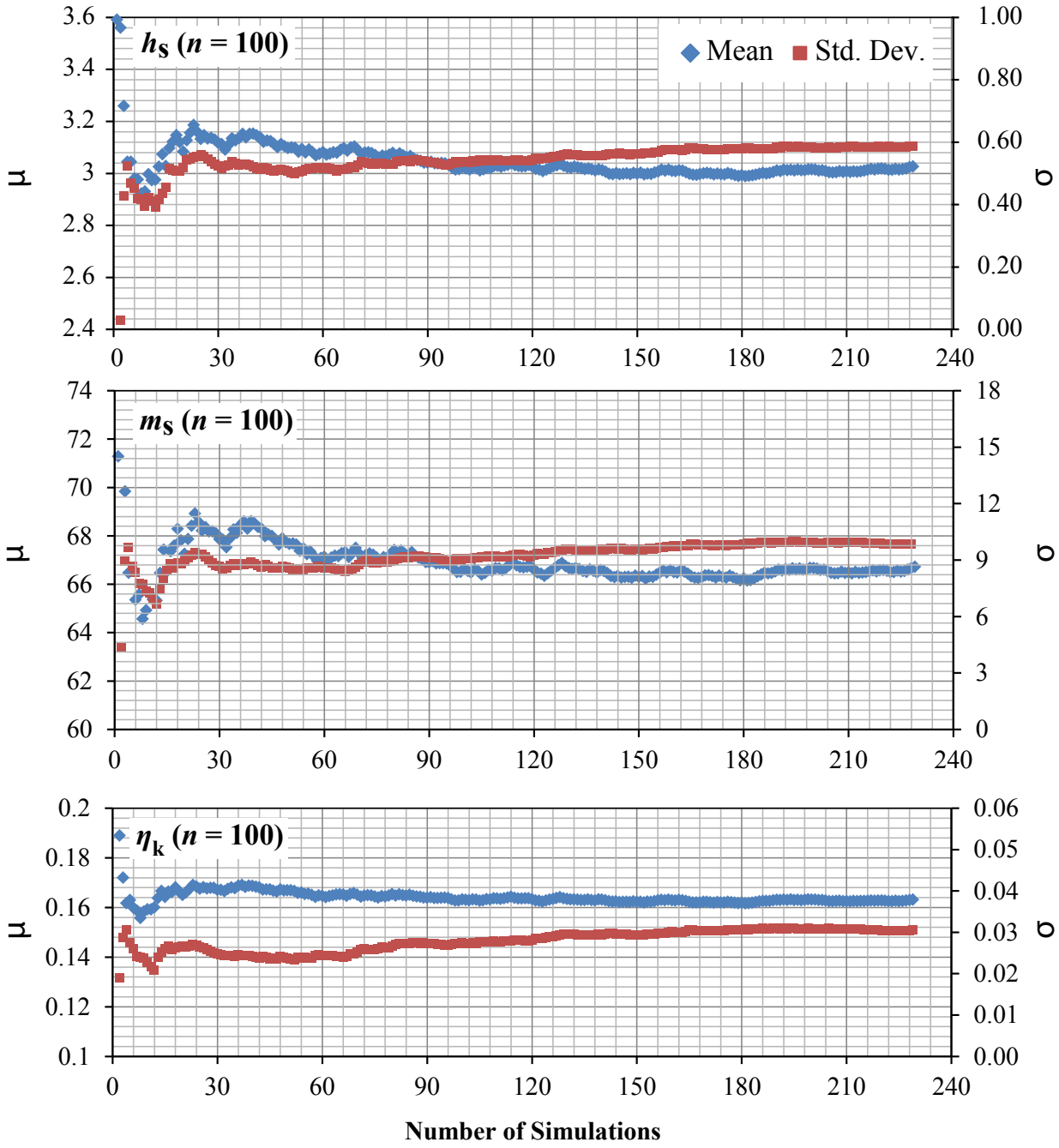

Figure 8-1: Back-analysis results of 230 randomly drawn samples, each containing mechanical data (M_o and H_o) from 100 randomly chosen indentation tests (n=100). Note the standard deviations of the m_s and h_s distributions (9.89 GPa and 0.59 GPa, respectively; Table 8.5).

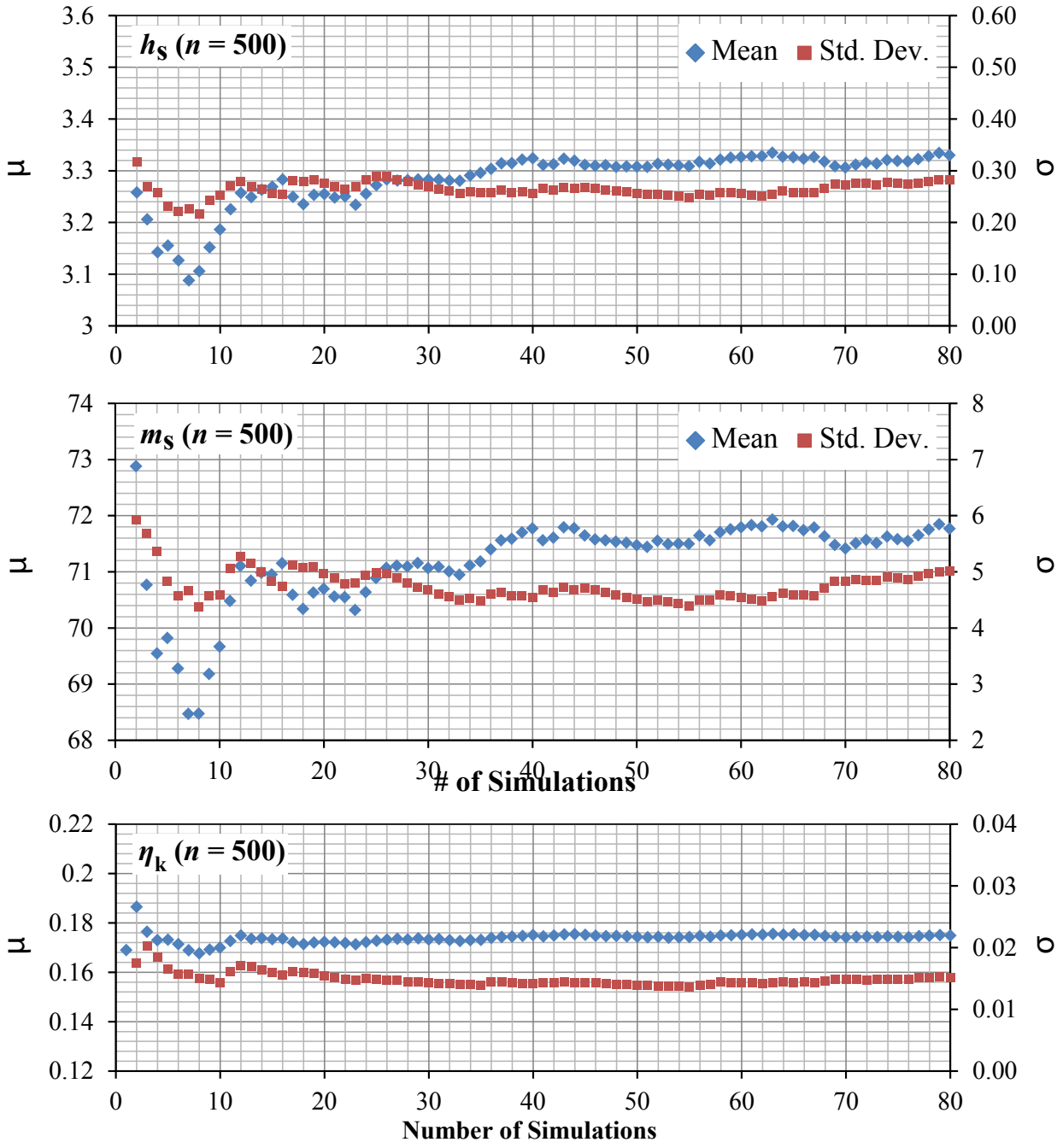

Figure 8-2: Back-analysis results of 80 different samples, each containing mechanical data (M_o and H_o) from 500 randomly chosen indentation tests (n=500). Note the reduction in the standard deviations of the m_s and h_s distributions (5.05 GPa and 0.29 GPa, respectively; Table 8.5) compared to those in Figure 8-1.

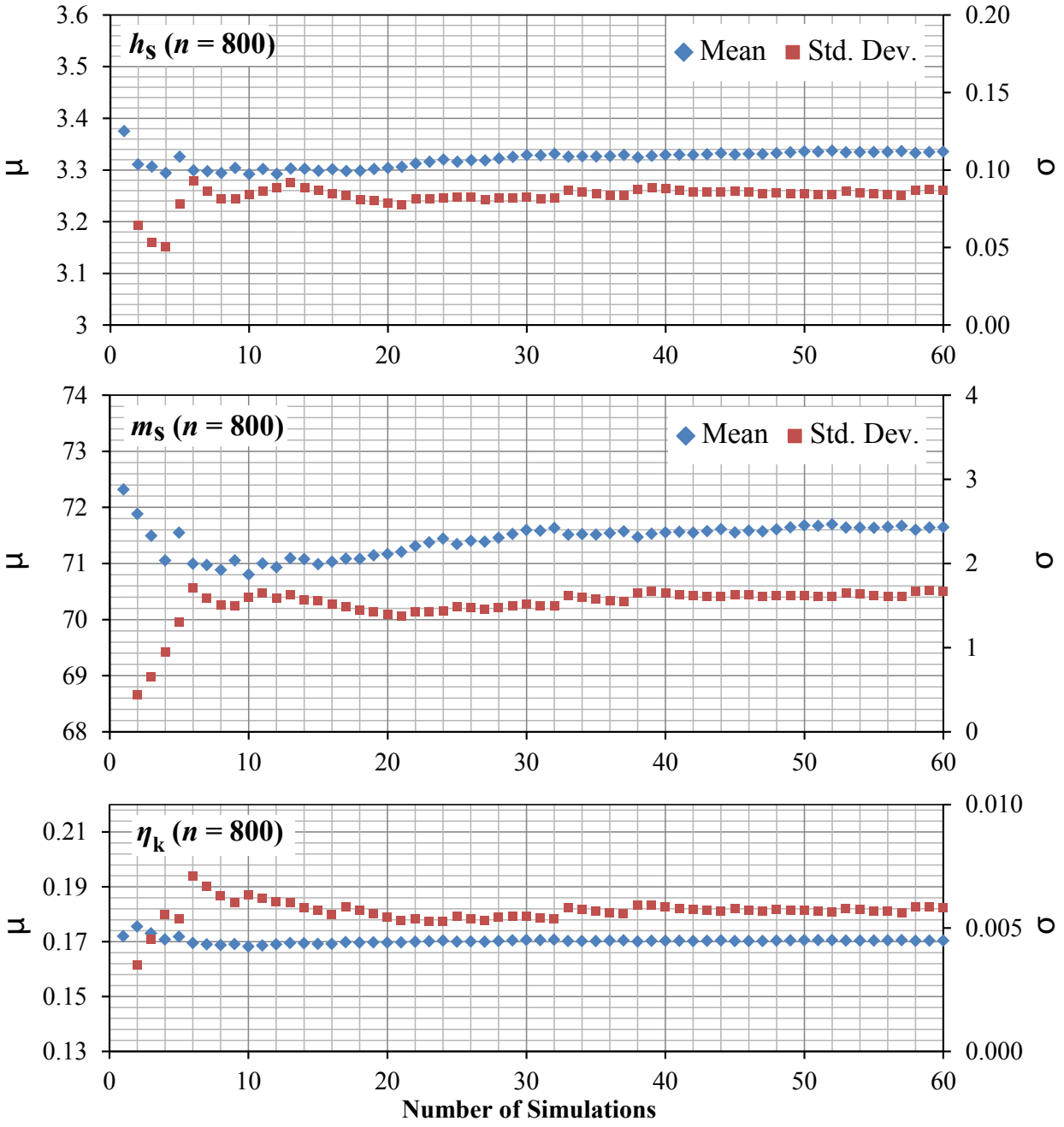

Figure 8-3: Back-analysis results of 60 different samples containing mechanical data (M_o and H_o) from 800 randomly chosen indentation tests (n=800).

reach convergence reflects the dependence of the back-analysis approach on sample size. For instance, to get a stable/uniform μ_{100} (mean of a solid property analyzing samples with $n =$ 100 data points each), 100 different samples are needed. When the sample size gets $5\times$ and $8\times$ larger, only 40 and 12 samples are needed, respectively. Therefore, the fewer the indentation tests analyzed at a time, the more scatter (high standard deviations of the distributions obtained from small sample sizes; see Table 8.1) is expected in the solid property values. We suspect that heterogeneity in the clay mineralogy (combinations of illite, smectite, muscovite, ...) and variability of the (micro)structure of the clay aggregates contribute to the scatter. Unfortunately, the chemical complexity of the clay minerals and the resolution of the EDS measurement (beam spot size $\sim 1\mu$ m) prevent us from distinguishing various clay minerals in the homogenized volumes under the indenter tip. Also, studying the microstructure of clay the aggregates is not part of this work (We refer the reader to work by Deirieh, 2016).

Indenting tens of grids on each sample surface is experimentally expensive. Also, collecting hundreds of data points to feed into the back-analysis algorithm makes the latter very computationally expensive. Therefore, errors introduced analyzing samples with sizes $n < N$ are estimated. The errors reflect the minimum sample size needed when analyzing the heterogeneous clay composites. With the assumption that the back-analysis of the whole population gives the "real" value of the solid properties of the clay particles parallel to their bedding planes ($m_{s,1}$= 71.89 GPa and h_s=3.29 GPa; Table 8.1), we calculate the deviation of the normalized sample means from unity and the error window ($\mu_n \pm \sigma_n$) introduced when analyzing data sets from individual indentation grids. Figure 8-4 shows that, if the error is to be reduced to $< 10\%$, a minimum of 400 nanoindentations ($\sim$ 2-3 grids) is needed in the clay composites to characterize their chemical and textural heterogeneity. With the above guidelines and expected errors when back-analyzing data from individual grids, the statistical analysis conducted shows the dependence of the back-analysis results on sample size before results converge to a unique set of solid properties.

8.5.1.2 Back-Analysis Results

Except for Antrim and Barnett, for which data from 2 indentation grids were combined (data courtesy of Dr. Sara Abedi), the back-analysis results (Figures 8-5 and 8-6; Tables 8.2-

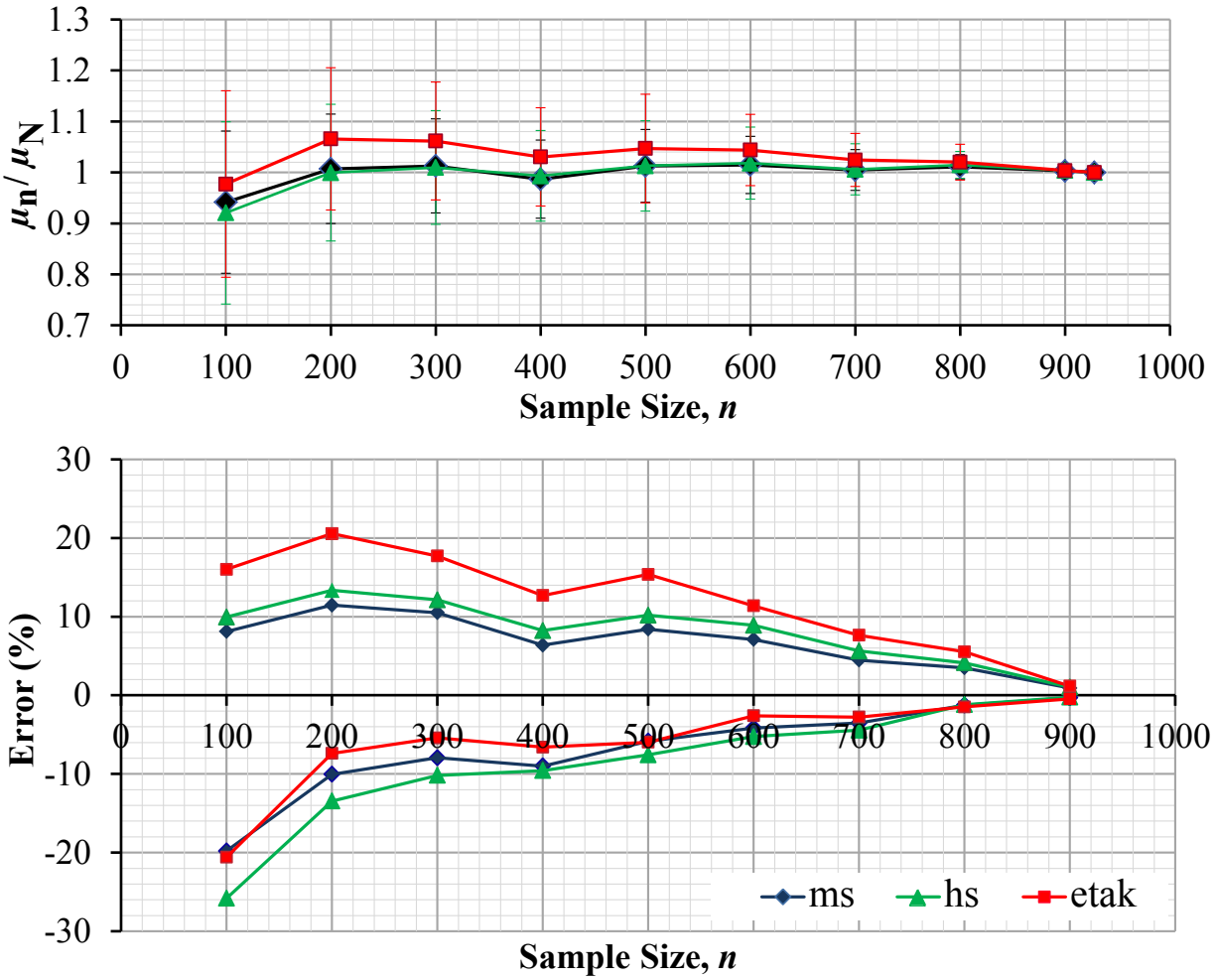

Figure 8-4: Normalized mean values of solid properties and packing density obtained from the back-analysis approach (top) and error window ($\mu \pm \sigma$) expected back-analyzing sample with different sizes (bottom). Large standard deviations and error intervals are seen with n <400.

8.4) are obtained analyzing mechanical data from individual indentation grids. Results from Woodford show extreme values for the elastic moduli. Three reasons can explain these results:

- Woodford is rich in quartz ($\sim$ 60 wt.%), not all of which occurs in the form of inclusions[4]. The resolutions of the nanoindentation technique and EDS do not allow the separation of fine-grained (amorphous) quartz in the clay composites. Indeed, the chemo-mechanical clustering analysis of Woodford data indicates high $\frac{Si}{Al}$ ratios

[4]Inclusion phases obtained from clustering analysis using Woodford data do not account for 60% of the grid areas.

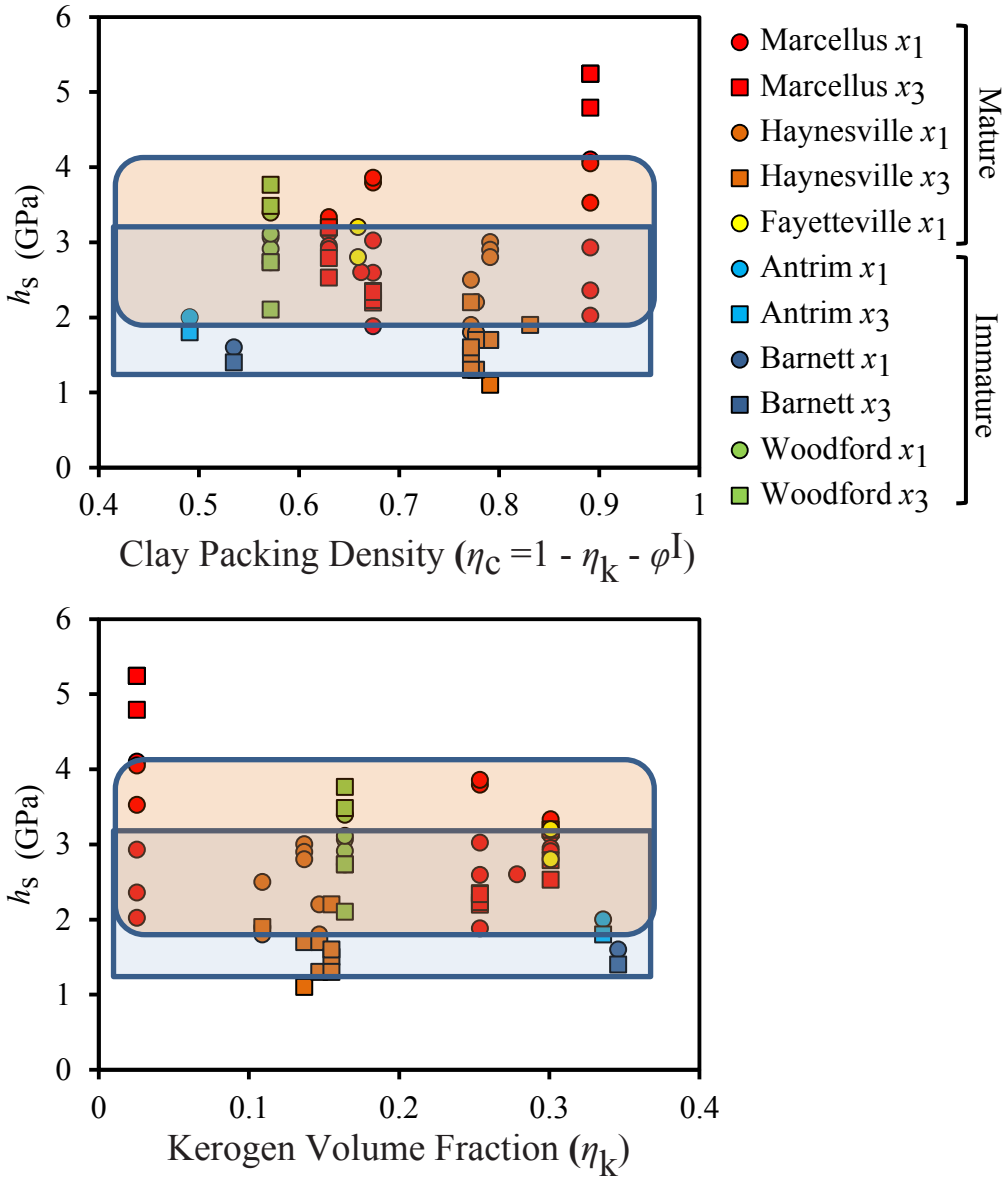

Figure 8-5: Clay particle hardness versus a) volume fraction of clay minerals and b) volume fraction of kerogen in the clay composites obtained from the back-analysis approach. Haynesville, Fayetteville, Antrim and Barnett results are courtesy of Dr. Sara Abedi. Pink and blue shaded areas indicate solid properties obtained in the x_1- and x_3-direction, respectively.

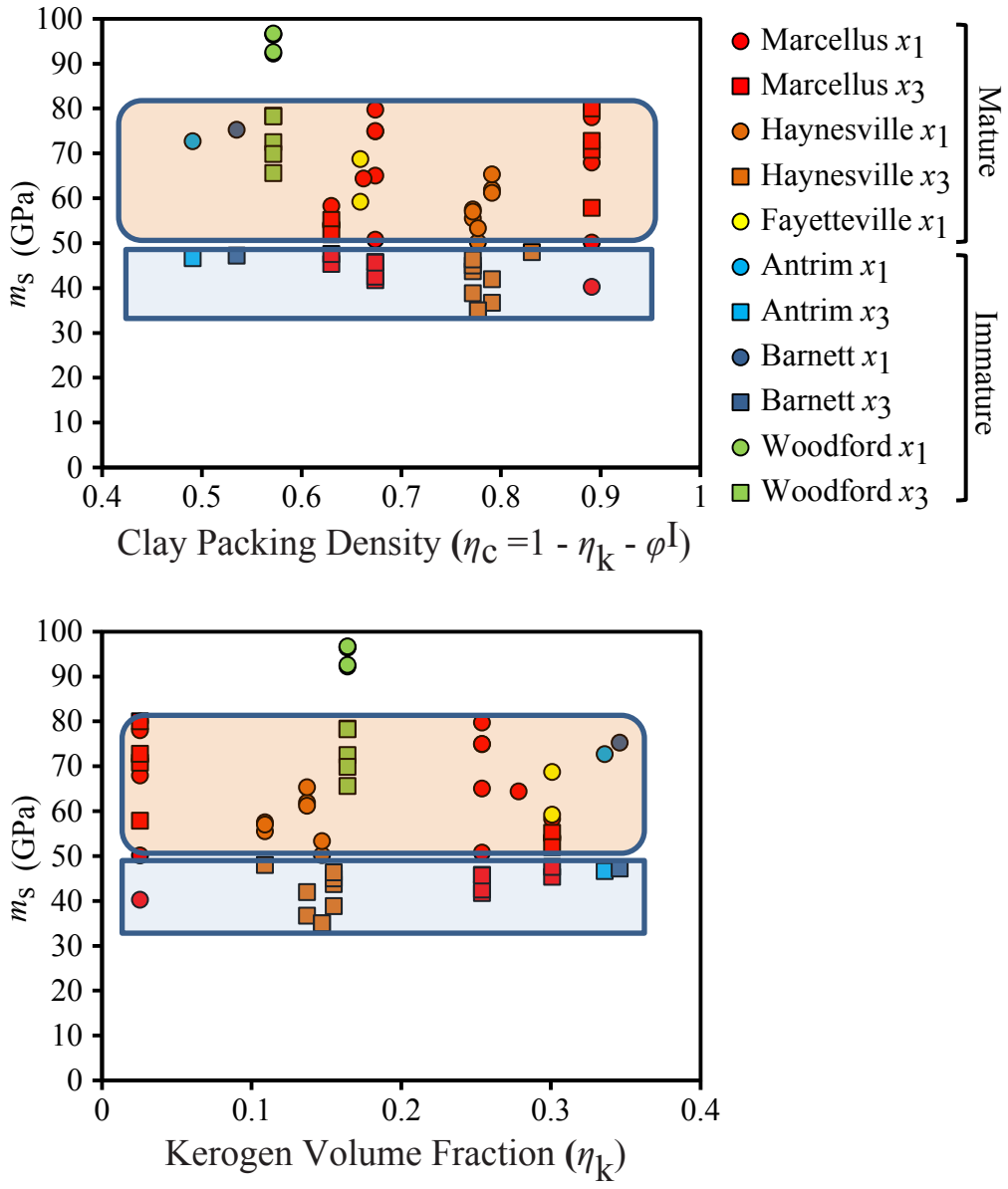

Figure 8-6: Clay particle elasticity modulus versus a) volume fraction of clay minerals and b) volume fraction of kerogen in clay composites obtained from the back-analysis approach. Haynesville, Fayetteville, Antrim and Barnett results are courtesy of Dr. Sara Abedi. Pink and blue shaded areas indicate solid properties obtained in thex_1- and x_3-direction, respectively.

Table 8.2: Clay particle solid properties obtained from the back-analysis of nanoindentation mechanical data of clay composites from the various Marcellus samples studied.

Sample	Grid	h_s	m_s	η_k	η_c
Mar46x_1	g0*	2.36	67.89	0.03	0.89
Mar46x_1	g1	2.02	40.22	0.03	0.89
Mar46x_1	g2	2.93	50.06	0.03	0.89
Mar46x_1	g3	4.10	71.30	0.03	0.89
Mar46x_1	g4	3.52	79.95	0.03	0.89
Mar46x_1	g5	4.05	78.02	0.03	0.89
Mar108x_1	g1	1.88	50.74	0.25	0.67
Mar108x_1	g2	3.02	74.85	0.25	0.67
Mar108x_1	g3	2.59	65.03	0.25	0.67
Mar108x_1	g4	3.79	79.69	0.25	0.67
Mar108x_1	g5	3.86	74.97	0.25	0.67
Mar150x_1	g0*	2.60	64.40	0.28	0.66
Mar151x_1	g1	3.13	53.91	0.30	0.63
Mar151x_1	g2	2.95	54.16	0.30	0.63
Mar151x_1	g3	3.33	58.24	0.30	0.63
Mar151x_1	g4	2.91	54.27	0.30	0.63
Mar46x_3	g1	5.24	57.86	0.03	0.89
Mar46x_3	g2	5.24	70.76	0.03	0.89
Mar46x_3	g3	5.24	72.77	0.03	0.89
Mar46x_3	g4	4.79	80.00	0.03	0.89
Mar108x_3	g3	2.20	41.69	0.25	0.67
Mar108x_3	g4	2.23	45.74	0.25	0.67
Mar108x_3	g5	2.35	42.50	0.25	0.67
Mar108x_3	g6	2.34	45.64	0.25	0.67
Mar151x_3	g1	3.19	55.16	0.30	0.63
Mar151x_3	g2	3.20	51.93	0.30	0.63
Mar151x_3	g3	2.79	45.34	0.30	0.63
Mar151x_3	g4	2.53	47.51	0.30	0.63

*Data courtesy of Dr. S. Abedi.

Table 8.3: Clay particle solid properties obtained from the back-analysis of nanoindentation mechanical data of clay composites from the various Haynesville and Fayetteville samples studied. Indentation tests and back-analysis results are courtesy of Dr. S. Abedi

Sample	Grid	h_s	m_s	η_k	η_c
A5Vx_1	g0a	1.90	57.50	0.11	0.77
A5Vx_1	g0b	1.80	55.50	0.11	0.77
A5Vx_1	g0c	2.50	57.00	0.11	0.77
A6Vx_1	g0a	3.00	61.90	0.14	0.79
A6Vx_1	g0b	2.90	61.20	0.14	0.79
A6Vx_1	g0c	2.80	65.30	0.14	0.79
A7Vx_1	g0a	1.80	50.20	0.15	0.78
A7Vx_1	g0b	2.20	53.30	0.15	0.78
A2Vx_3	g0a	1.50	43.70	0.16	0.77
A2Vx_3	g0b	1.30	38.80	0.16	0.77
A2Vx_3	g0c	2.20	45.00	0.16	0.77
A2Vx_3	g0d	1.60	46.30	0.16	0.77
A5Vx_3	g0	1.90	48.00	0.11	0.83
A6Vx_3	g0b	1.10	36.70	0.14	0.79
A6Vx_3	g0	1.70	41.90	0.14	0.79
A7Vx_3	g0b	1.30	35.00	0.15	0.78
A7Vx_3	g0	1.70	35.00	0.15	0.78
Fayetteville x_1	g0a	2.80	59.20	0.30	0.66
Fayetteville x_1	g0b	3.20	68.70	0.30	0.66

($\frac{Si}{Al} > 4$) in the clay composites, confirming the presence of (non-clay) Si in the form of fine-grained (amorphous) quartz.

- Porosity in the Woodford outcrop samples is estimated to be 12.6 %, which is the highest porosity among the samples studied. The assumption that all porosity in immature formations is in the clay composites gives a high level I porosity ($\phi^I = 26.4\%$). This ϕ^I might be contributing to the overestimate in the solid mechanical properties.

The mean values and standard deviations of the solid properties obtained from the back-analysis approach are (Table 8.5): $m_{s,1} = 67.7 \pm 15.0$ GPa, $m_{s,3} = 53.1 \pm 14.3$ GPa, $h_{s,1} = 2.8 \pm 0.7$ GPa, and $h_{s,3} = 2.7 \pm 0.7$ GPa. These results reveal anisotropy in the elastic properties and isotropy in the hardness properties.

Table 8.4: Clay particle solid properties obtained from the back-analysis of nanoindentation mechanical data of clay composites from the immature formations studied.

Sample	Grid	h_s	m_s	η_k	η_c
Antrimx_1	g0a,b*	2.00	72.70	0.34	0.49
Antrimx_3	g0a,b*	1.80	46.60	0.34	0.49
Barnettx_1	g0a,b*	1.60	75.20	0.35	0.54
Barnettx_3	g0a,b*	1.40	47.20	0.35	0.54
WoodfordAx_1	g1	2.73	92.19	0.16	0.57
WoodfordAx_1	g2	3.07	96.54	0.16	0.57
WoodfordAx_1	g3	3.39	96.43	0.16	0.57
WoodfordBx_1	g1	2.91	96.64	0.16	0.57
WoodfordBx_1	g2	3.11	92.55	0.16	0.57
WoodfordAx_3	g1	3.48	78.38	0.16	0.57
WoodfordAx_3	g2	2.73	72.50	0.16	0.57
WoodfordAx_3	g3	2.73	69.86	0.16	0.57
WoodfordBx_3	g1	3.76	78.22	0.16	0.57
WoodfordBx_3	g2	2.10	65.61	0.16	0.57

*Data courtesy of Dr. S. Abedi. Back-analysis uses data from 2 nanoindentation grids.

Table 8.5: Means and standard deviations of clay particle elastic modulus and hardness obtained from back-analyzing nanoindentation data in x_1- and x_3-direction.

Clay Composite	$\mathbf{m_{s,1}}$	$\mathbf{m_{s,3}}$	$\mathbf{h_{s,1}}$	$\mathbf{h_{s,3}}$
All Formations	67.7 ± 15.0	53.1 ± 14.3	2.8 ± 0.7	2.67 ± 1.2
All Formations Except Woodford	63.0 ± 10.4	48.7 ± 11.7	2.8 ± 0.7	2.3 ± 0.9

8.5.2 Back-Analysis Results: Validation and Discussion

The solid properties obtained in Section 8.5.1.1 by back-analyzing a large population ($N = 928$) of indentation measurements are $m_{s,1}^N = 71.86$ GPa and $h_{s,1}^N = 3.29$ GPa. Compared to values reported in Table 8.5 deviations of 6% in the elastic properties and $\sim 16\%$ in hardness are obtained by back-analyzing individual grids. As discussed in Section 8.5.1.1, these errors are expected (Figure 8-4) when the back-analysis approach is done using data sets from individual grids. Also, we recall that the source rocks studied formed in different depositional environments, had different diagenetic histories, and have different maturities. The spread in solid properties (Figures 8-5 and 8-6), within the same formation and among different formations, reflects the complex diagenetic history and a variable clay mineralogy (XRD data; Chapter 2) in the clay composites. In fact, results from Berthonneau et al. (in preparation), obtained nanoindenting various clay minerals (Table 6.7), reveal the complexity of the clay minerals and the range of their solid properties. In addition to this intrinsic complexity of the clay composites, the back-analysis results are also affected by potential errors measuring and/or estimating (from mineral and bulk densities) sample porosities and, to a lesser extent, the organic content.

8.5.2.1 Comparison to Experimental Results

In addition to the experimental work of Berthonneau et al. (in preparation), Bobko and Ulm (2008) extrapolated solid phase moduli from nanoindentation of organic-free shale formations rich in illite, smectite, and kaolinite. They report $\lim_{\eta=1} M_1 = 25$ GPa and $\lim_{\eta=1} M_3 = 16$ GPa. The discrepancy in the elastic properties between seal formations and source rocks can be due to differences in the hydration states (clay-bound water) of the clay minerals. The effect of mineral hydration on the mechanical properties of clay minerals was studied by Ebrahimi et al. (2012) using molecular simulation (next section).

8.5.2.2 Comparison to Molecular Simulation Results

Molecular simulations provide a means to determine the mechanical properties of minerals. Ebrahimi et al. (2012) used molecular simulations to study the effect of hydration on the

Table 8.6: Mean values of mechanical properties obtained using the stiffness tensor components from molecular simulations by Hantal et al. (2014) and Ebrahimi et al. (2012). The back-analysis results of Monfared and Ulm (2015) were obtained using sonic measurements of gas shale formations.

(GPa)	ReaxFF[a]	ClayFF[a]	Wyoming Na-montmorillonite[b]	Back-analysis Acoustic Data[c]
m_1	107.21*	150.16*	-	62.36*
m_3	39.85*	39.03*	31 ± 7	29.25*

*Using formulation for transverse isotropic solid (Equations (2.4) and (2.5); Delafargue and Ulm 2004).

[a] Hantal et al. (2014).

[b] Ebrahimi et al. (2012).

[c] Monfared and Ulm (2015).

mechanical properties of clay minerals. They report a modulus $m_{s,3} = 31 \pm 7$ GPa for dry Wyoming Na-montmorillonite. In another study, Hantal et al. (2014) obtained the components of the illite's stiffness tensor considering various force fields (reactive "ReaxFF" and non-reactive "ClayFF"; Table 2.10). In order to compare Hantal's results to our back-analysis results, we use Equations (2.4) and (2.5) relating the elastic properties of a transverse isotropic solid to components of its stiffness tensor (Delafargue and Ulm, 2004). As Table 8.6 shows, the resultant indentation moduli are: $m_1^{ReaxFF} = 107.21$ GPa, $m_3^{ReaxFF} = 39.85$ GPa, $m_1^{ClayFF} = 150.16$ GPa, and $m_3^{ClayFF} = 39.03$ GPa. Only results in the x_3-direction are in good agreement with our back-analysis results. The poor agreement between Hantal's $m_1^{ReaxFF,ClayFF}$ and our $m_{s,1}$ is due to modeling illite as a periodic system with infinite bedding planes. Such a structure is not an accurate depiction of real systems, in which solid particles have finite dimensions. As a result, instead of being subjected to contact forces leading to its bending, displacement, or rearrangement, the simulated illite structure, upon loading, shows a stick-slip behavior. With cohesion in the structure provided by non-covalent interactions rather than chemical bonds, the stick-slip behavior is interpreted as sliding of the clay sheets past one another (Hantal et al., 2014). Therefore, m_1^{ReaxFF} and m_1^{ClayFF} are not actual measurement of the stiffness of illite in a direction parallel to its sheet structure. Consequently, only the $m_3^{ClayFF,ReaFF}$ results are reliable for comparison with our back-analysis data.

8.5.2.3 Comparison to Back-Analysis of Sonic Data

Monfared and Ulm (2015) validated and calibrated a two-step homogenization model that uses continuum micromechanics and molecular results on kerogen. Their back-analysis approach uses sonic measurements on gas shale formations (Woodford and Haynesville) and produces a set of elastic properties (Table 8.6) that are in good agreement with values reported in literature for various clay minerals (Katahara, 1996; Vaughan and Guggenheim, 1986; Mavko et al., 1998. Table 2.10). Using Monfared and Ulm's solid stiffness tensor components in the transverse isotropic formulations (Equations (2.4) and (2.5)) gives the following moduli: $m_1 = 62.36$ GPa and $m_3 = 29.25$ GPa, which are in close agreement with our reported solid property values. Such a good agreement between our back-analysis results and those of Monfared and Ulm confirms the unsuitability of comparing our back-analysis results to m_1 obtained from molecular simulation. Consequently, it is unlikely to have clay sheets sliding in (well-confined) porous organic-rich clay composites subjected to indentation loads. Particle bending and/or rearrangement are more likely to occur. The good agreement also reflects the reliability of M_1 obtained indenting along a low-symmetry axis (parallel to bedding planes) and reflects accuracy in approximating the elliptical contact area (between indenter and material) to a circle. Finally, the comparison emphasizes the complexity of the clay mineralogy (e.g., Table 6.7) that is rarely captured with molecular simulations.

8.5.2.4 Elastic Anisotropy vs. Strength Isotropy

After comparing and validating the solid properties produced by the back-analysis approach, we look at the statistical significance of the results. Statistical t-tests of the solid property distributions (Figure 8-7) indicate the statistical elastic anisotropy and isotropic hardness of the clay particles. We recall that in the elasticity models adopted, stiffness anisotropy is assumed a priori at the clay particle level despite using isotropic particle shapes (spheres) to represent all phases (organic, inorganic, and pore space) in the clay composites. On the other hand, the hardness scaling relationships (Equations (8.3) and (8.4)) are based on microtexture and the strength isotropy of the clay particles. The latter, we recall, relates only to cohesion (c_s). Therefore, in addition to providing valid solid properties, the back-analysis results ($m_{s,1}$

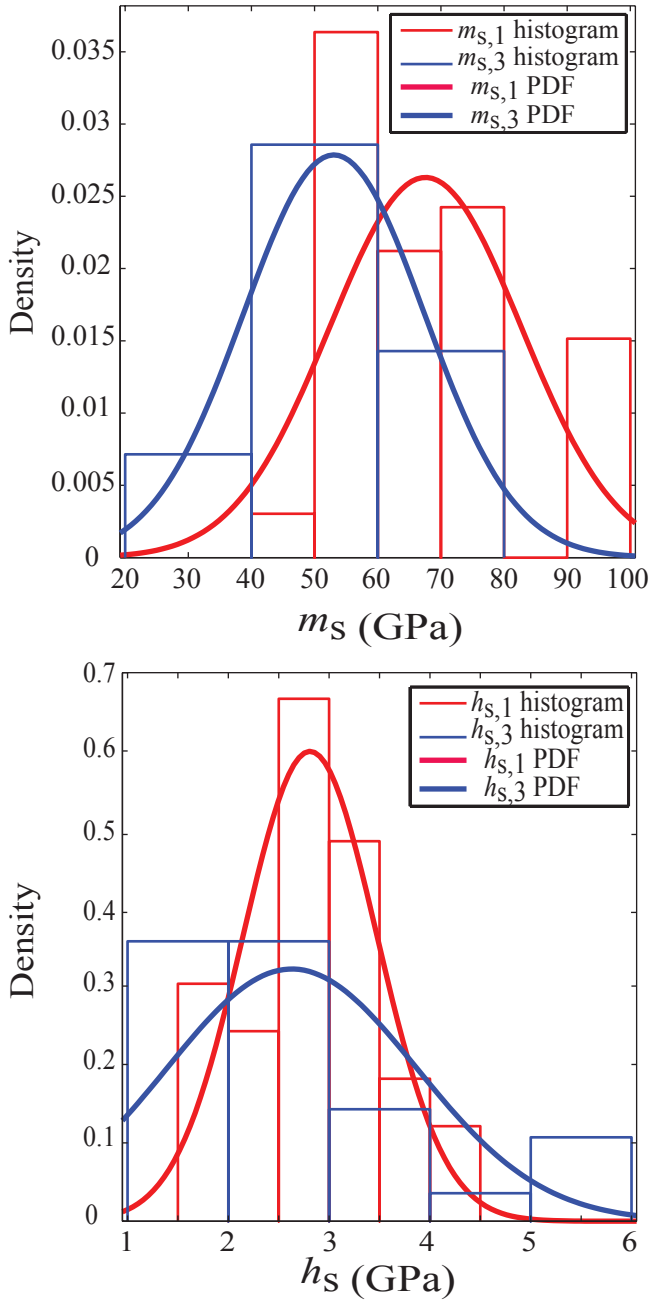

Figure 8-7: Normal distributions of the clay elastic moduli (top) and hardness (bottom) obtained from the back-analysis approach (red = x_1-direction; blue = x_3-direction).

and $m_{s,3}$) produce the anisotropy embedded in the elasticity models. Our findings confirm results and conclusions by Ulm et al. (2007) who showed that the anisotropy measured at level I (M_1 and M_3) is due to intrinsic anisotropy of the clay particles rather than to their structure or morphology. Similarly, the back-analysis hardness results reveal isotropic hardness at the particle level and confirm, a posteriori, the hardness model assumptions.

8.5.2.5 Prediction of Volume Fraction of Kerogen

With a constraint put on porosity, the back-analysis is run to produce, in addition to the clay particle solid properties, the volume fraction of kerogen in the clay composites (η_k) (Table 8.7). Figure 8-8 shows a fair agreement between the predicted η_k in every grid area and level I η_k calculated from TOC and $\rho_k = 1.2$ g/cc. The agreement is best in Antrim, Barnett, Haynesville, and the "organic-poor" facies of Marcellus. The back-analysis approach under-predicts η_k in Fayetteville and the organic-rich facies of (overmature) Marcellus. It also predicts unrealistic η_k values in Woodford. Several parameters contribute to these poor predictions. First, the η_k predictions are obtained from localized and small grid areas where small volumes of clay composites are homogenized under the indenter tip. Such volumes are small when compared to volumes of material treated for TOC measurements. Second, the random occurrence of kerogen in overmature samples can contribute to the error predicting η_k. Third, any variability in the density of the organic phase is not accounted for as a constant kerogen density (1.2 g/cm^3) is assumed in both mature and immature formations. This assumption introduces errors in the calculations of level I η_k from TOC data. Finally, the over-predicted η_k in Woodford could also be the consequence of over-predictions of solid properties in that formation for reasons discussed in Section 8.5.1.2.

8.5.3 Hypothesis Testing: Capturing Kerogen Maturity with Micromechanical Textural Modeling

Our hypothesis states that different mechanical microtextures describe clay composites of different maturity levels. The Matrix-inclusion morphology describes clay composites with immature kerogen, and the self-consistent morphology describes those with mature kero-

Table 8.7: Predicted volume fractions of kerogen in the clay composites using the back-analysis approach.

Sample	Grid	Predicted $\eta_k(\%)$	Sample	Grid	Predicted $\eta_k(\%)$
Mar46x_1	g0*	8.3	A5Vx_1	g0a*	15.6
Mar46x_1	g1	8.6	A5Vx_1	g0b*	16.3
Mar46x_1	g2	0	A5Vx_1	g0c*	15.5
Mar46x_1	g3	3.7	A6Vx_1	g0a*	17.0
Mar46x_1	g4	7.0	A6Vx_1	g0b*	11.8
Mar46x_1	g5	4.5	A6Vx_1	g0c*	15.2
Mar108x_1	g1	13.2	A7Vx_1	g0a*	11.2
Mar108x_1	g2	19.8	A7Vx_1	g0b*	12.1
Mar108x_1	g3	17.6	A2Vx_3	g0a*	15.0
Mar108x_1	g4	20.3	A2Vx_3	g0b*	12.3
Mar108x_1	g5	17.2	A2Vx_3	g0c*	15.0
Mar150x_1	g0*	20.7	A2Vx_3	g0d*	15.2
Mar151x_1	g1	14.4	A5Vx_3	g0*	11.3
Mar151x_1	g2	14.8	A6Vx_3	g0b*	13.8
Mar151x_1	g3	16.4	A6Vx_3	g0*	14.6
Mar151x_1	g4	16.1	A7Vx_3	g0b*	11.0
Mar46x_3	g1	4.1	A7Vx_3	g0*	14.0
Mar46x_3	g2	8.4	Antrimx_1	g0a,b*	35.0
Mar46x_3	g3	0	Antrimx_3	g0a,b*	40.0
Mar46x_3	g4	10.7	Barnettx_1	g0a,b*	38.8
Mar108x_3	g3	15.0	Barnettx_3	g0a,b*	36.8
Mar108x_3	g4	12.8	WoodfordAx_1	g1	38.0
Mar108x_3	g5	13.9	WoodfordAx_1	g2	40.0
Mar108x_3	g6	16.9	WoodfordAx_1	g3	40.0
Mar151x_3	g1	21.1	WoodfordBx_1	g1	42.0
Mar151x_3	g2	17.8	WoodfordBx_1	g2	39.0
Mar151x_3	g3	16.5	WoodfordAx_3	g1	38.0
Mar151x_3	g4	17.7	WoodfordAx_3	g2	38.0
Fayetteville x_1	g0a*	18.0	WoodfordAx_3	g3	40.0
Fayetteville x_1	g0b*	23.4	WoodfordBx_3	g1	43.0
			WoodfordBx_3	g2	39.0

*Data courtesy of Dr. S. Abedi.

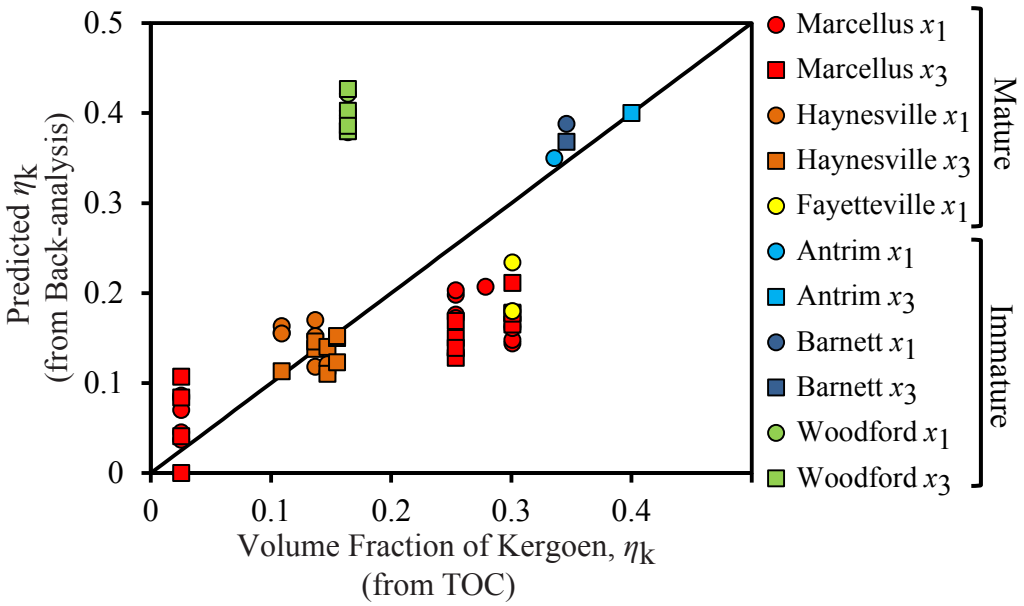

Figure 8-8: Comparison between the volume fractions of kerogen (η_k) in the clay composites calculated from TOC (x-axis) and those predicted with the back-analysis approach (y-axis).

gen. This hypothesis addresses and models well-documented textural changes that take place in source rocks with maturity (Prasad and Mukerji, 2003; Prasad et al., 2009, 2011; Zargari et al., 2011). After the back-analysis approach produced the solid properties of the clay particles (the elementary solid particles at level 0), these properties were validated against results from other experimental studies, molecular simulations, and back-analysis using sonic measurements (Bobko and Ulm, 2008; Ebrahimi et al., 2012; Monfared and Ulm, 2015; Berthonneau et al., in preparation). We find that, regardless of the formation analyzed or its maturity level, the solid properties obtained reflect unique anisotropic elastic properties and isotropic strength properties. Such results highlight the success of the microtextural models in capturing and isolating the effect of kerogen maturity and in producing the intrinsic solid particle properties. This success validates our hypothesis and promotes microtextural modeling as a means to predict the organic content and/or packing densities of the clay composites. Further, microtextural modeling is a means to obtain solid mechanical properties that are difficult to obtain experimentally or by molecular simulation.

8.6 Ductility and Energy Dissipation Modeling

Hydrocarbon-production potential in gas shale formations depends on, among other parameters, the network of naturally occurring and/or induced fractures in the formations. Fracture development in turn depends on the geomechanical properties of the rock, such as mineralogy (Kumar et al., 2012) and ductility. With the back-analysis results validated and Hypothesis I verified, the solid properties ($m_{s,1,3}$ and h_s) and the morphology-dependent scaling relationships ($\Pi_H^{MT,SC}$ and $\Pi_M^{MT,SC}$) can be used in a forward application to plot the elasticity and hardness envelopes for the two morphologies and to predict ductility (i.e., the deviation of the clay composites, under a prescribed load, from elastic behavior) and energy dissipation. Figures 8-9 and 8-10 show envelopes that contain experimental data and depict anisotropy in the composites' elasticity and isotropy of their hardness. Ductility, the ratio M_o/H_o, is inversely proportional to the elastic strain limit. Indented with a Berkovich tip, materials with pure elastic behavior have $(M/H)_e = 5.59$ (Constantinides and Ulm, 2007). Using the back-analysis results, the ductility of the clay particles is found to be: $d_{s,1} = \frac{m_{s,1}}{h_{s,1}} = 24.78 \pm 6.62$ and $d_{s,3} = \frac{m_{s,3}}{h_{s,3}} = 22.36 \pm 6.15$ in the x_1 and x_3-directions, respectively (Figure 8-11).
These ductility values reflect the plasticity of the clay minerals and fall within the ranges obtained by Berthonneau et al. (in preparation) (Table 6.7). Unlike Berthonneau et al.'s results obtained from indenting clay minerals, our back-analysis results suggest nearly similar plastic behavior parallel and orthogonal to the particle axis of symmetry. Also, the ductility envelopes (Figure 8-11) reflect favorable properties that promotes plastic deformation due to a low elastic strain limit. Finally, using solid properties and the scaling relationships gives $\frac{M_o^2}{H_o}$. This ratio is proportional to the energy dissipated due to plastic work and the formation of cracks during an indentation test. According to Bao et al. (2004), this ratio is related to a "recovery resistance factor," R_s, defined as:

$$R_s = 2.263\frac{E_r^2}{H} \tag{8.10}$$

where the constant depends on the indenter tip geometry, and E_r is the measured reduced

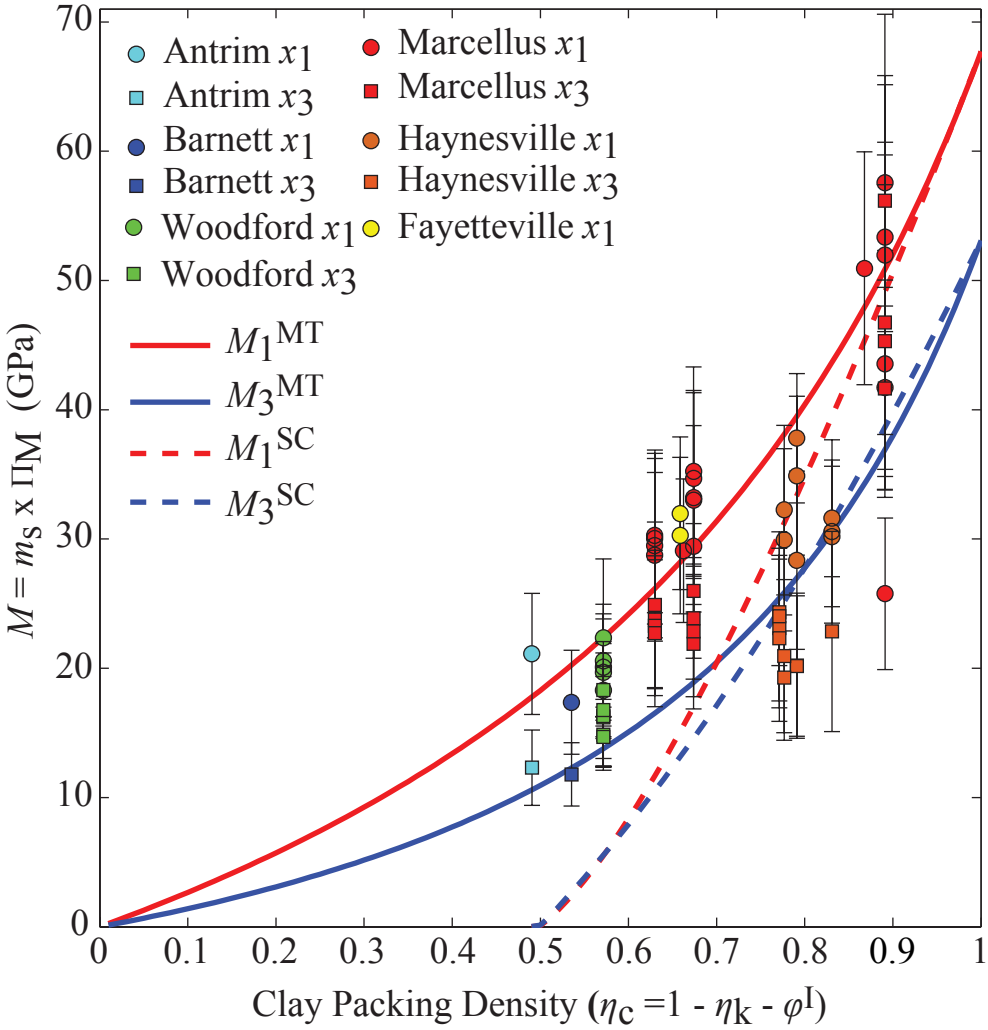

Figure 8-9: Modeled elasticity ($M = m_s \times \Pi_M$) vs. the clay volume fraction (η_c) in the clay composites. Curves are plotted using texture-dependent elasticity homogenization (Equations (7.45) and (7.46)) and solid stiffness components reported in Monfared and Ulm (2015) (Table 2.10). Solid and dashed curves represent the Mori-Tanaka (MT) and self-consistent (SC) morphologies, respectively. Red curves are obtained using $m_{s,1} = 67.7$ GPa. Blue curves are obtained using $m_{s,3} = 53.1$ GPa.

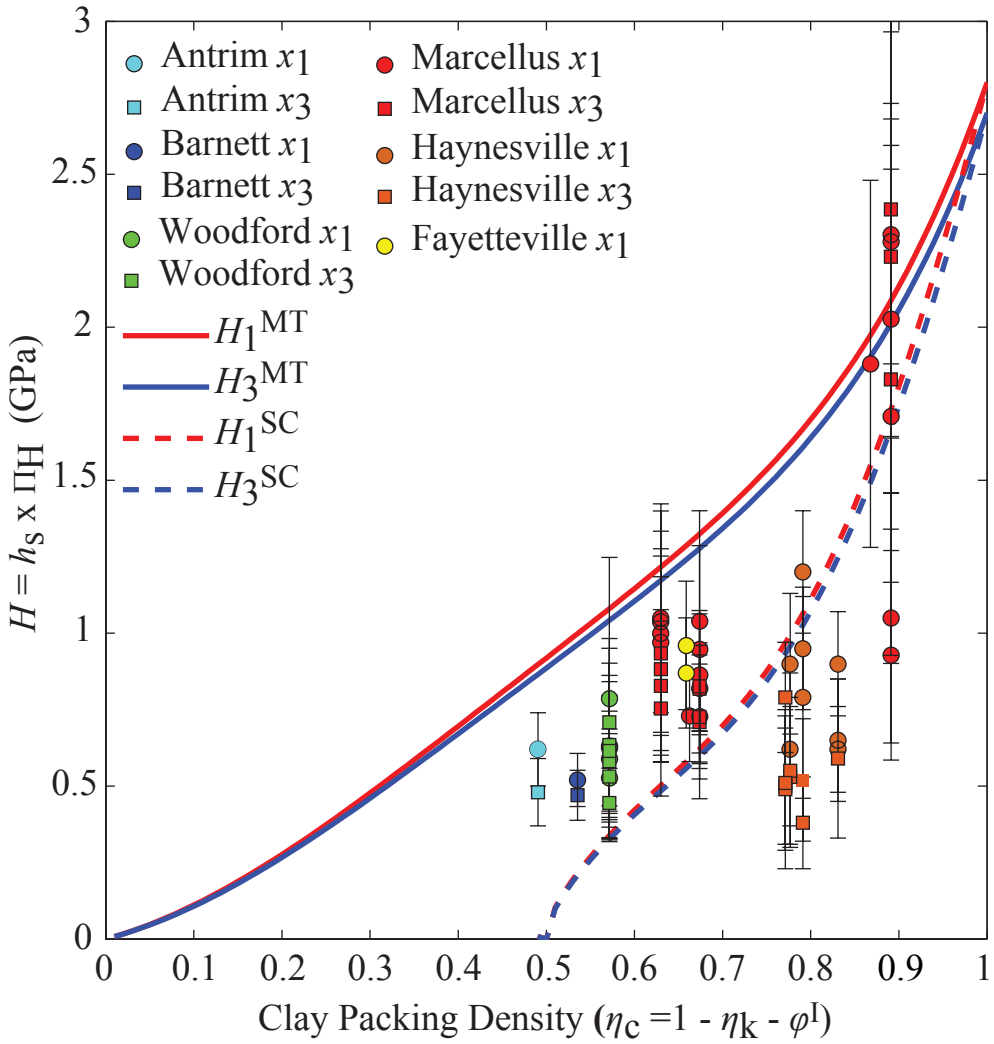

Figure 8-10: Modeled hardness ($(H = h_s \times \Pi_H)$) vs. the clay volume fraction (η_c) in the clay composites. Curves are plotted using texture-dependent scaling relationships (Equations (8.3) and (8.4)). Solid and dashed curves represent the Mori-Tanaka (MT) and self-consistent (SC) morphologies, respectively. Red curves are obtained using a $h_{s,1} = 2.8$ GPa. Blue curves are obtained using a $h_{s,3} = 2.7$ GPa.

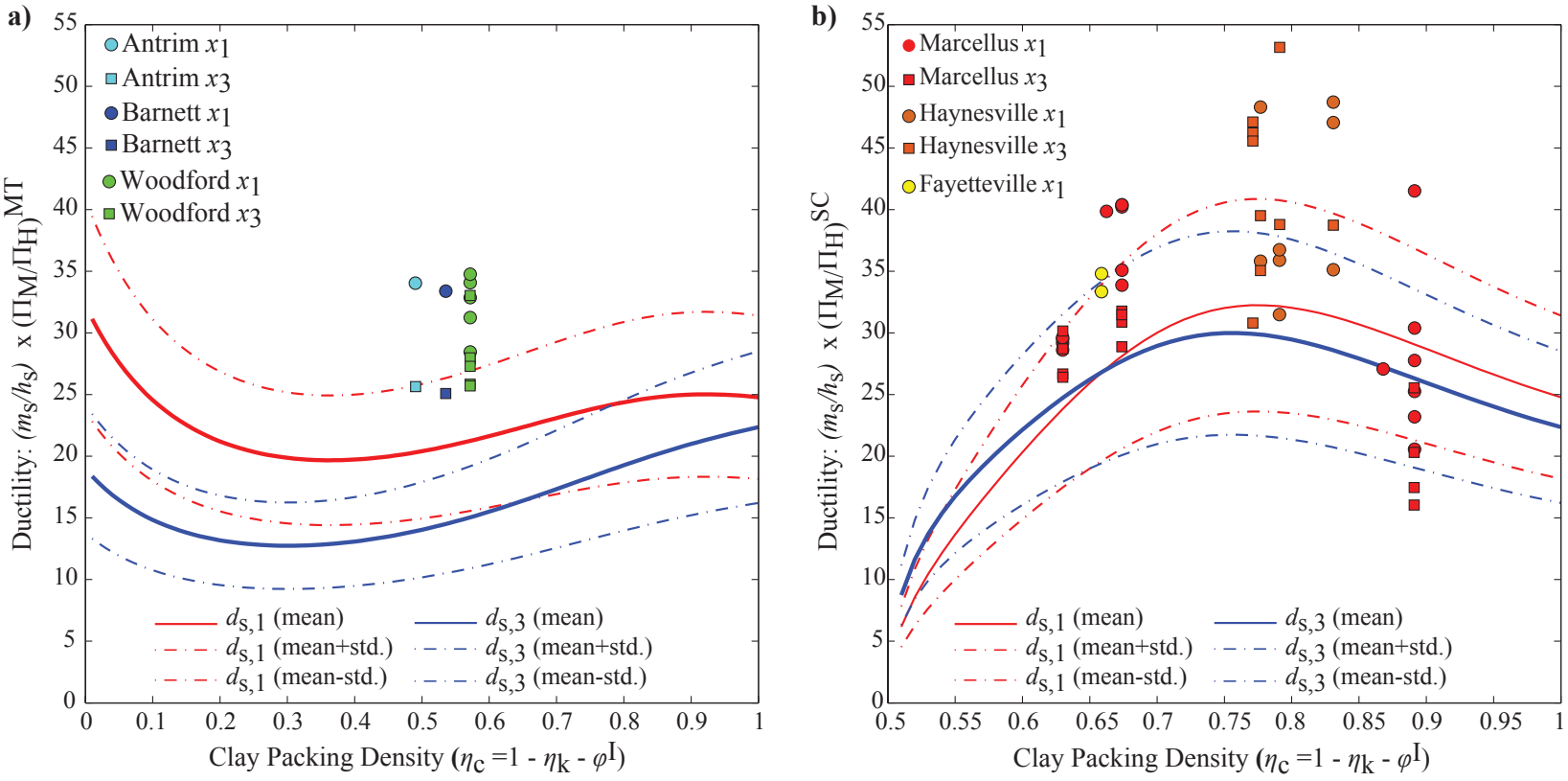

Figure 8-11: Ductility envelops using the solid properties obtained from the back-analysis approach and microtextural models scaling relationships for a) immature and b) mature formations. Formations' ductility are plotted using indentation results $(\frac{M_o}{H_o})$.

modulus[5]. We note that Bao et al. (2004) performed indentation tests with no hold phase (e.g., Figure 3-6). The $\frac{M_o^2}{H_o}$ ratio obtained using our indentation data include energy dissipated during both the loading and the 10 s hold phase. Figure 8-12 shows that when the microtexture of the material is no longer a factor (i.e., at $\eta_c = 1$), the calculated ratio $m_s^2/h_s = \lim_{\eta_c \longrightarrow 1} \frac{M_o^2}{H_o}$ gives a dissipation energy of the same order of magnitude (in TPa) as that obtained by Bao et al. (2004) for Mg-based bulk metallic glass. At any other packing density, the energy dissipation (shapes of the curves in Figure 8-12) appears to be a function of the microtexture and the microstructure of the material. The envelopes indicate plastic work/deformation taking place during the (short hold-time) nanoindentation tests due to either rearrangement of particles (low packing density material) or opening of cracks (high packing density material).

8.7 Chapter Summary

In this chapter, textural changes that take place with maturity of source rocks are modeled. Our hypothesis (Hypothesis I) states that the matrix-inclusion morphology describes clay composites in immature formations, and the self-consistent morphology describes those in mature formations. We implemented a back-analysis approach to validate Hypothesis I. The approach uses indentation data (M_o and H_o) to predict clay particle solid properties ($m_{s,1,3}$ and h_s) and kerogen volume fractions (η_k). The back-analysis approach produced unique clay particle solid properties; it also revealed anisotropy in the elastic solid properties ($m_{s,1} = 67.7 \pm 15.0$ GPa and $m_{s,3} = 53.1 \pm 14.3$ GPa) and an isotropy in the strength properties ($h_{s,1} = 2.8 \pm 0.7$ GPa and $h_{s,3} = 2.6 \pm 1.2$ GPa), both of which are proposed by the elasticity and strength homogenization models. Also, the elasticity results ($m_{s,1}$ and $m_{s,3}$) are in good agreement with experimental studies, molecular simulations, and a back-analysis approach using sonic data. Consequently, the back-analysis results both validate the microtextural modeling approach as a means to study highly heterogeneous materials and predict, within experimentally accepted errors, a unique set of clay particle solid properties.

[5] $\frac{1}{E_r} = \frac{1}{M} + \frac{1-\nu_i^2}{E_i}$ where M is the indentation modulus of the material. The variables ν_i and E_i are the Poisson's ratio and the elastic modulus of the indenter diamond tip, respectively. The reported M data in this work are obtained from the measured reduced modulus using $\nu_i = 0.07$ and $E_i = 1,141\,GPa$.

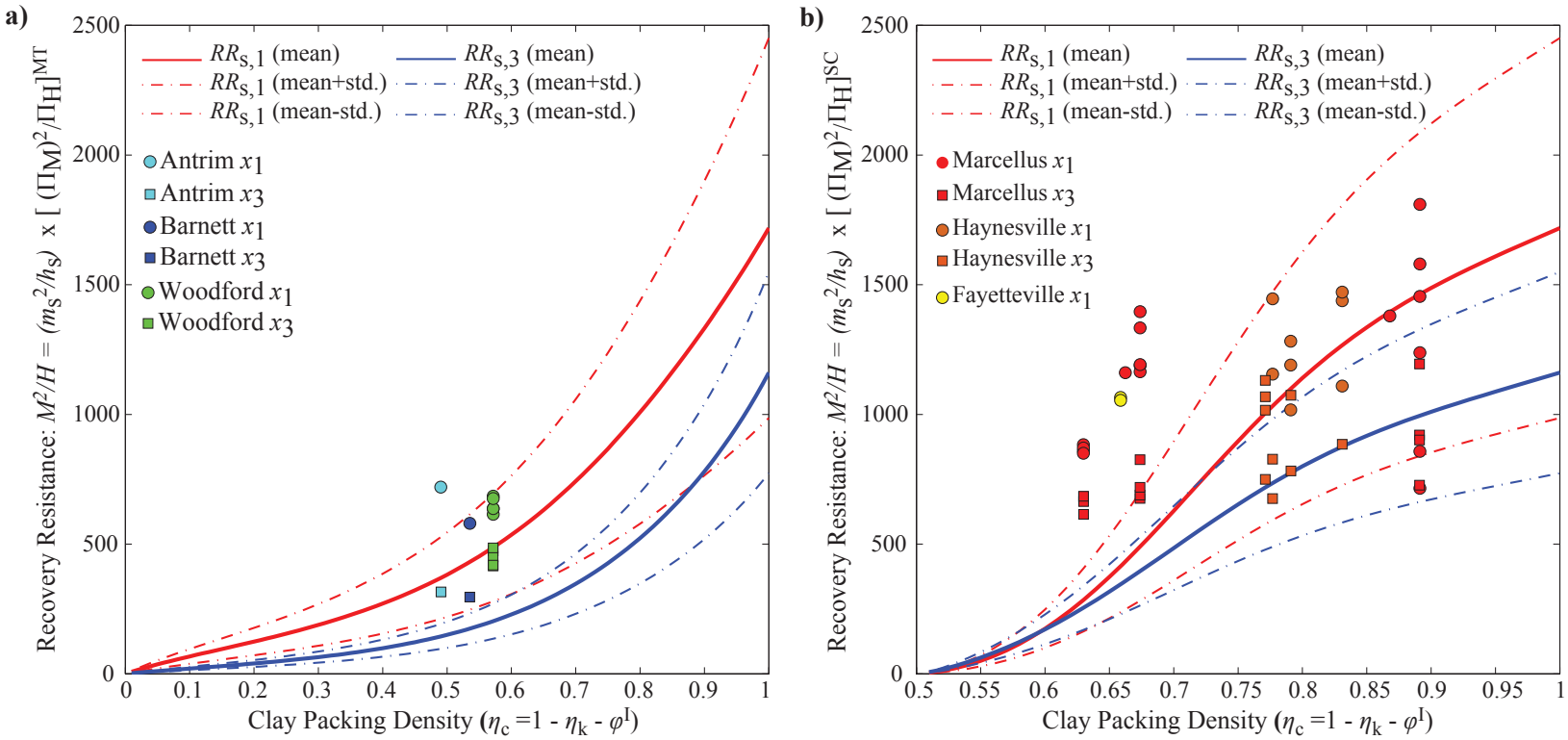

Figure 8-12: Recovery resistance curves using solid properties obtained from the back-analysis approach and microtextural models scaling relationships for a) immature and b) mature formations. Formations' data are plotted using indentation results ($\frac{M_o^2}{H_o}$).

When used in a forward approach, the predicted properties and micromechanical scaling relationships allow the construction of ductility and dissipated energy envelopes. The first predicts the deviation of the material from elastic behavior. The second predicts deformation. The energy dissipated with deformation is contained in the $\frac{M_o^2}{H_o}$ ratio, which is proportional to the recovery resistance factor, R_s, derived by Bao et al. (2004). The $\frac{M_o^2}{H_o}$ envelope indicates that the energy dissipated during a short hold-time nanoindentation test depends on the microtexture and the microstructure of the composite (level I). More plastic deformation is expected in mature formations due to their stiff kerogen.

With time-independent properties studied and deformation predicted, we investigate in Part IV the viscoelastic properties of the gas shale formations.

Part IV

Creep Properties of Gas Shale Formations: The Role of Kerogen

Chapter 9

Time-Dependent Mechanical Properties of Gas Shale Formations: Creep Rates of the Clay Composites

Studying viscous behavior of gas shale formations is important to understand and predict their performance in response to processes that disturb the stress equilibrium in the subsurface such as drilling, hydraulic fracturing (fracking), and production. These practices provide challenges in everyday production operations mainly to predict transport properties near a borehole, longevity of well production, the extent of fracture development, and reservoir compaction rates.

This part studies the time-dependent mechanical properties (M_{creep}, H_{creep}, and the contact creep modulus C) and creep behavior of the clay composites. The focus is to highlight the effect and role of organic matter driving creep behavior in source rocks at the microscale (level I) and macroscale (level II). Two hypotheses will be tested. Hypothesis II states that the organic matter drives the creep behavior within source rocks. Hypothesis III states that (three-minute) creep microindentations reflect long-time creep behavior seen at the macroscale. To test both hypotheses, three-minute creep nanoindentation (this chapter) and microindentation experiments along with creep homogenization modeling (Chapter 10) are performed and analyzed.

9.1 Introduction

This chapter reviews the theory of viscoelasticity and implements it to extract a contact creep compliance function and a contact creep modulus (C). The rate of the first describes viscoelastic behavior and accounts for plasticity taking place during loading. The second describes creep rates and is included in the clustering analysis to reveal the creep rates of the clay composites. By presenting and interpreting the creep nanoindentation results, we set the stage to test and verify Hypothesis II stating that organic matter is the driver for creep behavior. This chapter aims to answer the following:

- What are the creep kinetics at level 0 and level I?
- What are the phases that creep at the highest rates within the gas shale formations?
- How do stiffness and hardness change with viscoelastic deformations?
- What are the effect and role of organic matter driving the creep behavior?

9.2 Theory of Viscoelasticity

To use indentation creep testing to measure the viscous properties of gas shale formations, we employ the framework of viscoelasticity. Unlike either elastic materials that have the capacity to store mechanical energy without dissipating it, or Newtonian viscous fluids that have the capacity to dissipate energy without storing it, viscoelastic materials have the capacity to both dissipate energy and store it to be partially recovered later. Viscoelastic materials are characterized and studied via their response to an instantaneous change in strain or stress (e.g., a Heaviside step function). Compared to a Newtonian viscous fluid (that flows steadily in response to an instantaneous application of shear stress) and an elastic material (that undergoes instantaneous deformation that later remains constant in response to an instantaneous change in a stress state), a viscoelastic material exhibits an instantaneous elasticity and then relaxes/creeps with rates that change with time (Christensen, 1982). Therefore, in rheological models (Figure 9-1) describing time-dependent stress-strain behavior, a dashpot

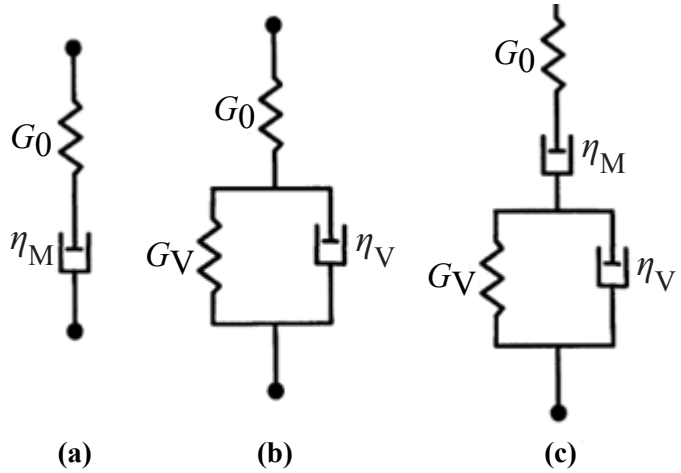

Figure 9-1: Three deviatoric creep models: a) the Maxwell model, b) the Kelvin-Voigt model, and c) Maxwell- Kelvin-Voigt model (after Vandamme, 2008). η_i has a unit of viscosity, G_i is the spring stiffness.

representing a Newtonian viscous behavior, is added to an elastic component (a string) in different combinations (Bland, 1960; Jaeger et al., 2007; Christensen, 1982).

9.2.1 Viscoelastic Stress-Strain Constitutive Laws

Viscoelastic behavior can be studied with either relaxation or creep experiments. In a relaxation experiment, the deformation is kept constant while stresses in the material relax. Creep, on the other hand, happens when a constant load is imposed and strain is allowed to evolve/increase with time. In addition to showing elastic and time-dependent behavior in response to instantaneous changes in a stress state, viscoelastic materials possess an ability to show "memory effect" to multiple loading events (Christensen, 1982); they respond not only to a current stress but also to all past stress states or history of deformation. In the linear viscoelastic theory, this is known as the Boltzmann superposition principal. For linear isotropic viscoelastic material, stress-strain constitutive relationships can be derived from (Christensen, 1982)[1]:

$$\sum_{i=0}^{i=I_1} p_i^d \frac{\partial^i}{\partial t^i} \boldsymbol{\sigma}^d(t) = \sum_{i=0}^{i=I_2} q_i^d \frac{\partial^i}{\partial t^i} 2\boldsymbol{\epsilon}^d(t) \tag{9.1}$$

[1]For a purely elastic material with a shear modulus, G_0, and bulk modulus, K_0, $I_1 = I_2 = J_1 = J_2 = 0$. $G_0 = \frac{q_0^d}{p_0^d} = \frac{E_0}{2(1+\nu_0)}$ and $K_0 = \frac{q_0^v}{p_0^v} = \frac{E_0}{3(1-2\nu_0)}$. E_0 is the Young's modulus and ν_0 is the Poisson's ratio.

$$\sum_{i=0}^{i=J_1} p_i^v \frac{\partial^i}{\partial t^i}\boldsymbol{\sigma}^v(t) = \sum_{i=0}^{i=J_2} q_i^v \frac{\partial^i}{\partial t^i} 3\boldsymbol{\epsilon}^v(t) \tag{9.2}$$

where $\boldsymbol{\sigma}^d$ and $\boldsymbol{\sigma}^v$ are, respectively, the deviator and volumetric parts of the stress tensor, $\boldsymbol{\sigma}$, ($\boldsymbol{\sigma} = \boldsymbol{\sigma}^d + \boldsymbol{\sigma}^v$). $\boldsymbol{\epsilon}^d$ and $\boldsymbol{\epsilon}^v$ are, respectively, the deviator and volumetric parts of the strain tensor, $\boldsymbol{\epsilon}$ ($\boldsymbol{\epsilon} = \boldsymbol{\epsilon}^d + \boldsymbol{\epsilon}^v$). p_i^d, p_i^v, q_i^d, and q_i^v are linear operators that describe the viscoelastic properties of the material (Lee and Radok, 1960; Vandamme and Ulm, 2006). In three dimensions (3D), Boltzmann superposition principal can be expressed in the following integral form[2]:

$$\boldsymbol{\epsilon}(t) = \int_0^t J(t-\tau)\frac{d\boldsymbol{\sigma}(\tau)}{d\tau}d\tau \tag{9.3}$$

$$\boldsymbol{\sigma}(t) = \int_0^t E(t-\tau)\frac{d\boldsymbol{\epsilon}(\tau)}{d\tau}d\tau \tag{9.4}$$

where a constant Poisson's ratio is assumed. $J(t)$ and $E(t)$ are the creep compliance and relaxation functions, respectively. These functions represent the mechanical properties describing time-dependent strain/stress responses of a linear viscoelastic material to a Heaviside input of stress/strain. The creep and relaxation functions and their first time derivatives are continuous on $0 \leq t < \infty$.

For isotropic materials, the relations generalize in terms of volumetric and deviatoric stress and strain components as follows:

$$\boldsymbol{\sigma}^v(t) = \boldsymbol{\sigma}_{mean}(t) - \frac{1}{3}(tr\boldsymbol{\sigma}.\mathbf{1}) = \int_0^t K(t-\tau)\,\frac{d\boldsymbol{\epsilon}^v(\tau)}{d\tau}d\tau \tag{9.5}$$

$$\boldsymbol{\sigma}^d(t) = S(t) = \boldsymbol{\sigma} - \boldsymbol{\sigma}^v(t) = \int_0^t 2G(t-\tau)\,\frac{d\boldsymbol{\epsilon}^d(\tau)}{d\tau}d\tau \tag{9.6}$$

$$\boldsymbol{\epsilon}^v(t) = (tr\boldsymbol{\epsilon}).\mathbf{1}) = \int_0^t J^v(t-\tau)\,\frac{\boldsymbol{\sigma}^v(\tau)}{d\tau}d\tau \tag{9.7}$$

$$\boldsymbol{\epsilon}^d(t) = e(t) = \boldsymbol{\epsilon} - \frac{1}{3}\boldsymbol{\epsilon}^v(t) = \int_0^t J^d(t-\tau)\,\frac{\boldsymbol{\sigma}^d(\tau)}{d\tau}d\tau \tag{9.8}$$

where $\mathbf{1}$ is the identity tensor, and $K(t)$ and $G(t)$ are the bulk and shear relaxation moduli, respectively. $J^v(t)$ and $J^d(t)$ are the volumetric creep and deviatoric creep compliance

[2]In 3D: $J(t-\tau)$ and $E(t-\tau)$ are replaced by 4^{th} order tensors of creep, $\mathbb{C}(t-\tau)$, and relaxation, $\mathbb{R}(t-\tau)$ functions.

functions, respectively. It is worth noting that $\boldsymbol{\sigma}_{ii}^{d}$ (or $\mathbf{S_{ii}}$)= $\boldsymbol{\epsilon}_{ii}^{d}$ (or $\mathbf{e_{ii}}$)=0.

9.2.2 Laplace Transform and the Correspondence Principle

The concept of a differential operator is used to generalize 1D model laws to 3D. Complex differential equations in 3D are solved using Laplace transforms. The Laplace transform, $\hat{u}$, of a function $u(t)$ is defined by:

$$\hat{u}(s) \equiv Lu(t) \equiv \int_0^\infty u(t)\, e^{-st} dt \tag{9.9}$$

where $\hat{u}$ is a function of the Laplace parameter, s, which is a complex number whose real part is sufficiently large to make the integral in Equation (9.9) converge (Jaeger et al., 2007). The Laplace transform of a time derivative of a function, $\dfrac{du(t)}{dt}$, is

$$L\Big\{\frac{du(t)}{dt}\Big\} \equiv \int_0^\infty \frac{du(t)}{dt}\, e^{-st} dt = s\hat{u}(s) - u(0) \tag{9.10}$$

Using Laplace transforms, a linear differential equation of a function, $u(t)$, becomes an algebraic equation in $\hat{u}(s)$ (Jaeger et al., 2007).

The correspondence principle states that if an elastic solution is known, this elastic solution remains valid in the Laplace domain using the s-multiplied transforms of the elastic properties assuming that the Laplace transforms of all time variables exist (Lee and Radok, 1960; Christensen, 1982). For instance, the Laplace transform of the indentation modulus, $M(t) = 4G(t)\dfrac{3K(t)+G(t)}{3K(t)+4G(t)}$, is (Vandamme and Ulm, 2006)

$$s\widehat{M(s)} = 4s\widehat{G(s)}\frac{3s\widehat{K(s)} + s\widehat{G(s)}}{3s\widehat{K(s)} + 4s\widehat{G(s)}} \tag{9.11}$$

$\widehat{K(s)}$ and $\widehat{G(s)}$ are the Laplace transforms of the bulk, $K(t)$, and shear, $G(t)$, relaxation moduli, respectively.

Using the Laplace transform method and the correspondence principle, the Laplace transformed viscoelastic solutions are obtained directly from the solutions of the corresponding elastic problem by simply replacing variables with their Laplace transforms. The time de-

pendency of the problem is eliminated by replacing all time-dependent moduli and properties by their Laplace transforms multiplied by the Laplace parameter, s (Equation (9.11)). Once found in the Laplace domain, solutions are transformed back into the time domain.

9.2.3 Viscoelastic Problems and Solutions

Isothermal and linear viscoelastic boundary value problems (BVP) are classified into various types based on their characteristics that simplify the means and forms of solutions (Lee and Radok, 1960; Christensen, 1982). When formulating a viscoelastic problem, the governing conditions follow from the theory of linear elasticity. The viscoelastic stress-strain relations, however, differ from the corresponding infinitesimal elasticity theory relations (Christensen, 1982). For instance, one form of the stress-strain relations given in terms of deviatoric and volumetric components is shown in Equations (9.5)-(9.8). Other forms of expressing isotropic stress-strain relations can be found in Christensen (1982). Solutions of contact boundary value problems (BVP), when considering quasi-static cases, can be obtained by special means using separation of variables. For such solutions to exist, it is usually assumed that the creep Poisson's ratio $\nu(t)$ (introduced later) is a real constant (Christensen, 1982; Vandamme et al., 2012). Also, when solving viscoelastic problems, the Laplace transform method is valid as long as the stress and displacement boundary conditions of a contact problem do not change with time. Except when using a punch, boundary conditions during an indentation tests do not remain constant as the contact area changes. With a changing contact area, the boundary conditions outside the area of contact also change. Lee and Radok (1960) addressed the limitation of the Laplace transform method and developed the method of functional equations valid for linear viscoelastic problems with time-dependent boundary conditions. Lee and Radok (1960)'s method remains valid as long as the contact area increases monotonically with time during creep. Otherwise, the contact conditions assumed during a contact problem (mainly, the indenter is in contact with the material within the area, and the material has a traction-free surface outside the area of contact) are violated. The monotonically increasing contact area condition is indeed met during the loading and hold phases of an indentation test. Despite the validity of Lee and Radok's method, its limitation was removed by Ting (1966) for "very specific load histories, indenter shapes, and material

behavior". Vandamme and Ulm (2006) extended Ting's solution to the onset of unloading. The authors used the s-multiplied Laplace transform method (formulated by Lee, 1955 and extended by Lee and Radok, 1960) with time-dependent boundary conditions and analyzed indentation tests done with axisymmetric indenters. They showed that, when indenting with a sharp indenter, the area of contact between indenter and material increases monotonically during the creep phase and keeps on doing so at the very beginning of the unloading phase. Therefore, the contact conditions of a contact problem are indeed met during the creep (hold) phase and during the very beginning of the unloading phase. That is, the correct use of the correspondence principle that underlines the validity of Equation (9.11) is ensured.

9.2.4 Contact Creep Compliance Function

We recall from Chapter 3 the Galin solution for indentation by rigid axisymmetric indenters on an elastic solid:

$$P(t) = \phi M_0 h^{1+\frac{1}{d}}(t) \tag{9.12}$$

where

$$\phi = \frac{2}{(B\sqrt{\pi})^{\frac{1}{d}}} \frac{d}{1+d} \left[\frac{\Gamma(\frac{d}{2}+\frac{1}{2})}{\Gamma(1+\frac{d}{2})} \right]^{\frac{1}{d}} \tag{9.13}$$

Here ϕ is a factor reflecting the indenter geometry and having a dimension $[\phi] = L^{1-\frac{1}{d}}$. $d \geq 0$ is the degree of the homogeneous function describing the probe geometry (d =1 for a conical indenter). B is the shape function of the indenter at unit radius (Table 9.1). $\Gamma(x)$ is the Euler Gamma function, $\Gamma(x) = \int_0^\infty t^{x-1}\, e^{-t} dt$. M_o is the instantaneous indentation modulus.

Applying the method of functional equations (Lee and Radok, 1960) to Equation (9.12), when indenting viscoelastic material, gives

$$P(t) = \phi \int_0^t M(t-\tau) \frac{dh^2(\tau)}{d\tau} d\tau \tag{9.14}$$

where $M(t)$ is the contact relaxation modulus of the indented material, and $M(t=0^+) = M_o$.

The application of the correspondence principle to Equation (9.14) gives P in the Laplace

domain:

$$\widehat{P(s)} = \phi\widehat{M(s)}\widehat{h^2(s)} \tag{9.15}$$

In this work, the basic concept underlying the linear viscoelastic theory is used to get the viscoelastic response of a material to a step load of the form

$$P(t) = P_{max}H(t) \tag{9.16}$$

$H(t)$ is the Heaviside step function. The Laplace transform of $P(t)$, as defined in the above equation, is:

$$\widehat{P(s)} = \frac{P_{max}}{s} \tag{9.17}$$

As in the case of indentation relaxation tests, applying the method of functional equations to Equation (9.12) of creep indentation tests, Vandamme (2008) derived the following depth solution for step loading:

$$l(t) \overset{\text{def}}{=} \frac{\phi}{P_{max}}h^{1+\frac{1}{d}}(t) \tag{9.18}$$

$l(t)$ is "homogeneous to a compliance" with dimension $[l] = L^{-1}$ (Vandamme, 2008; Table 9.1). The Laplace transform of $l(t)$ is:

$$\widehat{l(s)} = \frac{\phi}{P_{max}}\widehat{h^{1+\frac{1}{d}}(s)} \tag{9.19}$$

Using Equations (9.11), (9.15), and (9.19),

$$\widehat{l(s)} = s\widehat{L(s)}\frac{\widehat{P(s)}}{P_{max}} \overset{H(t)}{=} s\widehat{L(s)} \tag{9.20}$$

A link between the contact modulus in the Laplace domain and the contact creep compliance can then be established

$$\frac{1}{s\widehat{L(s)}} = s\widehat{M(s)} \tag{9.21}$$

where $\widehat{L(s)}$ is the Laplace transform of the contact creep compliance function, $L(t)$. $L(t)$ is the equivalent of $P(t)$ (Equation (9.16)) measured by creep indentation with a step load

Table 9.1: $l(t)$ for different indenter types (after Vandamme, 2008).

Indenter Type	d	B	$l(t)$
Flat Punch	$\rightarrow \infty$	$\frac{1}{a^n}$	$\frac{2a}{P_{max}}h(t)$
Spherical	2	$\frac{1}{2R}$	$\frac{4\sqrt{R}}{3P_{max}}h^{\frac{3}{2}}(t)$
Conical	1	$\cot(\theta)$	$\frac{2\tan(\theta)}{\pi P_{max}}h^2(t)$

function on a linear viscoelastic material and is given by (Vandamme and Ulm, 2009):

$$L(t) = 2\frac{a_U(t) \triangle h(t)}{P_{max}} + constant \tag{9.22}$$

Herein, $a_U(t) = \sqrt{\frac{A_c(t)}{\pi}}$ is the radius of contact between the indenter and the indented material. $\triangle h(t) = h(t) - h_0$ is the change in the indenter penetration depth measured during the hold or creep phase, and h_0 is the indenter depth at the start of the creep phase. P_{max} is the maximum load reached during a creep test, i.e., the constant load at which creep is measured.

Equation (9.22) is valid only for linear viscoelastic materials with no plastic deformation taking place during the loading and hold phases of a creep indentation test. This is not the case during indentation with sharp indenters. Due to the concentration of stresses at the indenter tip (conical indenters), plastic deformation does take place below the tip. Errors estimating the contact creep compliance and the viscous properties of the material indented are likely if the plasticity is not accounted and corrected for. To account for plasticity, Vandamme et al. (2012) designed a thought experiment consisting of loading-unloading-reloading-creep cycles. They report that plastic deformation and build-up of residual stresses occur after the loading-unloading cycle. They argue that residual stresses cause only an offset in the indenter displacement without affecting the indenter penetration rates during the reloading-creep cycle. Vandamme et al. (2012) then treat the reloading-creep cycle as

a linear viscoelastic indentation on a deformed, non-flat surface. The reloading-creep cycle, in the absence of residual stresses, becomes simply an investigation of elastic indentation on material surface of unknown shape using an indenter of known geometry. This investigation is analogous to studying creep indentation on a flat surface using an indenter of unknown geometry ($a_U = f(h)$). For such an indenter, the BASh formula (Equation (3.24)), relating the slope of the unloading phase to the elastic modulus and indenter-material contact area, can be written as follows:

$$S = \frac{dP}{dh} = 2M_0\, f(h) \tag{9.23}$$

and the load becomes

$$P = 2M_0\, F(h) \tag{9.24}$$

where $F(h)$ is the primitive of $f(h)$. The contact creep compliance and contact creep compliance rate are, respectively (Vandamme, 2008; Vandamme and Ulm, 2013):

$$L(t) = 2\frac{F(h(t))}{P_{max}} \tag{9.25}$$

$$\dot{L}(t) = \frac{d}{dt}\Big(\frac{2F(h)}{P_{max}}\Big) = \frac{2f(t)\dot{h}(t)}{P_{max}} = \frac{2a_U(t)\dot{h}(t)}{P_{max}} \tag{9.26}$$

Using finite element modeling, Vandamme et al. (2012) show that results given by Equation (9.26) are independent of any plasticity taking place during loading but do not correct or account for plasticity taking place during the creep phase (Vandamme, 2008; Vandamme et al., 2012). They show that, despite a localized plasticity when using a Berkovich indenter, Equation (9.26) overestimates the contact creep compliance rate. The overestimate can reach up to 36% in material with $M_o/H_o \approx 51$. To reduce the error given using Expression (9.26), Vandamme et al. (2012) suggest shortening the creep phase duration so that changes in the contact radius during creep remain within 10%. Such a negligible increase in the contact area during creep translates into writing $a_U(t) \approx a_U$ and reduces the overestimate in $\dot{L}(t)$ to only 10%[3].

[3]Vandamme et al. (2012) then argue that a 10% overestimate $\dot{L}(t)$ balances the error introduced by not correcting the BASh formula, accounting for radial displacement of the surface and pile-up effect when using conical indenters (Section 3.4.1).

9.3 Mechanical Properties from Creep Indentation

In order to use an indentation test to measure creep behavior and mechanical properties, Vandamme and Ulm (2006) and Vandamme (2008) showed that the method of functional equations remains valid at the very beginning of the unloading phase. Vandamme and Ulm (2006) and Vandamme (2008) estimated the effect of viscous properties on the initial slope of the unloading curve, or creep contact stiffness, $S_U = \frac{dP}{dh} \mid_{h=h_{max}}$. They showed that S_U differs from the elastic contact stiffness ($S = \frac{2}{\sqrt{\pi}} M_o \sqrt{A_c}$; M_o is the instantaneous elastic indentation modulus), and, applying Laplace transforms to the Galin-Sneddon solution, the viscoelastic and elastic contact stiffnesses are related by (Feng and Ngan, 2002):

$$\frac{1}{S} = \frac{1}{S_U} + \frac{\dot{h}_H}{|\dot{P}|} \tag{9.27}$$

where $\dot{h}_H$ is the rate of indentation at the end of the holding phase and $\dot{P}$ is the unloading rate.

9.3.1 Creep Indentation Modulus

Equation (9.27) shows that viscous deformation during unloading leads to underestimating the elastic contact compliance ($\frac{1}{S} \leq \frac{1}{S_U}$). Viscoelasticity can also affect the determination of the projected contact area. Thus, applying the BASH formula using S_U and/or a wrong contact area calculation can lead to overestimating the stiffness modulus. In addition to viscous effects, plasticity also takes place during the loading and holding phases as discussed in Section 9.2.4.

Two ways were suggested by Vandamme and Ulm (2006) and Vandamme (2008) to address inaccuracies calculating S_U and lead to design of a creep indentation test that minimizes viscous effects (Figure 9-2). First, increasing the unloading rate $\dot{P}$ (i.e., decreasing the unloading time) minimizes viscous effects. The unloading curve can be used to calculate S_U and the area of contact. Second, increasing the hold-phase duration decreases $\dot{h}_H$ at the end

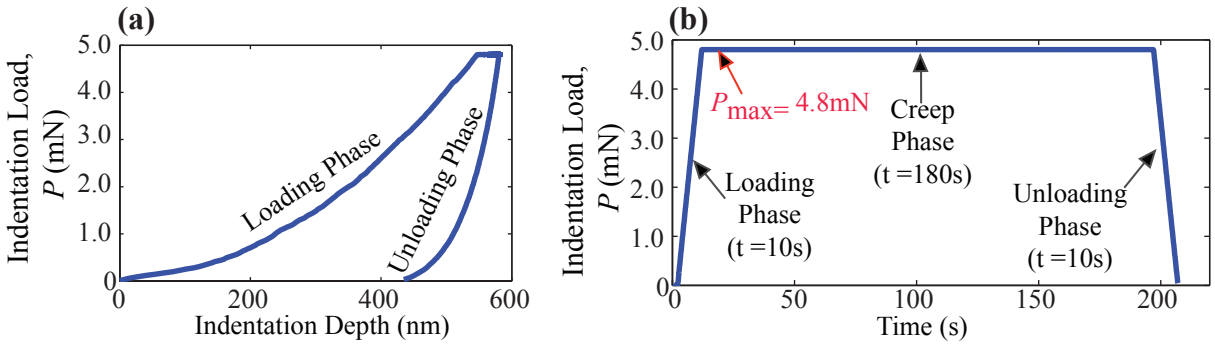

Figure 9-2: a) The load-displacement curve of a creep nanoindentation test. b) The load-time profile of the same creep nanoindentation test in (a) showing the duration of the different phases. The maximum load, P_{max}, reached in this example is 4.8 mN. Some creep microindentation tests conducted had load reaching up to 50 mN. (The test shown is done using the Hysitron machine that adds a 5 s for drift correction at the beginning of the creep phase).

of the holding phase[4].

With the above guidelines to account for both viscous and plasticity effects, Vandamme and Ulm (2006) and Vandamme (2008) recommended a creep indentation test with 1) an infinitely "fast" loading phase; 2) a hold phase short enough so that changes in the area of contact during creep remain within 10%, but "long enough" to measure creep behavior and record enough decrease in creep rates with time; and 3) a fast unloading phase so that the unloading time is much smaller than the relaxation time unit in both a Maxwell and a combined Maxwell-Kelvin-Voigt models (Figure 9-1; Vandamme and Ulm, 2006). In fact, Chudoba and Richter (2001) reported, from creep indentation on metals, that the errors in determining the modulus can be neglected if the hold time is at least 45 s long. The advantage of a long creep phase is that it also reduces the effect of thermal drift. The latter becomes negligible when the duration of the test from start to the onset of unloading, t_h, is much larger than the duration of the unloading phase, t_U (Feng and Ngan, 2002).

As with elasto-plastic cases, a difference between the loading and unloading curves (Figure 9-2a) exists when we indent cohesive-frictional viscoelastic material; this difference indicates a loss in the self-similarity of the indentation test (Section 3.3). As a result, the loading and unloading phases no longer depend on the same parameters, and the projected area depends on material behavior (Section 3.3). Assuming no viscous effect in a fast loading

[4]In solid materials, creep rates decrease with time to less than 1 nm/sec after few seconds of creep (Chudoba and Richter, 2001).

creep test in elasto-plastic material, dimensional analysis of the contact area during loading yields (Vandamme, 2008):

$$Ac = f(M_o, \nu, \mu, c, h, B) \tag{9.28}$$

The area of contact at the end of the creep phase depends on the plastic and viscous deformations that take place during the creep phase, and thus:

$$Ac(t) = f(L(t), \sigma_y, \nu, \mu, c, h_{max}, B) \tag{9.29}$$

With the right creep test design, the term $\frac{\dot{h}_H}{|\dot{P}|}$ in Equation (9.27) can be neglected as it approaches zero, and $\frac{S_U}{S} \approx 1$. Also, assuming that the contact area during the creep phase changes minimally, one can write, using the BASh formula:

$$M_{creep} = M_o \frac{S_U}{S} \sqrt{\frac{A_c}{A_c(t)}} \approx M_o \sqrt{\frac{A_c}{A_c(1+x)}} = \gamma \times M_o \tag{9.30}$$

where x is the change, in percentage, of the contact area during the creep phase.

9.3.2 Creep Indentation Hardness

The indentation hardness measured from creep indentation tests is defined as:

$$H_{creep} = \frac{P_{max}}{A_c(t)} \tag{9.31}$$

where P_{max} is the maximum load reached during the creep indentation tests and the load at which the creep is measured. $A_c(t)$ is the contact area measured at the end of the creep phase.

As with the indentation modulus, hardness, H_{creep}, is also affected by the duration of the hold-phase (Figure 9-3) of an indentation test. Short hold-time indentation tests give a hardness that represents strength properties. During the hold-phase of creep indentation tests, the contact area keeps increasing at constant load, leading to a decrease in the creep indentation hardness, H_{creep}. H_{creep} represents the material after both plastic and viscous

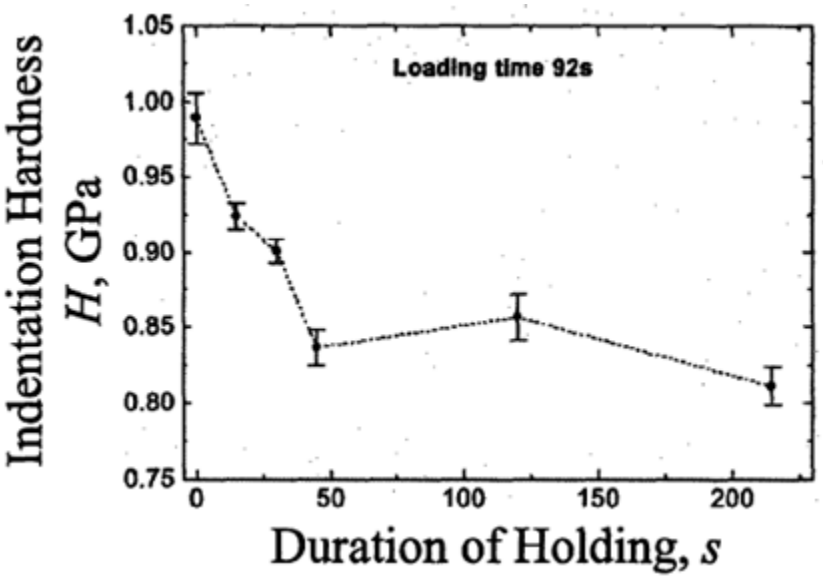

Figure 9-3: Indentation hardness variations with the duration of the hold-phase of an indentation test (after Chudoba and Richter, 2001).

deformations occur. Using Equation (9.31), one can write:

$$H_{creep} = \frac{A_c}{A_c(t)} \times H_o = \gamma^2 \times H_o \tag{9.32}$$

9.4 Creep Nanoindentation Tests

Throughout this work, the creep test protocol designed and tested by Vandamme and Ulm (2006) and Vandamme (2008) for cement is adopted. The loading and unloading phases are 10 s each (as in short-hold time indentations; Chapter 6). The hold-time, or creep phase, is three minutes long (Figure 9-2). As discussed in Section 9.3.1, this creep indentation protocol minimizes thermal drift (as $t_h = 10s + 180s > t_U$) and viscous effects during unloading. The creep behavior is measured at $P_{max} = 4.8$ mN. Indentations with bad indenter-material contact, bad fit (noisy experimental data), and/or fits showing a decrease in creep rates with time (due to bad drift correction) are eliminated. A creep grid is referred to by appending the following to its name: the name of the formation (Mar=Marcellus, A=Haynesville, etc.), directions of indentation (x_1 = parallel to bedding planes, x_3 = perpendicular to bedding

planes), "cg" designating a creep indentation grid, and a grid number to differentiate multiple creep grids performed on the same sample surface. For example, grid A5Hx_1-cg1 is the first creep grid performed parallel to bedding planes on Haynesville sample A5H. Creep nanoindentation tests were acquired mainly using the Hysitron triboIndenter (Hysitron, 2011). Using the Hysitron, depth is inferred, and the creep properties are determined assuming linear viscoelastic material. Corrections were applied to the Hysitron creep nanoindentation data to account for such simplistic viscoelastic model assumptions. All Hysitron data reported in this chapter are corrected as detailed in Appendix B. A few creep nanoindentation grids were done using the Ultra Nanoindentation Tester (UNHT) (CSM-Instrument, 2013), which measures depths.

9.5 Creep Nanoindentation Test Results

Our objectives presenting and interpreting the creep nanoindentation results are to achieve the following goals:

1. Determine the creep kinetics and rates at the nanoscale (level 0) and microscale (level I),

2. Reveal the phases, in the gas shale formations, that creep with the highest rates,

3. Show changes in elasticity and hardness with a longer hold-phase nanoindentations in the clay composites. This is done by comparing elasticity and hardness from creep indentations (M_{creep} and H_{creep}) to those obtained from short hold-time nanoindentation tests (M_o and H_o),

4. Identify functional relationships between mechanical properties (M_{creep} and H_{creep}),

5. Show changes in anisotropy in the mechanical response due to viscous deformation, and

6. Highlight the effect of the organic content and maturity on viscoelastic behavior and their role driving creep behavior.

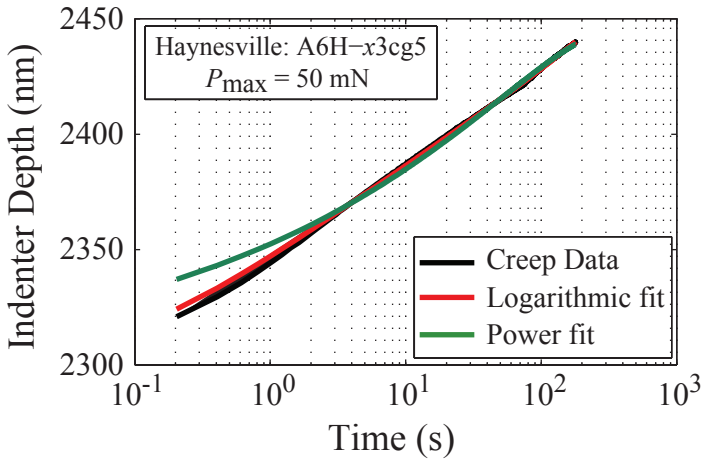

Figure 9-4: Depth variation during the creep phase of a creep microindentation test (black curve) and logarithmic (red) and power fit (green) functions. Data are obtained from creep microindentation performed with $P_{max} = 50$ mN on a Haynesville sample.

9.5.1 Logarithmic Creep Behavior

The change in depth during the creep phase can be fit with either a power or a logarithmic function, both of which fit the experimental curves adequately (Figure 9-4). In the case of a power fit of the form:

$$\triangle h(t) = h(t) - h_0 = \alpha t^{\beta} + \gamma t + \delta \tag{9.33}$$

the power exponent obtained from creep nanoindentation tests falling in the organic-rich clay composites was $\beta = 0.293 \pm 0.044$ in immature Antrim (e.g., Antrim-$x_1$cg1) and $\beta = 0.220 \pm 0.027$ in overmature Marcellus (e.g., Marcellus3-$x_1$cg2). Similarly, fitting Equation (9.33) to creep microindentation data (e.g., Haynesville2-$x_3$cg5 performed with $P_{max} = 50$ mN; Figure 9-4) gave $\beta = 0.221 \pm 0.061$. At even a larger scale, Sone (2012) used a power fit function of the form $J(t) = Bt^n$ to creep data obtained from triaxial creep tests on Barnett-2H and Haynesville-1V core plugs. He reported a power exponent $n = 0.009$ and $n = 0.046$, respectively. Such small values for the power exponent at various scales suggest that a logarithmic creep reflects better the viscous behavior of the gas shale formations. Using the Matlab's non-linear least-square solver, the creep phase depth-time $(h - t)$ data, isolated in every creep nanoindentation test (Figure 9-5), are fit to a normal log function (red fitting

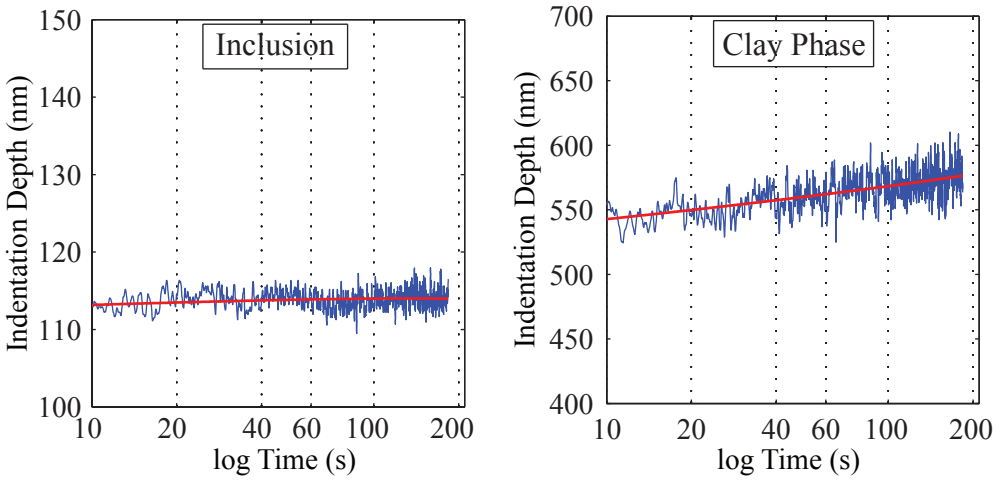

Figure 9-5: Creep phase (blue curves) isolated in creep tests on an inclusion (left) and a clay phase (right). P_{max} reached in the example shown is 4.8 mN. The red curves are logarithmic functions fitted to experimental data. We note the total indentation depth reached in an inclusion vs. a clay composite and the negligible depth variation during creep in the inclusion. The small depth variation reflects slow creep rates compared to higher creep rates seen in the clay composites.

curves in Figure 9-5) of the form (Vandamme and Ulm, 2013):

$$\triangle h(t) = h(t) - h_0 = x_1 \ln(x_2 t + 1) + x_3 t + x_4 \tag{9.34}$$

where h_0 is the depth reached during the loading phase (first 10 s of the test). The fitting parameters x_1,..., x_4 are determined by the regression fit; x_3 and x_4 are not related to material properties. The ratio $(\frac{1}{x_2})$ is the characteristic viscous time of creep behavior. Values of $\frac{1}{x_2}$ are much smaller than the duration of the creep phase. For instance, the characteristic time in A5H-$x_1$cg1 is 1.44 s $\pm$ 1.03 s (Figure 9-6).

9.5.2 The Contact Creep Modulus

The logarithmic time-dependence of the creep behavior implies that the long-term creep compliance rate is proportional to the inverse of time ($\dot{L}(t) \propto \frac{1}{t}$). Vandamme and Ulm

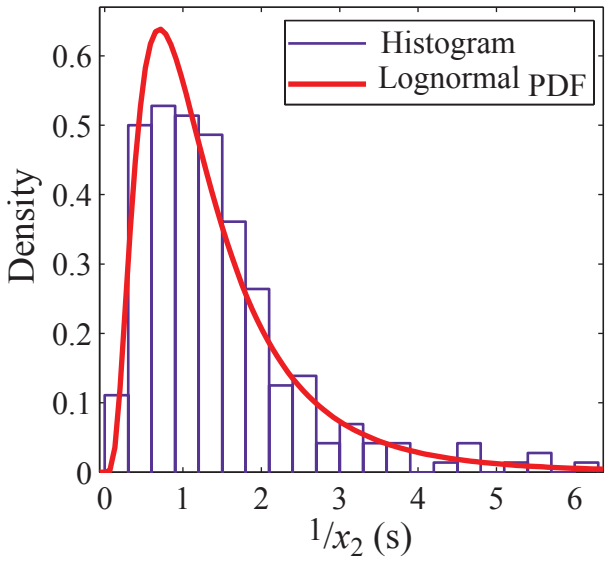

Figure 9-6: The distribution of the characteristic viscous time data, $\frac{1}{x_2}$, from creep nanoindentation tests performed in the clay phase of Haynesville sample A5H-$x_1$cg1.

(2013) showed that $\dot{L}(t)$ is given by:

$$\dot{L}(t) = 2\frac{a_U(t)\dot{h}(t)}{P_{max}} = \frac{1}{Ct} \tag{9.35}$$

where C is the contact creep modulus. C represents the long-term creep behavior of the material and reflects its creep rate. It is related to the fitting parameter, x_1, obtained from the fit in Equation (9.34) as follows (Vandamme and Ulm, 2013):

$$C = \frac{P_{max}}{2a_U(t)x_1} \tag{9.36}$$

The contact creep modulus is an additional mechanical parameter that will be used to isolate clay composites, using clustering analysis, revealing their long-term creep behavior. Including C in clustering analysis provides the creep rates of the clay composites.

9.5.3 Contact Creep Modulus of Clay Composites Constituents (Level 0)

To better interpret and understand the creep rates of the clay composites (level I), we first investigate the creep rates of their constituents: the organic matter and clay particles. Only samples with high mature organic content (pyrobitumen and shungite) were available to indent. These will be used as a proxy to study the creep rates of mature kerogen.

9.5.3.1 Contact Creep Modulus of Porous Organic Matter

Pyrobitumen and shungite samples were investigated. Due to their small sample size and the scarcity of the material available, the organic samples were indented without surface polishing. Small indentation grids (5×5 and 8×8) were performed on visually selected flat areas. In contrast to the composite investigation, no EDS could be performed on the grid areas, as the indentation imprints could not be located with a scanning electron microscope (SEM) due to the sample's surface conditions and/or image low intensity (abundance of carbon). Consequently, no chemo-mechanical data coupling was done, and the clustering analysis used only mechanical data (M_{creep}, H_{creep}, and C) as input. Various clusters with different mechanical properties were identified in the pyrobitumen (Figures 9-7; Table 9.2) and shungite samples (Figure 9-8; Table 9.3). These results indicate the presence of phases other than just organic matter in both samples.

Table 9.2: Elastic moduli (M_{creep}), hardness (H_{creep}), contact creep moduli (C), and total penetration depths (h_{creep}) reached in the various phases isolated in the pyrobitumen sample with mechanical clustering analysis. Creep nanoindentation data are acquired at $P_{max} = 4.8$ mN. μ = mean value and σ = standard deviation.

	H_{creep} (GPa)		M_{creep} (GPa)		C (GPa)		h_{creep} (nm)	
	μ	σ	μ	σ	μ	σ	μ	σ
Phase 1	0.07	0.04	3.77	1.48	26.40	15.65	2,082.92	935.76
Phase 2	0.18	0.06	6.42	1.43	84.80	36.87	1,078.10	187.10
Phase 3	0.43	0.15	10.18	2.62	215.14	111.68	677.65	116.28
Phase 4	0.78	0.28	13.43	4.21	517.92	231.97	514.93	116.97

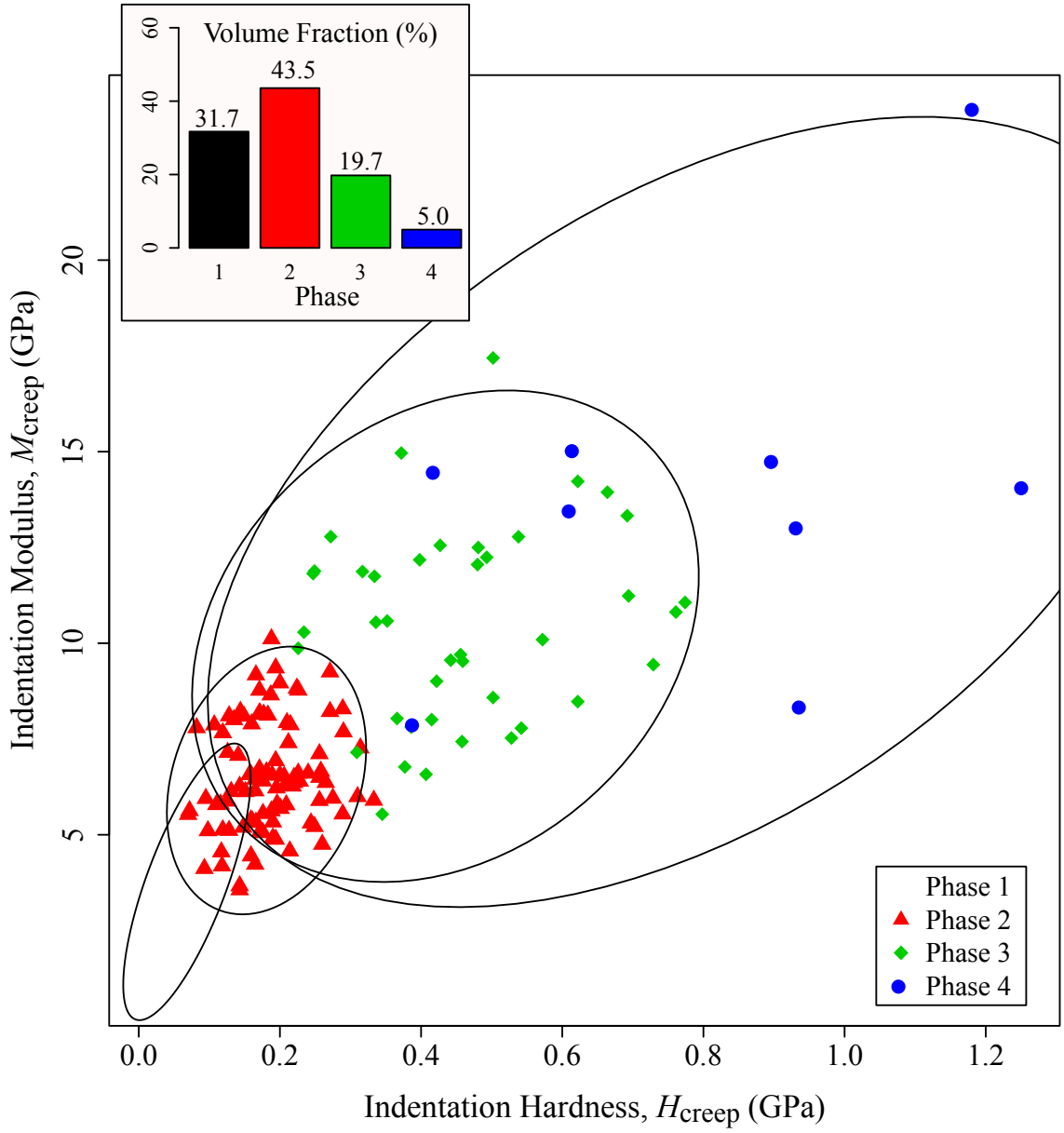

(a)

Figure 9-7: Clustering analysis results from pyrobitumen creep nanoindentation data. Inputs to clustering analysis are M_{creep}, H_{creep}, and C. (a) The M_{creep}-H_{creep} plot shows a top view of the Gaussian distributions (ellipses) of the various phases. The inset shows the volumes fractions of the various phases in the indentation grid area.

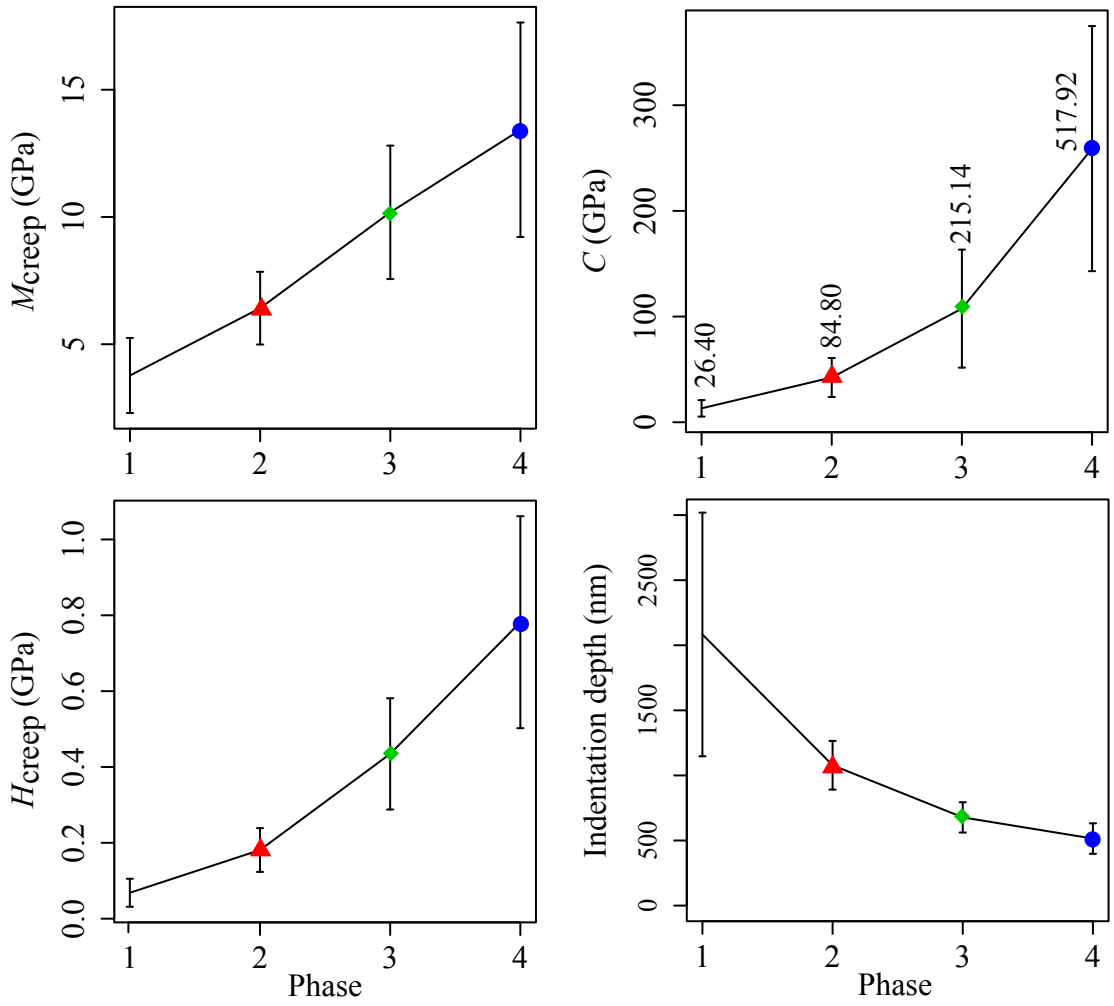

(b)

Figure 9-7: (Cont'd) (b) Plots of the mechanical properties of the various phases identified in the pyrobitumen sample and the final indentation depth reached in each. Note that Phases 1 and 2, which are organic-rich, have the highest creep rates (lowest C).

Table 9.3: Elastic moduli (M_{creep}), hardness (H_{creep}), contact creep moduli (C), and total penetration depths (h_{creep}) reached in the various phases isolated in the shungite sample with mechanical clustering analysis. Creep nanoindentation data are acquired at $P_{max} = 4.8$ mN. μ = mean value and σ = standard deviation.

	H_{creep} (GPa)		M_{creep} (GPa)		C (GPa)		h_{creep} (nm)	
	μ	σ	μ	σ	μ	σ	μ	σ
Phase 1	0.10	0.05	7.03	2.42	21.79	12.91	1,493.93	469.80
Phase 2	0.36	0.16	14.85	7.18	91.50	51.19	768.40	184.85
Phase 3	0.89	0.33	21.08	5.86	356.24	215.06	470.78	84.85

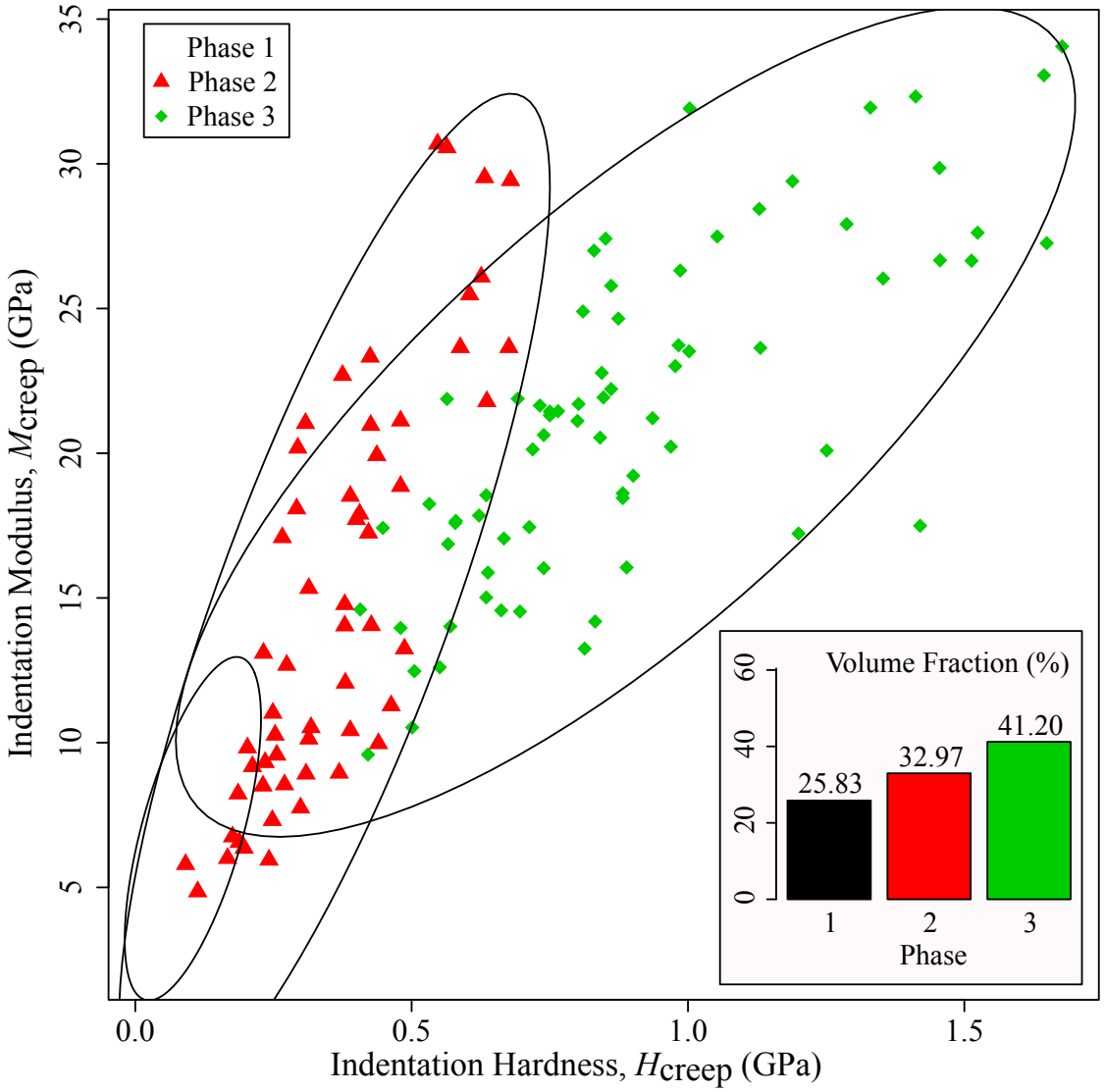

(a)

Figure 9-8: Clustering analysis results from shungite creep nanoindentation data. Inputs to clustering analysis are M_{creep}, H_{creep}, and C. (a) The M_{creep}-H_{creep} plot shows a top view of the Gaussian distributions (ellipses) of the various phases. The inset shows the volumes fractions of the various phases in the indentation grid area.

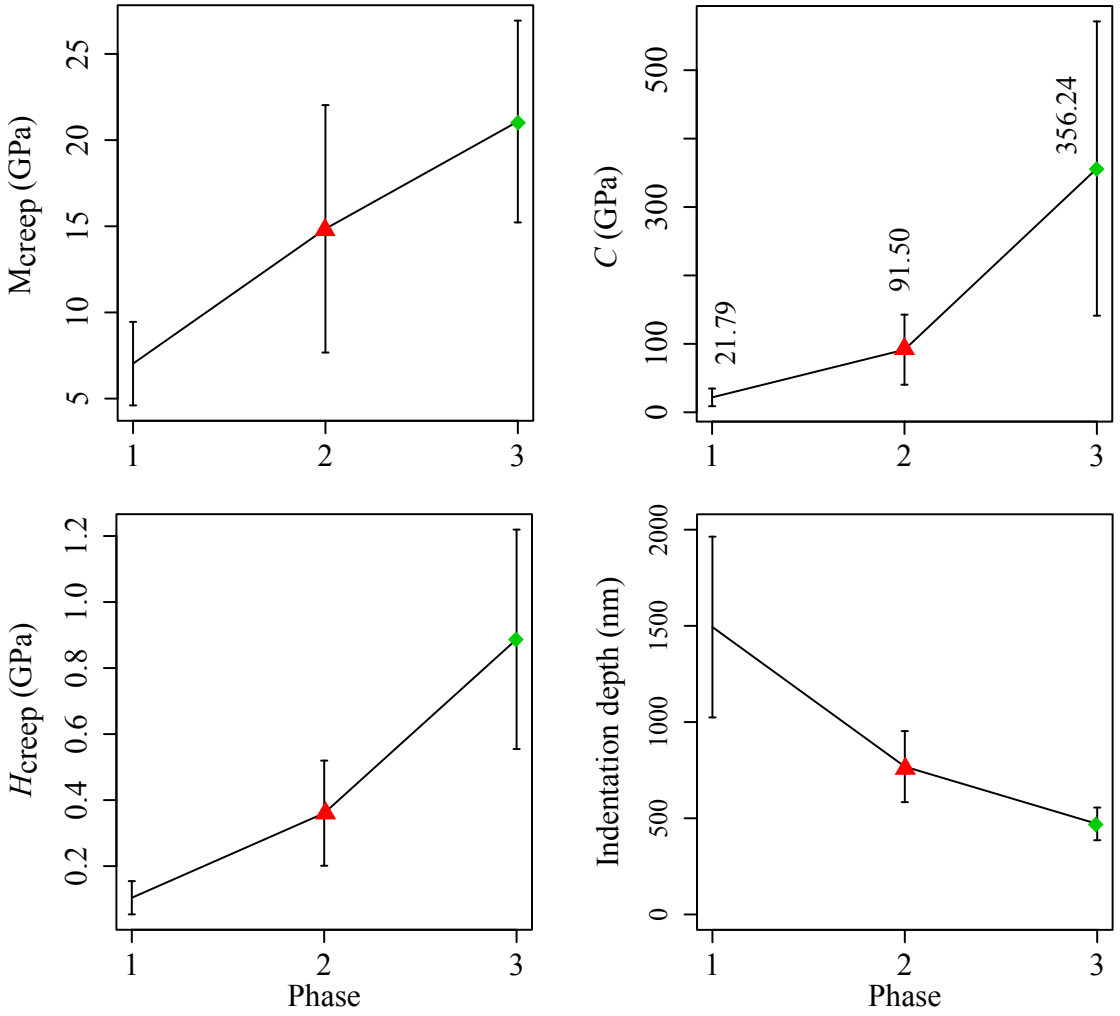

(b)

Figure 9-8: (Cont'd) (b) Plots of the mechanical properties of the various phases identified in the shungite sample and the final indentation depth reached in each. Note that Phases 1 and 2 have the highest creep rates (lowest C).

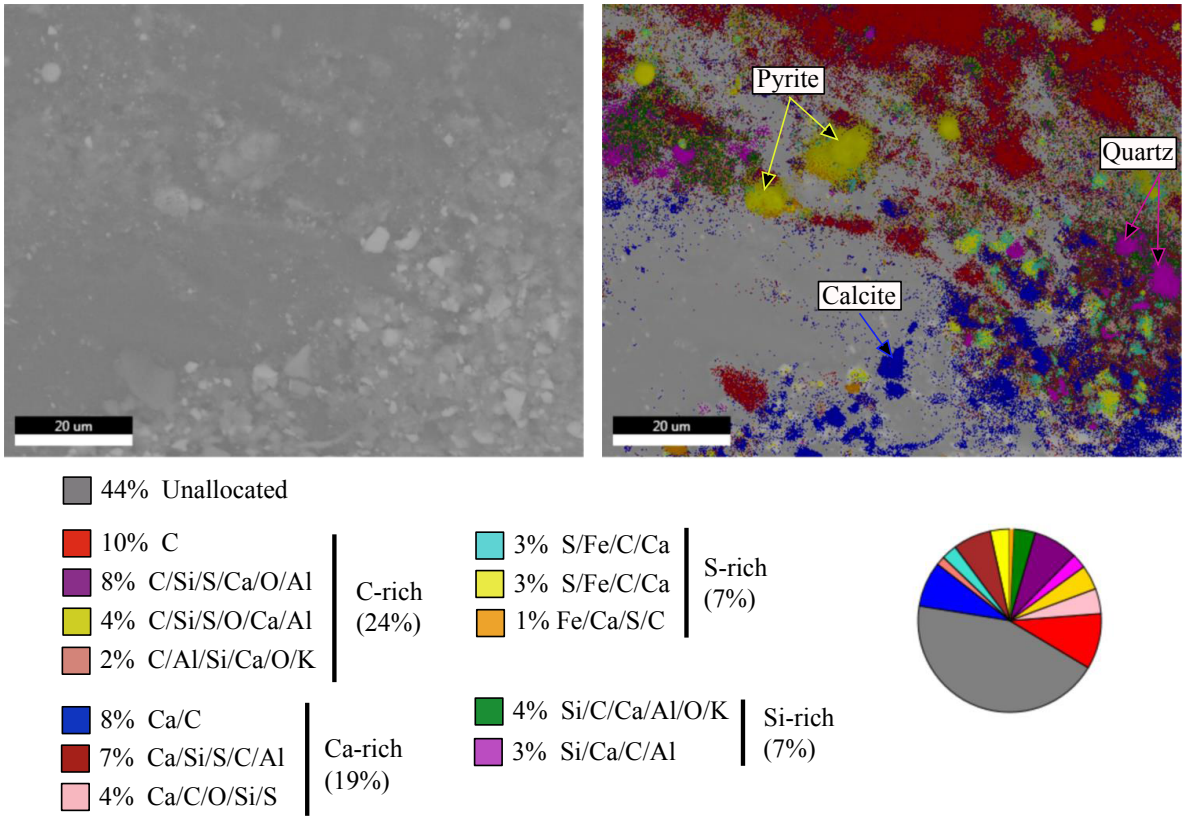

Figure 9-9: A phase map (right) obtained using the TEAM EDAX software analyzing the K-line emission EDX data from a randomly chosen area (left) on the pyrobitumen sample. The phase map shows the various phases making the analyzed area. For an interpretation of the "unallocated" phase, refer to text and the phase spectrum (Figure 10-4).

Pursuant EDS elemental maps were acquired over random areas from the pyrobitumen and shungite samples. The TEAM EDS Analysis System (Figure 9-9) was used to analyze the EDS elemental maps from the pyrobitumen sample. The phase map shows that the pyrobitumen sample is a multi-phase "rock-like" sample that is rich in organic matter. The area coverage of each chemical phase (number of pixels) reflects the volume fractions of the phase in the sample. We infer that the pyrobitumen sample contains 24% carbon-rich phases, 19% calcium-rich phases, 7% sulfur-rich phases, and 7% silicon-rich phases. These phases are interpreted to represent an organic-rich phase, calcite, pyrite, and quartz, respectively. The SEM image in Figure 9-9 shows a low intensity region (grey area) covering 44% of the image area. This region is interpreted as a chemically "unallocated" phase. A closer look at the phase elemental analysis of the unallocated (Table 9.4) and

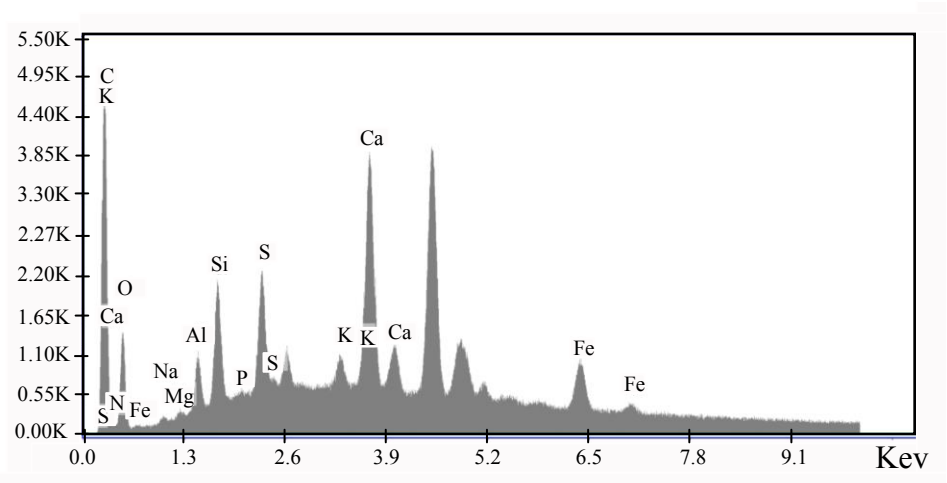

Figure 9-10: The K-line spectrum of the unallocated phase in Figure 9-9 revealing that it is carbon-rich with some inorganic impurities, mainly calcite. The phase is interpreted to be an organic phase.

spectrum (Figure 9-10) shows that it is carbon-rich with ∼16 wt.% calcium, assumed to be coming from calcite. The phase is, thus, interpreted to be kerogen-dominated with inorganic impurities. We keep these impurities in mind for the following analysis of the clusters based on their mechanical property. The volume fractions of the mechanical clusters

Table 9.4: The TEAM EDS Analysis (K-line emission) of the unallocated phase in Figure 8-16. The K ratio is the ratio of intensities from the Kα and Kβ lines (K indicates the shell whose electrons interacted with the SEM electron beam. α and β indicate groups to which a line belongs). Z, A, and F stand for corrections for atomic number effects, absorption, and fluorescence, respectively).

Element	Weight %	Atomic %	Error	K ratio	Z	A	F
C	50.89	68.34	7.14	0.23	1.06	0.43	1.00
O	20.67	20.84	11.12	0.03	1.02	0.13	1.00
Si	0.98	0.56	9.21	0.01	0.93	0.78	1.01
S	2.19	1.10	5.37	0.02	0.91	0.93	1.02
K	0.65	0.27	16.40	0.01	0.86	1.00	1.09
Ca	15.65	6.30	2.12	0.14	0.87	1.01	1.01
Fe	8.98	2.59	4.88	0.07	0.78	1.00	1.00

(inset in Figure 9-7a) are consistent with the chemical phase volume fractions from the EDS phase map (Figure 9-9). This consistency leads us to a chemical description of the various mechanical clusters in the pyrobitumen sample: Phases 1, 2, 3, and 4 (Figure 9-9) are,

respectively, a highly-porous kerogen phase with low/negligible mineral impurities, a porous kerogen with inorganic impurities, a mixture phase (containing pyrite), and an inclusion (quartz) phase. EDS on the shungite sample was acquired with an SEM without the TEAM software or capability for phase analysis. Nevertheless, the results of the clustering analysis of the shungite's mechanical data (Figure 9-8) also suggest a rock-like texture and are consistent with those obtained in pyrobitumen (Figure 9-7). EDS maps of Shungite indicate the presence of Si, Ca, and S.

Clustering analyses of the pyrobitumen and shungite mechanical data show that organic-dominated phases (Phases 1 and 2 in Figures 9-7 and 9-8) exhibit the highest creep rates. We choose Phase 2 in both samples to represent the mechanical properties of mature porous organic matter in the clay composite for the following two reasons:

- Elastic moduli of 5.9 GPa and 11.9 GPa were obtained by nanoindenting kerogen in the Bazhenov (R_o = 0.78) and Lockatong (R_o = 2.58) Formations, respectively, by Ahmadov et al. (2009). Similarly, Kumar et al. (2012) reported a modulus of 5-6 GPa obtained by indenting kerogen in Woodford and Kimmeridge Formations. The elastic modulus of Phase 2 in both pyrobitumen and shungite samples is comparable to the elastic moduli reported by Ahmadov et al. (2009) and Kumar et al. (2012).

- Mechanical polishing can pluck material (e.g., clay particles), causing high apparent porosity. Indents with very low elastic moduli and very high depths are more likely to be caused by mechanical polishing than by materials creeping at unreasonably high rates. Also, if we remember that the organic samples could not be polished before indentations, high indentation depths and high creep rates of Phase 1 in both the pyrobitumen and shungite samples are very likely to be effects of surface roughness.

Therefore, Phase 2 in pyrobitumen, the organic-rich sample which is properly analyzed with EDS, is taken to represent porous organic matter. From this analysis, we thus retain a contact creep modulus of C^k = 80 GPa in what follows. We note that no immature organic-matter was available to test and compare to creep rate values obtained for pyrobitumen.

Table 9.5: Mechanical data from creep indentation tests performed on muscovite. Indentations were performed parallel to sheet structure at 2 different maximum loads.

	H_{creep} (GPa)		M_{creep} (GPa)		C^* (GPa)		h_{creep} (nm)	
	μ	σ	μ	σ	μ	σ	μ	σ
Musc. x_1cg1**	6.13	1.01	97.85	7.78	5,455	2,341	165.67	29.43
Musc. x_1cg2***	5.80	0.88	97.31	6.91	2,386	1,049	301.93	25.36

*The Hysitron creep data are corrected following the approach detailed in Appendix B.

**Creep grid 1 is done with $P_{max} = 4.8$ mN and consists of 347 indentation tests.

***Creep grid 2 is done with $P_{max} = 10.0$ mN and consists of 231 indentation tests.

9.5.3.2 Contact Creep Modulus of Muscovite

Creep indentations at two different maximum load levels, P_{max}, parallel to muscovite sheets provided values for the contact creep modulus of this clay mineral. The contact creep modulus of muscovite is found to be two orders of magnitude greater than that of porous organic matter (Table 9.5; Figure 9-11). Creep nanoindentation with a load of 4.8 mN gives $C =$ 5,455 GPa. We acknowledge that indenting muscovite minerals masks the effect of primary porosity, which is trapped among clay particles and expected to increase creep rates (reduce the value of C).

9.5.3.3 Contact Creep Modulus of Synthetic Clay Samples

Unfortunately, no organic-free, natural, and highly packed (4-9% porosity) clay sample was available for indentation to check the effect of porosities on creep rates of clay aggregates. Instead, consolidated clay samples (illite sample with 30% porosity consolidated by Taylor Nordquist, and a Na-montmorillonite (SWy-2) sample with porosity $> 40\%$), and a polycrystalline non-cohesive talc sample (courtesy of Dr. Jeremy Berthonneau, MIT) with predicted porosity of 30%[5] were indented. Results of creep nanoindentation tests on the polycrystalline

[5]Porosity calculation is courtesy of Dr. Christian Hoover. Porosity was predicted using a 1-phase textural model back-analyzing mechanical data acquired performing nanoindentation tests with hold-time duration of 30 s.

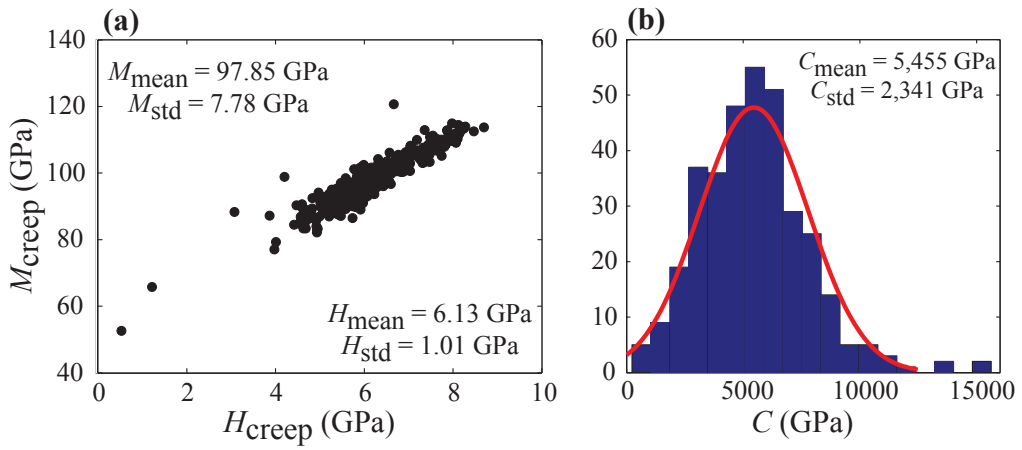

Figure 9-11: Creep nanoindentation results from muscovite-x_1cg1 performed with P_{max} = 4.8 mN. a) A plot of modulus vs. hardness. b) A histogram (blue bars) and probability distribution function (red curve) of the contact creep modulus data.

samples are reported in Table 9.6. The results from the polycrystalline samples show that they have very low contact creep moduli ascribed to low cohesion[6] and, unrealistically, high porosities (30%). The samples, therefore, are a poor choice of material to consider as a proxy for non-organic shale formations (caprocks); the samples do not reveal the effect of clay particle aggregation and realistic porosity values on creep behavior in organic-free rocks. The effect of 4-8% porosity trapped among the clay particles on creep behavior can, therefore, be assessed only by studying the creep behavior of the clay composites in the gas shale formations. A homogenized response, combining the effect of all the constituents (porosity, organic matter, and clay particles) on the creep behavior appears next.

[6]The consolidated samples were easily leaving streaks on the polishing pads.

Table 9.6: Mechanical data from creep nanoindentation tests performed on polycrystalline talc and consolidated clay samples. Creep indentation acquired at $P_{max} = 4.8$ mN.

	H_{creep} (GPa)		M_{creep} (GPa)		C^* (GPa)		h_{creep} (nm)	
	μ	σ	μ	σ	μ	σ	μ	σ
Polycryst. Talc**	0.19	0.10	19.29	7.45	96.68	62.72	1,092.08	354.25
SWy-2 cg1***	0.09	0.09	6.53	2.04	29.83	21.57	1,361.74	251.20
SWy-2 cg2	0.19	0.10	9.68	2.90	70.11	44.06	1,103.55	443.13
Illite cg1 ****	0.13	0.26	4.53	3.30	37.80	36.20	1,846.83	753.22

*The Hysitron creep data are corrected following approach detailed in Appendix B.

**220 indentation creep tests were performed on talc. Backanalysis of M_o and H_o (short hold-time indentation tests; courtesy of Dr. Christian Hoover and Dr. Jeremy Berthonneau) gives an average porosity of 30%.

***Na-Montmorillonite from the Cretaceous New Castle formation, Wyoming. The sample is 5-10% quartz, consolidated, and subjected to a final axial load of 6 MPa. Backanalysis of M_o (5.12 $\pm$1.48 GPa) and H_o(0.10 $\pm$0.12 GPa) from short hold-time indentation test using a 1-phase textural model gives an unrealistic porosity of 61%. cg1 and cg2 consist of 99 and 210 creep nanoindentation tests, respectively.

****Consolidated illite sample. Porosity $\sim$ 30%. cg1 consists of 196 creep nanoindentation tests.

Table 9.7: Phases obtained from clustering analysis of A6Hx_3-cg2 and corresponding mechanical data. The data show that the clay composite has the highest creep rate. (μ = mean value and σ = standard deviation)

	Phase 1: Clay		Phase 2: Mixture		Phase 3: Mixture		Phase 4: Inclusions	
(GPa)	μ	σ	μ	σ	μ	σ	μ	σ
H_{creep}	0.67	0.29	1.04	0.64	2.52	1.51	7.54	4.22
M_{creep}	37.51	6.88	41.44	11.63	52.48	14.71	70.43	20.95
C	342.04	203.42	622.07	550.45	3,273	3,037	16,464	18,424*

*Standard deviations are obtained assuming normal distributions.

9.5.4 Creep Rates of Clay Composites

As with short-hold time indentation tests (Chapter 6), chemo-mechanical clustering analysis is used to isolate the clay composites in creep indentation grid areas. With the contact creep modulus obtained in every creep indentation test, a total of three mechanical parameters (M_{creep}, H_{creep}, and C) is available to couple with chemical data to input into clustering analysis. The advantage of adding C to clustering is that it reflects the creep rates, defined as $\frac{1}{C}$, of every isolated phase/cluster. For instance, the clustering analysis results of chemo-mechanical data (using M_{creep}, H_{creep}, C, Al, Si, Ca, and S) from A6H$x_1$cg2 (Figure 9-12) indicate four different phases (Table 9.7). The mechanical properties (M_{creep} and H_{creep}) and the Si/Al ratio ($\frac{Si}{Al} = 2.29$) of Phase 1 (red squares) reveal that the latter represents creep indentation tests falling within the clay composite in the grid area. As shown in the inset of Figure 9-12, the clay composites in A6H$x_1$cg2 creeps with the highest rates (lowest C values). Phase 2 (Figure 9-12; Table 9.7) has a C of the same order of magnitude as Phase 1. However, the scatter in the me-

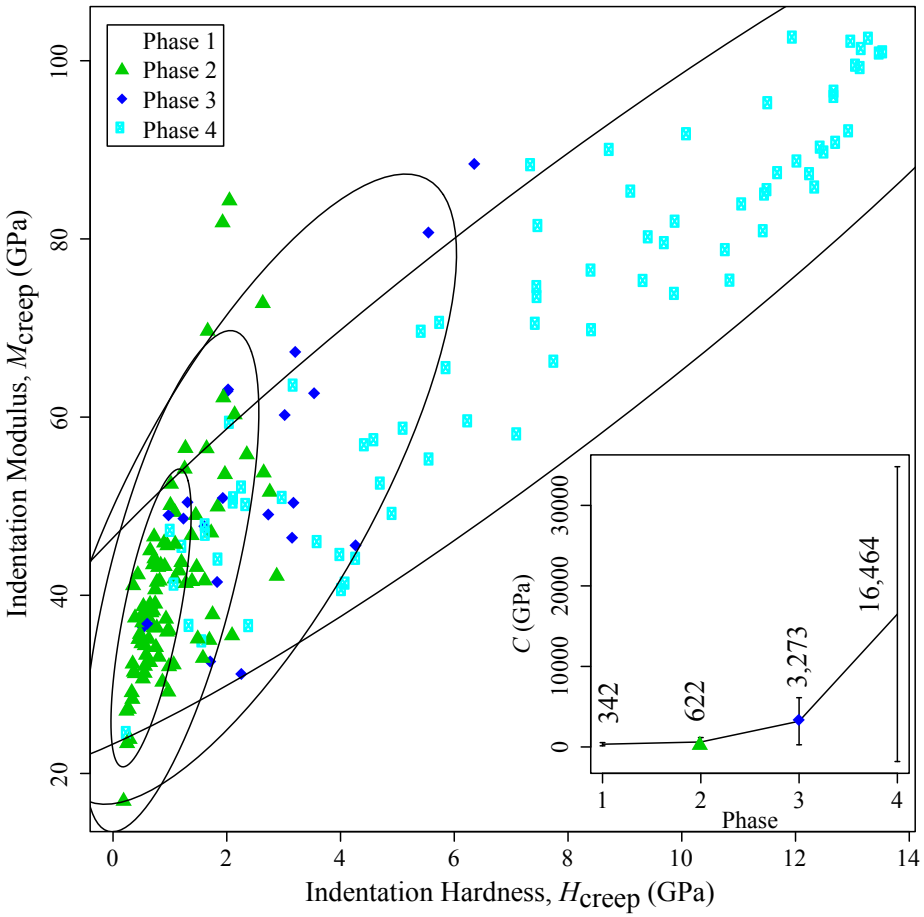

Figure 9-12: Clustering analysis results from A6H-$x_1$cg2. The plot shows M_{creep} vs. H_{creep} of the various phases (clusters) and a top view of their Gaussian distributions (ellipses). The inputs to clustering analysis are M_{creep}, $_{Hcreep}$, and C and the chemical elements Si, Al, Ca, and S. The inset shows mean values of contact creep moduli of the various phases. The phase with the lowest C (highest creep rate) is the clay composite (phase 1: red squares; Si/Al =2.3).

chanical properties of Phase 2 as well as its high Ca-content (not presented) suggest that it is a clay-dominated phase contaminated with Ca-rich minerals (mainly carbonates and, to a lesser extent, feldspar). Therefore, Phase 1 is a better representative of the clay composites in this Haynesville sample (A6H). As in mature formations, clustering analysis results using creep indentation data from immature formations also indicate that the clay composites are the phases with the highest creep rates. This fact is illustrated in the clustering analysis of creep data from Antrim (Figure 9-13). Multiple creep indentation grids were performed on the mature (Marcellus and Haynesville) and immature (Antrim, Barnett, Woodford) gas shale formations. Tables 9.8 and 9.9 report the contact creep modulus of the clay composite phase isolated, with clustering analysis, in each grid. The C values reported from mature and immature creep grids match the magnitude of C of the clay composites in A6H$x_1$cg2 and Antrim$x_3$cg1, respectively. The clay composite isolated in each grid, therefore, has the lowest C value (highest creep rates) when compared to the rest of the clusters/phases. This establishes that the clay composites are the phases, within the gas shale formations, that creep with the highest rates.

9.5.4.1 Isotropy of Creep Rates in the Clay Composite

All the creep data from one formation are combined to get a formation creep rate values in both x_1- and x_3-directions. Tables 9.10 and 9.11 summarize these formation averages. The data clearly reveal weak to negligible anisotropy in the creep rates.

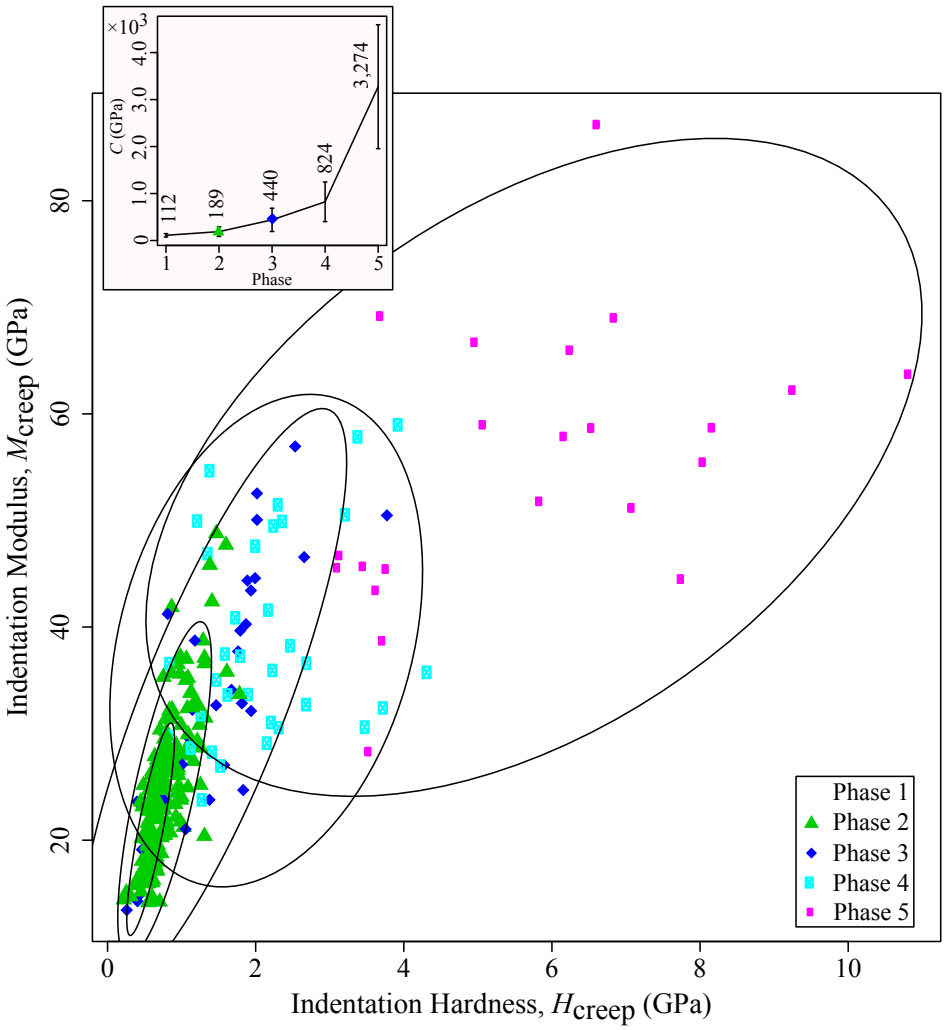

Figure 9-13: Clustering analysis results from Antrim-$x_3$cg1. The plot shows M_{creep} vs. H_{creep} of the various phases (clusters) and a top view of their Gaussian distributions (ellipses). The inputs to clustering analysis are M_{creep}, H_{creep}, and C and the chemical elements Si, Al, Ca, and S. The inset shows mean values of contact creep moduli of the various phases. The phases with the lowest C (highest creep rate) are the clay composite (phases 1 and 2: Si/Al =2.23 and 2.43, respectively).

Table 9.8: Contact creep modulus, C, from individual creep nanoindentation grids performed on mature formations using . Creep nanoindentation tests were acquired at P_{max} = 4.8 mN. (Mar = Marcellus; A = Haynesville samples. x_1= indentation parallel to bedding planes. x_3 = indentation perpendicular to bedding planes. cg = creep grid. The phase column indicates the phase/cluster number (from clustering analysis) that represents the clay composite. μ = mean value and σ = standard deviation).

Sample/Grid	Phase	# of Indents	C (GPa)	
			μ	σ
Mar46$x_1$cg1*	2	108	51.55	25.53
Mar46$x_1$cg2**	1	152	460.50	212.27
Mar49$x_1$cg1	1	167	355.46	147.46
Mar108$x_1$cg1	1	122	355.66	170.49
Mar108$x_1$cg2**	1	250	363.98	178.26
Mar108$x_1$cg3**	1	345	382.88	215.74
Mar151$x_1$cg1	1,2	278	395.80	162.64
Mar151$x_1$cg2	1,2	317	374.13	174.04
Mar151$x_1$cg6**	1	248	540.97	130.75
A5V$x_1$cg0**,***	1	293	268.38	109.59
A5V$x_1$cg1	1	240	318.92	123.36
A5V$x_1$cg2	1,2	251	391.68	179.52
A6V$x_1$cg1	1	203	143.07	72.27
A6V$x_1$cg2	1	250	342.04	203.42
A7H$x_1$cg1	1	170	297.68	133.20
A7H$x_1$cg2	1	193	375.42	166.60
Mar46$x_3$cg1	1	185	138.00	86.51
Mar46$x_3$cg2	2	182	533.31	242.95
Mar108$x_3$cg1	1	155	284.69	161.84
Mar108x_3 cg2	1,2	326	306.65	178.34
Mar151$x_3$cg1	1	201	315.34	139.08
Mar151$x_3$cg1	2	59	358.80	149.48
A6Vx_3 cg1	1	231	387.24	250.66
A6V$x_3$cg2	1,3	299	387.24	250.67
A7H$x_3$cg3	1	134	322.47	158.65

*Phase affected by localized apparent high porosity/microcracks.

**Grids indented with the UNHT machine.

***Data courtesy of Dr. Sara Abedi. No EDS done on grid area.

Table 9.9: Contact creep modulus, C, from individual creep nanoindentation grids performed on immature formations. Creep nanoindentation tests were acquired at P_{max} = 4.8 mN. (Woodf.=Woodford. x_1= indentation parallel to bedding planes. x_3 = indentation perpendicular to bedding planes. cg = creep grid. The phase column indicates the phase/cluster number (from clustering analysis) that represents the clay composite. μ = mean value and σ = standard deviation)

Sample/Grid	Phase	# of Indents	C (GPa)	
			μ	σ
Antrim$x_1$cg0*,**	1	199	246.27	52.19
Antrim$x_1$cg1	1	219	165.38	70.86
Antrimx_1 cg2	1	193	173.51	65.42
Barnett$x_1$cg0*,**	1	192	161.66	27.82
Barnett$x_1$cg0*,**	2	145	247.96	62.93
Barnett$x_1$cg1	1,2	307	186.66	90.03
Barnett$x_1$cg2	1,2	214	191.92	84.23
Woodf. A$x_1$cg1	1	169	147.65	54.792
Woodf. B$x_1$cg1**	1	183	180.76	57.02
Antrim$x_3$cg0	1	254	201.92	60.68
Antrim$x_3$cg1	1,2	240	258.87	145.42
Antrim$x_3$cg2	1,2	243	258.01	177.40
Barnett$x_3$cg0*,**	1	268	143.84	28.56
Barnett$x_3$cg0*,**	2	129	248.43	81.28
Barnett$x_3$cg1	1,2	303	183.63	116.19
Barnett$x_3$cg2**	1,2	340	199.04	94.15
Woodf. A$x_3$cg1	1,2	285	111.23	90.84
Woodf. A$x_3$cg2	1,2	242	212.84	184.65

*Data courtesy of Dr. Sara Abedi.

Grids indented with the UNHT machine.

**Clay phase isolated with clustering using mechanical data only.

Table 9.10: Contact creep moduli (C) mean, μ, and standard deviations, σ, values obtained from creep nanoindentation tests on the mature formations studied.

Mature Fms.	C (GPa)	
	μ	σ
Marcellus x_1	384.07	198.52
Marcellus x_3	323.33	204.43
Haynesville x_1	323.98	159.91
Haynesville x_3	351.75	199.25

Table 9.11: Contact creep moduli (C) mean, μ, and standard deviations, σ, values obtained from creep nanoindentation tests on the immature formations studied.

Immature Fms.	C (GPa)	
	μ	σ
Antrim x_1	207.73	60.30
Antrim x_3	258.44	162.01
Barnett x_1	188.82	87.65
Barnett x_3	191.79	105.29
Woodford x_1	190.10	74.13
Woodford x_3	164.57	156.09

9.5.4.2 Maturity Effect on Clay Composite Creep Rates

To highlight the effect of maturity on the creep rates of the clay composites, mean C values using all data from mature formations, on one hand, and immature formations, on the other are calculated. This approach is justified as creep rates measured along the x_1- and x_3-directions show negligible anisotropy (previous section). It is found that $C^{mat,all} = 348.07 \pm 190.26$ GPa, and $C^{imm,all} = 187.68 \pm 113.03$ GPa. These results clearly indicate

faster creep rates in the clay composites in immature gas shale formations compared to those in mature ones.

Creep indentation results from clay composites, mature kerogen samples, and muscovite show that the contact creep moduli of these materials are 188 (immature formations)-348 (mature formations) GPa, 80 GPa, and 5,455 GPa, respectively.

9.5.5 Creep NanoIndentation Modulus and Hardness

In Chapter 6, the time-independent mechanical properties of the clay composites obtained from short hold-time nanoindentation tests show higher stiffness and hardness in mature gas shale formations compared to immature ones. Also, the results show stiffness anisotropy with the indentation moduli are higher in the x_1-direction than in the x_3-direction. This stiffness anisotropy is due to stiffer mature organic matter compared to immature one (Bousige et al., 2016). This section discusses changes in the indentation modulus, hardness, and anisotropy as a result of creep deformation (Tables 9.12 and 9.13).

The maximum depth reached as well as the final contact area between indenter and material are expected to be larger at the end of the creep phase than in short hold-time nanoindentations. In the clay composites, the depth-time data show that the contact area increases by 10-18% during the three-minute creep. This increase represents the value of x in Equation (9.30). Accordingly, the factor γ (Equations (9.30) and (9.32)) ranges between 92.1-95.4 %. Equations (9.30) and (9.32) suggest smaller changes in the indentation modulus than in the hardness due to creep deformation. Our experimental data confirm these predictions. The indentation modulus

Table 9.12: M_{creep}, H_{creep}, and total penetration depth (h_{creep}) obtained from creep nanoindentation grids performed on mature gas shale formations. $P_{max} = 4.8$ mN. Mar = Marcellus, A = Haynesville, x_1 = indentation parallel to bedding planes. x_3 = indentation perpendicular to bedding planes. cg = creep grid. The phase column indicates the phase/cluster number (from clustering analysis) that represents the clay composite. μ = mean value and σ = standard deviation.

Sample/Grid	Phase	H_{creep}(GPa)		M_{creep} (GPa)		h_{creep} (nm)	
		μ	σ	μ	σ	μ	σ
Mar46$x_1$cg1	2	0.21	0.09	43.15	12.87	917.92	189.62
Mar46$x_1$cg2*	1	0.88	0.39	39.30	9.22	503.32	243.80
Mar49$x_1$cg1	1	0.79	0.27	49.95	7.48	468.69	109.85
Mar108$x_1$cg1	1	0.66	0.18	36.57	5.86	486.93	69.57
Mar108$x_1$cg2*	1	0.71	0.26	26.95	5.61	527.54	99.43
Mar108$x_1$cg3*	1	0.73	0.32	26.62	6.09	523.88	89.19
Mar151$x_1$cg1	1,2	0.81	0.22	36.26	5.93	436.48	63.37
Mar151$x_1$cg2	1,2	0.76	0.23	35.01	5.65	453.40	74.00
Mar151$x_1$cg6*	1	1.10	0.24	37.17	7.10	471.70	58.31
A5V$x_1$cg0*,**	1	0.58	0.24	29.34	7.38	-	-
A5V$x_1$cg1	1	0.67	0.16	37.70	5.74	475.88	66.48
A5V$x_1$cg2	1,2	0.74	0.23	37.86	5.58	445.62	78.09
A6V$x_1$cg1	1	0.59	0.22	34.85	7.57	560.77	134.00
A6Vx_1 cg2	1	0.67	0.29	37.51	6.88	529.62	130.51
A7Hx_1 cg1	1	0.58	0.20	34.31	5.25	506.03	90.32
A7H$x_1$cg2	1	0.69	0.20	37.92	6.36	460.06	87.03
Mar46$x_3$cg1	1	0.49	0.26	51.45	17.93	637.36	214.64
Mar46x_3 cg2	2	0.99	0.34	43.25	7.02	419.54	98.55
Mar108$x_3$cg1	1	0.60	0.19	27.58	4.83	519.94	89.66
Mar108$x_3$cg2	1	0.62	0.24	26.1	4.77	535.25	99.34
Mar151$x_3$cg1	1	0.61	0.22	26.99	5.11	543.02	154.33
Mar151$x_3$cg1	2	0.70	0.18	32.76	6.11	484.31	74.17
A6H$x_3$cg1	1	0.71	0.24	30.00	6.18	567.96	135.76
A6H$x_3$cg2	1,3	0.59	0.23	23.81	4.65	507.02	91.03
A7H$x_3$cg3	1	0.62	0.24	27.60	6.15	597.85	135.54

*Grids indented with UNHT machine.

**Data courtesy of Dr. Sara Abedi. No EDS done on grid area.

Clay phase isolated with clustering analysis using mechanical data only.

Table 9.13: Elastic modulus (M_{creep}, hardness (H_{creep}) and total penetration depth (h_{creep}) obtained from creep nanoindentation grids performed on immature gas shale formations using a maximum load $P_{max} = 4.8$ mN. (Woodf. = Woodford. x_1= indentation parallel to bedding planes. x_3 = indentation perpendicular to bedding planes. cg = creep grid. The phase column indicates the phase/cluster number (from clustering analysis) that represents the clay composite. μ = mean value and σ = standard deviation)

Sample/Grid	Phase	H_{creep} (GPa)		M_{creep} (GPa)		h_{creep} (nm)	
		μ	σ	μ	σ	μ	σ
Antrim$x_1$cg0*	1	0.68	0.14	25.39	4.25	-	-
Antrim$x_1$cg1	1	0.50	0.15	25.56	5.54	552.60	131.44
Antrim$x_1$cg2	1	0.59	0.15	27.47	6.29	586.72	93.79
Barnett$x_1$cg0*	1	0.50	0.08	19.79	3.94	688.27	57.94
Barnett$x_1$cg0*	2	0.73	0.12	24.09	4.69	579.75	47.17
Barnett$x_1$cg1	1,2	0.53	0.18	20.63	5.92	624.15	109.04
Barnett$x_1$cg2	1,2	0.53	0.14	21.68	4.87	617.45	89.85
WoodA$x_1$cg1	1	0.43	0.11	21.60	3.33	605.23	82.33
WoodB$x_1$cg1**	1	0.56	0.15	26.61	4.70	504.93	84.03
Antrim$x_3$cg0*	1	0.59	0.17	19.34	3.79	-	-
Antrim$x_3$cg1	1,2	0.74	0.25	24.08	6.29	538.41	90.20
Antrim$x_3$cg2	1,2	0.73	0.30	24.69	6.33	551.99	105.52
Barnett$x_3$cg0*	1	0.45	0.08	13.36	2.06	744.55	69.04
Barnettx_3 cg0*	2	0.77	0.21	18.64	3.56	589.69	72.87
Barnett$x_3$cg1	1,2	0.50	0.20	16.04	4.05	660.28	124.05
Barnett$x_3$cg2**	1,2	0.55	0.17	17.01	4.24	623.49	90.31
WoodfA$x_3$cg1	1,2	0.49	0.17	18.60	3.02	646.46	171.33
WoodA$x_3$cg2	1,2	0.54	0.32	18.4	4.74	592.5	163.46

*Data courtesy of Dr. Sara Abedi. Grids indented with the UNHT machine.

No EDS done on grid area.

**No EDS done on grid area.

Clay phase isolated with clustering analysis using mechanical data only.

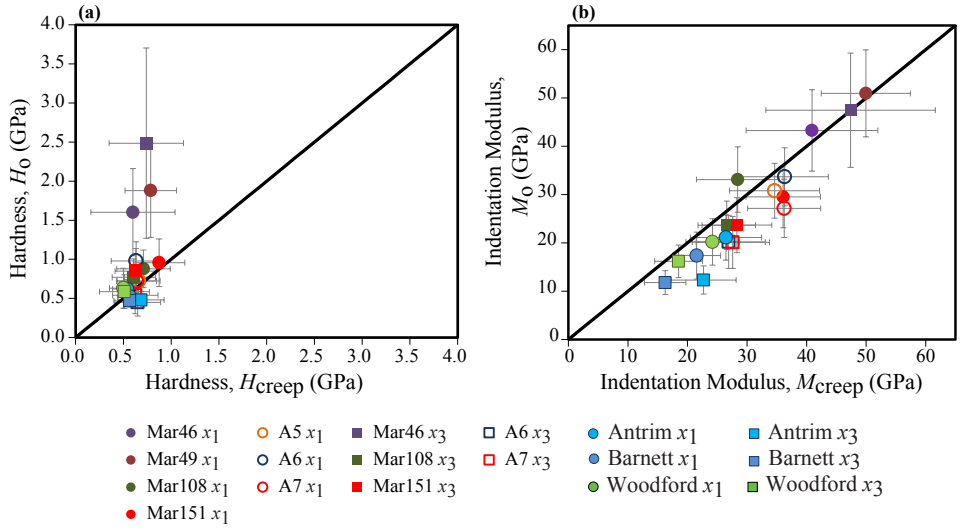

Figure 9-14: (a) Indentation hardness and (b) elastic moduli of the organic-rich clay phases from creep nanoindentation tests (x-axis), compared to data from short hold-time (10 s) nanoindentation tests (y-axis). Mar = Marcellus; A = Haynesville samples. Nanoindentation tests are performed using P_{max} = 4.8 mN.

(Figure 9-14b) shows insignificant increase with creep deformation. We remark that the organic-poor samples (Marcellus 46 and 49) show the least change in elasticity after creep. A remarkable decrease in hardness is seen in organic-poor samples as well (Marcellus 46 and 49; Figure 9-14a).

With creep deformation, a power scaling relationship still relates M_{creep} and H_{creep} (Figure 9-15). Another observation of interest is the decrease in anisotropy, mainly that of stiffness, due to creep deformation. This is exemplified in Figure 9-16 in form of M_1-M_3 and H_1-H_3 plots for short hold-time (left) and creep (right) nanoindentation tests, respectively.

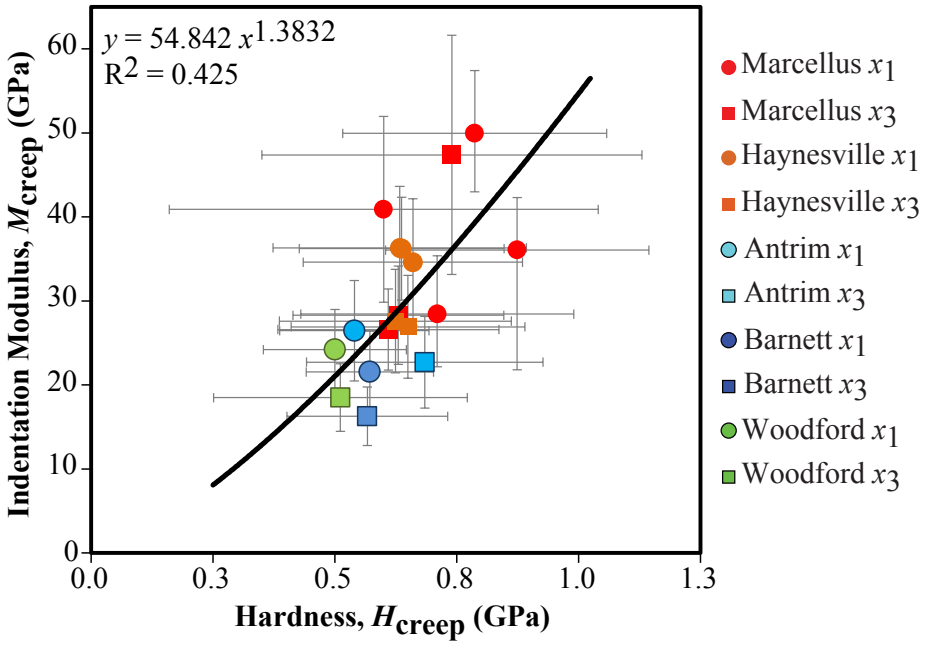

Figure 9-15: A plot of the indentation moduli and hardness obtained from creep nanoindentation tests. The plot shows a weak correlation between M_{creep} and H_{creep}. Nanoindentation tests are performed using P_{max} = 4.8 mN.

9.6 Discussion

The creep nanoindentation results show kinetic phenomena depending on $ln(t)$ in the clay composites (level I) and organic matter (level 0). Creep kinetic phenomena depending on $ln(t)$ have long been observed in metallic glass (e.g., Spaepen, 1977), metals (Wyatt, 1953), and other crystalline material (Cottrell, 1997; Nabarro, 2001) to explain deformation and flow. Three phenomena (discussed in more detail in Chapter 10) explain the creep kinetics we see in the composites (level I) and organic matter (level 0). These are mainly changes in packing density, structural rearrangement, and creep

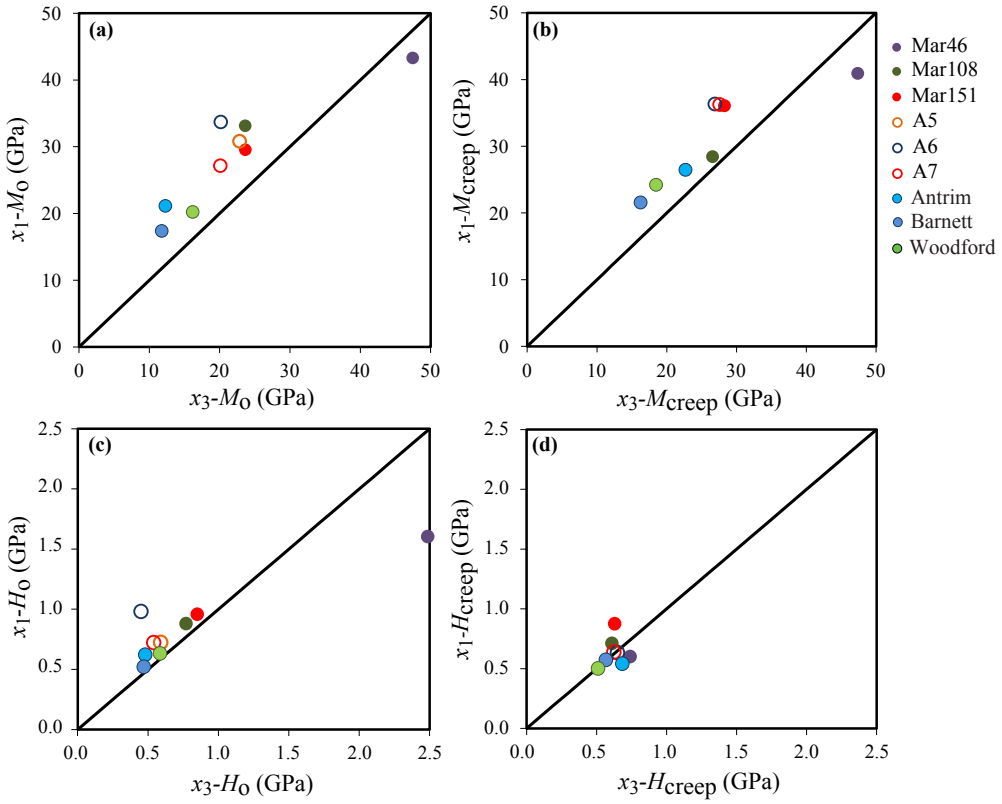

Figure 9-16: Elasticity and hardness anisotropy from nanoindentation tests with (a,c) 10 s hold-time and (b,d) 180 s hold-time (creep) tests done in x_1- and x_3-directions. Reduction in the anisotropy of mechanical properties is seen after viscoelastic deformation. Mar = Marcellus; A = Haynesville samples. Nanoindentation tests are performed using P_{max} = 4.8 mN.

in the clay skeleton at level I. Creep of the organic phase (level 0) affects the structure, volume, and mobility of the organic molecules.

Many experimental results suggest that kerogen drives creep behavior at level I. These are the following:

1. The organic-rich clay composites are the phases that creep with the highest rates (as indicated by clustering analysis) in both mature and immature formations,

2. The contact creep moduli of kerogen and that of muscovite differ by two orders of magnitude ($C^k << C^{muscovite}$), reflecting the much higher creep rates in the organic matter than in the clay particles. Besides, the creep rates in the clay composites are close in magnitude to those of mature kerogen ($C^k \approx C^{composite}$),

3. Mature formations have higher C (slower creep rates) than immature ones. This reflects the more brittle nature of mature kerogen compared to a more ductile immature organic matter (Bousige et al., 2016), and

4. A negligible anisotropy in creep rates ($C_{x_1} \approx C_{x_3}$) is seen within every gas shale formation. This minimal anisotropy reflects the role of isotropic phases (organic matter and porosity) that drive creep behavior.

The above observations highlight the role of kerogen and validate Hypothesis II, that kerogen drives creep behavior at level I.

The changes in the contact area with creep are expected to affect hardness and elasticity measurements. In general, we see insignificant changes in both hardness and elasticity (Figure 9-14) in most of the formations, indicating indeed minor changes in the contact area during the creep phase.

Haynesville samples A5-x_1 and A7-x_1, Antrim-x_1, and Barnett-x_1 show the least change in hardness with creep. On the other hand, samples with the lowest organic content (Marcellus 46 and Marcellus 49 with TOC of 0.49 and 1.04 wt.%, respectively) exhibit remarkable decrease in hardness. The absence of an organic phase within the clay aggregates in these Marcellus facies increases the contact stress between the clay particles under load. Such a stress concentration leads to the formation of microcracks, decreasing the hardness of the material. This distinct behavior of low-organic content source rocks also provides insight into the mechanical role of kerogen: subjected to load, energy is dissipated in the microstructure by either creep or cracking. In the case of high organic content, creep dominates. The opposite case, cracking and dilation, holds in low organic content source rocks.

The insignificant change seen in M_{creep} compared to M_o proves that M_{creep} is (still) instantaneously determined from the initial slope of unloading curves at the end of the creep phase. This comparison attests to the premise of the creep indentation test design (duration of the hold phase and the fast unloading phase) minimizing both viscous effects during unloading and the errors determining M_{creep}. The small increase of stiffness with creep deformation may be attributed to changes (increase) in packing density. The fact that organic-poor samples show no change in elasticity (Figure 9-14b) can reflect a simultaneous increase in packing density balanced by the formation of microcracks (as explained in the last paragraph), resulting in no changes in stiffness.

9.7 Summary

Time-dependent mechanical properties acquired using creep nanoindentation tests show a logarithmic creep behavior at level 0 (organic matter and clay particle level) and level I (clay composite level). Clustering analysis, incorporating the contact creep modulus, shows that the clay composites are the phases that creep with the highest rates ($\propto 1/C$). Compared to that of mature kerogen and muscovite ($C^k < C^{composite} << C^{muscovite}$), the creep rates of the clay composites suggest that kerogen plays a pivotal role in defining the creep properties of the clay composites. TOC-related changes in hardness and elasticity also hint at the role of organic matter: it contributes in changing the elastic and strength properties after creep deformations in some formations.

Given the creep nanoindentation results, we return, in Chapter 10, to the toolbox of continuum micromechanics, the theory of consolidation, and the free volume theory to infer the creep deformation mechanisms. Creep homogenization modeling is also done to ascertain the role of kerogen in the gas shale formations' creep properties.

Chapter 10

Creep Deformation and the Role of Kerogen

The creep nanoindentation results, presented in Chapter 9, show the creep behavior of the various components of the clay components and hint at the role of isotropic phases (porosity and organic matter) driving the creep behavior within the clay composites. This chapter tests two hypotheses. Hypothesis II is revisited. We recall that it states that the organic matter drives the creep behavior within the clay composites as well as the source rocks. Hypothesis III states that (three-minute) creep microindentation reflect long-time creep behavior seen at the macroscale. To test Hypotheses II and III, we first try to answer the following:

- What are the creep kinetics in the clay composites? What deformation mechanisms are responsible for the creep behavior at the clay composite level (level I)?
- What determines the creep rate magnitude, i.e., the contact creep

modulus, C?

- What links can be established between microscale creep rates (from creep microindentation data) and macroscale creep?

This work highlights two creep deformation mechanisms. The first is the structural rearrangement of the clay particles in the clay composites causing compaction at level I. The second is creep in the organic matter at level 0, most likely resulting in stretching and mobility of organic matter under load. We explain the level I deformation mechanism by drawing an analogy to soil mechanics showing a linear scaling relationship between C and H_{creep} and using micromechanical models, this time predicting changes in packing density with creep. Then, the role of kerogen driving creep behavior within the clay composite (level I) is emphasized with creep homogenization modeling. Finally, creep results from microindentation tests are compared to macroscale creep data.

10.1 Level I Creep Kinetics and Deformation Mechanisms

In Chapter 9, changes in indentation hardness (H_{creep}) due to creep in organic-poor source rocks hints at structural changes in the material due to plastic and viscoelastic deformations. In this section, two approaches are used to infer creep kinetics and deformation mechanisms taking place in the clay composites. The first uses the analogy between a creep indentation test and an oedometer test (introduced in the next section). We seek to specify a relationship between creep properties (C) and creep hardness (H_{creep}). The

second approach uses the micromechanical tool box. The creep mechanical properties (M_{creep} and H_{creep}) are used in the back-analysis approach (presented in Chapter 8) to predict the packing density of the clay composites after creep (η_{creep}). Differences between η_{creep} and η_o (packing density predicted in the clay composites using short hold-time nanoindentation results, M_o and H_o) reflect structural changes within the clay composites.

10.1.1 Secondary Consolidation in Soil

In soil mechanics, relations between consolidation properties and applied stresses are common, as related to Terzaghi's theory of consolidation, to distinguish time-dependent deformation related to seepage from deformation due to skeleton creep (Germaine and Germaine, 2009; Jain and Nanda, 2010)). The latter is also called secondary consolidation. An oedometer test (set-up shown in the inset of Figure 10-1) is a test in which a saturated soil sample is consolidated under a constant load under drained conditions. The load is applied on a piston having the same surface area as the sample. At every applied load, the sample undergoes primary and secondary consolidations. Primary consolidation consists of pore pressure dissipation as a reaction to the applied loads. In contrast, secondary consolidation consists of creep of the soil mass (Jain and Nanda, 2010) and the viscous behavior of the clay-water system. Soil particles get rearranged, leading to better packing (Lambe and Whitman, 1969). It is known in soil mechanics that the "time rate of secondary compression is larger for highly plastic soils and especially for organic soils" (Lambe and Whitman, 1969. See also Mesri and Castro, 1987; Table 10.1). It is expressed in the form of the coefficient of secondary consolidation, $C_{\alpha\epsilon}$. The latter is the slope of the straight

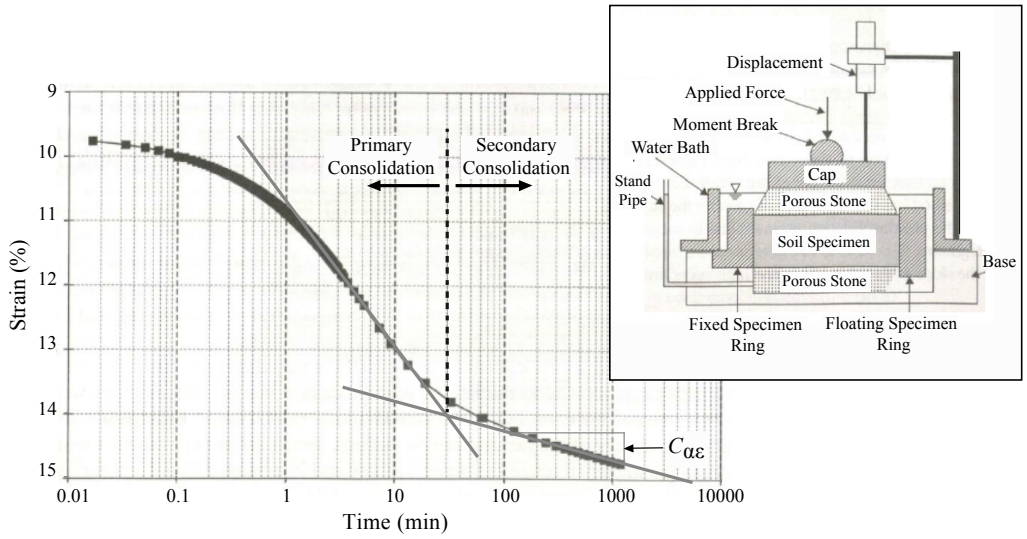

Figure 10-1: A "time curve" for a load increment in an oedometer test depicting the "Log-Time method" to determine the end of the primary consolidation. Inset: Sketch of a typical oedometer (modified after Germaine and Germaine, 2009).

portion of the strain-log(t) plot of a consolidation test under oedometric conditions (Figure 10-1), after the primary consolidation stage (Germaine and Germaine, 2009):

$$C_{\alpha\epsilon} = \frac{-\Delta\epsilon_\alpha}{\Delta \log t} \tag{10.1}$$

The analogy of an indentation test to an oedometer test can be employed to interpret the creep nanoindentation results in the clay composites. In the latter, the stress applied, σ, is equivalent to indentation hardness, H_{creep}, representative of the average pressure below the indenter. The changes in strain with respect to time, $\dot{\epsilon} = \frac{\dot{V}}{V_0}$ (V_0 is the original volume of the sample, the area of which remains constant during the test), correspond to changes in the sample void ratio with respect to time, $\dot{e}$, (e =volume of pores/volume

Table 10.1: Values of $C_{\alpha\epsilon}/C_c$ for geotechnical materials (from Mesri, 2003); C_c is the compression index $= \dfrac{-\Delta e}{\Delta \log \sigma'_v}$ where e =volume of pores/volume of solids, and σ'_v is the effective vertical stress

Material	$C_{\alpha\epsilon}/C_c$
Granular soils including rockfill	0.02±0.01
Shale and mudstones	0.03±0.01
Inorganic clays and silts	0.04±0.01
Organic clays and silts	0.05±0.01
Peat	0.06±0.01

of solids) and is equal to $\eta_0 \dot{e}$, with η_0 being the original packing density of the sample (η_0 =1-ϕ, where ϕ is the porosity). Using Equation (10.1) and $\sigma = H_{creep}$, the strain in a consolidation test evolves as follows (Vandamme and Ulm, 2013):

$$\dot{\epsilon} = \frac{\eta_0 C_{\alpha\epsilon}}{t} = \frac{\sigma}{t}\frac{\eta_0 C_{\alpha\epsilon}}{H_{creep}} \tag{10.2}$$

Rearranging terms in the above equation gives the contact creep compliance rate, $\dot{L}(t)$,

$$\frac{\dot{\epsilon}}{\sigma} = \dot{L}(t) = \frac{\eta_0 C_{\alpha\epsilon}}{H_{creep}}\frac{1}{t} \tag{10.3}$$

If we remind ourselves of Equation (9.35), that is, $\dot{L}(t) = \dfrac{1}{Ct}$, we obtain a linear expression that links the creep modulus, C, and the indentation hardness, H_{creep}. This link is defined by the coefficient of secondary consolidation (Vandamme and Ulm, 2013):

$$C = \frac{1}{\eta_0 C_{\alpha\epsilon}} H_{creep} \tag{10.4}$$

10.1.2 Linear C-H Relationship in Organic-Rich Clay Composites

The relevance of the application of Equation (10.4) for our samples is shown in Figure 10-2 in the form of C-H_{creep} cross plots. The figure emphasizes that the creep modulus, C, scales in first order with the creep hardness. This scaling holds irrespective of TOC, maturity, anisotropy, or mineralogy. Deviations from this scaling are attributable to the initial packing density, η_0, and variations in the coefficient of secondary consolidation, $C_{\alpha\epsilon}$, both of which no doubt relate to the burial history of the samples. The latter is known to affect clay mineralogy, water content, and organic content and maturity.

In highly packed systems (η_0 = 92-94%) such as the gas shale formations studied, calculating $C_{\alpha\epsilon}$ using Equation (10.4) and $\frac{C}{H_{creep}} = 342$ (342 is from fitting experimental data from immature formations, as seen in Figure 10-2b), gives a $C_{\alpha\epsilon}$ of 0.003. This value obtained for $C_{\alpha\epsilon}$ from the immature gas shale formations is comparable to values reported in literature for shale samples. For instance, Mesri and Castro (1987) reported a value of 0.029 for $\frac{C_{\alpha\epsilon}}{C_c}$ for (Bearpaw) shale (where C_c is the compression index[1] that ranges between 0.075-0.2). For this specific shale, $C_{\alpha\epsilon}$ is found to range between 0.0022 and 0.0058, a range that includes the calculated $C_{\alpha\epsilon}$ using the C-H_{creep} scaling relationship in immature formations.

The successful application of the above concept to organic-rich clay composites provides insight into the creep deformation mechanisms at level I

[1] $C_c = \frac{-\Delta e}{\Delta \log \sigma'_v}$; where e = is as defined in the text, and σ'_v is the effective vertical stress. C_c is the slope of the consolidation curve on a semi-log plot of e vs. σ'_v.

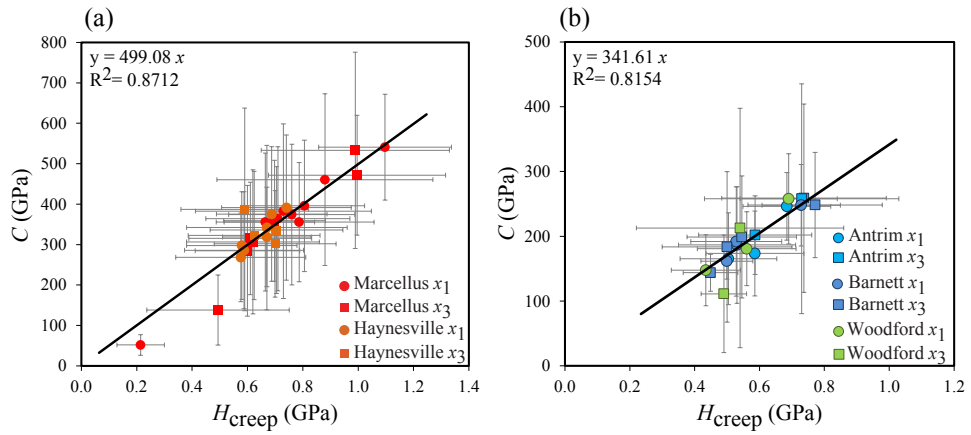

Figure 10-2: A plot of contact creep modulus, C, versus hardness, H_{creep}, in mature (left) and immature (right) formations showing a maturity-dependent linear correlation between the 2 mechanical properties. Data are from creep nanoindentation tests performed at $P_{max} = 4.8$ mN using both the UNHT and Hysitron (Appendix B).

in the gas shale formations and suggests particle rearrangement and compaction of the composites. A similar compaction mechanism was invoked by Sone and Zoback (2013) based on creep measurements on core plugs from various gas shale formations. The authors ascribed the overall reduction in sample volume during axial creep to "slight pore compaction".

In return, rephrased in terms of the rich body of soil mechanics characterization, the linear relation (Equation (10.4)) between two mechanical quantities (creep modulus, hardness) links an observation to a fundamental mechanism that merits further investigation. This is shown next.

10.1.3 Assessment of Packing Density Variations at Level I Using Textural Models

In this section, the secondary consolidation that occurs during the creep phase is assessed. This requires determining the porosity, under the indenter tip, before and after creep deformation. To achieve this goal, the back-analysis scheme (Chapter 8) is applied to both short-term (M_o and H_o) and creep (M_{creep} and H_{creep}) nanoindentation data. With a focus on determining the change in solid packing density distribution, a two-step procedure is herein employed:

- Assessment of initial packing density distribution: Using the short-term data (M_o and H_o), the particle properties (m_s, h_s) are assessed and either the average kerogen content η_k (if the clay porosity is known), or the (mean) packing density $\eta_o = \overline{\eta_s(x,t_o)}$ or clay porosity $\overline{\phi_o} = 1 - (\overline{\eta_s(x,t_o)} + \eta_k)$ (if the kerogen content is known). The particle properties and the clay kerogen content are assumed not to be affected by creep deformation.

- Assessment of packing density distribution after creep deformation: Using the long-term data (M_{creep} and H_{creep}), and the previously determined particle properties (m_s, h_s) and kerogen content η_k, the packing density distribution, $\eta_s = \eta_s(x, t = t_o + \Delta t)$ after the Δt =180 s hold phase is assessed; and condensed into the mean packing density $\overline{\eta_s(x, t = t_o + \Delta t)} = \eta_{creep}$, or porosity after creep deformation, $\overline{\phi_t} = 1 - (\overline{\eta_s(x, t = t_o + \Delta t)} + \eta_k)$.

By way of example, Figure 10-3 illustrates the application of this two-

step procedure for Haynesville A6x_1 and Marcellus 108x_1 samples, in the form of the initial and final packing density distributions. A statistical test, the t-test, of the results reveals statistically insignificant changes in the packing density in the Haynesville samples. On the other hand, the Marcellus data show statistically significant dilation due to creep (Figure 10-3b). The statistical analyses of the packing density distributions from the rest of the samples studied make us conclude that significant statistical variations in packing density are obtained only when the latter changes by more than $\pm 0.5\%$. The distributions thus obtained are then condensed into the mean packing density change , $\eta_{creep} - \eta_o = \overline{\phi_0} - \overline{\phi_t}$. Thus, $\eta_{creep} - \eta_o > 0$ is representative of a compaction, whereas $\eta_{creep} - \eta_o < 0$ implies dilation. The results are displayed in Figure 10-4, in the form of plots displaying $(\eta_{creep} - \eta_o)$ vs. measured clay porosity (Figure 10-4, left), and TOC (Figure 10-4, right), respectively. Compaction appears as a deformation mechanism driving creep in mature Haynesville (A5, A6, and A7) and overmature Marcellus (Marcellus 151). Significant compaction is seen in Haynesville A6x_3 and Mar151x_1. This provides an independent confirmation of the secondary consolidation mechanism we found from analyzing the linear C-H_{creep} functional relation of the clay composites (Figure 10-2). In contrast, a dilation mechanism appears to characterize the creep response of Marcellus 46 and Marcellus 108. Dilation in Marcellus 46 does not come as a surprise, recalling its low organic content (0.49 wt.%). In fact, this dilation behavior is consistent with the softening behavior previously found from analyzing the difference in hardness between the short-term tests and the long-term tests (Figure 9-14). This behavior supports the suggestion that the absence of cushioning kerogen entails microcrack deformations which are always associated with

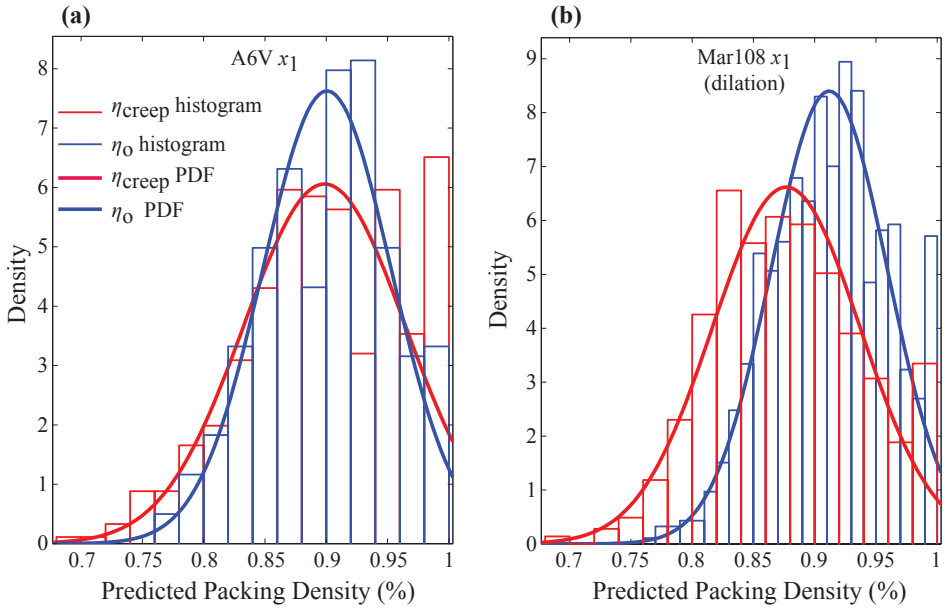

Figure 10-3: Results of the 2-step inverse/back-analysis procedure giving clay-phase packing density $(1 - \phi^I)$ distributions from short hold-time indentation grids (η_o) and creep nanoindentation grids (η_{creep}) performed in the x_1-direction. (a) Haynesville sample A6V that shows no change in packing density with creep, and (b) Marcellus 108 that shows dilation with creep.

an overall dilation-as found by our back-analysis technique. Dilation in the high TOC Marcellus 108 sample seems to be the exception to the interpretation given above. Dilation in Marcellus 108 might be due to indenting regions with localized stiff overmature organic matter or the structure/type of the clay mineral and the kerogen-clay association. Marcellus 108 has 36.3 wt.% of illite (the highest among the Marcellus samples). Unlike a smectitic structure that allows intercalation between the clay structure and organic matter, an illite structure has less spacing available within its lattice for cations and organic molecules. The smectite-illite transition with maturity

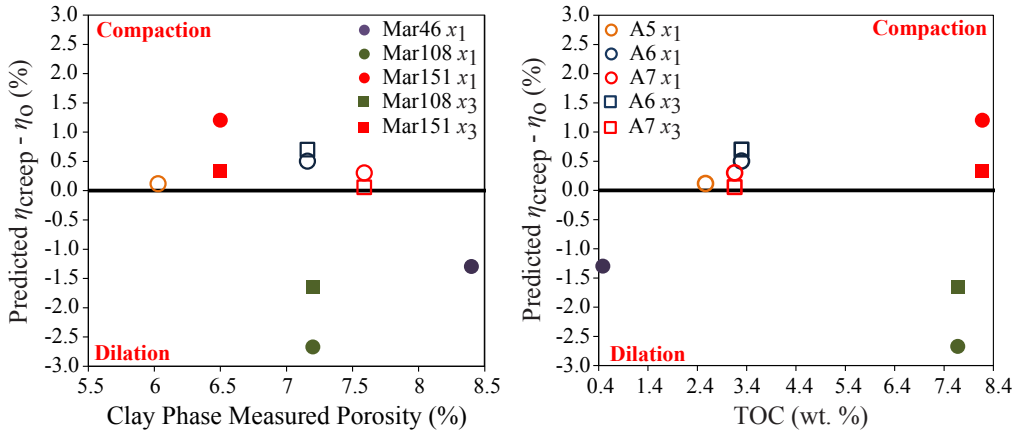

Figure 10-4: Results from the 2-step back-analysis procedure showing changes in packing density due to creep plotted against clay-phase measured porosity (left) and TOC (right). Mar = Marcellus. A = Haynesville.

produces more illite structures and can be causing a dissociation between the organic matter and the clay mineral. This dissociation seems to produce the same effect as a low organic content.

All the back-analysis approach findings are subject to the following considerations:

1. The changes in packing density distributions are relatively small, typically on the order of 1%, which appears small compared to the distribution of packing density in the clay composite. This reflects the high heterogeneity of the material even at the scale of the porous clay-kerogen composite. One should keep in mind that the observed consolidation of 1% needs to be seen in relation with the low porosity of the system: typically 6-9%. As the system thus compacts under the high indentation load (in effect, hardness), the additional 1% compaction due to creep is significant.

2. The accuracy of the porosity determined by the two-step back-analysis procedure can be investigated. The continuum micromechanics models use nanoindentation data. Indeed, for the mature samples so far investigated, a comparison with measured porosity values (by weighting) shows that this "mechanistic" technique consistently overestimates (by ∼1-2 p.u.) the clay phase porosity (Figure 10-5) regardless of whether the data analyzed is from short hold-time nanoindentations (to obtain $\overline{\phi_o} = 1 - (\overline{\eta_s(x, t_o)} + \eta_k)$, or creep nanoindentations (to obtain $\overline{\phi_t} = 1 - (\overline{\eta_s(x, t = t_o + \Delta t)} + \eta_k)$. This overestimation can be ascribed to inaccuracies of measured porosities (no one method is satisfactory and accurate in measuring porosities in materials with such low porosity), actual high local porosities in the areas indented (reflecting possible polishing effects), and statistical effects (difference in number of tests). On the other hand, one should bear in mind that the observed compaction/dilation results from the difference of two mean packing density values, and not from the absolute values; so that any systematic error would cancel out.

Yet, within the limits of these considerations, it appears to us that the rate-determining creep mechanism in organic-rich source rocks involves a compaction process at the scale of the porous organic-rich clay composites.

10.1.4 Creep Kinetics at Level I

Compaction mechanisms, with kinetics depending on $log(t)$, have long been observed in metallic glass (e.g., Spaepen, 1977) and metals (Wyatt, 1953) explaining deformation and flow. Compaction models of granular material (Knight et al., 1995; Boutreux and de Gennes, 1997; Nowak et al., 1998)

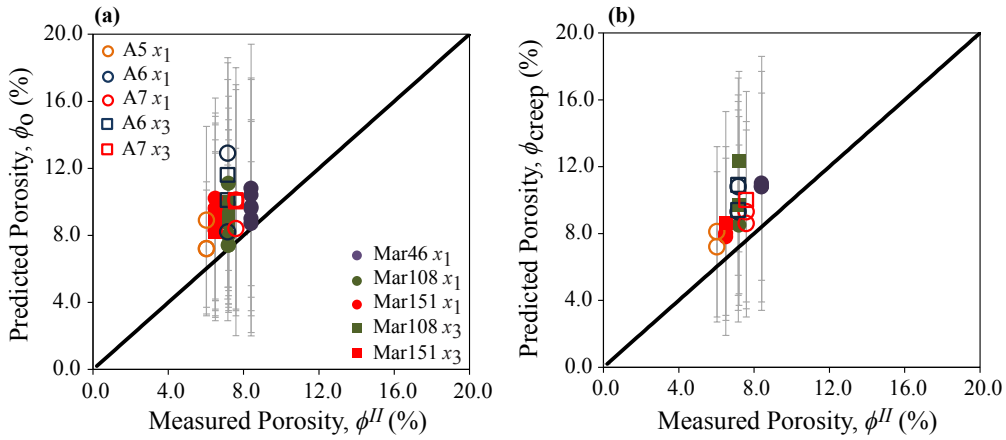

Figure 10-5: Sample measured porosities versus grid-specific porosities obtained from the 2-step back-analysis procedure using mechanical data from a) short-hold time nanoindentation tests (M_o and H_o) and b) creep nanoindentation tests (M_{creep} and H_{creep}).

relate material density changes to the natural logarithm of an external excitation (e.g., number of taps). Similarly, studies show that slope relaxation in sand piles (Jaeger et al., 1989) decays as $log(t)$ when vibrations are introduced. These studies emphasize that the compaction process is "exceedingly slow" and "density approaches its final steady state value approximately logarithmically" (Nowak et al., 1998). Barker and Mehta (1993) ascribed the slow relaxation phenomenon to the motion of clusters, in contrast with "faster" relaxation driven by the motion of independent particles. Such a structural rearrangement follows from the free volume theory. The free volume theory of granular physics (reviewed in Cohen and Turnbull, 1959; Boutreux and de Gennes, 1997; Nowak et al., 1998) explains logarithmic creep and accounts for both volumetric (dilation) and deviatoric (particle sliding) creep (Lemaître, 2002). In what follows, we summarize Boutreux and de Gennes (1997)'s approach explaining the free volume dynamics with

one component. We start with a system with n grains per unit volume, each with volume w. The packing densities at two different packing states are η and η_{lim}, with the latter being the packing density at a limit packing state. The average free volume per grain is:

$$v = w\Big(\frac{1}{\eta} - \frac{1}{\eta_{lim}}\Big) \tag{10.5}$$

At steady-state, i.e., with small variations in packing density around the limit packing density, the above equation can be approximated by:

$$v \sim w\Big(\frac{\eta - \eta_{lim}}{\eta_{lim}^2}\Big) \tag{10.6}$$

For compaction to take place, the grains in a system should have access to the right free volume to move to and rearrange themselves. In other words, the voids the grains can fit into should have volumes Ω greater than w. A Poisson distribution is assumed for the size distribution of voids:

$$P(\Omega \geq w) = exp\Big(\frac{-w}{v}\Big) \tag{10.7}$$

The above probability is assumed to determine compaction and the rate of change of the packing density:

$$\dot{\eta} \propto exp\Big(\frac{-\eta_{lim}^2}{\eta_{lim} - \eta}\Big) \tag{10.8}$$

Solution of the above equation shows that $t \propto exp\Big(\frac{\eta_{lim}^2}{\eta_{lim} - \eta}\Big)$. Therefore, $\dot{\eta} \propto \frac{1}{t}$. Within the limits of these considerations, it appears that the initiation of the creep mechanism in organic-rich source rocks involves a com-

paction process at the scale of the porous organic-rich clay composites. This tendency of the packing density of a system to reach a steady-state value explains the logarithmic creep kinetics, that is, a creep rate $\propto \frac{1}{t}$. In contrast, it cannot explain the magnitude of the creep rate, and thus the creep modulus, C.

10.2 Multiscale Creep Modeling: The Role of Kerogen

The aims of the modeling efforts hereafter employed are multifold: (1) to highlight the role of organic and inorganic phases on the creep rates, (2) to propagate our thus derived understanding of the creep behavior of gas shale's constituents (Section 9.5.3) to the composite scale and the source rock, and by doing so (3) to check whether the creep properties measured by indentation are representative of creep of the source rock as assessed by classical macroscopic means such as triaxial creep testing (Sone and Zoback, 2013). Our objective is to set the stage, in coming sections, to test our hypotheses. This entails highlighting the role of kerogen in driving creep behavior in source rocks (Hypothesis II), and checking whether the creep indentation reflects long-term creep behavior (Hypothesis III).

10.2.1 Creep Modeling Approach and Assumptions

In the creep modeling, only a few assumptions need to be adopted based on key observations of our nanoindentation investigation of creep properties (kinetics and magnitude) and the effect of kerogen maturity on porosity and

texture.

10.2.1.1 Creep Kinetics

We hypothesize that the creep kinetics is independent of the scale of observation and that all that changes from one scale to the other is the creep rate magnitude. This model assumption, of a scale-independent creep kinetics proportional to t^{-1}, allows us to reduce the upscaling to only the creep magnitude: the creep modulus, C. As seen in previous sections (Sections 9.5.1 and 10.1.4), the creep kinetics of the clay composites is defined by a logarithmic creep (respectively by a creep rate that scales with the inverse of time). This creep kinetics originates from the creep of the porous kerogen (at level 0) confined by clay particles (at level I). It can be explained by the free volume theory (Section 10.1.4), and has been found to be accompanied mainly by a compaction mechanism (Section 10.1.3).

10.2.1.2 Creep Magnitude

The creep magnitude of gas shales is dominated by the creep rate of porous kerogen, while the solid clay particles and other inorganics/inclusions contribute only insignificantly to the creep rate. We come to this conclusion from a comparison of the (logarithmic) creep modulus of the organic-rich clay composites and that of their constituents (Chapter 9). From a modeling perspective within the framework of linear viscoelasticity, we thus consider the porous kerogen phase as the sole phase within the composite with a finite creep modulus, $C^k = 80$ GPa; whereas the inorganic phases are considered to have an infinite creep modulus, $C^{clay} \to \infty$ and $C^{inc} \to \infty$. From a mechanics-of-materials perspective, this (asymptotic) consideration aims

at highlighting the reinforcing effect which clay and inclusions play in such highly compacted systems. From a theoretical point of view, invoking the correspondence principle of linear viscoelasticity, this assumption comes to attribute a role of rigid inclusions to the clay particles and other minerals.

There are several implications of the above two modeling assumptions (derived from experimental observations) that merit further discussion based on our understanding and findings of the effect of kerogen maturity on porosity (Chapter 2) and texture (Chapter 8).

10.2.1.3 Maturity and Kerogen Porosity

In the creep modeling, we consider that all the porosity resides in the kerogen phase. Studies relating development of porosity in organic matter to thermal maturity (Curtis et al., 2012) highlight the importance of correlating organic content and porosity (Prasad et al., 2009; refer to Section 2.4). While certainly a conveniently simplifying assumption (as shown here below), our modeling hypothesis that all porosity is situated in the kerogen is motivated by two complementary experimental observations. First, cross-correlations of segmented CT scans reveal that Euclidean distances between kerogen and mesoporosity becomes shorter with maturity (Hubler et al., submitted). Second, the contact creep moduli of the organic-rich clay composites in both mature (Table 9.10) and immature formations (Table 9.11) exhibit an insignificant (or no) anisotropy. The sensitivity of the creep modulus of the porous kerogen phase to maturity is ascribed to two competing effects. While an increase in maturity is expected to enhance the molecular bonds of kerogen's solid backbone and thus reduce the creep deformation; this tighter bonding entails at the same time an increase of the porosity in

kerogen. Mechanically, the effect of an increase in kerogen stiffening with thermal maturity seems to be dominant compared to the effect of increase in kerogen porosity.

10.2.1.4 Texture Effects: Creep Isotropy and Morphology

We recall, from Chapter 8, the success in capturing the effect of kerogen maturity on texture, defining the role played by the various composite components in each texture (load-bearing matrix in the matrix-inclusion morphology vs. no phase assuming a matrix role in the self-consistent scheme). At least two implications follow from considering organic matter as the sole creeping phase and all inorganic phases as rigid inclusions (within the framework of the correspondence principle of linear viscoelasticity). First, the predictable creep rate of the composite will be necessarily isotropic, as shape and viscoelastic anisotropy, potentially associated with the solid clay phase, is excluded. The creep modulus values of the organic-rich clay composites obtained by nanoindentation for both immature and mature formations (Tables 9.11 and 9.10) are supportive of this assumption. Second, one may be tempted to consider the embedding of rigid inclusions in a creeping porous kerogen phase as an *a-priori* choice of a matrix-inclusion morphology for creep modeling. Such a texture may indeed be relevant for immature gas shale samples, as highlighted by segmented CT scans of immature Antrim exhibiting continuity in the pore and organic phases (Hubler et al., submitted). However, it certainly fails for mature samples, for which pores and organic matter do not occur in connected networks at a micrometer length scale, as found by CT scans on a Haynesville sample (Hubler et al., submitted). For such a mature system, the porous kerogen appears in isolated pockets sur-

rounded by clay and other inclusions without any of these phases assuming the role of a matrix. This impact of maturity on texture is somewhat similar to the situation encountered for elasticity and strength modeling, in which two asymptotic cases were considered for (respectively) mature and immature formations, except for a subtle difference: In the (poro)elasticity model, we considered the clay phase as the load-bearing phase; whereas in the creep model, following the correspondence principle of linear viscoelasticity, it is the kerogen phase.

With the model assumptions thus well defined, the next section is dedicated to the model development from the scale of constituent creep to the macroscale of core plug creep measurements.

10.2.2 Effective Creep Properties of the Porous Organic-Rich Clay Composites

At the core of the forthcoming developments is the observation of a logarithmic creep, over long times, which translates into an indentation creep compliance rate, as defined by Equation (9.35), which we recall:

$$\dot{L} = \frac{1}{Ct} \tag{10.9}$$

The next objective is to relate C to the volumetric and deviatoric compliance functions. We first recall two properties of the Laplace transform:

$$\mathscr{L}(tf(t)) = -\frac{d}{ds}\mathscr{L}(f(t)) = -\frac{d}{ds}\hat{f}(s) \tag{10.10}$$

$$\mathscr{L}(f'(t)) = s\mathscr{L}(f(t)) - f(0) = s\hat{f}(s) - f(0) \tag{10.11}$$

Following the developments proposed by Vandamme and Ulm (2013) (Section 9.2.2), and using the final value theorem (reviewed in Dyke, 2001) and the above properties of the Laplace transform, Equation (10.9) becomes:

$$\begin{aligned}\frac{1}{C} &= \lim_{t\to\infty} t\dot{L} = \lim_{s\to 0} s\mathscr{L}(t\dot{L}) \\ &= \lim_{s\to 0} -s\frac{d}{ds}\mathscr{L}(\dot{L}) = \lim_{s\to 0} -s\frac{d}{ds}(s\mathscr{L}(L) - L(0)) \\ &= \lim_{s\to 0} -s\frac{d}{ds}(s\mathscr{L}(L)) = \lim_{s\to 0} -s\frac{d}{ds}(s\hat{L})\end{aligned} \tag{10.12}$$

From the above, one can see that $\frac{d}{ds}(s\hat{L}) \approx \frac{1}{-sC}$ for small s. Therefore,

$$\hat{L} \approx -\frac{lns}{sC} \tag{10.13}$$

The contact creep modulus, C, relates to the volumetric and deviatoric creep compliance functions j^v and j^d:

$$\lim_{t\to\infty} tj^v = \frac{1}{C^v} \quad \text{and} \lim_{t\to\infty} tj^d = \frac{1}{C^d} \tag{10.14}$$

by:

$$C = 4C^d \frac{3C^v + C^d}{3C^v + 4C^d} \tag{10.15}$$

Equation (10.15), which results from an application of the correspondence principle of linear viscoelasticity for long-term logarithmic creep (Section 9.2.2), is at the core of the homogenization approach developed below. Indeed, all that it takes is to homogenize the volumetric and deviatoric creep compliances using the microelasticity solution for the different morphology

systems together with the s-multiplied Laplace transform. Using this approach, several solutions have been proposed in literature relevant for our study.

10.2.2.1 Matrix-Inclusions Morphology with Slippery Interfaces

Consider a (porous kerogen) matrix with rigid (clay) inclusions. The microelasticity solution for inclusions with slippery interfaces (permitting free sliding at the inclusion-matrix interface) obtained by the Mori-Tanaka scheme reads (Gathier, 2008; Vandamme and Ulm, 2013):

$$K^{comp} = \frac{1}{3}\frac{3K^k + 4\eta_c G^k}{1-\eta_c} \tag{10.16}$$

$$G^{comp} = \frac{1}{3}\frac{[(15+9\eta_c)K^k + (24+8\eta_c)G^k]G^k}{(5-2\eta_c)K^k + (8-4\eta_c)G^k} \tag{10.17}$$

where η_c is the inclusion (clay particle) volume fraction. K^k and G^k are the kerogen matrix bulk and shear moduli, respectively. With the help of the correspondence principle considering the matrix as the sole component that creeps in the system, the creep modulus of the composite is obtained by application of Equation (10.15) with:

$$C_v^{comp} = \frac{1}{3}\frac{3C_v^k + 4\eta_c C_d^k}{1-\eta_c} \tag{10.18}$$

$$C_d^{comp} = \frac{1}{3}\frac{[(15+9\eta_c)C_v^k + (24+8\eta_c)C_d^k]C_d^k}{(5-2\eta_c)C_v^k + (8-4\eta_c)C_d^k} \tag{10.19}$$

The above relations can be further simplified when prescribing a link between the two (logarithmic) creep compliance moduli, $lim_{t\to\infty}\, tj_v^k = \frac{1}{C_v^k}$ and $lim_{t\to\infty}\, tj_d^k = \frac{1}{C_d^k}$, by means of a constant creep Poisson's ratio (which should

not be confused with the 'real' Poisson's ratio related to the elasticity of the material):

$$\nu_k^{creep} = \frac{1}{2}\frac{3C_v^k - 2C_d^k}{3C_v^k + C_d^k} \tag{10.20}$$

For instance, a pure deviatoric creep corresponds to $\nu_k^{creep} = \frac{1}{2}$ and $C_v^k \to \infty$; Equations (10.18) and (10.19) simplify as follows:

$$C_v^{comp} \to \infty \tag{10.21}$$

$$C_d^{comp}(\nu_k^{creep} = \frac{1}{2}) = \frac{5 + 3\eta_c}{5 - 2\eta_c} C_d^k \tag{10.22}$$

The contact creep modulus for the deviatoric logarithmic creep is obtained by substituting Equations (10.21) and (10.22) into Equation (10.15):

$$C^{comp}(\nu_k^{creep} = \frac{1}{2}) = 4C_d^{comp}(\nu_k^{creep} = \frac{1}{2}) = 4\frac{5 + 3\eta_c}{5 - 2\eta_c} C_d^k = \frac{5 + 3\eta_c}{5 - 2\eta_c} C^k \tag{10.23}$$

Similar solutions are developed for two other constant values of the creep Poisson's ratio; namely $\nu_k^{creep} = 0$, for which $3C_v^k = 2C_d^k$, and $\nu_k^{creep} = 0.2$, for which $3C_v^k = 4C_d^k$. In this case, the contact creep modulus for the matrix-inclusion morphology reads (Vandamme and Ulm, 2013):

$$\begin{cases} C^{comp}(\nu_k^{creep} = 0) = \dfrac{(17 + 14\eta_c - 13\eta_c^2)(17 + 7\eta_c)}{(17 + 2\eta_c - 10\eta_c^2)(17 - 8\eta_c)} C^k \\ \\ C^{comp}(\nu_k^{creep} = 0.2) = \dfrac{(55 + 18\eta_c - 25\eta_c^2)(11 + 5\eta_c)}{5(11 - 5\eta_c^2)(11 - 5\eta_c)} C^k \end{cases} \tag{10.24}$$

where C^k is the contact creep modulus of the matrix.

10.2.2.2 Granular (Self-Consistent) Morphology with Slippery Interfaces

In an analogous fashion, expressions can be developed for a granular morphology (self-consistent scheme) of one creeping phase self-consistently mixed up with rigid inclusions and slippery interfaces. Using the elastic solution (Gathier, 2008), the corresponding expressions for the volumetric and deviatoric creep moduli characterizing logarithmic creep read as:

$$C_v^{comp} = \frac{1}{18}\frac{1}{(1-\eta_c)(2-3\eta_c)}\Big[3(8\eta_c^2-23\eta_c+12)C_v^k + 8\eta_c(3-2\eta_c)C_d^k + \ldots \\ \eta_c\sqrt{225C_v^{k2}+720C_v^kC_d^k-1392C_v^kC_d^k\eta_c-720C_v^{k2}\eta_c+576C_d^{k2}\ldots \\ \overline{-768C_d^{k2}\eta_c+256C_d^{k2}\eta_c^2+528C_v^kC_d^k\eta_c^2+576C_v^{k2}\eta_c^2}\Big] \tag{10.25}$$

$$C_d^{comp} = \frac{1}{24}\frac{1}{(2-3\eta_c)}\Big[(24-16\eta_c)C_d^k-(15-24\eta_c)C_v^k+\sqrt{225C_v^{k2}\ldots \\ \overline{+720C_v^kC_d^k-1392C_v^kC_d^k\eta_c-720C_v^{k2}\eta_c+576C_d^{k2}\ldots} \\ \overline{-768C_d^{k2}\eta_c+256C_d^{k2}\eta_c^2+528C_v^kC_d^k\eta_c^2+576C_v^{k2}\eta_c^2}\Big] \tag{10.26}$$

The self-consistent solution exhibits an asymptote at an inclusion volume fraction of $\eta_c = \frac{2}{3}$, for which both compliance moduli become infinite and for which creep stops. The self-consistent solution simplifies when imposing a constant creep Poisson's ratio. In fact, with $\nu_k^{creep} = \frac{1}{2}$, it is readily found that $C_v^{comp} \to \infty$, which implies that any observable (logarithmic) creep deformation is deviatoric. Considering the two cases, $\nu_k^{creep} = 0$ for which

$3C_v^k = 2C_d^k$, and $\nu_k^{creep} = 0.2$ for which $3C_v^k = 4C_d^k$, we obtain:

$$\begin{cases} C^{comp}(\nu_k^{creep} = 0) = \dfrac{(-A-7)\left[(55-51\eta_c)+(1+3\eta_c)A\right]}{24(-2+3\eta_c)\left(19-18\eta_c+A\right)}C^k \\ \\ C^{comp}(\nu_k^{creep} = 0.2) = \dfrac{(-A-7)\left[(55-51\eta_c)+(1+3\eta_c)A\right]}{30(-2+3\eta_c)\left(19-18\eta_c+A\right)}C^k \end{cases} \tag{10.27}$$

where $A = \sqrt{289 - 504\eta_c + 216\eta_c^2}$. When recalling the asymptote at $\eta_c = \frac{2}{3}$, it is evident that the inclusion volume fractions (e.g., of clay) beyond this threshold value cannot be captured with a disordered granular morphology.

10.2.2.3 Application of Composite Models to Nanoindentation Results

By way of application, we employ the characteristic values of C^{comp} obtained by nanoindentation on the porous organic-rich clay composite, and divide the composite values with the characteristic creep modulus obtained for a pyrobitumen sample, $C^k = 80$ GPa. Consistent with the assumption that all porosity, ϕ, at this scale is situated within the kerogen, we plot the results as a function of the clay volume fraction, $\eta_c = 1-(\eta_k+\phi)$; and compare the experimental results with model predictions (obtained using Equations (10.23), (10.24), and (10.27)). The results displayed in Figure 10-6 show that the matrix-inclusion (Mori-Tanaka) model provides a lower bound to the experimental values, whereas the granular morphology defines an upper bound. This is not surprising, if we remind ourselves of the modeling assumptions:

- The matrix-inclusion morphology considers a continuous kerogen phase with clay as non-creeping ("rigid") inclusions−a morphology that

is relevant for immature systems.

- The granular morphology assumes disordered creeping kerogen particles mixed up in a self-similar fashion with non-creeping ("rigid") inclusions, which restrain the creep deformations of the kerogen particles much more than in the matrix-inclusion case. Such a granular morphology is relevant for highly mature systems.

With creep composite modeling results, two conclusions are emphasized. First, kerogen is the dominant creeping phase driving the creep rate magnitude in the clay composites. Clay particles creep at a rate two orders of magnitude smaller than that of porous kerogen. They play, therefore, the role of rigid inclusions, the volume fraction of which constrains the creep rate magnitude in the clay composites, and can even stop it. This first conclusion verifies Hypothesis II (stating that kerogen drives the creep behavior within source rocks). Second, it has been established that kerogen maturity affects the texture of the clay composites. These textures define two bounds for the creep rate magnitude of the clay composites: An upper bound defines a mature disordered system in which kerogen is dispersed and isolated; and a lower bound represents immature composites in which the kerogen is a continuous creeping matrix.

10.3 Kerogen Creep Kinetics and Deformation Mechanisms

Creep homogenization modeling at level I highlighted the role of the organics phase in driving the magnitude of the creep rates. It is in order, then,

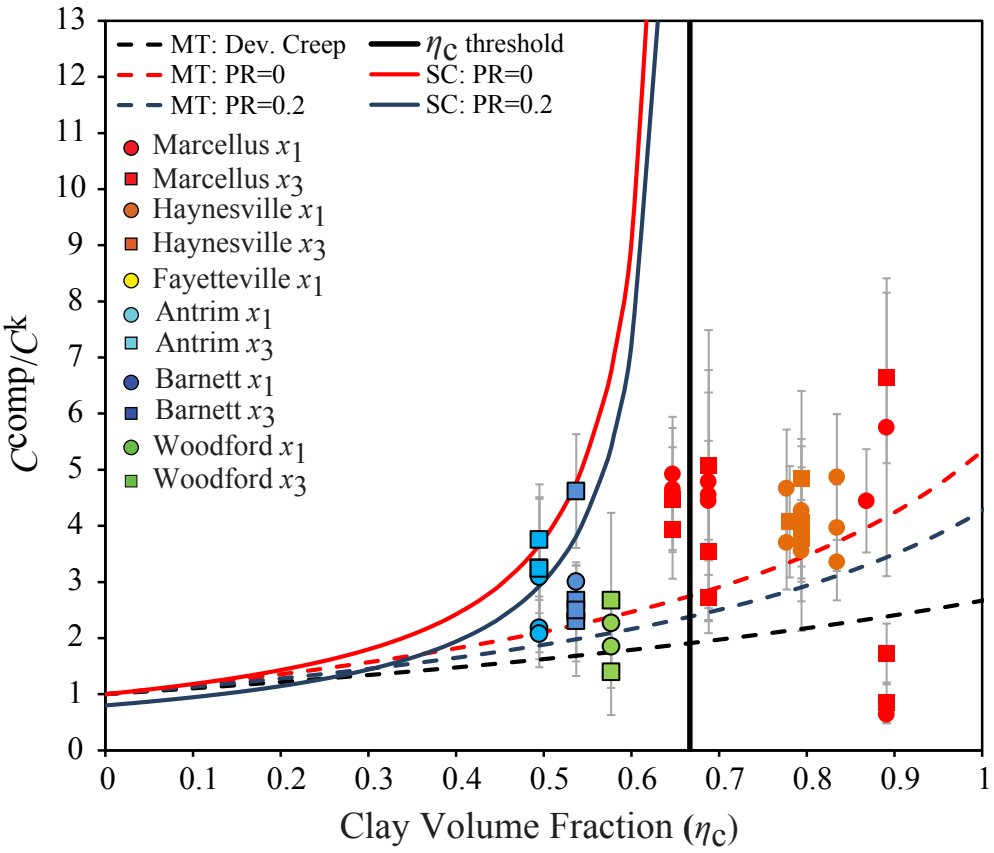

Figure 10-6: Creep homogenization models depicting relationship between creep behavior of organic-rich clay composites and their texture driven by thermal maturity. Models were built using $C^k = 80$ GPa. (MT = Mori-Tanaka formulation; SC = self-consistent formulation; PR = Poisson's ratio; η_c threshold: $\eta_c \leq \frac{2}{3}$; x_1 = data from indenting parallel to bedding planes; x_3 = data from indenting perpendicular to bedding planes).

to comment on the creep deformation at the kerogen level. Creep nanoindentation tests performed on mature organic-rich samples (pyrobitumen and shungite; Section 9.5.3) indicated a logarithmic kinetics at level 0. Creep models describing creep behavior in polymers can be adapted to immature organic matter, which was not available to test in this work. For instance, Yang et al. (2004) showed that a generalized Kelvin model describes polymeric creep behavior.

Time-dependent properties of polymers and organic matter are an active area of research. Creep deformation mechanisms in organic matter are not well understood. The complexity of organic molecules (density, skeleton chain length, bond hybridization$-sp^2$ vs. sp^3- and strength, fractions of aliphatic and aromatic compounds, to name just a few) makes molecular simulation the right tool to study chemical transitions in such material (Brenner et al., 2002) and relate their energy landscape to their mechanical properties. Only by imposing the right loading conditions in molecular studies, will one obtain and understand the creep mechanisms in an organic system, highlighting the interplay of its chemical, vibrational, and mechanical properties. Still, one intuitive way to answer the question of how kerogen creeps is to draw an analogy to the compaction mechanism at level I. The structure of a kerogen with a nanoporosity is expected to compact if subjected to compressive loads. This is a feasible mechanism as long as the bulk modulus, which varies exponentially with density (Bousige et al., 2016), allows a change in volume; or until the structure is no longer chemically stable under load, the effect of which is similar to temperature that reduces the activation energy of some reactions. Molecular simulations can highlight the extent and feasibility of such a scenario. Another possible

deformation mechanism in kerogen can simply be a chemical transformation in C-C bond hybridization and strength, leading to molecule chain breakage. A reconstruction of type II mature (from Marcellus) and immature (from Marine Type II and EagleFord) kerogen by Bousige et al. (2016) showed that, under tensile confined stress conditions, immature and mature kerogens behave in ductile and brittle manner, respectively. Such behavior is ascribed to variations in the C-C bond types. The authors show that, in immature kerogen, increasing strain leads to breaking sp^3 bonds into alkane chains and sp^2 bonds. This transformation in s-p hybridization causes the ductile behavior of immature systems. It might likewise favor deformation, stretching, and chain slippage. In comparison to stiff mature kerogen, rich in aliphatic compounds, chain slippage increases flow/mobility of an alkane chain and can explain the high creep rates of immature kerogen.

10.4 Creep Microindentation of Gas Shales: Relating Nanoscale to Macroscale Creep Properties

Creep microindentation testing is a natural step after defining creep kinetics and creep rate magnitudes at the clay composite level. Creep properties and behavior from creep microindentation tests help (1) bridge the scale gap between nanoscale and engineering scale; (2) reveal the role of kerogen in driving creep at a scale larger than that of the composite, thus, testing Hypothesis II beyond level I; and (3) compare creep from microindentation tests to macroscale creep experiments performed by Sone and Zoback (2013).

The comparison is our approach to test Hypothesis III.

10.4.1 Comparison of Macro-Creep Data and Creep Microindentation Results

It is valuable to show that creep indentation data, whether obtained experimentally or analytically by means of composite modeling, are creep properties relevant for engineering applications. This is achieved by comparing macroscopic creep data obtained by classical triaxial testing to creep microindentation data. Unfortunately, no macroscopic creep data are available for our specific samples. Typical triaxial creep tests on soils and rocks take days, weeks, or months to reach the secondary consolidation phase that can be compared with our creep measurements (Germaine and Germaine, 2009). It is thus not surprising that little macroscopic creep data on organic-rich shales are available in the open literature. Among those few, the creep investigation by Sone (2012) and Sone and Zoback (2013) is the most suitable one. The authors report strain measurements in orthogonal directions of three-hour-long creep experiments on core plugs (1-2 in long; 1 in diameter) of Haynesville-1V (V stands for vertical, indicating axial load perpendicular to bedding planes, i.e., along the x_3-direction) and Barnett-1H (H stands for horizontal, indicating axial load parallel to bedding planes, i.e., along the x_1-direction). Table 10.2 summarizes the chemistry of Sone (2012)'s specimen and compares it to our Barnett and Haynesville samples. A major difference between Barnett-1H and our Barnett sample is maturity. Unlike our Barnett, which is an immature source rock, Barnett-1H is mature (oil to wet gas window; T_{max} = 445-465°C) with R_o = 0.85-0.91. Haynesville-1V is

Table 10.2: Haynesville-1V and Barnett-1H compositions (in wt.%) and porosities as reported in Sone (2012). Q= quartz, F= feldspar, and P = pyrite.

	QFP	Carbonates	Clay	Kerogen	Porosity
Barnett-1H*	50-52	0-3	36-39	9-11	4-9
Barnett**	43.54	2.64	41.78	12.2	7.3
Haynesville-1V*	32-35	20-22	36-39	8	6
H2,H5, H6, H7***	40-50	9-22	38-45	2.6-3.3	6-7.6

*From Sone (2012).

**Reproduced from Table 2.2.

***Reproduced from Table 2.3.

an overmature rock (dry gas window; T_{max} = 525-545°C). Therefore, comparing our Haynesville samples to Sone and Zoback's Haynesville-1V, both being mature samples, is justifiable. On the other hand, we do not expect similarity in creep behavior between our Barnett and Sone's Barnett-1H.

To translate strain measurements from Sone's samples into creep moduli, we proceed as follows:

1. We use triaxial creep test conditions (creep load and confining stress) to build the triaxial experiment stress tensor:

$$\boldsymbol{\sigma}_{ij} = \begin{bmatrix} P_{diff} + P_c & 0 & 0 \\ 0 & P_c & 0 \\ 0 & 0 & P_c \end{bmatrix} \tag{10.28}$$

This allows us to obtain the deviatoric stress tensor,

$$\boldsymbol{s} = \boldsymbol{\sigma}_{ij} - \sigma_{mean}\mathbf{I} \tag{10.29}$$

where $\sigma_{mean} = \frac{1}{3}(\sigma_{11} + \sigma_{22} + \sigma_{33})$; and calculate the deviatoric stress magnitude,

$$s^d = \sqrt{\frac{1}{2}\boldsymbol{s} : \boldsymbol{s}} \tag{10.30}$$

2. We trace the axial (ϵ_{11}) and the lateral strain ($\epsilon_{22} = \epsilon_{33}$) data, interpolate strain data to the same time vector, and build a strain tensor:

$$\epsilon_{ij}(t) = \begin{bmatrix} \epsilon_{11}(t) & 0 & 0 \\ 0 & \epsilon_{22}(t) & 0 \\ 0 & 0 & \epsilon_{33}(t) \end{bmatrix} \tag{10.31}$$

This allows us to calculate $tr\epsilon = \epsilon_{11} + 2\epsilon_{22}$, obtain the deviatoric strain tensor,

$$\boldsymbol{e} = \boldsymbol{\epsilon}_{ij} - \epsilon_{mean}\mathbf{I} \tag{10.32}$$

and calculate the distortion magnitude:

$$\gamma = \sqrt{\frac{1}{2}\boldsymbol{e} : \boldsymbol{e}} = \sqrt{\frac{1}{3}} \mid \epsilon_{11} - \epsilon_{22} \mid \tag{10.33}$$

where $\epsilon_{mean} = \frac{1}{3}(\epsilon_{11} + \epsilon_{22} + \epsilon_{33})$.

3. We then plot $tr\epsilon(t)$ and $\gamma(t)$ and fit logarithmic functions (Figures 10-7 and 10-8) to the triaxial experimental data.

4. The volumetric and deviatoric creep compliance functions are thus obtained from their definitions (Equations (9.7) and (9.8)):

$$J^v(\frac{1}{MPa}) = \frac{tr\epsilon}{\sigma_{mean}} \tag{10.34}$$

$$J^d(\frac{1}{MPa}) = \frac{\gamma}{S^d} \tag{10.35}$$

5. These creep compliance rates allow for the following simplifications provided that the characteristic times << creep test duration (Chapter 9). Finally, we calculate the creep moduli from the creep compliance rate expressions:

$$\dot{J}^v(\frac{1}{s.MPa}) \sim \frac{a}{\sigma_{mean}t} = \frac{1}{C^v t} \tag{10.36}$$

$$\dot{J}^d(\frac{1}{s.MPa}) \sim \frac{c}{S^d t} = \frac{1}{C^d t} \tag{10.37}$$

where a and c are constants (see Figures 10-7 and 10-8). It should be noted that the use of time derivatives excludes anisotropic effects related to the anisotropic elastic behavior of the samples.

6. Using the determined volume and deviatoric creep moduli (C^v and C^d) as input, the contact creep modulus, C, is calculated from its very definition (10.15).

Tracing the lateral strain data in Barnett-1H was a challenging task as the data was very noisy and lateral strain negligible. We assume therefore no

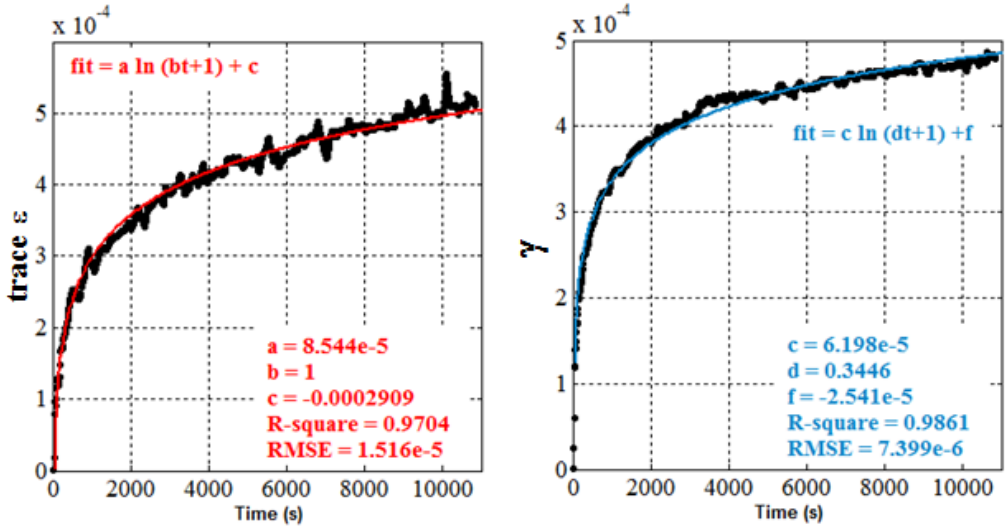

Figure 10-7: Logarithmic functions fitting the trace of the strain tensor (left) and distortion (right) of Sone and Zoback (2013) strain data from triaxial creep test on Haynesville-1V. Confining pressure, P_c, is 30 MPa and differential stress, P_{diff}, is 29 MPa. Constants a and c are the fitting coefficients needed in Equations (10.36) and (10.37). Characteristic times are 1 s and 2.9 s for the trace and distortion fits, respectively.

lateral strain in Barnett-1H during the axial creep ($\epsilon_{22} = \epsilon_{33} = 0$) and work only with axial strain. Calculation of C^v and C^d for Haynesville-1V and Barnett-1H are given in Table 10.3.

Table 10.3: Creep moduli of Haynesville-1V and Barnett-1H obtained from a logarithmic fit to strain data reported by Sone and Zoback (2013).

	Haynesville-1V	Barnett-1H
C^v (GPa)	464	1,963
C^d (GPa)	270	2,617
C (GPa)	726	5,444

To compare creep results obtained from the macroscale triaxial creep tests of Sone and Zoback (2013), widely-spaced (10 to 50 μm) creep microin-

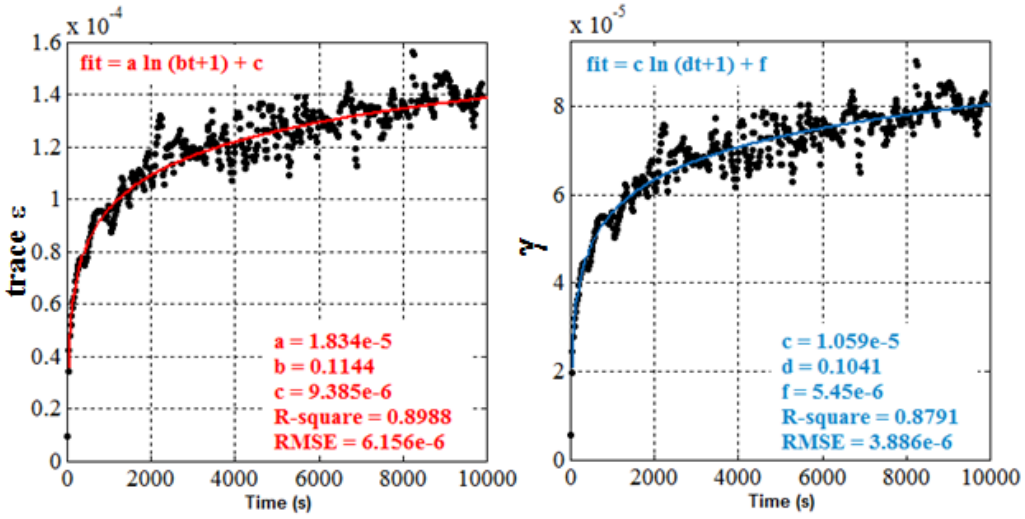

Figure 10-8: Logarithmic functions fitting the trace of the strain tensor (left) and distortion (right) of Sone and Zoback (2013) strain data from triaxial creep test on Barnett-1H. Confining pressure, P_c, is 20 MPa and differential stress, P_{diff}, is 48 MPa. Constants a and c are the fitting coefficients needed in Equations (10.36) and (10.37). Characteristic times are 8.7 s and 8.3 s for the trace and distortion fits, respectively.

dentation tests with loads ranging from 12 mN to 50 mN[2] were performed on all formations studied.

High-load creep indentations, i.e., microindentations, allow the indenter to reach deeper into the material (Figure 2-14). Larger volumes are thus homogenized (Section 2.6) to add the effect of inclusions to the mechanical response. As a reminder (Section 3.3), indentation depth scales, for a homogeneous material indented by a cone (or a Berkovich probe), with the square root of the load, $h \propto P^{\frac{1}{2}}$. That is, the increase in load from $P_{max} = 4.8$ mN to $P_{max} = 12$ mN, for instance, is expected to increase the indentation depth by $(\frac{h_1}{h_2})$=1.58. The same depth increase results from in-

[2]Tests with loads greater than 50 mN could not be performed due to the load capacity of the microindenter machine.

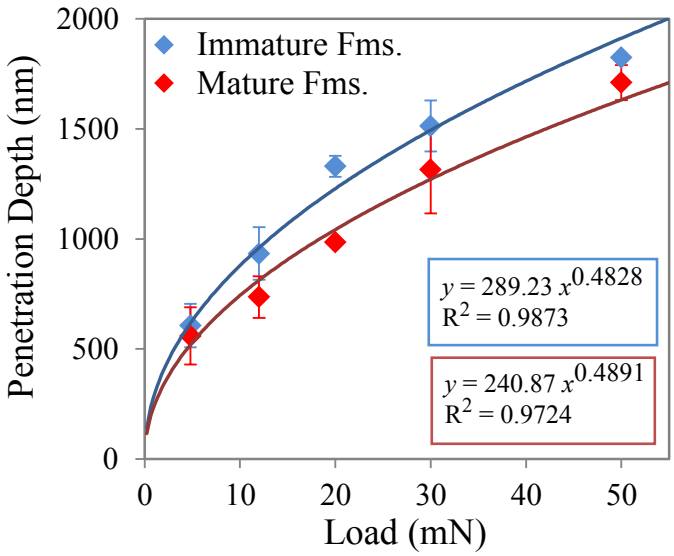

Figure 10-9: P-h plots of indentation depths reached in mature and immature formations.

creasing P_{max} from 12 mN to 30 mN. Figure 10-9 shows that the mature and immature formations studied adhere to this load-depth scaling relationship. Comparing depths (Tables 9.12, 9.13, and 10.4-10.6) experimentally, an average increase of $(\frac{h_1}{h_2})$=1.32 for mature formations and $(\frac{h_1}{h_2})$=1.33 for immature formations is seen. The lower increase than theoretically predicted is attributable to the heterogeneity of the samples; that is, while nanoindentation (with our chemomechanical clustering method) probes the clay-kerogen composite (level I), microindentation probes the clay-kerogen-inclusion composite (level II). As the material volume probed by indentation scales with the indentation depth (typically 3-5 $\times$ h_{max}; Ulm et al., 2010), a microindentation test probes a volume double or triple in characteristic size than the volume probed by nanoindentation. The size distribution of inclusions was not investigated in this research. However, monitoring how

Table 10.4: Mechanical properties and penetration depths from creep microindentation tests with different loads on Haynesville.

Sample*	Machine	Load	H_{creeep} (GPa)		M_{creeep} (GPa)		h_{creeep} (nm)		C (GPa)	
		(mN)	μ_x	σ_x	μ_x	σ_x	μ_x	σ_x	μ_x	σ_x
A5H$x_1$cg3	HYS	12	1.39	0.36	42.14	4.94	701.69	92.75	761.32	336.74
A5H$x_1$cg4,5	UNHT	12	1.43	0.87	45.96	7.67	755.28	133.46	625.11	382.22
A5H$x_1$cg6	UNHT	20	1.13	0.47	43.74	7.89	984.80	149.48	593.92	303.26
A6H$x_1$cg3	HYS	12	1.12	0.67	50.30	12.83	807.58	231.69	498.96	422.23
A6$x_1$cg5,6	UNHT	12	1.06	0.33	44.13	7.42	793.37	145.34	512.61	167.38
A6H$x_1$cg4	UNHT	30	0.98	0.28	44.73	8.10	1273.75	161.64	520.47	189.32
A7H$x_1$cg3	HYS	12	1.44	0.91	49.90	9.41	719.1	170.72	671.59	651.60
A5H$x_3$cg1	HYS	12	1.28	1.06	30.45	9.87	811.70	229.56	755.37	883.06
A5H$x_3$cg4	UNHT	30	0.66	0.33	30.20	7.54	1644.08	377.22	288.02	202.72
A6H$x_3$cg3a	HYS	12	1.15	0.5	36.84	8.33	788.33	152.47	585.82	411.40
A6H$x_3$cg3b	HYS	12	1.18	0.62	35.16	7.54	813.65	155.85	596.87	526.66
A6H$x_3$cg4	UNHT	30	0.82	0.53	29.11	10.48	1534.53	354.60	383.36	222.00
A6H$x_3$cg5	UNHT	50	0.99	0.50	31.70	8.35	1791.48	325.52	453.88	224.51
A7H$x_3$cg4	HYS	12	1.60	0.96	48.97	14.2	717.16	210.58	854.31	623.48

*Phases are separated with clustering analysis using mechanical data.

Averages and standard deviations are calculated combining all phases, except the inclusion phase (refer to text).

Table 10.5: Mechanical properties and penetration depths from creep microindentation tests with different loads on Marcellus.

Sample*	Machine	Load	H_{creeep} (GPa)		M_{creeep} (GPa)		h_{creeep} (nm)		C (GPa)	
		(mN)	μ_x	σ_x	μ_x	σ_x	μ_x	σ_x	μ_x	σ_x
Mar46$x_1$cg4	Hys	12	1.43	0.76	59.52	16.34	792.51	481.18	631.55	376.78
Mar49$x_1$cg2	Hys	12	1.48	0.58	59.65	13.56	745.35	380.51	641.64	330.76
Mar49$x_1$cg4	UNHT	12	1.88	0.50	64.09	9.83	574.65	75.21	957.12	321.22
Mar49$x_1$cg3	UNHT	30	1.58	0.30	55.23	6.29	1000.07	97.70	856.47	219.90
Mar108$x_1$cg4	HYS	10	1.70	0.70	53.20	9.30	609.22	109.48	641.94	405.96
Mar108$x_1$cg7	HYS	12	1.50	0.50	50.76	6.84	697.37	101.84	669.28	369.98
Mar108$x_1$cg8	UNHT	30	0.93	0.19	37.57	6.19	1303.16	120.69	513.67	171.14
Mar108$x_1$cg9	UNHT	50	0.94	0.29	37.36	6.13	1707.94	243.98	521.15	181.15
Mar151$x_1$cg3	Hys	12	1.50	0.81	47.58	9.89	658.98	134.96	714.35	602.85
Mar151$x_1$cg5	UNHT	12	1.16	0.32	36.54	6.06	742.78	86.08	613.69	211.18
Mar151$x_1$cg4	UNHT	30	1.08	0.37	35.75	5.58	1245.73	171.10	601.41	231.12
Mar46$x_3$cg3	HYS	12	1.90	1.24	58.21	14.28	615.75	158.12	1003.12	1007.32
Mar49$x_3$cg1	HYS	12	1.60	0.96	48.97	14.23	717.16	210.58	854.31	625.52
Mar49$x_3$cg2	UNHT	30	1.17	0.34	38.83	6.49	1197.49	184.11	541.59	185.34
Mar49$x_3$cg3	UNHT	50	1.11	0.47	32.74	6.47	1631.70	276.09	517.81	240.01
Mar108$x_3$cg3	HYS	12	1.12	0.42	35.33	7.15	789.76	227.91	498.03	291.14
Mar151$x_3$cg2	HYS	12	0.95	0.55	34.23	12.51	999.82	612.64	472.80	348.93
Mar151$x_3$cg4	UNHT	12	1.09	0.44	31.20	7.70	813.86	144.41	573.84	282.75
Mar151$x_3$cg3	UNHT	30	0.99	0.38	30.63	7.27	1321.24	199.92	580.78	246.46

*Phases are separated with clustering analysis using mechanical data.

Averages and standard deviations of all phases, except inclusion phase, are reported (refer to text).

Table 10.6: Mechanical properties and penetration depths from creep microindentation tests with different loads on Antrim, Barnett, and Woodford.

Sample*	Machine	Load	H_{creeep} (GPa)		M_{creeep} (GPa)		h_{creeep} (nm)		C (GPa)	
		(mN)	μ_x	σ_x	μ_x	σ_x	μ_x	σ_x	μ_x	σ_x
Antrim$x_1$cg4	HYS	12	0.83	0.44	28.25	6.22	844.82	300.73	295.06	233.25
Antrim$x_1$cg5	UNHT	12	1.01	0.51	32.53	7.52	849.23	149.11	408.76	265.75
Antrim$x_1$cg3	UNHT	30	1.01	0.51	33.48	7.18	1330.39	229.97	389.12	240.93
Antrim$x_1$cg6,7	UNHT	50	0.88	0.30	30.91	6.26	1824.32	246.83	332.32	133.29
Antrim$x_3$cg3	HYS	12	1.03	0.67	24.34	6.47	773.17	177.69	407.02	406.35
Antrim$x_3$cg4	UNHT	30	0.84	0.37	23.76	5.93	1465.38	247.15	345.91	190.16
Barnett$x_1$cg3	HYS	12	0.71	0.44	22.49	5.98	949.72	325.30	263.63	238.69
Barnett$x_1$cg4	UNHT	30	0.66	0.26	223.81	4.97	1595.03	218.57	254.99	108.19
Barnett$x_3$cg3	HYS	12	0.70	0.40	18.53	4.49	911.08	157.40	263.56	225.42
Barnett$x_3$cg4	UNHT	30	0.65	0.17	22.86	4.56	1596.97	213.47	236.77	73.34
WoodfA$x_1$cg6	HYS	12	0.63	0.34	22.33	3.74	976.67	184.13	203.83	168.41
WoodfA$x_1$cg3	UNHT	12	0.79	0.39	23.62	5.31	1017.84	222.21	249.08	128.28
WoodfA$x_1$cg4	UNHT	20	0.82	0.32	24.93	3.80	1295.80	187.12	241.57	95.49
WoodfA$x_1$cg5	UNHT	30	0.68	0.25	24.23	4.51	1578.59	235.88	243.23	95.87
WoodfA$x_3$cg3	UNHT	20	0.65	0.35	20.58	5.41	1363.74	270.43	216.74	108.20

*Phases are separated with clustering analysis using mechanical data.

Averages and standard deviations are calculated combining all phases, except the inclusion phase (refer to text).

mechanical properties change with increasing loads (occasionally reaching 50 mN) reflects the extent of homogenization under the indenter tip. This homogenization shows whether (or not) inclusions are being incorporated in the mechanical response, and whether the microindentation response represents the right mechanical properties of the REV at the microscale. Finally, from every creep microindentation grid, the various phases were isolated via clustering analysis using only mechanical parameters (C, M_{creep}, and H_{creep}).

Due to the high loads applied, large volumes are homogenized under the indenter tip (Figure 2-14). Clustering analysis is expected to produce mixture (clay composites and inclusions) and inclusion phases. Figure 10-10 shows results of a clustering analysis using mechanical data from Antrim. The data is obtained from two microindentation grids performed in the x_1-direction with a load of 50 mN. Two mixture phases (Phases 1 and 2) are seen. Phase 3 is interpreted to be a cluster combining microindentation tests falling on inclusions. Compared to the mixture phases, the inclusion phase has a high contact creep modulus and a low measured depth, both of which indicate low creep rates and a homogenized volume dominated by the size of inclusion(s). The mechanical properties of Phase 3, therefore, represent inclusions' properties rather than those of the REV at the microscale. In what follows, the inclusion phases in every microindentation grid performed are disregarded. Data reported in Tables 10.4 to 10.6 are averages of mechanical properties of the mixture phases in every grid.

The creep microindentation data shows that, as load increases, mean C values do not change in immature formations and fluctuate within 100-250 GPa around a mean value in mature ones. The difference in the mean C values in mature formations can be due to:

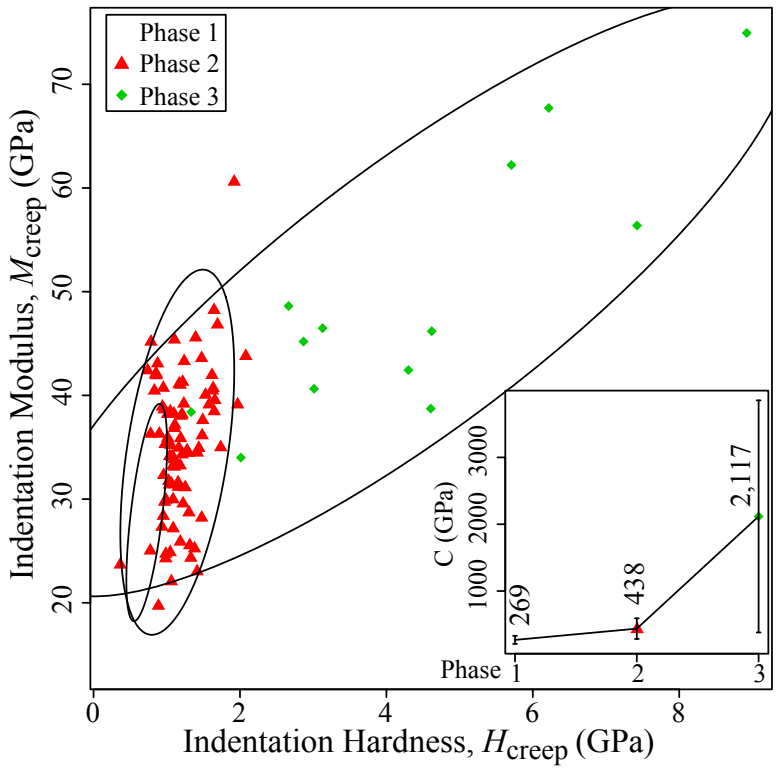

Figure 10-10: The results of clustering analysis using mechanical data from Antrimx_1-cg6 and Atrimx_1-cg7. Creep microindentation tests were obtained applying a load of 50 mN. Phases 1 and 2 are mixture phases in which homogenized creep properties are from clay composites and inclusions. Phase 3 is an inclusion phase, which is not considered in our microindentation data.

- The phase distribution is random in a mature texture. The volumes tested at every indentation location can include different material producing different properties. This is reflected in the high standard deviations (calculated using $\sqrt{\frac{(x-\overline{x})^2}{n-1}}$; where n is the sample size, and $\overline{x}$ is the sample mean) in the C values obtained in grids done with 12 mN.

- Data is obtained averaging all microindentation tests except those

clearly falling on inclusions. As load increases (20, 30, and 50 mN), a better material homogenizing (than a simple averaging of results acquired with 12 mN) produces the true mechanical response at the microscale, reducing the standard deviation of C.

Creep microindentations on Haynesville and Barnett samples provide a mean indentation creep moduli of $C = 616.68$ GPa and $C = 258.90$ GPa, respectively. The C values are obtained from averaging all microindentation tests performed on all Haynesville (A5H, A6H, and A7H) and Barnett grids in both x_1- and x_3-directions. This averaging is justified as creep anisotropy is negligible in gas shales. As expected when inclusions are added to the homogenized volume under the indenter tip, C values from microindentation tests are higher than the values obtained in the porous organic-rich clay composites using nanoindentations. From Chapter 9, we recall that the contact creep moduli of the clay composites in Haynesville and Barnett were $C = 324$-352 GPa and $C = 189$-192 GPa, respectively. We note, therefore, that the order of magnitude of the contact creep moduli obtained from nano- and microindentation tests remains the same. Therefore, at the scale of microindentation, the porous kerogen-clay composite still dominates the overall creep rate magnitude, especially in immature formations containing less stiff organic matter.

A comparison of the macro-creep values with the values obtained by microindentation is now in order. For reference, the contact creep modulus for Sone and Zoback (2013)'s data (Table 10.3) is $C = 726$ GPa and $C = 5{,}444$ GPa for the Haynesville-1V and Barnett-1H, respectively. We find a remarkable agreement between the mean $C = 617$ GPa obtained from microindenting our Haynesville samples (A5H, A6H, and A7H) and $C =$

726 GPa for the Haynesville-1V plug tested by Sone and Zoback (2013). The low creep rate obtained for the Barnett-1H (C = 5,444 GPa) can be due to the fact that 1) unlike our immature Barnett, Barnett-1H is a mature sample (T_{max} = 435°C; HI = 824); 2) Barnett-1H has a high quartz content; and 3) we ignored the radial strain data from the triaxial tests. In fact, if the quartz in Barnett-1H was finely intermixed with the clay particles, the creep deformation of the kerogen phase would be further confined not only by the solid clay particles, but also by the quartz inclusions. This would entail a level I creep modulus typically one order of magnitude greater than the one we determined by assuming scale separability between the clay particles and quartz particles (our two-scale model; explained below).

In addition to the experimental result comparison, we use the self-consistent relation (10.27) of the creep upscaling models to predict the creep rate magnitude in the macrosamples. This requires as input the volume fractions of the material at different scales. Thus, using the XRD data (Table 10.2), TOC (determined through pyrolysis), and porosity (reported in Sone, 2012), we estimate the volume fractions at levels I and II of Sone's over-mature Haynesville-1V and mature Barnett-1H by considering, according to our creep model assumptions, that all porosity is in kerogen. These volume fractions, summarized in Table 10.7, show an almost identical volumetric make-up between Haynesville-1V and Barnett-1H. We also note that, at the macroscopic scale, the inorganic phase occupies more than two-thirds of the volume; which means that the application of the self-consistent scheme will lead to an infinite contact creep modulus. It is for this reason, that we employ the self-consistent model in a two-step fashion in two different forward approaches, the 2-scale model approach and 1-scale model approach:

Table 10.7: Creep modulus predictions in Sone and Zoback (2013)'s Haynesville-1V and Barnett-1H samples using the creep homogenization scheme in mature samples. C values reported are in GPa.

	Haynesville-1V		Barnett-1H	
Volume Fraction	Level I	Level II	Level I	Level II
Non-Clay Inclusion	N.A.	0.45	N.A.	0.44
Clay Inclusion	0.58	0.23	0.57	0.24
Porous Kerogen	0.42	0.31	0.43	0.32
C_{exp}		726*		5444*
C_{model}, forward application				
2-scale: PR=0(0.2)	561(449)**	1651(1057)	505(404)**	1425(1140)
1-scale: PR=0(0.2)	338***	994(795)	191****	528(431)
C_{model} inverse application				
2-scale: PR=0, $C^k = 35$	246	722	221	624
2-scale: PR=0.2, $C^k = 55$	309	727	278	784

*From bulk and shear creep moduli of Sone and Zoback (2013), Table 10.7.

**Self-consistent scheme with C=80 GPa for porous kerogen and a creep Poisson's ratio of 0 (and 0.2).

***From creep nanoindentation on mature A5H, A6H, and A7H.

****From creep nanoindentation on our immature Barnett sample.

- C_{model} (2-scale): we first homogenize the level I constituent properties using a contact creep modulus for kerogen of C= 80 GPa, the clay inclusion volume fraction at level I, and relation (10.27). The composite values so obtained of C are then used with the additional non-clay inclusion volume fraction to predict level II properties of Haynesville-1V and Barnett-1H. The values are reported in Table 10.7 (labeled as "C_model, forward application/(2-Scale)") for two creep Poisson's ratios ($\nu = 0$ and 0.2).

- C_{model} (1-scale): we use Level I C values obtained from creep nanoindentation tests. C values at level II are obtained using creep nanoindentation results, the non-clay inclusion volume fraction, and relation (10.27).

With the forward approaches defined, we remind ourselves that Barnett-1H, compared to Haynesville-1H, shows much less axial strain and no lateral strain (Figure 10-8). This is reflected in the remarkably low experimental creep rates calculated for Barnett-1H using the triaxial creep test results (Table 10.3). Also, due to similar maturities between our Haynesville samples and Haynesville-1V, we expect the 1-scale and 2-scale model approaches to produce similar results for the Haynesville but not for Barnett. The creep nanoindentation results obtained from our immature Barnett should not reflect the level I creep rate in Sone's mature Barnett-1H sample. Indeed, they do not. Using the 1-scale model upscaling to level II gives the right order of magnitude of C in Haynesville-1V, but fails to predict C at level II for Barnett-1H. The 2-scale homogenization model works better for both samples; the overestimate of level I composite properties in both samples isattributed to the value C^k = 80 GPa used. We recall that this value of C^k is obtained from pyrobitumen, which might not be representative of the organic matter in Sone's samples. At level II, the 2-scale model results substantially improve for Barnett-1H, giving the right order of magnitude for C (refer to Table 10.3). The good agreement between the creep model results and experimental data on Haynesville encourages us to use the model in an inverse application to predict C^k in Sone's samples. Relation (10.27) reproduces the experimental C values in Haynesville-1V for a C^k = 35-55 GPa (Table 10.7). In fact, relation (10.27) using a Poisson's ratio $\nu = 0.2$ and C^k = 55 GPa reflects excellent agreement with both creep nanoindentation results (C^{LevelI} =

338 GPa) as well as macroscale triaxial creep tests ($C^{LevelII}$ = 726 GPa). However, values of C^k = 35-55 GPa still fail to predict the experimental results of Barnett-1H.

The creep homogenization models prove to be good predictors of creep rates at levels I and II. In Section 10.2.2.3, the models produce two texturally-defined asymptotes: a lower bound that reflects the role of a creeping kerogen matrix in immature composites, and an upper bound that reflects the role of dispersed creeping kerogen in mature composites. These texturally-defined asymptotes attest to the role of kerogen driving creep rates in the clay composites. Also, the creep homogenization models demonstrate an adequate potential to predict creep rates at level II. The 1-scale and 2-scale forward approaches produced C values in good agreement with experimental results from creep triaxial tests for a given maturity (Sone and Zoback, 2013). The creep modeling predictions can greatly improve when the creep properties of the organic matter are well understood and measured. Unfortunately, this is rarely the case; thus, the homogenization models, if implemented in an inverse application, can prove a valuable tool to predict creep rates of organic matter.

10.4.2 Microscale C-H Scaling: The Role of Kerogen Maturity

The role of kerogen in driving the creep rate of source rocks was seen in experimental and modeling results. Experimental results (Chapter 9) and creep modeling (Section 10.2.2.3) showed that:

- The clay composites are the phases with the highest creep rates (Section 9.5.4);
- The mechanical anisotropy decreases with creep deformation (Figure 9-16), and creep properties show negligible anisotropy (Tables 9.10 and 9.11), highlighting the role of the isotropic porous organic phase driving creep;
- The difference in magnitude between creep rates of mature organic matter (pyrobitumen) and clay mineral (muscovite) suggests that the clay particles play the role of rigid inclusions that contribute minimally to creep rates; and
- The multi-scale creep modeling reflects maturity-dependent textures (Hubler et al., submitted).

In this section, we recall one specific experimental result seen at the clay composite level, that is the $C = \alpha H$ scaling relationship (Figure 10-2), which is found to depend on maturity at level I. With creep microindentation tests performed on mature and immature formations, the C-H scaling is revisited with the following objectives in mind: 1) to emphasize the role of the clay particles as rigid inclusions limiting creep deformation, and 2) to highlight differences, if any, in what the linear C-H scaling captures at different scales.

Figures 10-11 and 10-12 show the C-H scaling using creep microindentation tests performed with loads of 12 mN[3] and higher (20, 30, and 50 mN), respectively. These C-H scaling relationships (Figures 10-11 and 10-12) show consistent C-H scaling regardless of the scale probed. The only difference is the scaling factor (α) between rocks with different maturities. As this C-H scaling is scale-independent, all creep indentation data (acquired at all loads) are combined. This combination produces α^{mat}= 497 and α^{imm}= 357 (Figure 10-13; Table 10.8). The constant C-H scaling factor, α, for formations of the same maturity but with variable original packing densities (η_0) indicates that the creep deformation mechanism (secondary consolidation and compaction) is solely driven by the organic phase: the phase with the highest creep rates in the source rocks. Consequently, the coefficient of secondary consolidation, $C_{\alpha\epsilon}$[4], scales as η_0^{-1}. The fact that α is scale-independent captures the effect of kerogen at the organic-rich clay composite level (level I) as well as the microscale (level II). The role of clay particles, therefore, is that of non-creeping rigid inclusions, as assumed in our multiphase creep model. Finally, the dependence of α on maturity ($\alpha^{mat} > \alpha^{imm}$) evokes changes in the void ratio in the organic phase (e^k) with maturity[5]. The experimental data ($\alpha^{mat} > \alpha^{imm}$) thus suggests a higher void ratio in immature formations than mature ones, given by:

$$e^{k,mat} = \frac{\phi^{k,mat}}{1 - \phi^{II}} \tag{10.38}$$

[3]As with the case of creep nanoindentations, the Hysitron creep microindentation results performed with $P_{max} = 12$ mN were corrected to match creep microindentation results obtained with the UNHT (Appendix B).

[4]The α in the subscript of the coefficient of secondary consolidation is not to be confused with the C-H scaling factor.

[5]$e^k = \dfrac{1-\eta^I}{\eta} = \dfrac{\phi^k}{1-\phi^{II}}$ where η is the packing density, and ϕ is porosity.

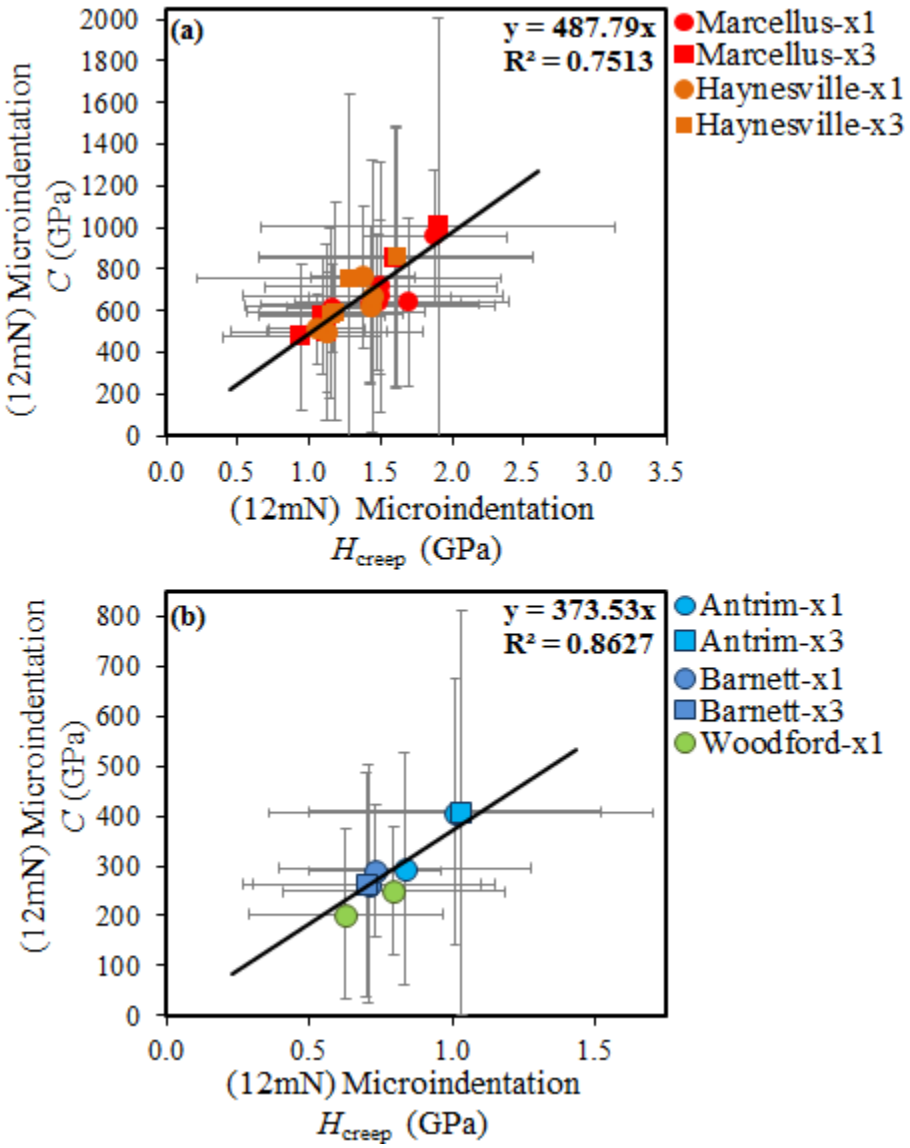

Figure 10-11: A plot of contact creep modulus, C, versus hardness, H_{creep}, in (a) mature and (b) immature formations showing a maturity-dependent linear correlation between the 2 mechanical properties. Data are from creep nanoindentation tests performed at $P_{max} = 12$ mN using both the UNHT and Hysitron (Appendix B).

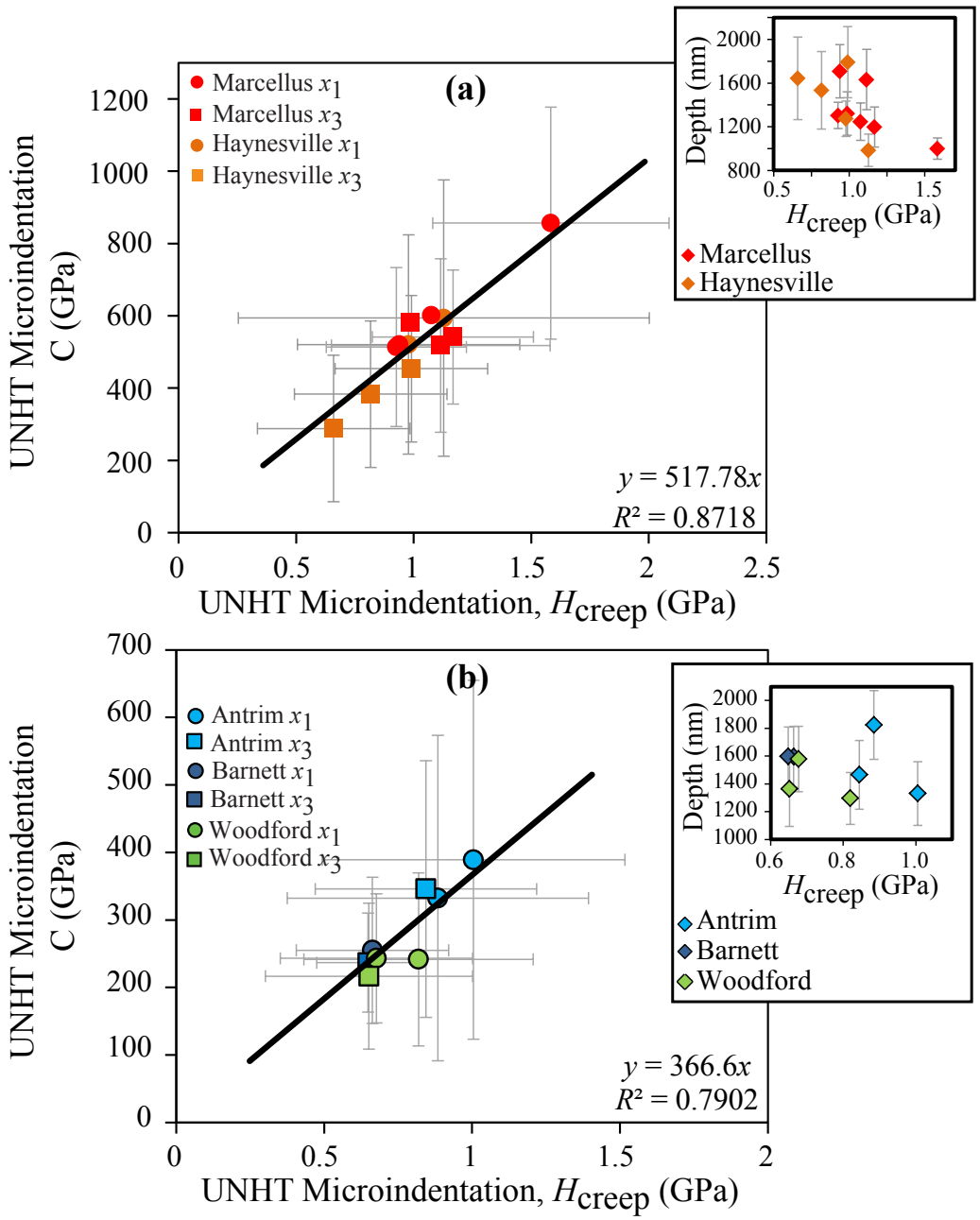

Figure 10-12: A plot of contact creep modulus, C, versus hardness, H_{creep}, in (a) mature and (b) immature formations showing a maturity-dependent linear correlation between the 2 mechanical properties. Data are from creep nanoindentation tests performed at P_{max} = 20, 30, and 50 mN on the UNHT. Insets show the depths of penetration reached in both types of formations.

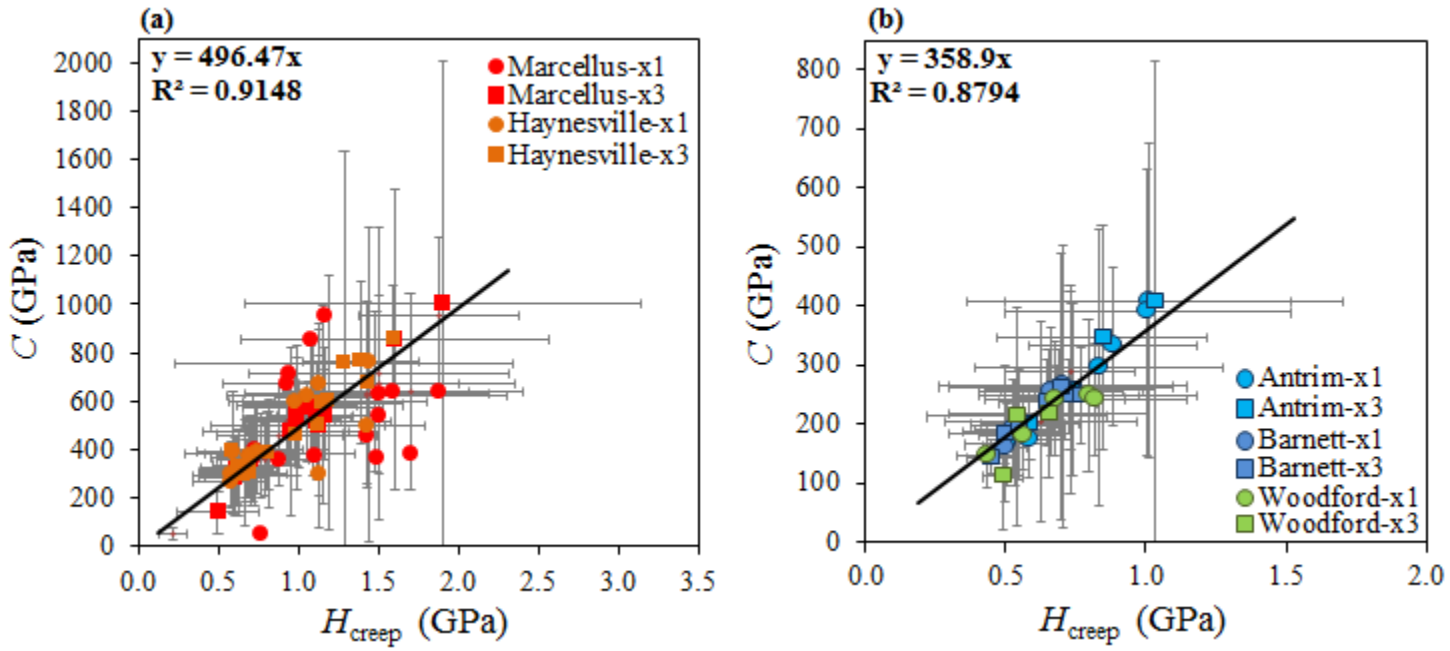

Figure 10-13: A plot of contact creep modulus, C, versus hardness, H_{creep}, in (a) mature and (b) immature formations showing a maturity-dependent linear correlation between the 2 mechanical properties. Data are from creep indentation tests performed varying P_{max} (4.8, 12, 20, 30, and 50 mN) using both machines (UNHT and Hysitron).

Table 10.8: The C-H scaling parameter, α, obtained from creep nano- and microindentations performed on mature and immature source rocks using the UNHT and Hysitron. Data shows that the C-H scaling is scale-independent (mat = mature, imm = immature).

Load	Mature Fms.			Immature Fms.		
(mN)	α^{UNHT}	$\alpha^{corr.HYS}$	α^{all}	α^{UNHT}	$\alpha^{corr.HYS}$	α^{all}
4.8	491	503	499	343	344	341
12	495	496	488	377	378	374
20, 30, 50	518	N.A.	518	367	N.A.	367
all loads	$\alpha^{mat} = \mathbf{497}$			$\alpha^{imm} = \mathbf{359}$		

$$e^{k,imm} = \frac{\phi^{k,imm}}{1 - \phi^{II}} \tag{10.39}$$

where ϕ^{II} is the sample porosity. k, 'mat', and 'imm' stand for kerogen, mature, and immature, respectively.

The results thus obtained, reflecting higher void ratios in immature formations than mature ones, implies the following. The C-H scaling factor captures maturity but fails to capture the nanoporosity (pores $<$ 10 nm) generated in maturing organic matter. Experimental results suggesting an $e^{k,mat} < e^{k,imm}$ are better perceived as proxies to qualitatively describe effective (macro) porosity in facies with different maturity: In immature facies, a continuous organic phase accesses and connects micro (< 0.75 μm), and macroporosity (≥ 0.75 μm), creating a higher effective porosity. This is not the case in mature systems in which the organic phase, despite its nanoporosity, is randomly dispersed and isolated.

Our results, therefore, reflect the role of kerogen in creating an effective porosity in a source rock. They also hint at the importance of differentiating maturity levels of organic pockets within the same source rock (e.g., see Figure 2-11, which shows two kerogen regions with remarkably different nanoporosities) and quantifying their nanoporosity that our C-H scaling factor fails to capture.

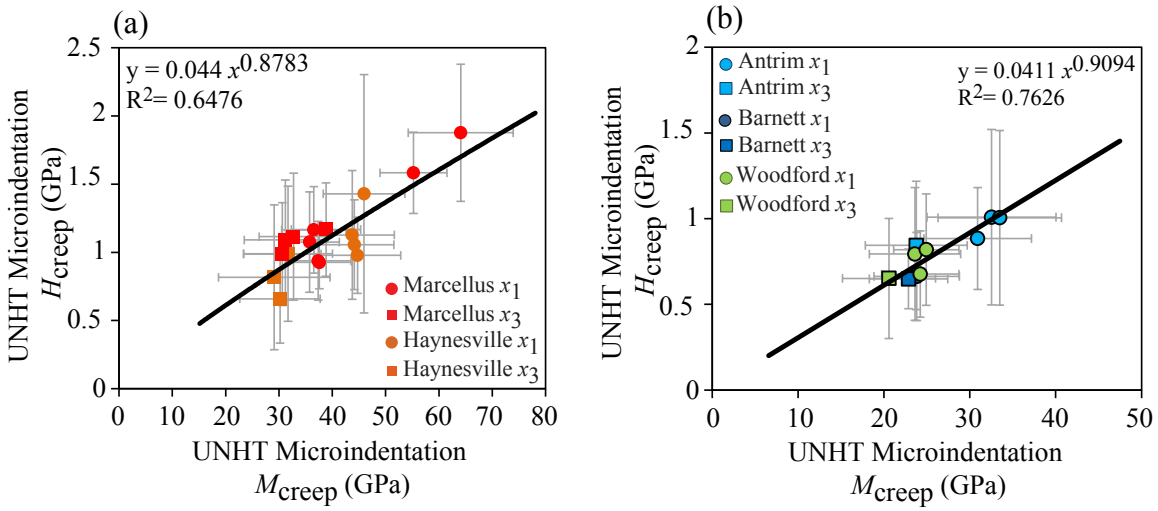

Figure 10-14: M_{creep}-H_{creep} from creep microindentation tests performed using the UNHT machines with loads ranging between 12 to 50 mN on a) mature and b) immature formations.

10.5 Microscale Functional Scaling Relationship

Time-independent and time-dependent nanoindentation tests produced M and H related via a power law. Bao et al. (2004) showed that a relation of the form $E_r = 0.6647\sqrt{HR_s}$ exists between M and H. The ratio $\frac{M^2}{H}$ (as seen in Chapter 8) describes the energy dissipation inside the material due to indentation. In their theoretical derivation of R_s, Bao et al. (2004) relied on a key feature of an indentation test: the elastic deformation at the perimeter of indentation reflected in the depth h_s (Figure 3-8). We here argue that the deformation at the contact perimeter is no longer purely elastic during creep indentation tests. In fact, Vandamme et al. (2012) showed that plastic phenomena occur at the material-indenter contact during creep tests. Therefore, after creep deformation, M_{creep} and H_{creep} are no longer expected to be related as described by Bao et al. (2004). Indeed, our creep microindentation results show that M_{creep} and H_{creep} are related by a power law in mature formations (Figure 10-14a) and linearly in immature formations (Figure 10-14b). These M_{creep}-H_{creep} scaling relationships (Figure 10-14) along with the maturity-dependent C-H_{creep} (Figure 10-13) allow us to relate

C and M_{creep} as follows:

$$C = \alpha H_{creep} = \alpha\beta M_{creep}^{\gamma} \tag{10.40}$$

Experimentally, Equation (10.40) translates into the scaling shown in Figure 10-15 between C and M_{creep}. We note that the C-M_{creep} relationship is valid despite the creep deformation as no significant changes are seen between M_o (obtained from short hold-time nanoindentation tests) and M_{creep} (Figure 9-14). Consequently, M_{creep} still describes the elastic properties of the indented material.

The rationale behind the above exercise is the norm in petrophysics and well-log interpretation to derive mechanical properties from sonic measurement and relate stiffness to sonic velocities (correcting for the measurement frequency effects). Therefore, a C-M_{creep} relationship is of great value as it allows direct access to creep rates from sonic and density measurements, usually acquired in almost every drilled well. A C log constructed from sonic-while-drilling measurements or after open/cased hole logging helps determine, at a very early stage, good-quality facies for fracking. This key property helps predict the production lifetime of a fracking stage. If integrated in well/field cost estimates, better decisions can be made about fracking formations and completing wells.

10.6 Chapter Summary

The overall picture which emerges from creep indentation tests can be summarized as follows:

- Creep in organic-rich shales is logarithmic and driven by the porous kerogen phase. We come to this conclusion from different angles: (i) inspection of nano- and microindentation creep curves, as well as macroscopic triaxial creep data; (ii) an analysis of the secondary consolidation adapting the relevant tools of clay science and soil mechanics to nanoindentation (e.g., linear C-H relationship); and (iii) an inspection of the change in packing density of the kerogen-rich porous clay phase

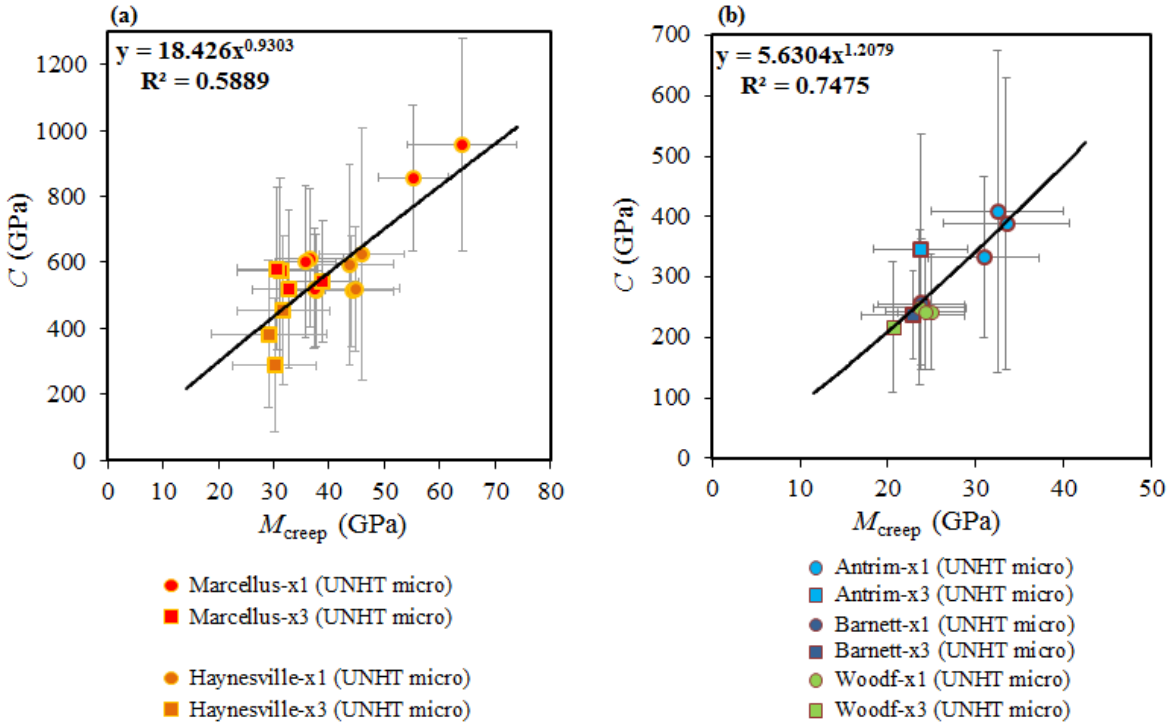

Figure 10-15: A plot of contact creep modulus, C, versus Indentation stiffness, M_{creep}, in (a) mature and (b) immature formations. Data are from creep microindentations done with loads ranging from 12 mN to 50 mN using the UNHT machines.

for a large variety of organic rich shales tested.

The logarithmic creep kinetics is most likely related to a free-volume phenomenon that initiates compaction at level I. Compaction decreases fast as the composites are already highly packed. Upon reaching a jammed state due to low composite porosity, dilation takes place. The latter is especially seen in organic-poor formations and overmature samples in which illite no longer contains organic molecules in their structures. Dilation, therefore, is the result of stress concentration at particle contacts in the absence of viscous organic matter to facilitate particle rearrangement.

- The creep rate magnitude is driven by the porous kerogen phase, which has −by far− the lowest creep modulus among all the constituents of organic-rich source rocks. This creep rate magnitude is constrained by the inorganic phases. Those

creep at a rate that is at least one to two orders of magnitude smaller than the creep rate of the porous kerogen. This finding heavily relies on using a "rate-approach" in contrast to the (integrated) compliance approach, which makes it difficult to separate elasticity phenomena from viscous phenomena. Using the rate approach, it is possible to show that the creep rate in these formations is almost isotropic. This isotropy is an independent confirmation that the relevant creep rate is driven by isotropic constituents: pores and kerogen. A second independent confirmation comes from the application of creep composite models within the framework of the correspondence principle of linear viscoelasticity. In fact, application of this framework shows that the relevant creep rate (respectively the contact creep modulus characterizing the logarithmic creep) of the organic-rich porous clay phase is situated within two asymptotes defined by texture: an upper bound defined by the self-consistent scheme representing mature disordered systems; a lower bound defined by a continuous creeping matrix of immature kerogen with rigid clay inclusions. These two types of morphologies relate to the connectivity of the porous kerogen phase, and thus to maturity.

- With both kinetics and creep rate magnitude thus defined, it becomes possible to move from understanding to predicting the time-dependent properties of organic-rich shale. A comparison of creep microindentation data from Haynesville with triaxial creep test data shows that three-minute long indentation tests, properly analyzed with a novel composite understanding, can substitute for much longer (here, three hours) classical triaxial creep tests. This validates creep indentation as a means to understand, quantify, and ultimately predict creep behavior of organic-rich source rocks far beyond the indentation test duration.

- A maturity-dependent linear C-H scaling at both nano- and microscale underlines the role of porous kerogen in driving creep rates and the role of clay particles as non-creeping rigid inclusions. Along with a C-H scaling relationship, an empirical C-M scaling relationship can be used in the petrophysical and well-log

interpretation workflow to indicate maturity during exploration and/or point to facies with good fracking-quality.

The above findings bring us back to the two hypotheses we set out to test in this last part. Hypothesis I, stating that the kerogen drives creep rates in source rocks, is verified based on the following: 1) the experimental results strongly point to the role of isotropic phases (kerogen and porosity) driving the creep rates; 2) the good agreement between these results and predictions of the creep homogenization models (at both level I and level II) iterates the role of kerogen. It also reveals the role of the clay particles, along with other inclusions, as phases that constrain creep rates in source rocks; and 3) the scale-independent, but maturity-dependent, C-H scaling relationship points to a common phase, kerogen, driving creep rates at various scales.

Indenting small material volumes under a very sharp tip decreases the characteristic time needed to reach long-term logarithmic creep behavior. The good agreement between C obtained from creep microindentation tests and C derived from triaxial creep test data (on Haynesville) validates Hypothesis III: a three-minute creep microindentation test is a measurement that saves time and material while giving access to long-term creep behavior.

Part V

Summary and Perspective

Chapter 11

Summary of Results and Implications

This research was motivated by the difficulties faced by oil and gas operators determining and understanding the mechanical properties of gas shale formations required to predict their deformation. The classical industry approach to understand gas shale formations is based on correlating mechanical properties with mineralogy, TOC, and maturity. In contrast to this approach, ours consisted of reaching a more fundamental understanding of the formations' properties and behavior and focusing on revealing and modeling the role of the organic phase. To understand the role of kerogen, we focused on isolating the organic-rich phases: the porous organic-rich clay composites. These composites are the most important phases in source rocks as they contain the elements (porosity, clay minerals, and organic matter) that affect the rocks' mechanical behavior and petrophysical properties the most; and they are the ones whose texture can be modeled for better mechanical understanding and analysis.

A proper understanding of the clay composites and their mechanical characterization (anisotropy, stiffness, hardness, and creep rates) has motivated a novel modeling approach that focuses on texture, which is dictated by the maturity of the organic phase (kerogen). The various micromechanical textural models, depicting maturity-dependent composite textures, have proven to be powerful tools to capture and isolate the effect of organic matter. The successful implementation of the approach promotes textural

modeling as a means to obtain clay particle solid properties and predict composite packing densities and organic content, all of which are hard to obtain experimentally.

Creep indentation tests provided the creep rates of clay composites and their constituents (kerogen and clay minerals) and highlighted the role of organic matter in driving creep rates at both the composite level and at the macroscale. Compared to macroscale creep tests on core plugs, creep microindentation reveals creep behavior seen in macrosamples.

The main findings and contributions of this work are summarized below. The findings shaped the main perspectives gained using small sample volumes and the indentation technique to mechanically characterize source rocks. This characterization is expected to improve decision-making in the field, reducing completion and fracking costs and the environmental impact. The limitations of the work to directly address specific diagenetic processes are addressed, with recommendations for future work.

11.1 Main Findings

Our experimental and modeling work revealed eight main findings highlighting the effect of the organic matter on texture, mechanical properties, and creep behavior of gas shale formations:

- The maturity of kerogen dictates its distribution and continuity in the source rocks and, consequentially affecting their textures. The latter can be described with microtextural mechanical models, with which we showed that the self-consistent morphology depicts a mature composite texture, and the matrix-inclusion morphology depicts that of an immature composite.

- The microtextural models capture and isolate the effects of kerogen maturity on mechanical properties and prove to be good tools to obtain properties (e.g., clay particle solid properties and packing density) that are hard to obtain experimentally.

- The porous organic matter is the phase that creeps with the highest rates. It drives creep rates in the clay composites and in the source rocks.

- A logarithmic creep kinetics is observed in the clay composite and organic material. Particle rearrangement and compaction are the main creep deformation mechanisms at the composite (microscale) level. Such deformation can explain embedment rates along fractures as well as declines in production rates with time. Dilation can also take place in organic-poor formations due to a high packing density structure under high stresses.

- Multiscale creep modeling reveals the role of clay particles and other inclusions as agents limiting creep rates. In parallel, a scale-independent relationship between the contact creep modulus (C) and hardness (H) captures the effect of kerogen driving creep rates at multiple scales. The linear C-H scaling relationship also relates to mechanical compaction, and captures an effective mesoscale porosity at the composite level rather than the nanoscale organic porosity generated with maturity.

- Nanoindentation testing of source rocks shows the effect of maturity on the mechanical properties of the clay composites. The clay composites are stiffer and harder in mature formations than in immature ones. Our nanoindentation test results quantify this microscale mechanical anisotropy in the source rocks.

- Creep rates obtained from three-minute-long creep microindentation tests are comparable to (long-term) creep behavior obtained from macroscale triaxial creep tests. This similarity in results between microindentation and macroscale triaxial creep tests promotes the former as an approach with a great potential to save testing time and material.

- Creep microindentation tests reveal a power-law correlation between the contact creep modulus and stiffness. This scaling relationship relates to creep deformation

and energy dissipation in the composites. It provides a means to correlate creep rates at the macroscale with sonic measurements.

11.2 Research Contributions

The main research contributions are the following:

- The implementation of the chemo-mechanical clustering analysis (used in cement research and tested on organic-free shale rocks) proved successful for isolating clay composites from otherwise very heterogeneous material. This approach allows us to distinguish the mechanical properties of organic-rich clay composites. Specifically, it reveals the microscale anisotropy in the gas shale formations, the effect of kerogen on mechanical properties, and its role driving creep rates.

- A mechanical characterization of gas shale formations is performed at the nano- and microscales. Hundreds of indentation tests performed provide stiffness, hardness, and creep rates at both scales. These tests provide insight into the heterogeneity, mechanical anisotropy, and creep rates at the tested scales. The amassed experimental data also provide mechanical property distributions that can be used in microporomechanics homogenization and upscaling models. Moreover, the mechanical characterization at the nano- and microscales is a first step to bridge the scale gap between mechanical properties obtained from molecular simulations (e.g., depicting clay mineral structure and/or organic matter under a prescribed stress field) and macroscale laboratory measurements (e.g., core plugs).

- Textural models were tested as a means to isolate the effect of organic maturity and produce clay mineral solid properties and porosity. This successful approach promotes textural models as tools to obtain solid properties and porosity. It also provides a more comprehensive understanding than simple correlations in relating microtexture, microstructure, and mechanical properties.

- This work has presented experimental and modeling proofs that highlight the role of kerogen, along with porosity, as the phases driving creep rates in gas shale formations. We have presented maturity-dependent scaling relationships between the various mechanical properties (C-H and C-M) that relate to creep kinetics and deformation. These scaling relationships are potential additions to petrophysical workflows; they provide a means to obtain a creep rate log from acoustic measurements and, consequently, predict proppant embedment rates.

- Creep microindentation results promote the indentation technique as a substitute for macroscale creep testing. The merits of such an experimental approach are that it saves sampling material and testing time.

11.3 Oil and Gas Industry Benefits

The direct impacts of our findings for oil and gas operators can be summarized as follows:

1. Our experimental and modeling results provide a fundamental understanding of the mechanical properties and creep behavior of source rocks at the nano- and microscales.

2. Indentation is validated as a testing technique that requires neither large intact specimens, usually hard and expensive to obtain, nor long testing time.

3. A database of elasticity, strength, and creep properties from nano- and microindentation tests is amassed. These results are useful to populate rock physics models and reservoir simulation applications. Properly upscaled data can be correlated to sonic logs and/or help calibrate seismic inversion models.

4. Instead of the conventional approach that correlates mechanical properties with other rock characteristics, textural models can be used as proxy to predict prop-

erties that are otherwise hard to obtain, such as porosity, TOC, and particle solid properties,.

5. Maturity-dependent functional relationships among various mechanical properties can be integrated into petrophysical workflows to generate creep rate logs. The latter can help predict embedment rates very early in the lifetime of a well (while drilling or after logging). Such early predictions improve decision-making for drilling (well stability and trajectory), completing, and fracking (proppant type, size, and volume) a well.

6. Maturity-dependent scaling relationships between mechanical properties can also prove useful in mapping maturity levels in a field. This mapping can help in inferring past geothermal gradients, subsidence, and/or sedimentation rates.

11.4 Work Limitations and Future Work

Despite using a very elaborate approach that couples mechanical and chemical data, the resolution of the EDS measurement and its semi-quantitative nature did not allow us to distinguish the various clay minerals in the samples. This inability was mitigated by the extent of indentation testing (hundreds of indents) to capture the heterogeneity of the clay composites. Experimental techniques with higher resolutions (e.g., AFM, TEM imaging, and TEM chemical analysis) are more appropriate candidates to resolve specific diagenetic processes and effects causing transformation in the clay mineralogy (smectite/illite transition), cementation, aggregate structure, and maturity.

Unfortunately, access to facies at different maturities, but from the same formation (or basin), was not possible. This lack of access prevented us from systematically studying changing rock characteristics with maturity, thus minimizing the effects of varying depositional environments and basin histories (affecting mineralogy, textures, cementation type and extent, clay content, mineral transformation, and porosity evolution). An extension of this work would be a more systematic specimen sampling and testing

of immature and mature facies of the same formation. Such an investigation would permit tracking porosity changes, clay mineral transformation, and textural evolution, ascribing all these changes to burial history, diagenetic processes, and maturity.

At least one-third of the nanoindentations performed (mixture and inclusion clusters) were not used. These data sets contain a wealth of information that can be employed in upscaling models. Careful work can be conducted to relate the mixture phases obtained from clustering analysis of nanoindentation tests to those obtained from microindentation data. Probing potential correlations between these data sets can prove useful in calibrating upscaling models linking the nanoscale to the microscale and have potential for predicting inclusion size distributions. Those can be linked to the mechanical properties and prove useful in multi-phase textural models that incorporate inclusions' properties.

Appendix A

Phase Volume Fraction Calculations: Level I and II

In this appendix, we summarize the XRD results of the various gas shales samples studied and the relationships used to calculate volume fractions at both level I and II (Refer to the shale model in Chapter 2). Detailed calculations of level II volume fractions, f^i, of the various minerals in each sample are presented. f^i is calculated according to:

$$f^i = (1 - \phi^{II}) \frac{\frac{m_i}{\rho_i}}{\Sigma_{k=1}^{N} (\frac{m_k}{\rho_k})} \tag{A.1}$$

where N is the number of phases (including kerogen) in the formation. m_i is the mass fraction of a phase from the XRD results, and ρ_i is the corresponding mass density. ϕ^{II} is the porosity obtained either experimentally by GRI methods (GAS Research Institute crushed shale analysis), BET (Brunauer-Emmett-Teller), or estimated from measuring the volume and mass of a sample. At level II, we have:

$$\Sigma_{k=1}^{N} f^i + \phi^{II} = 1 \tag{A.2}$$

Equation A.2 can also be written as:

$$f_{inc} + f_c + f_k + \phi^{II} = 1 \tag{A.3}$$

As the name suggests, the organic-rich clay composites in every sample contain the clay minerals, the organic phase (kerogen), and porosity. Collectively, these components (clay minerals, kerogen, and pore space) make what we refer to as level I. Therefore, at level I, we have:

$$\eta_c + \eta_k + \phi^I = 1 \tag{A.4}$$

where η_c and η_k are the level volume fractions of clay and kerogen, respectively. ϕ^I is the porosity of the clay phase. Depending on the maturity of the gas shale sample and our assumption of whether porosity is distributed among all phases (self-consistent texture in mature samples; Tables A.1 to A.10) or concentrated, along with kerogen, in the clay phase (matrix-inclusion texture in immature samples; Tables A.11 to A.13), the clay-phase volume fraction and porosity are calculated as follows:

Self-Consistent Morphology:

$$\phi^I = \phi^{II} \tag{A.5}$$

$$\eta_k = \frac{f_k}{f_k + f_c + \phi^I} \tag{A.6}$$

$$\eta_c = \frac{f_c}{f_k + f_c + \phi^I} \tag{A.7}$$

Matrix-Inclusion Morphology:

Level I porosity, ϕ^I, is:

$$\phi^I = \frac{\phi^{II}}{f_k + f_c + \phi^{II}} = \frac{\phi^{II}}{1 - f^{incl}} \tag{A.8}$$

$$\eta_k = \frac{f_k}{f_c + f_k + \phi^{II}} \tag{A.9}$$

$$\eta_c = \frac{f_c}{f_c + f_k + \phi^{II}} \tag{A.10}$$

We note that we assumed a constant mass density for kerogen of 1.2 g/cm^3 regardless of its maturity. The kerogen content of a sample gets washed away during sample preparation for XRD measurement. Therefore, XRD weights percentages, adding up to values different than 100%, were corrected/recalculated (fourth column in the tables) to account for the sample kerogen content.

Table A.1: XRD results and volume fraction calculations of the constituents of Haynesville A2V-H. Level I volume fractions of clay minerals, η_c, and kerogen, η_k, in the organic-rich clay phase are reported. Kerogen density is assumed to be 1.2 g/cm^3. ρ = mineral density (g/cm^3).

A2V-H	Mineral Density (g/cc)	XRD wt.%	Corrected wt.% (m_i)*	$\frac{m_i}{\rho_i}$	$(1-\phi^{II})(\frac{m_i}{\rho})$	$f_i = (1-\phi^{II})\frac{\frac{m_i}{\rho_i}}{\Sigma_{k=1}^{N}(\frac{m_k}{\rho_k})}$	η_c	η_k
Quartz	2.65	27.00	26.10	9.85	9.12	23.42		
Feldspar	2.68	9.00	8.70	3.25	3.01	7.72		
Carbonates	2.71	22.00	21.27	7.85	7.27	18.66		
Others	2.85	4.00	3.87	1.36	1.26	3.23		
Clay	2.65	38.00	36.73	13.86	12.83	32.96	77.11	15.49
Total XRD wt. %		100.00						
		kerogen	3.34	2.78	2.58	6.62		
				$\Sigma_{k=1}^{N}(\frac{m_k}{\rho_k})$	38.94			
				Level II / macroporosity $=\phi^{II}$	0.074			

*XRD weight percentages were re-calculated to account for the kerogen content in a 100 g sample.

Table A.2: XRD results and volume fraction calculations of the constituents of Haynesville A5V-H. Level I volume fractions of clay minerals, η_c, and kerogen, η_k, in the organic-rich clay phase are reported. Kerogen density is assumed to be 1.2 g/cm^3. ρ = mineral density (g/cm^3).

A5V-H	Mineral Density (g/cc)	XRD wt.%	Corrected wt.% (m_i)*	$\frac{m_i}{\rho_i}$	$(1-\phi^{II})(\frac{m_i}{\rho})$	$f_i = (1-\phi^{II})\frac{\frac{m_i}{\rho_i}}{\Sigma_{k=1}^{N}(\frac{m_k}{\rho_k})}$	η_c	η_k
Quartz	2.65	31.00	29.90	11.28	10.60	27.43		
Feldspar	2.68	9.00	8.68	3.24	3.04	7.88		
Carbonates	2.71	11.00	10.61	3.92	3.68	9.52		
Others	2.85	5.00	4.82	1.69	1.59	4.11		
Clay	2.65	45.00	43.41	16.38	15.39	39.82	83.10	10.87
Total XRD wt. %		101.00						
		kerogen	2.57	2.14	2.01	5.21		
			$\Sigma_{k=1}^{N}(\frac{m_k}{\rho_k})$	38.65				
			Level II / macroporosity $=\phi^{II}$	0.060				

*XRD weight percentages were re-calculated to account for the kerogen content in a 100 g sample.

Table A.3: XRD results and volume fraction calculations of the constituents of Haynesville A6V-H. Level I volume fractions of clay minerals, η_c, and kerogen, η_k, in the organic-rich clay phase are reported. Kerogen density is assumed to be 1.2 g/cm^3. ρ = mineral density (g/cm^3).

A6V-H	Mineral Density (g/cc)	XRD wt.%	Corrected wt.% (m_i)*	$\frac{m_i}{\rho_i}$	$(1-\phi^{II})(\frac{m_i}{\rho})$	$f_i = (1-\phi^{II})\frac{\frac{m_i}{\rho_i}}{\Sigma_{k=1}^{N}(\frac{m_k}{\rho_k})}$	η_c	η_k
Quartz	2.65	32.00	31.26	11.79	10.95	28.06		
Feldspar	2.68	11.00	10.74	4.01	3.72	9.54		
Carbonates	2.71	9.00	8.79	3.24	3.01	7.72		
Others	2.85	4.00	3.91	1.37	1.27	3.26		
Clay	2.65	43.00	42.00	15.85	14.71	37.71	79.11	13.73
Total XRD wt. %		99.00						
		kerogen	3.30	2.75	2.55	6.54		
				$\Sigma_{k=1}^{N}(\frac{m_k}{\rho_k})$	39.02			
				Level II / macroporosity $=\phi^{II}$	0.072			

*XRD weight percentages were re-calculated to account for the kerogen content in a 100 g sample.

Table A.4: XRD results and volume fraction calculations of the constituents of Haynesville A7V-H. Level I volume fractions of clay minerals, η_c, and kerogen, η_k, in the organic-rich clay phase are reported. Kerogen density is assumed to be 1.2 g/cm^3. ρ = mineral density (g/cm^3).

A7V-H	Mineral Density (g/cc)	XRD wt.%	Corrected wt.% (m_i)*	$\frac{m_i}{\rho_i}$	$(1-\phi^{II})(\frac{m_i}{\rho})$	$f_i = (1-\phi^{II})\frac{\frac{m_i}{\rho_i}}{\Sigma_{k=1}^{N}(\frac{m_k}{\rho_k})}$	η_c	η_k
Quartz	2.65	28.00	27.12	10.23	9.46	24.41		
Feldspar	2.68	10.00	9.68	3.61	3.34	8.62		
Carbonates	2.71	12.00	11.62	4.29	3.96	10.23		
Others	2.85	12.00	11.62	4.08	3.77	9.73		
Clay	2.65	38.00	36.80	13.89	12.83	33.13	77.68	14.73
Total XRD wt. %		100.00						
		kerogen	3.16	2.63	2.43	6.28		
			$\Sigma_{k=1}^{N}(\frac{m_k}{\rho_k})$	38.73				
			Level II / macroporosity $=\phi^{II}$	0.076				

*XRD weight percentages were re-calculated to account for the kerogen content in a 100 g sample.

Table A.5: XRD results and volume fraction calculations of the constituents of Marcellus 46. Level I volume fractions of clay minerals, η_c, and kerogen, η_k, in the organic-rich clay phase are reported. Kerogen density is assumed to be 1.2 g/cm^3. ρ = mineral density (g/cm^3).

Mar46	Mineral Density (g/cc)	XRD wt.%	Corrected wt.% (m_i)*	$\frac{m_i}{\rho_i}$	$(1-\phi^{II})(\frac{m_i}{\rho})$	$f_i = (1-\phi^{II}).\frac{\frac{m_i}{\rho_i}}{\Sigma_{k=1}^{N}(\frac{m_k}{\rho_k})}$	η_c	η_k
Quartz	2.65	19.70	19.60	7.40	6.78	18.43	89.10	2.50
Plagioclase	2.68	3.20	3.18	1.19	1.09	2.96		
Calcite	2.71	30.60	30.45	11.24	10.29	27.99		
Dolomite	2.86	4.40	4.38	1.53	1.40	3.81		
Siderite	3.96	0.50	0.50	0.13	0.12	0.31		
Pyrite	5.01	1.50	1.49	0.30	0.27	0.74		
Anatase	3.89	0.20	0.20	0.05	0.05	0.13		
Muscovite	2.82	10.70	10.65	3.78	3.46	9.40		
Illite+IS	2.65	23.00	22.89	8.64	7.91	21.51		
Chlorite	2.90	6.20	6.17	2.13	1.95	5.30		
Total XRD wt. %		100.00						
		kerogen	0.49	0.41	0.37	1.02		
				$\Sigma_{k=1}^{N}(\frac{m_k}{\rho_k})$	36.783			
				Level II / macroporosity $=\phi^{II}$	0.084			

*XRD weight percentages were re-calculated to account for the kerogen content in a 100 g sample.

Table A.6: XRD results and volume fraction calculations of the constituents of Marcellus 49. Level I volume fractions of clay minerals, η_c, and kerogen, η_k, in the organic-rich clay phase are reported. Kerogen density is assumed to be 1.2 g/cm^3. ρ = mineral density (g/cm^3).

Mar49	Mineral Density (g/cc)	XRD wt.%	Corrected wt.% (m_i)*	$\frac{m_i}{\rho_i}$	$(1-\phi^{II})(\frac{m_i}{\rho})$	$f_i = (1-\phi^{II}).\frac{\frac{m_i}{\rho_i}}{\Sigma_{k=1}^{N}(\frac{m_k}{\rho_k})}$	η_c	η_k
Quartz	2.65	18.70	18.51	6.98	6.43	17.37	86.78	5.32
Plagioclase	2.68	3.50	3.46	1.29	1.19	3.21		
Calcite	2.71	32.70	32.36	11.94	11.00	29.70		
Dolomite	2.86	3.60	3.56	1.25	1.15	3.10		
Siderite	3.96	0.70	0.69	0.17	0.16	0.44		
Pyrite	5.01	1.80	1.78	0.36	0.33	0.88		
Anatase	3.89	0.10	0.10	0.03	0.02	0.06		
Muscovite	2.82	9.60	9.50	3.37	3.10	8.38		
Illite+IS	2.65	24.00	23.75	8.96	8.25	22.29		
Chlorite	2.90	5.30	5.24	1.81	1.67	4.50		
Total XRD wt. %		100.00						
		kerogen	1.04	0.87	0.80	2.16		
			$\Sigma_{k=1}^{N}(\frac{m_k}{\rho_k})$	37.02				
			Level II / macroporosity $=\phi^{II}$	0.079				

*XRD weight percentages were re-calculated to account for the kerogen content in a 100 g sample.

Table A.7: XRD results and volume fraction calculations of the constituents of Marcellus 108. Level I volume fractions of clay minerals, η_c, and kerogen, η_k, in the organic-rich clay phase are reported. Kerogen density is assumed to be 1.2 g/cm^3. ρ = mineral density (g/cm^3).

Mar108	Mineral Density (g/cc)	XRD wt.%	Corrected wt.% (m_i)*	$\frac{m_i}{\rho_i}$	$(1-\phi^{II})(\frac{m_i}{\rho})$	$f_i = (1-\phi^{II}).\frac{\frac{m_i}{\rho_i}}{\Sigma_{k=1}^{N}(\frac{m_k}{\rho_k})}$	η_c	η_k
Quartz	2.65	29.60	27.33	10.31	9.57	24.47	67.38	25.42
Plagioclase	2.68	6.00	5.54	2.07	1.92	4.90		
Calcite	2.71	3.10	2.86	1.06	0.98	2.51		
Dolomite	2.86	1.40	1.29	0.45	0.42	1.07		
Siderite	3.96	0.70	0.65	0.16	0.15	0.39		
Pyrite	5.01	8.70	8.03	1.60	1.49	3.80		
Anatase	3.89	0.40	0.37	0.09	0.09	0.23		
Barite	4.48	1.50	1.38	0.31	0.29	0.73		
Muscovite	2.82	10.20	9.42	3.34	3.10	7.92		
Illite+IS	2.65	36.30	33.51	12.65	11.74	30.01		
Chlorite	2.90	2.10	1.94	0.67	0.62	1.59		
Total XRD wt. %		100.00						
kerogen			7.68	6.40	5.94	15.19		
$\Sigma_{k=1}^{N}(\frac{m_k}{\rho_k})$				39.11				
Level II / macroporosity $=\phi^{II}$				0.072				

*XRD weight percentages were re-calculated to account for the kerogen content in a 100 g sample.

Table A.8: XRD results and volume fraction calculations of the constituents of Marcellus 150. Level I volume fractions of clay minerals, η_c, and kerogen, η_k, in the organic-rich clay phase are reported. Kerogen density is assumed to be 1.2 g/cm^3. ρ = mineral density (g/cm^3).

Mar150	Mineral Density (g/cc)	XRD wt.%	Corrected wt.% (m_i)*	$\frac{m_i}{\rho_i}$	$(1-\phi^{II})(\frac{m_i}{\rho})$	$f_i = (1-\phi^{II}).\frac{\frac{m_i}{\rho_i}}{\Sigma_{k=1}^{N}(\frac{m_k}{\rho_k})}$	η_c	η_k
Quartz	2.65	29.40	27.19	10.26	9.66	24.52	66.24	27.86
Plagioclase	2.68	4.80	4.44	1.66	1.56	3.96		
Calcite	2.71	13.30	12.30	4.54	4.27	10.85		
Dolomite	2.86	2.40	2.22	0.78	0.73	1.85		
Siderite	3.96	0.40	0.37	0.09	0.09	0.22		
Pyrite	5.01	7.30	6.75	1.35	1.27	3.22		
Anatase	3.89	0.40	0.37	0.10	0.09	0.23		
Muscovite	2.82	10.00	9.25	3.28	3.09	7.84		
Illite+IS	2.65	31.70	29.32	11.06	10.41	26.44		
Chlorite	2.90	0.50	0.46	0.16	0.15	0.38		
Total XRD wt. %		100.20						
kerogen			7.32	6.10	5.74	14.58		
$\Sigma_{k=1}^{N}(\frac{m_k}{\rho_k})$				39.37				
Level II / macroporosity $=\phi^{II}$				0.059				

*XRD weight percentages were re-calculated to account for the kerogen content in a 100 g sample.

Table A.9: XRD results and volume fraction calculations of the constituents of Marcellus 151. Level I volume fractions of clay minerals, η_c, and kerogen, η_k, in the organic-rich clay phase are reported. Kerogen density is assumed to be 1.2 g/cm^3. ρ = mineral density (g/cm^3).

Mar151	Mineral Density (g/cc)	XRD wt.%	Corrected wt.% (m_i)*	$\frac{m_i}{\rho_i}$	$(1-\phi^{II})(\frac{m_i}{\rho})$	$f_i = (1-\phi^{II}).\frac{\frac{m_i}{\rho_i}}{\Sigma_{k=1}^{N}(\frac{m_k}{\rho_k})}$	η_c	η_k
Quartz	2.65	36.20	33.24	12.54	11.73	29.93	62.99	30.51
Plagioclase	2.68	5.60	5.14	1.92	1.79	4.58		
Calcite	2.71	3.00	2.75	1.02	0.95	2.43		
Dolomite	2.86	1.50	1.38	0.48	0.45	1.15		
Siderite	3.96	0.30	0.28	0.07	0.07	0.17		
Pyrite	5.01	11.70	10.74	2.14	2.00	5.12		
Anatase	3.89	0.50	0.46	0.12	0.11	0.28		
Muscovite	2.82	9.00	8.26	2.93	2.74	6.99		
Illite+IS	2.65	31.80	29.20	11.02	10.30	26.29		
Chlorite	2.90	0.40	0.37	0.13	0.12	0.30		
Total XRD wt. %		100.00						
kerogen			8.18	6.82	6.37	16.27		
$\Sigma_{k=1}^{N}(\frac{m_k}{\rho_k})$				39.18				
Level II / macroporosity $=\phi^{II}$				0.065				

*XRD weight percentages were re-calculated to account for the kerogen content in a 100 g sample.

Table A.10: XRD results and volume fraction calculations of the constituents of the Fayetteville sample. Level I volume fractions of clay minerals, η_c, and kerogen, η_k, in the organic-rich clay phase are reported. Kerogen density is assumed to be 1.2 g/cm^3. ρ = mineral density (g/cm^3).

Fayette-ville	Mineral Density (g/cc)	XRD wt.%	Corrected wt.% (m_i)*	$\frac{m_i}{\rho_i}$	$(1-\phi^{II})(\frac{m_i}{\rho})$	$f_i = (1-\phi^{II}).\frac{\frac{m_i}{\rho_i}}{\Sigma_{k=1}^{N}(\frac{m_k}{\rho_k})}$	η_c	η_k
Quartz	2.65	28.80	27.38	10.33	9.92	25.25		
Albite	2.65	6.30	5.99	2.26	2.17	5.52		
Calcite	2.71	22.80	21.68	8.00	7.68	19.55		
Dolomite	2.86	8.90	8.46	2.96	2.84	7.23		
Pyrite	5.01	2.50	2.38	0.47	0.46	1.16		
Halite	2.17	3.10	2.95	1.36	1.30	3.32		
Others	2.85	2.50	2.38	0.83	0.80	2.04	65.88	30.12
Illite+IS	2.65	23.90	22.72	8.58	8.23	20.95		
Chlorite	2.90	1.20	1.14	0.39	0.38	0.96		
Total XRD wt. %		100.00						
kerogen			4.92	4.10	3.94	10.02		
$\Sigma_{k=1}^{N}(\frac{m_k}{\rho_k})$				39.29				
Level II / macroporosity $=\phi^{II}$				0.040				

*XRD weight percentages were re-calculated to account for the kerogen content in a 100 g sample.

Table A.11: XRD results and volume fraction calculations of the constituents of the Antrim sample. Level I volume fractions of clay minerals, η_c, and kerogen, η_k, in the organic-rich clay phase are reported. Kerogen density is assumed to be 1.2 g/cm^3. ρ = mineral density (g/cm^3).

Antrim	Mineral Density (g/cc)	XRD wt.%	Corrected wt.% (m_i)*	$\frac{m_i}{\rho_i}$	$(1-\phi^{II})(\frac{m_i}{\rho})$	$f_i = (1-\phi^{II})\frac{\frac{m_i}{\rho_i}}{\Sigma_{k=1}^{N}(\frac{m_k}{\rho_k})}$	η_c	η_k	ϕ^{I}**
Quartz	2.65	40.91	40.53	15.30	13.95	33.68			
Albite	2.65	3.47	3.44	1.30	1.18	2.86			
Dolomite	2.86	4.38	4.34	1.52	1.38	3.34			
Pyrite	5.01	3.11	3.08	0.62	0.56	1.35			
Sanidine	2.52	7.95	7.88	3.13	2.85	6.88			
Illite+IS	2.65	25.57	25.33	9.56	8.72	21.05	49.05	33.99	0.17
Chlorite	2.90	5.84	5.79	2.00	1.82	4.39			
Total XRD wt. %		91.23							
kerogen			9.61	8.01	7.30	17.64			
$\Sigma_{k=1}^{N}(\frac{m_k}{\rho_k})$				41.41					
Level II / macroporosity $=\phi^{II}$				0.088					

*XRD weight percentages were re-calculated to account for the kerogen content in a 100 g sample.

**Level I porosity = porosity of the organic-rich clay phase assuming all porosity and kerogen are in phase.

Table A.12: XRD results and volume fraction calculations of the constituents of the Barnett sample. Level I volume fractions of clay minerals, η_c, and kerogen, η_k, in the organic-rich clay phase are reported. Kerogen density is assumed to be 1.2 g/cm^3. ρ = mineral density (g/cm^3).

Barnett	Mineral Density (g/cc)	XRD wt.%	Corrected wt.% (m_i)*	$\frac{m_i}{\rho_i}$	$(1-\phi^{II})(\frac{m_i}{\rho})$	$f_i = (1-\phi^{II}).\frac{\frac{m_i}{\rho_i}}{\Sigma_{k=1}^{N}(\frac{m_k}{\rho_k})}$	η_c	η_k	ϕ^{I}**
Quartz	2.65	29.73	29.68	11.20	10.38	23.82			
Albite	2.65	2.20	2.20	0.83	0.77	1.76			
Calcite	2.71	2.64	2.64	0.97	0.90	2.07			
Pyrite	5.01	0.53	0.53	0.11	0.10	0.22			
Microcline	2.55	3.25	3.24	1.27	1.18	2.71			
Gypsum	2.32	7.83	7.82	3.37	3.12	7.17			
Illite+IS	2.65	39.67	39.60	14.94	13.85	31.78	53.54	34.74	0.12
Chlorite	2.90	2.11	2.11	0.73	0.67	1.54			
Total XRD wt. %		87.96							
kerogen			12.20	10.17	9.42	21.62			
$\Sigma_{k=1}^{N}(\frac{m_k}{\rho_k})$				43.58					
Level II / macroporosity $=\phi^{II}$				0.073					

*XRD weight percentages were re-calculated to account for the kerogen content in a 100 g sample.

**Level I porosity = porosity of the organic-rich clay phase assuming all porosity and kerogen are in phase.

Table A.13: XRD results and volume fraction calculations of the constituents of the Woodford sample. Level I volume fractions of clay minerals, η_c, and kerogen, η_k, in the organic-rich clay phase are reported. Kerogen density is assumed to be 1.2 g/cm^3. ρ = mineral density (g/cm^3).

Woodford	Mineral Density (g/cc)	XRD wt.%	Corrected wt.% (m_i)*	$\frac{m_i}{\rho_i}$	$(1-\phi^{II})(\frac{m_i}{\rho})$	$f_i = (1-\phi^{II})\frac{\frac{m_i}{\rho_i}}{\Sigma_{k=1}^{N}(\frac{m_k}{\rho_k})}$	η_c	η_k	ϕ^{I}**
Quartz	2.65	60.60	58.05	21.91	19.15	48.96			
Albite	2.65	2.80	2.68	1.01	0.88	2.26			
Pyrite	5.01	2.60	2.49	0.50	0.43	1.11			
Illite+IS	2.65	30.90	29.60	11.17	9.76	24.96			
Chlorite	2.90	3.10	2.97	1.02	0.90	2.29	57.16	16.41	0.26
Total XRD wt. %		100.00							
		kerogen	4.20	3.50	3.06	7.82			
			$\Sigma_{k=1}^{N}(\frac{m_k}{\rho_k})$	39.11					
Level II / macroporosity $=\phi^{II}$				0.126					

*XRD weight percentages were re-calculated to account for the kerogen content in a 100 g sample.

**Level I porosity = porosity of the organic-rich clay phase assuming all porosity and kerogen are in phase.

Appendix B

Indentation Machines, Calibrations, and Measurements

Two indentation machines were used to perform indentation tests: the Hysitron TI 950 TriboIndenter (Hysitron) and the Anton Paar Ultra Nanoindentation Tester (UNHT). This appendix summarizes machine specifications and calibrations needed before every indentation job. Different depth-measurement approaches during creep tests are followed by the machines. This created discrepancies in depth measurements at constant load. Therefore, load-dependent corrections of the mechanical results obtained by the Hysitron are proposed and validated in order to reconcile data obtained from static (UNHT) and dynamic (Hysitron) testing.

B.1 Factors Affecting Indentation Data

Many factors affect indentation depth measurements during an indentation test and lead to erroneous depth measurements and, consequently, mechanical results.

B.1.1 Drift

Drift behavior is observed in indentation. It is ascribed to either creep within the specimen at constant load and/or changes in the dimensions of the instrument due to thermal expansion or contraction. Changes in instrument dimensions produce a thermal drift error that needs correction. The rate of change in depth reading at constant load is usually measured before an indentations test. Thermal drift is computed and applied to subsequent depth readings. Feng and Ngan (2002) showed that thermal drift can be minimized by test design making the hold phase long enough (> 45 s) and the unloading rate fast enough.

B.1.2 Contact Depth

The penetration depth in an indentation test is calculated from the sample free surface. A contact between the indenter and material has to be established before displacement can be measured. This contact is in practice established and recognized at a small contact force (P_i) defined by the user. Regardless of the P_i chosen, a corresponding penetration of the indenter (h_i) is seen, introducing error to the displacement measurements. In elastic material, a depth correction, $h^{'}$, is needed:

$$h^{'} = h + h_i \tag{B.1}$$

The Hertz contact equations in elastic material predict the following load-depth relationship:

$$h \propto P^{m1} \tag{B.2}$$

Therefore,

$$h = kP^m - h_i = kP^m - kP^i \tag{B.3}$$

[1] $m = \frac{1}{2}$ for conical indenters

where k is a constant that depends on the shape of the indenter. To solve for m and k for material of unknown properties, h and P data are recorded. A plot of h vs. $(P^m - P_i)$ is linear with a slope k. h_i is then obtained using

$$h_i = kP_i^m \tag{B.4}$$

B.1.3 Surface Roughness

A correct depth measurement is crucial for accurately determining the contact area between indenter and material. The surface roughness of the material indented affects the recognition of the contact point between indenter and material and, consequently, gives errors in the measured depth. To reduce the error introduced by surface roughness, samples are polished (Refer to Chapter 3).

B.1.4 Indenter Tip Bluntness

Tip rounding or bluntness affects the calculation of the indenter penetration depth. Usually, this is a concern indenting films of material (hundreds of nm thick) and performing indentations with a penetration depth < 50 nm.

B.2 Indentation Instruments

B.2.1 The Hysitron TI 950 Indenter

The Hysitron TI 950 indenter was used to perform creep and non-creep indentation tests with a maximum loads reaching 4.8 mN and 12 mN. The core of the Hysitron system is the patented three-plate capacitive force/displacement transducer. The transducer provides a high sensitivity allowing light load measurements ($< 25\,\mu N$). It, also, minimizes sensitivity to external vibrations. Positioned higher than the sample stage, a 3-axis piezo scanner provides probe precision positioning of ± 20 nm and allows imaging of the sample. The Hysitron stage is mounted with X/Y-axis and Z-axis staging

systems. The $X/Y-$axis system is encoded to a resolution of 500 nm with a 50 nm microstepping resolution. The Z-axis system is operated with a stage controller that provides a microstepping resolution of 3.1 nm and accurate and repeatable test placements. The maximum normal force available from the standard transducer is 12 mN. The load resolution is 10 nN. The maximum displacement is 5 μm with a resolution of 0.04 nm. Creep indentation tests using the Hysitron are performed with a modulated force applied in addition to a quasistatic load. The dynamic force and displacement are used to calculate a sample damping coefficient, storage stiffness, and infer a "dynamic" depth.

B.2.2 The Anton Parr Ultra Nanoindentation Tester

The Anton Parr Ultra Nanoindentation Tester (referred to as UNHT) was mainly used for creep microindentation tests with loads reaching 50 mN, the load capacity of the machine. The UNHT uses a top surface referencing technique (http://www.csm-instruments.com/en/Indentation; (CSM-Instrument, 2013; SA, 2013)), a differential measurement between the sample surface (at a reference point) and the indentation depth measured at the indenter tip. This surface referencing technique allows accurate depth measurements, a rapid measurement cycle time, and a negligible thermal drift. Every time a specimen is loaded to be tested, an adjust depth offset (ADO) is done to estimate vertical variation between the reference and the indenter tip. ADO helps estimate sample surface tilt.

The advantage of using the UNHT is that it has a wider load and displacement ranges convenient for creep microindentation testing. Also, unlike the Hysitron, thermal drift is minimized by design. Creep is performed with a static load, and depth is continuously measured instead of being inferred.

B.3 Calibrations and Corrections

Periodic calibrations are needed when operating indentation machines. The following corrections are done to address errors introduced when measuring loads and depths:

B.3.1 Stage Calibration

Stage calibration is done to ensure accuracy in distance between the optics in the machine and indenter's tip. This calibration is done periodically or every time the indenter tip is removed for cleaning or replacement.

B.3.2 Tip Calibration

The indenter tip calibration is a must to predict tip rounding. It is done to ensure accuracy in depth measurement and update the instrument with the right tip area function. The latter is important to convert indenter penetration depth to indenter-material contact area (Equation 3.27). The tip calibration is done indenting material with known properties (e.g., fused quartz).

B.3.3 Machine Compliance

When depth is measured, the instrument usually registers the displacement of the machine as a reaction to the applied load. The load frame, indenter shaft, and specimen mount contribute to the machine compliance, C_f. The latter is defined as "the deflection of the instrument divided by the load applied during a test" (Fischer-Cripps, 2011). A machine compliance correction is needed according to:

$$\frac{dh}{dP} = \frac{1}{S} + C_f \tag{B.5}$$

where $\frac{dh}{dP}$ is the measured total compliance. S is the measured unloading stiffness.

To obtain C_f, a series of indentation tests that span the load range of the instrument are done on a material of known properties (e.g., fused silica). A plot of total compliance $\frac{dh}{dP}$ vs $\frac{1}{h_c}$ (for Berkovich indenter) for an elastic unloading and a range of h_{max} is prepared. The plot is linear with a slope proportional to $\frac{1}{E^*}$ (E^* being the composite modulus), and an intercept equals to C_f.

B.3.4 Hysitron Dynamic Air Calibration

Dynamic air calibration (also called "nanoDMA" air calibration) is needed before using the Hysitron for creep indentation. NanoDMA defines ranges of forces and frequencies to solve for in order to calculate the dynamic compliance of the system. With the nanoDMA calibration done, the instrument shaft spring constant (K_s), mass (m), and damping of the transducer are calculated.

B.3.5 Hysitron Air Calibration

The air calibration allows accurate force and displacement measurements. It is done before every job to determine the plate spacing (distance between the scanner center and bottom plates) and electrostatic force constant ($\mu m/v^2$). It is a good indicator of how clean the indenter tip is.

B.3.6 Drift Correction

A thermal drift rate is calculated before every indentation test. A contact, at a small constant contact load, is established between the indenter and the specimen surface, and depth is recorded. Once determined, drift rate correction is applied to subsequent depth measurements. As mentioned, drift correction needed operating the UNHT machine is minimized by machine design and the use of the top surface referencing technique. Drift rates estimated by the Hysitron machine before every test are adequate and applicable for short hold-phase tests and up to 1-min long creep tests. With our creep indentation

tests lasting 180 s, the drift correction estimated by the Hysitron is not adequate for the test duration. Errors in the depth inferred by the Hysitron are expected.

B.3.7 Hysitron nanoDMA/Dynamic Analysis

In creep indentation tests, the Hysitron uses the nanoDMA analysis, a protocol used to infer, instead of measure, depth during long creep tests (Hysitron, 2011). The protocol consists of adopting a reference frequency testing technique to infer the indenter-material contact area independently from measuring depth. A 5 s reference segment is added to the creep hold phase (180 s) to obtain "reference tests parameters" (e.g., a reference modulus). During the reference segment, the indenter oscillates at a reference frequency. The depth of the indenter is measured (as errors introduced by thermal drift are negligible and corrected for), the contact area is calculated, and a reference stiffness/modulus, S_{ref}, is determined. In turn, S_{ref} allows defining a sample modulus at the specific frequency and is used, along with the contact area measured during the reference 5 s segment, to calculate a reference storage modulus, E'_{ref} (Hysitron, 2011) according to:

$$E'_{ref} = \frac{K_{ref}\sqrt{\pi}}{2\sqrt{A(h_c)}} \tag{B.6}$$

E'_{ref} is then used for the rest of the creep phase to infer the contact area (A_c) knowing the contact stiffness, S:

$$A_c = \left(\frac{S\sqrt{\pi}}{2E'_{ref}}\right)^2 \tag{B.7}$$

The Hysitron uses a dynamic analysis (detailed in Fischer-Cripps, 2011) to obtain the mechanical properties from a creep test. This analysis involves oscillatory motion and the determination of a "transfer function". The oscillatory motion is added applying a small modulated force (Figure B-2) with a frequency ω and amplitude P_o (Fischer-Cripps, 2011):

$$P = P_o e^{i\omega t} \tag{B.8}$$

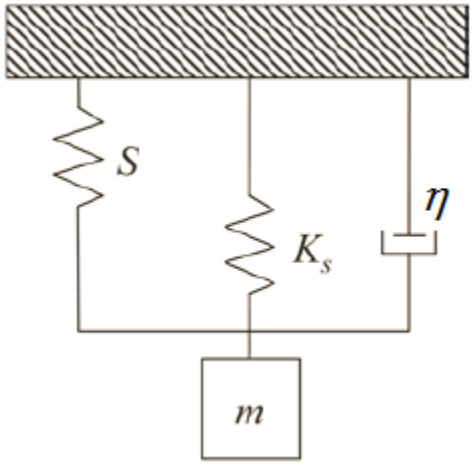

Figure B-1: A dynamic mechanical model of a nanoindentation instrument. S is the contact stiffness ($\frac{dP}{dh}$), η is a damping coefficient associated with the contact, and K_s is the stiffness of the indenter shaft support springs (modified after Fischer-Cripps, 2011).

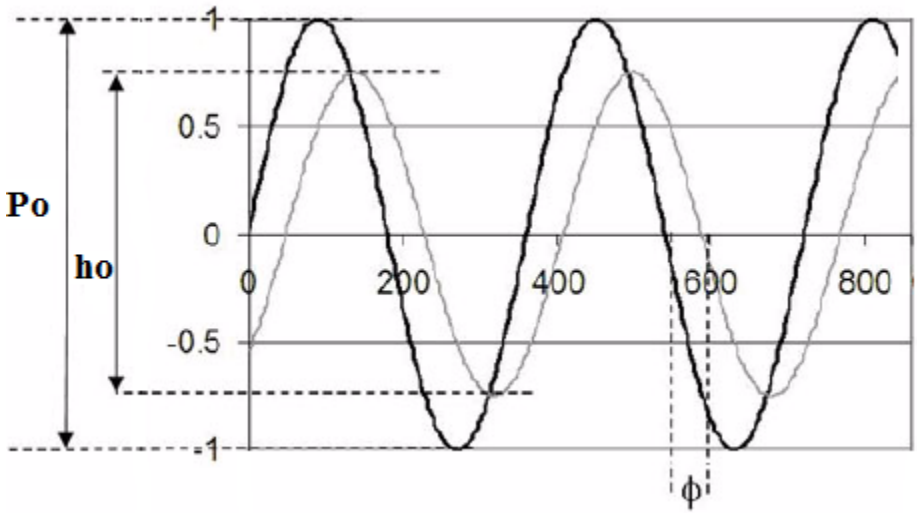

Figure B-2: A small dynamic load of amplitude P_o is applied during a nanoDMA test to the quasistatic force at user-defined frequency. A displacement signal having h_o amplitude is analyzed using a lock-in amplifier. A phase shift, ϕ, can exist between the load and displacement signals (modified after Hysitron, 2011).

Displacement (Figure B-2) is affected by the dynamics of the instrument as well as the indenter-material interaction. It has the same frequency as the load but may have a phase shift, ϕ:

$$h = h_o e^{i(\omega t + \phi)} \tag{B.9}$$

For the viscoelastic model shown in Figure B-1, the magnitude of the contact stiffness ($S = \frac{dP}{dh}$) is obtained combining the stiffness and damping terms:

$$\frac{P_o}{h_o} = \sqrt{(S + K_s - m\omega^2)^2 + \omega^2\eta^2} \tag{B.10}$$

where K_s is the stiffness of the indenter shaft support springs. η is a damping coefficient, and m is the mass of the component determined during air calibration. The phase shift is determined from:

$$\tan\phi = \frac{\omega\eta}{S + K_s - m\omega^2} \tag{B.11}$$

A transfer function has a from that depends on the viscoelastic model (e.g., Figure B-1) assumed to describe the tested material and the material-indenter interaction. For instance, a transfer function of a voigt model is (Fischer-Cripps, 2011):

$$TF = K - m\omega^2 + i\omega\eta \tag{B.12}$$

The imaginary and real parts of the transfer function of this model are:

$$TF_{re} = S + K_s - m\omega^2 \tag{B.13}$$

$$TF_{im} = \omega\eta \tag{B.14}$$

where K_s and m are obtained by fitting the transfer function to results oscillating the indenter in the air (i.e., doing the nanoDMA air calibration).

This superimposing of oscillatory motion to the conventional load-displacement response allows a continuous measure of S as depth increases. To account for machine compliance, Equations B.10 andB.11 become:

$$\frac{P_o}{h_o} = \sqrt{((\frac{1}{S} + C_f)^{-1} + K_s - m\omega^2)^2 + \omega^2\eta^2} \tag{B.15}$$

$$\tan\phi = \frac{\omega\eta}{(\frac{1}{S} + C_f)^{-1} + K_s - m\omega^2} \tag{B.16}$$

B.4 Machine-Dependent Creep Test Results

Due to the simplified linear viscoelastic model assumed by the Hysitron machine, the inferred depth at constant load does not faithfully depict the evolution of the creep behavior in the gas shale formations. Therefore, depth changes during the creep phase inferred by the Hysitron might not match depths measured using the UNHT. Errors inferring depths at constant loads affect the evolution of the creep behavior with time and/or the calculations of the contact area at maximum depth[2] .

This section addresses the above described depth discrepancies between the Hysitron and the UNHT. We propose a method to reconcile the mechanical properties obtained from Hysitron indentation to those obtained from the UNHT. Toward that end, creep nanoindentation and microindentation tests using the same protocol (loading and unloading rates, hold phase duration, and P_{max}) are performed on both machines. The C-H scaling relationships from both machines are used to construct correction factors. The latter are load-dependent and will be used to reconcile Hysitron data to match UNHT data. Our correction approach is validated by comparing corrected Hysitron results to UNHT results. The following abbreviations will be used: HYS = Hysitron indenter, UNHT = ultra nanoindenter tester, mat = mature, imm = immature, nano = creep nanoindentation, micro = creep microindentations, and corr = corrected data. As all mechanical properties referred to in this section come from creep indentation tests, the subscript creep will be dropped from the M and H for simplicity.

[2]The contact creep modulus, C, is obtained fitting a logarithmic function of the form $\Delta(t) = h - h_o = x_1 ln(x_2 t + 1) + x_3 t + x_4$ to the displacement-time data at constant load (Chapter 9). The expression used to calculate C is $\frac{P_{max}}{2a_u x_1}$; where P_{max} is the maximum load reached at which creep takes place, and $a_u = \sqrt{\frac{A_c}{\pi}}$ is the radius of the contact area between the indenter and material. As a result, the potential source of error and discrepancy in C obtained from the UNHT and Hysitron is either the fitting parameter, x_1, the contact area, A_c, or both.

B.4.1 Hysitron Creep Nanoindentation Model Correction

Creep nanoindentation tests with $P_{max} = 4.8$ mN were done on the Hysitron and UNHT. Figure B-3 shows comparable M and H obtained from both machines at this scale. This indicates that the overall depth measurement, specifically h_{max} reached at the end of the creep phase, coincides between machine. Therefore, no contact area correction is needed for the clay composite stiffness, $M^{HYS,nano}$, and hardness, $H^{HYS,nano}$, acquired.

Figure B-4a shows discrepancy in the contact creep modulus calculated from nanoindentation performed on both machines. As no contact-area correction was needed for M and H, the discrepancy comes from the logarithmic fit to the displacement-time data, and, consequently, the fitting parameter, x_1 used to calculate C. To correct the Hysitron creep results, the C-H scaling relationship are checked. Both machines give linear C-H scaling depicting secondary consolidation and compaction in the material volumes indented (Figures B-5 and B-6):

$$C^{UNHT} = \alpha^{UNHT} H^{UNHT} \tag{B.17}$$

$$C^{HYS} = \alpha^{HYS} H^{HYS} \tag{B.18}$$

A ratio of the scaling parameters, $\left(\frac{\alpha^{UNHT,nano}}{\alpha^{HYS,nano}}\right)^{\gamma}$, is calculated in both mature and immature formations (Table B.1). It is found that a first order α-ratio ($\gamma = 1$) corrects the Hysitron $C^{HYS,nano}$ data (Figure B-4b). This correction reconciles the C-H scaling between machines (Figure B-5 and B-6). We see that $C^{corrHYS,nano}$-$H^{HYS,nano}$ scaling matches that obtained from with the UNHT data for both mature and immature formations (Figure B-7; Table B.1). Figure B-8 shows the nanoscale C-H scaling using all (UNHT and corrected Hysitron) creep nanoindentation data.

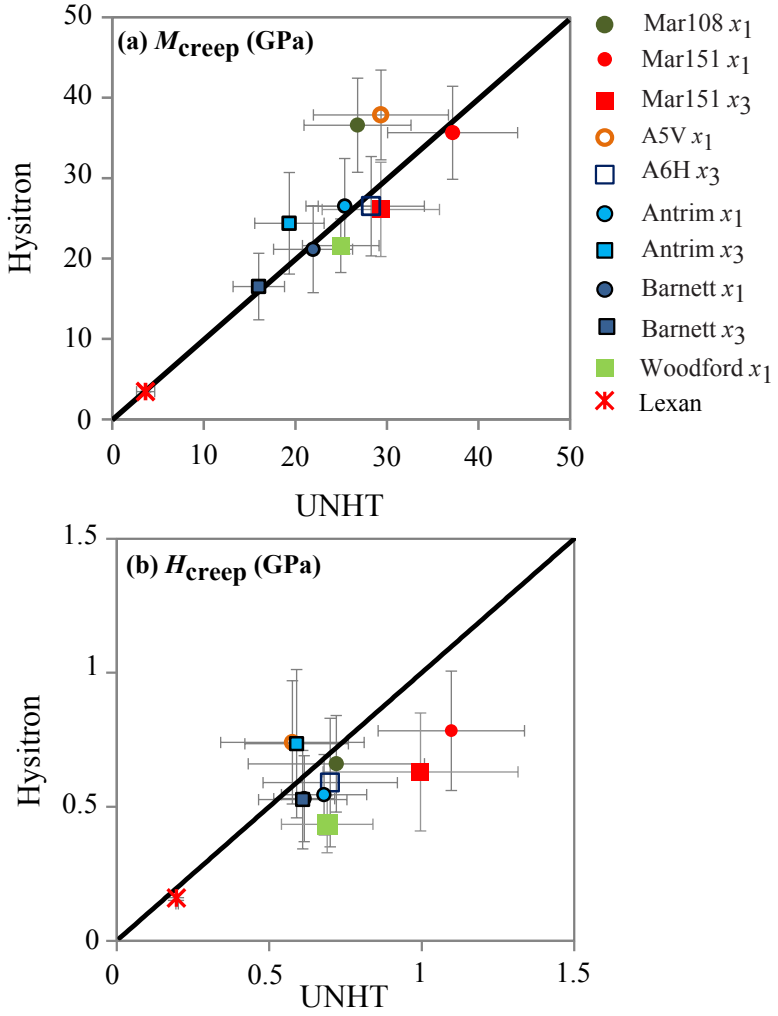

Figure B-3: A Comparison between a) modulus and b) hardness of the clay composites obtained from creep nanoindentation ($P_{max} = 4.8$ mN) tests performed on the UNHT (x-axis values) and the Hysitron (y-axis values).

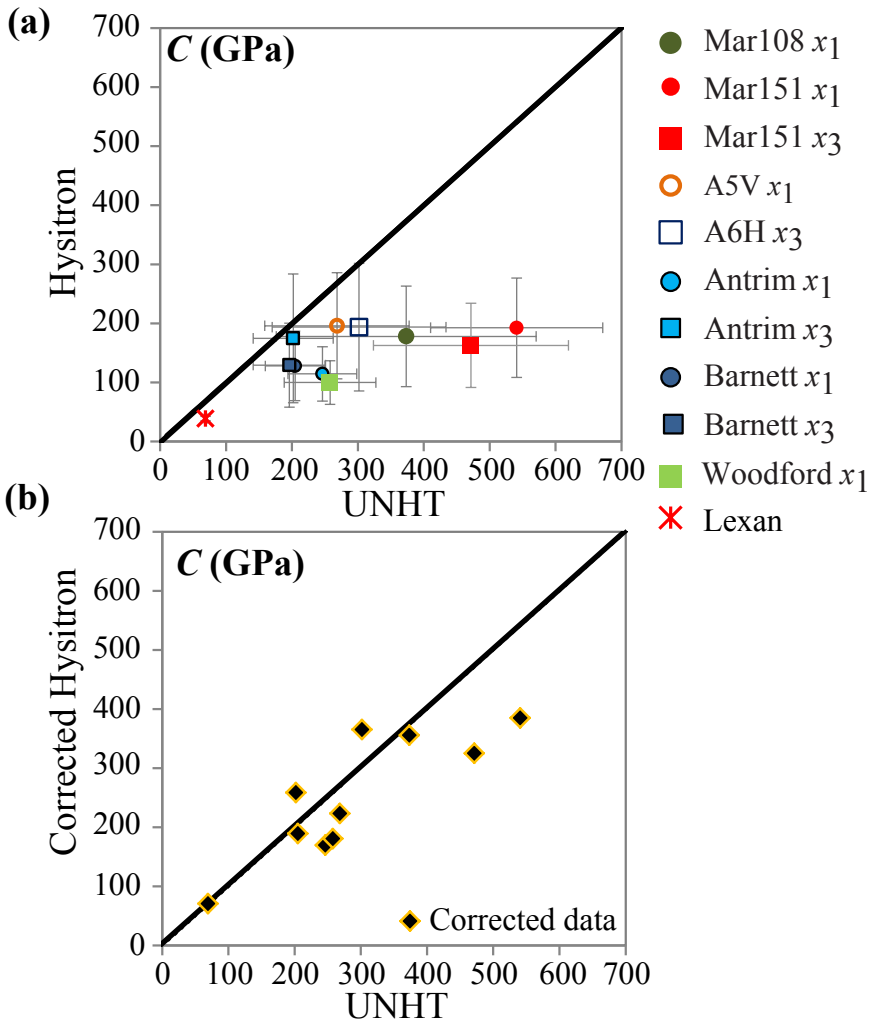

Figure B-4: (a) A Comparison between the nanoindentation contact creep modulus obtained from the UNHT (x-axis values) and Hysitron (y-axis values). (b) Corrected contact creep modulus obtained by the Hysitron machine using $C^{corrHYS,nano} = \frac{\alpha^{UNHT,nano}}{\alpha^{HYS,nano}} C^{HYS,nano}$.

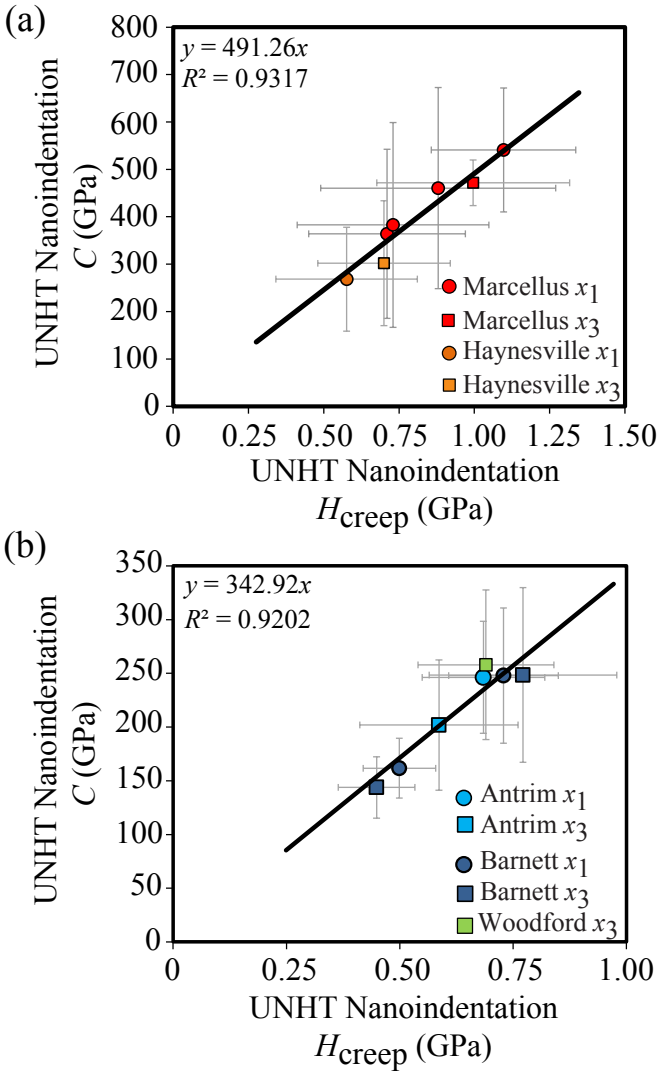

Figure B-5: Linear $C^{UNHTnano}$-$H^{UNHTnano}$ scaling from creep nanoindentation tests performed with the UNHT on (a) mature and (b) immature formations. Note that $\alpha^{UNHTnano,mat} = 491$ and $\alpha^{UNHTnano,imm} = 343$.

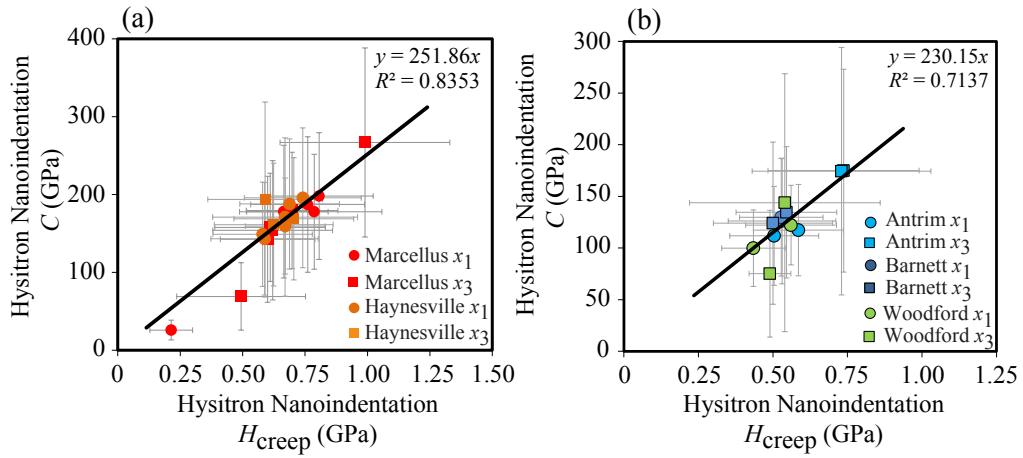

Figure B-6: Linear $C^{HYSnano}$-$H^{HYSnano}$ scaling from (uncorrected) creep nanoindentation results of tests performed with the Hysitron on (a) mature and (b) immature formations. Note that $\alpha^{HYSnano,mat} = 252$ and $\alpha^{HYSnano,imm} = 230$.

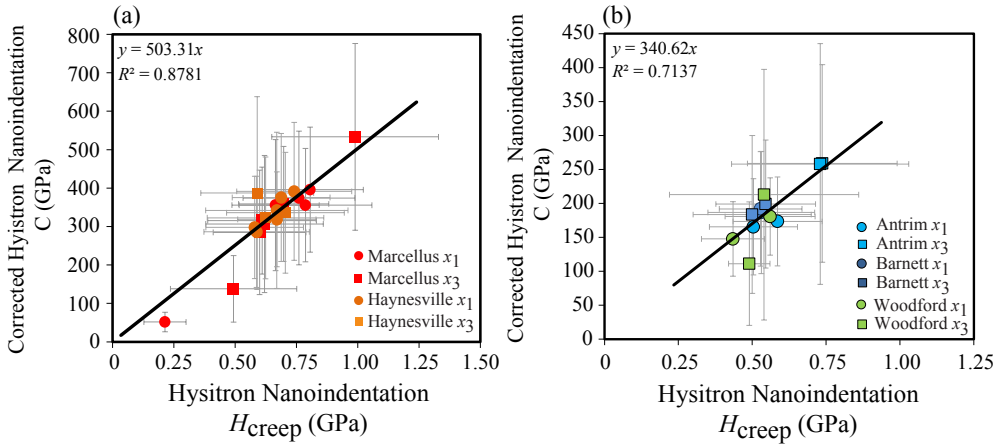

Figure B-7: Linear $C^{corr.HYSnano}$-$H^{HYSnano}$ scaling obtained from creep nanoindentation tests performed with the Hysitron on (a) mature and (b) immature formations. Note that the scaling relationships from the corrected Hysitron data are similar to the ones obtained from the UNHT (Figure B-5; Table B.1).

Table B.1: The C-H scaling parameters obtained from creep nanoindentations done on the UNHT and Hysitron on both mature and immature source rocks. Note the proposed correction factor (column 4) to correct $C^{HYSnano}$ and the resultant Hysitron $C^{corr.HYSnano}$-H scaling (column 5) matching that obtained from the UNHT.

P_{max} = 4.8 mN	UNHT C-H scaling (α^{UNHT})	Hysitron C-H scaling (α^{HYS})	Correction Factor $\frac{\alpha^{UNHT}}{\alpha^{HYS}}$	Corrected Hysitron C-H scaling $\alpha^{corr.HYS}$
Mature	491	252	2.0	503
Immature	343	230	1.5	341

B.4.2 Hysitron Creep Microindentation Correction

Creep microindentation tests at $P_{max} = 12$ mN were also performed on the UNHT and the Hysitron. The maximum depths reached at the end of the creep phase and the evolution of depth with time at constant load do not match between the two machines. This is due to the linear viscoelastic model assumed, by the Hysitron, to depict material creep behavior. Consequently, the contact area calculated from the Hysitron depth and the logarithmic fit of the Hysitron depth-time curve producing the fitting parameter, x_1, are not accurate. These inaccuracies produce errors in $M^{HYS,micro}$, $H^{HYS,micro}$ and $C^{HYS,micro}$ (Figures B-9). Figure B-10 shows the $C^{HYS,micro}$-$H^{HYS,micro}$ scaling and reflects a mismatch with the $C^{UNHT,micro}$-$H^{UNHT,micro}$ (Figure B-11). Corrections are again needed to reconcile Hysitron results to those of the UNHT. As with creep nanoindentation tests, a ratio of the C-H scaling parameters of both machines, $\left(\frac{\alpha^{UNHT,micro}}{\alpha^{HYS,micro}}\right)^{\gamma}$, is calculated in both mature

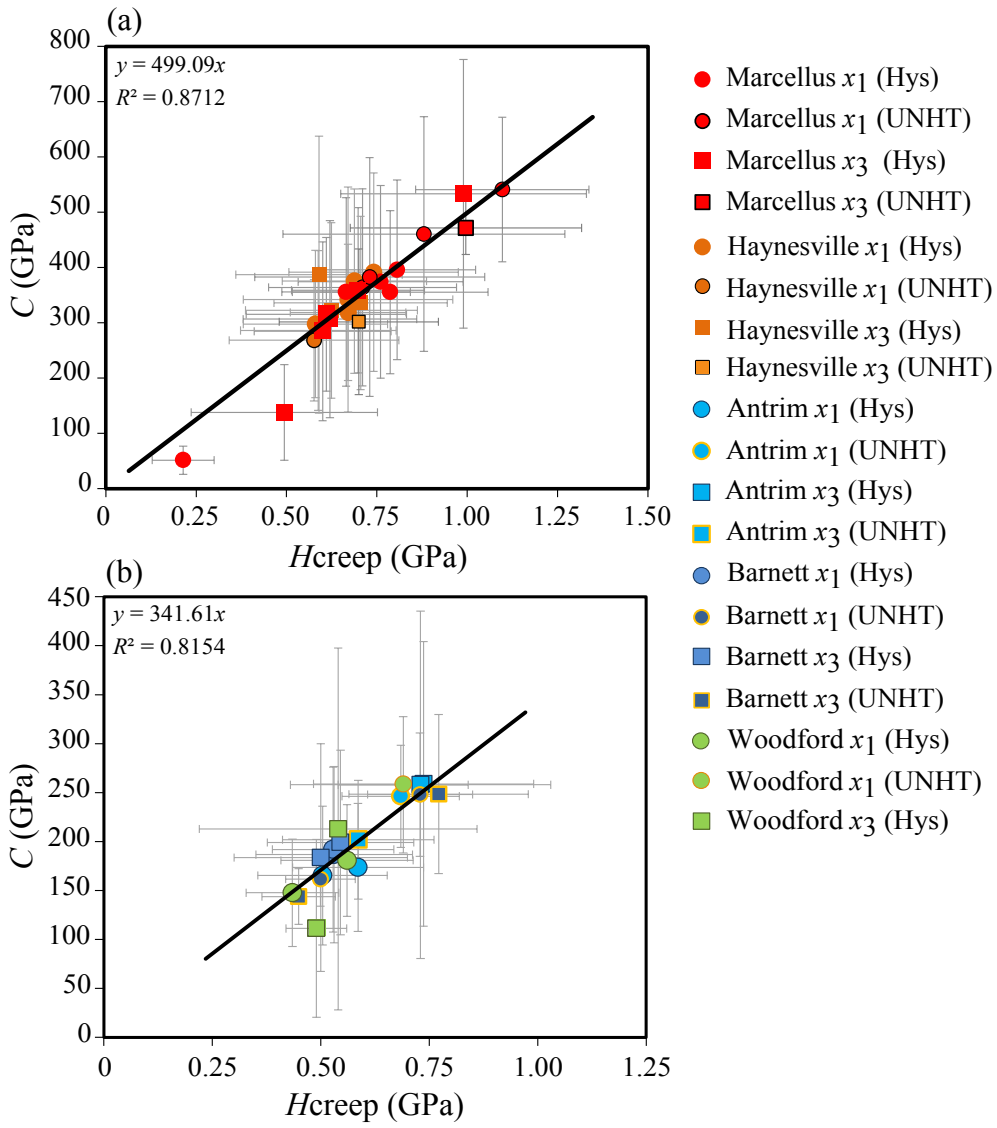

Figure B-8: Linear C^{nano}-H^{nano} scaling obtained from using UNHT and corrected Hysitron creep nanoindentation tests on (a) mature and (b) immature formations.

and immature formations (Table B.2; Figures B-10 and B-11).

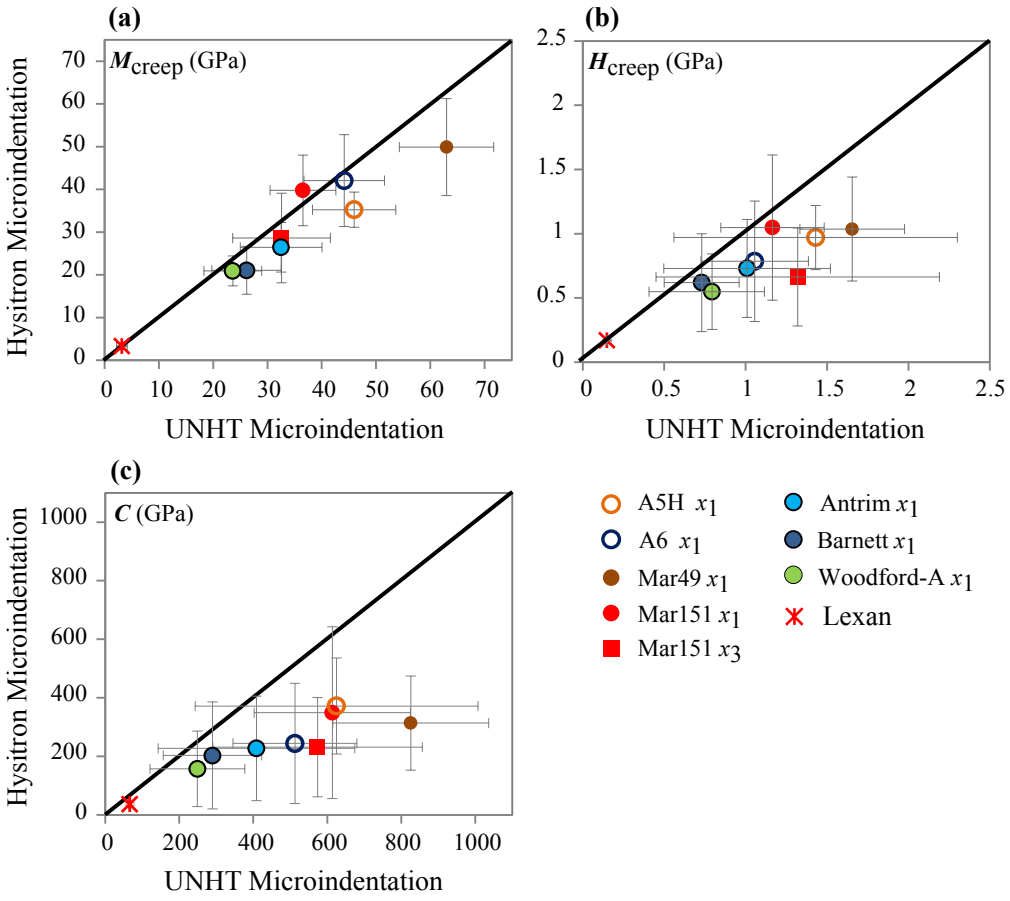

Figure B-9: A Comparison between a) modulus, b) hardness, and c) contact creep modulus obtained from the UNHT (x-axis values) and the Hysitron (y-axis values) performing microindentation tests with $P_{max} = 12$ mN.

It is found that the correction needed (the value of γ) depends on the mechanical property to be corrected. The correction factor (α-ratio) scales as the contact area in the M and H expressions ($M = \frac{\sqrt{\pi}}{2}\frac{S}{\sqrt{A_c}}$ and $H = \frac{P}{A_c}$) such that,

$$M^{corrHYS,micro} = \sqrt{\frac{\alpha^{UNHT,micro}}{\alpha^{HYS,micro}}}\, M^{HYS,micro} \tag{B.19}$$

$$H^{corrHYS,micro} = \frac{\alpha^{UNHT,micro}}{\alpha^{HYS,micro}}\, H^{HYS,micro} \tag{B.20}$$

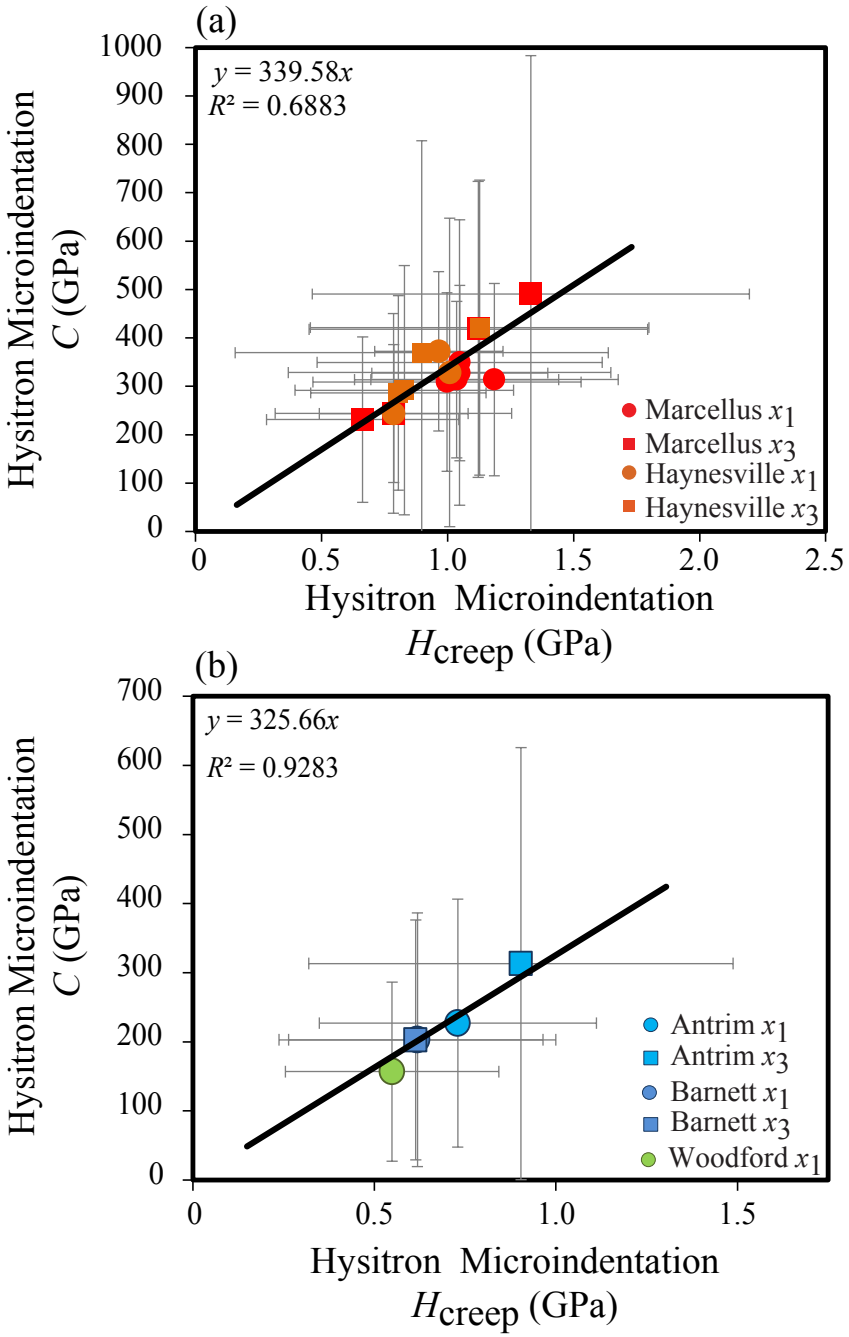

Figure B-10: Linear $C^{HYS,micro}$-$H^{HYS,micro}$ scaling from (uncorrected) creep microindentation results of tests performed with the Hysitron on (a) mature and (b) immature formations using $P_{max} = 12$ mN. Note that $\alpha^{HYS,micro,mat} = 340$ and $\alpha^{HYS,micro,imm} = 326$.

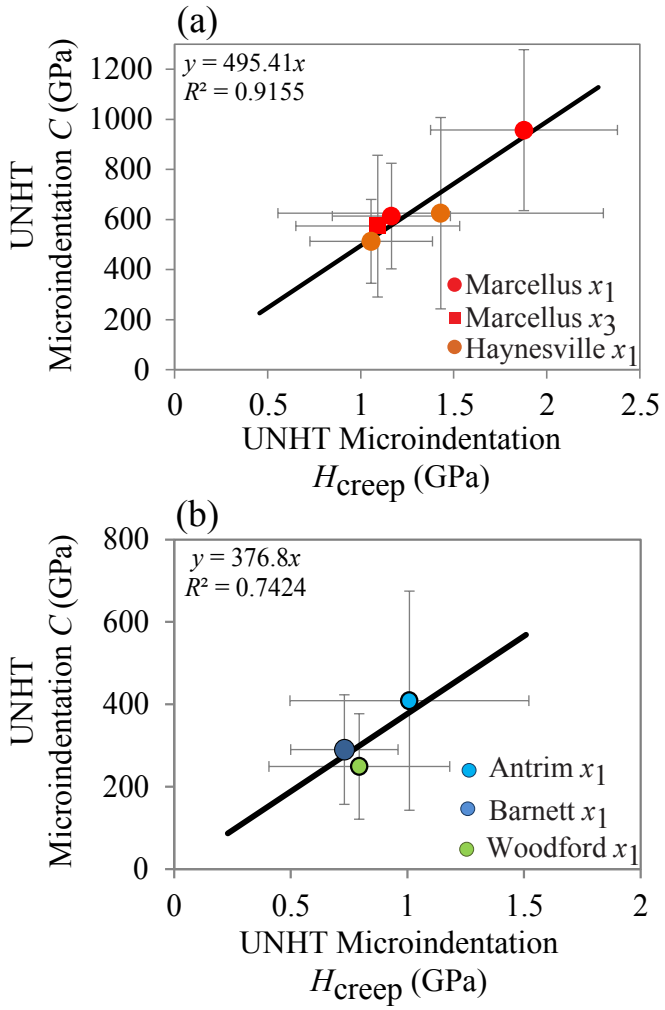

Figure B-11: Linear $C^{UNHT,micro}$-$H^{UNHT,micro}$ scaling from creep microindentation tests performed with the UNHT machine on (a) mature and (b) immature formations using $P_{max} = 12$ mN. Note that $\alpha^{UNHT,micro,mat} = 495$ and $\alpha^{UNHT,micro,imm} = 377$.

Table B.2: The C-H scaling parameters obtained from creep microindentations performed on the UNHT and Hysitron on both mature and immature source rocks using $P_{max} = 12$ mN. Note the proposed correction factor (column 4). Different values of γ are proposed to correct the different mechanical properties. γ is $\frac{1}{2}$, 1, and 2 to correct $M^{HYS,micro}$, $H^{HYS,micro}$, and $C^{HYS,micro}$, respectively. Note the $C^{corrHYS,micro}$-$H^{corrHYS,micro}$ (last column) obtained with corrected Hysitron data matching the UNHT scaling (column 2).

$P_{max} =$ 12 mN	UNHTmicro C-H scaling $\alpha^{UNHT,micro}$	HYSmicro C-H scaling $\alpha^{HYS,micro}$	Correction Factor $\left(\frac{\alpha^{UNHT,micro}}{\alpha^{HYS,micro}}\right)^{\gamma}$	Corr. HYSmicro C-H scaling $\alpha^{corrHYS,micro}$
Mature	495	340	$(1.46)^{\gamma}$	496
Immature	377	326	$(1.16)^{\gamma}$	378

With both fitting parameters and contact area affecting values of the contact creep modulus, the following correction is needed for $C^{HYS,micro}$:

$$C^{corrHYS,micro} = \left(\frac{\alpha^{UNHT,micro}}{\alpha^{HYS,micro}}\right)^{2} C^{HYS,micro} \tag{B.21}$$

Applying the proposed corrections (Equations B.19, B.20, and B.21), a better match is seen between the mechanical results from both indentation machines (Figure B-12). The matching C-H scaling between machines (Figures B-11 and B-13) for both mature and immature formations validates the proposed corrections.

The C-H scaling from creep microindentation tests performed with loads > 12 mN is $\alpha^{mat} = 518$ and $\alpha^{imm} = 367$ (Figure B-14; Table B.3). These results confirm, as argued in Chapter 9, that the C-H scaling in gas shale

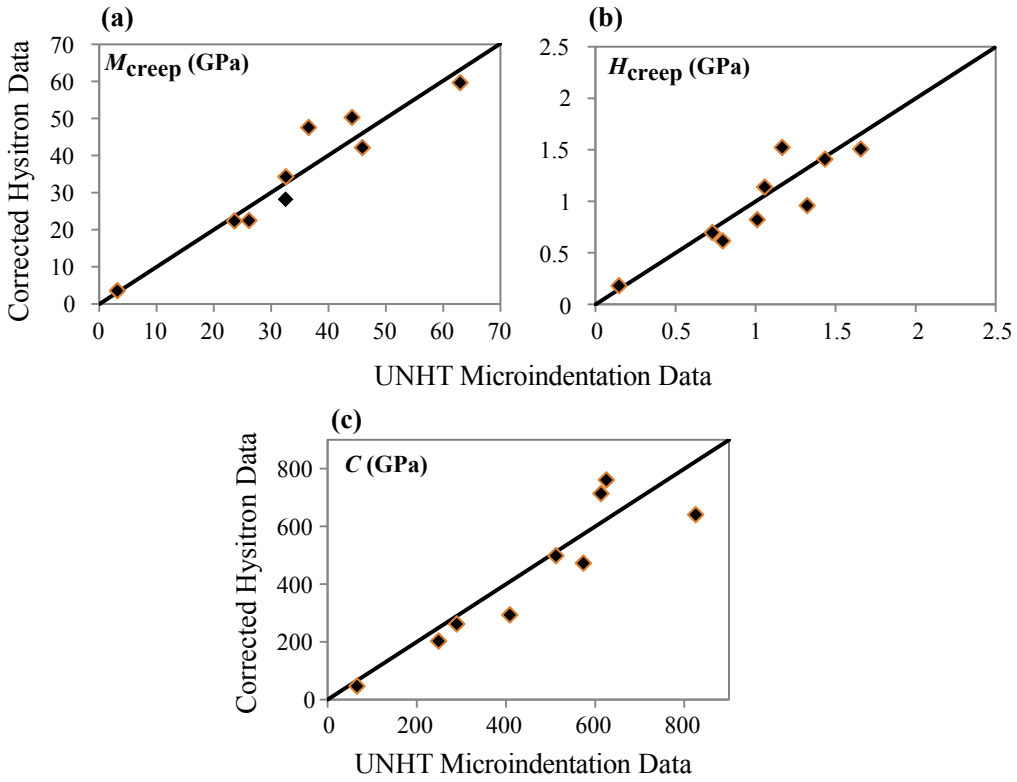

Figure B-12: Corrected Hysitron creep results (y-axis values) from microindentation tests performed sing $P_{max} = 12$ mN compared to those obtained from the UNHT (x-axis values).

formations is maturity-dependent rather than scale- or machine-dependent.

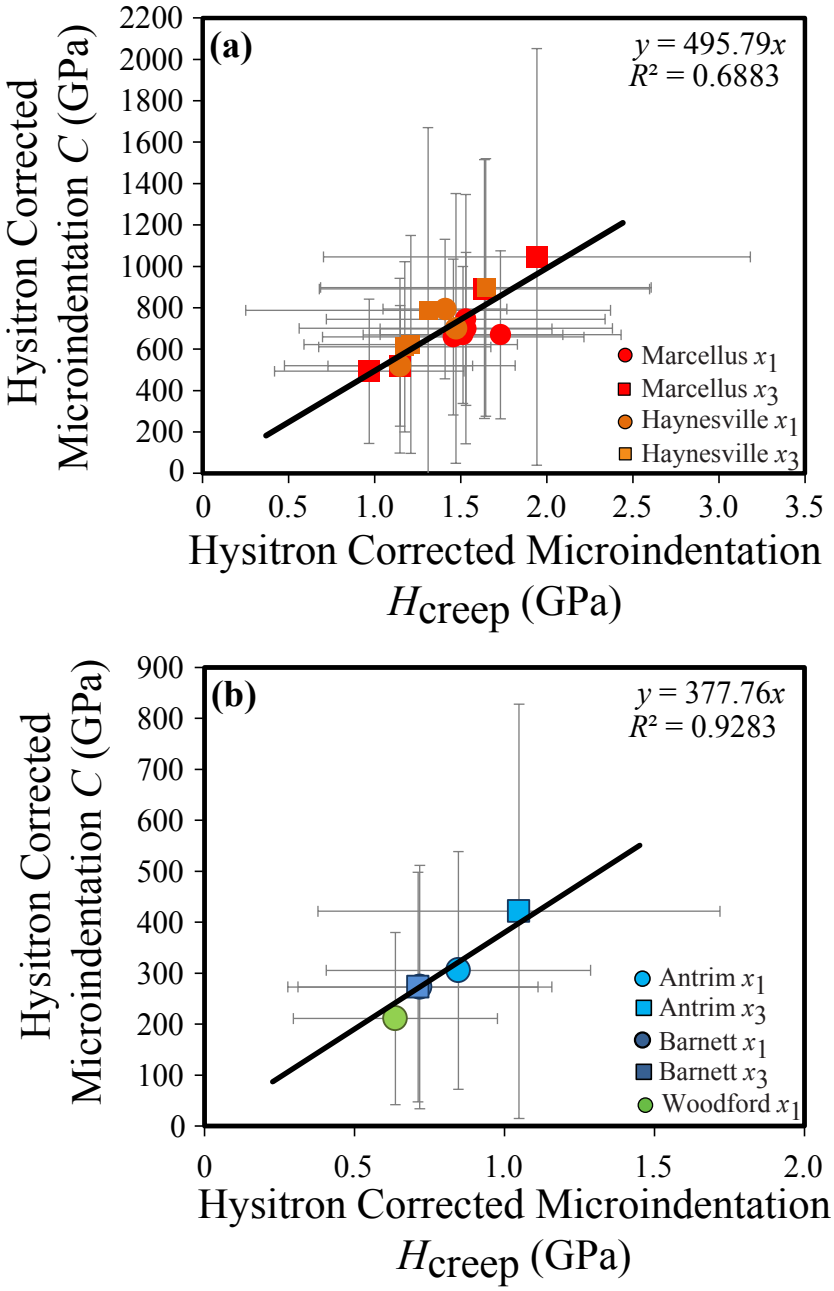

Figure B-13: Corrected linear H-$C^{corr.hys}$ scaling from creep microindentation tests performed with the Hysitron machine on (a) mature and (b) immature formations using $P_{max} = 12$ mN. Note that the scaling relationships are similar the ones obtained from the UNHT machine (Figure B-11).

Table B.3: The C-H scaling parameters obtained from creep indentations at different scales and performed using different machines on both mature and immature formations. The scaling consistency across scales and machine confirms that the C-H scaling is maturity-dependent.

Load	Mature Formations		Immature Formations	
(mN)	UNHT	Corr. HYS	UNHT	Corr. HYS
4.8	491	503	343	341
12	495	496	377	378
20, 30, 50	518	N.A.	367	N.A.

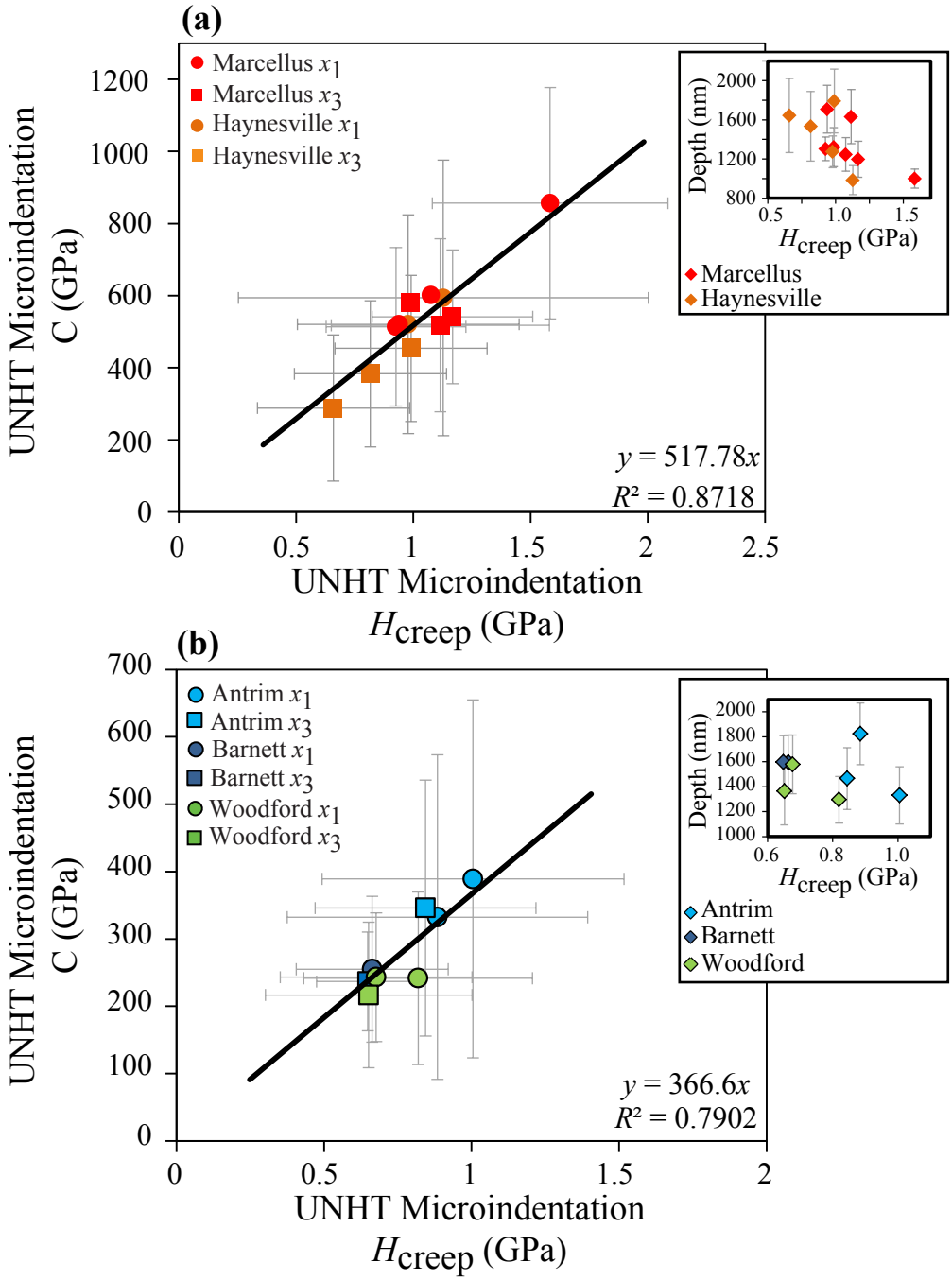

Figure B-14: Linear C-H scaling from creep microindentation tests performed with UNHT using 20 mN, 30 mN, and 50 mN loads on (a) mature and (b) immature formations. The scaling relationships are similar to the ones obtained from the UNHT machine using a 4.8 mN load (Figure B-5) and 12 mN (Figure B-11).

Bibliography

Abedi, S., Slim, M., and Ulm, F.-J., in preparation. Nano-mechanics of organic rich shales: The role of thermal maturity and organic matter content.

Ahmadov, R., Vanorio, T., and Mavko, G., 2009. Confocal laser scanning and atomic-force microscopy in estimation of elastic properties of the organic-rich bazhenov formation. *The Leading Edge*, **28**(1):18–23.

Akaike, H., 1974. A new look at the statistical model identification. *Automatic Control, IEEE Transactions on*, **19**(6):716–723.

Akaike, H., 1998. Information theory and an extension of the maximum likelihood principle. In Selected Papers of Hirotugu Akaike, 199–213. Springer.

Bagault, C., Nélias, D., and Baietto, M.-C., 2012. Contact analyses for anisotropic half space: effect of the anisotropy on the pressure distribution and contact area. *Journal of tribology*, **134**(3):031401.

Banfield, J. D. and Raftery, A. E., 1993. Model-based gaussian and non-gaussian clustering. *Biometrics*, 803–821.

Bao, Y. W., Wang, W., and Zhou, Y. C., 2004. Investigation of the relationship between elastic modulus and hardness based on depth-sensing indentation measurements. *Acta Materialia*, **52**(18):5397–5404.

Barenblatt, G. I., 1996. Scaling, self-similarity, and intermediate asymptotics: dimensional analysis and intermediate asymptotics, volume 14. Cambridge University Press, Cambridge.

Barker, G. and Mehta, A., 1993. Transient phenomena, self-diffusion, and orientational effects in vibrated powders. *Physical Review E*, **47**(1):184.

Barthélémy, J.-F. and Dormieux, L., 2004. A micromechanical approach to the strength criterion of drucker-prager materials reinforced by rigid inclusions. *International Journal for Numerical and Analytical Methods in Geomechanics*, **28**(7-8):565–582.

Baskin, D. K., 1997. Atomic H/C ratio of kerogen as an estimate of thermal maturity and organic matter conversion. *AAPG bulletin*, **81**(9):1437–1450.

Bennett, R. H., O'Brien, N. R., and Hulbert, M. H., 1991. Determinants of clay and shale microfabric signatures: Processes and mechanisms. Springer.

Benveniste, Y., 1987. A new approach to the application of Mori-Tanaka's theory in composite materials. *Mechanics of materials*, **6**(2):147–157.

Berthonneau, J., Hoover, C. G., Grauby, O., Baronnet, A., Pellenq, R. J.-M., and Ulm, F.-J., in preparation. The crystal-chemical control of the elastic properties of 2:1 phyllosilicates minerals.

Biernacki, C. and Govaert, G., 1999. Choosing models in model-based clustering and discriminant analysis. *Journal of Statistical Computation and Simulation*, **64**(1):49–71.

Binder, D. A., 1978. Bayesian cluster analysis. *Biometrika*, **65**(1):31–38.

Bland, D. R., 1960. The theory of linear viscoelasticity. Pergamon Press.

Bobko, C., 2008. Assessing the mechanical microstructure of shale by nanoindentation: The link between mineral composition and mechanical properties. PhD dissertation, Civil and Environmental Engineering Department, Massachusetts Institute of Technology, Cambridge, MA.

Bobko, C. and Ulm, F.-J., 2008. The nano-mechanical morphology of shale. *Mechanics of Materials*, **40**(4):318–337.

Bobko, C. P., Gathier, B., Ortega, J. A., Ulm, F.-J., Borges, L., and Abousleiman, Y. N., 2011. The nanogranular origin of friction and cohesion in shale – a strength homogenization approach to interpretation of nanoindentation results. *International Journal for Numerical and Analytical Methods in Geomechanics*, **35**(17):1854–1876.

Boggs, S., 2009. Petrology of sedimentary rocks. Cambridge University Press, Cambridge.

Borges, L. A., Zouain, N., and Huespe, A. E., 1996. A nonlinear optimization procedure for limit analysis. *European Journal of Mechanics Series A Solids*, **15**:487–512.

Borodich, F. M., 1993. The hertz frictional contact between nonlinear elastic anisotropic bodies (the similarity approach). *International Journal of Solids and Structures*, **30**(11):1513–1526.

Borodich, F. M. and Galanov, B. A., 2002. Self-similar problems of elastic contact for non-convex punches. *Journal of the Mechanics and Physics of Solids*, **50**(11):2441–2461.

Borodich, F. M., Keer, L. M., and Korach, C. S., 2003. Analytical study of fundamental nanoindentation test relations for indenters of non-ideal shapes. *Nanotechnology*, **14**(7):803.

Bousige, C., Ghimbeu, C. M., Vix-Guterl, C., Pomerantz, A. E., Suleimenova, A., Vaughan, G., Garbarino, G., Feygenson, M., Wildgruber, C., Ulm, F.-J., and Coasne, B., 2016. Realistic molecular model of kerogen/'s nanostructure. *Nature materials*.

Boussinesq, J., 1885. Applications des potentiels a l'étude de équilibre et du mouvement des solides élastiques. *Gautier-Villars, Paris*.

Boutreux, T. and de Gennes, P. G., 1997. Compaction of grains: a free volume model. *Physica A xx*, **244**:59–67.

Brenner, D. W., Shenderova, O. A., Harrison, J. A., Stuart, S. J., Ni, B., and Sinnott, S. B., 2002. A second-generation reactive empirical bond order (rebo) potential energy expression for hydrocarbons. *Journal of Physics: Condensed Matter*, **14**(4):783.

Broz, M. E., Cook, R. F., and Whitney, D. L., 2006. Microhardness, toughness, and modulus of mohs scale minerals. *American Mineralogist*, **91**(1):135–142.

Budiansky, B., 1965. On the elastic moduli of some heterogeneous materials. *Journal of the Mechanics and Physics of Solids*, **13**(4):223–227.

Bulychev, S. I., Alekhin, V. P., Shorshorov, M. H., Ternovskii, A. P., and Shnyrev, G. D., 1975. Determining Young's modulus from the indentor penetration diagram. *Ind. Lab.*, **41**(9):1409–1412.

Burke, K. and Dewey, J. F., 1973. Plume-generated triple junctions: key indicators in applying plate tectonics to old rocks. *The Journal of Geology*, 406–433.

Cardott, B. J. and Lambert, M. W., 1985. Thermal maturation by vitrinite reflectance of Woodford Shale, Anadarko Basin, Oklahoma. *AAPG Bulletin*, **69**(11):1982–1998.

Cariou, S., Ulm, F.-J., and Dormieux, L., 2008. Hardness–packing density scaling relations for cohesive-frictional porous materials. *Journal of the Mechanics and Physics of Solids*, **56**(3):924–952.

Carmichael, R. S., 1989. Physical properties of rocks and minerals.

Carter, K. M., Harper, J. A., Schmid, K. W., and Kostelnik, J., 2011. Unconventional natural gas resources in Pennsylvania: The backstory of the modern Marcellus Shale play. *Environmental Geosciences*, **18**(4):217–257.

Celeux, G. and Govaert, G., 1995. Gaussian parsimonious clustering models. *Pattern Recognition*, **28**(5):781–793.

Chalmers, G. R., Bustin, R. M., and Power, I. M., 2012. Characterization of gas shale pore systems by porosimetry, pycnometry, surface area, and field emission scanning electron microscopy/transmission electron microscopy image analyses: Examples from the Barnett, Woodford, Haynesville, Marcellus, and Doig units. *AAPG bulletin*, **96**(6):1099–1119.

Cheng, Y.-T. and Cheng, C.-M., 2004. Scaling, dimensional analysis, and indentation measurements. *Materials Science and Engineering: R: Reports*, **44**(4):91–149.

Christensen, R. M., 1982. Theory of viscoelasticity: An introduction. Academic Press Inc., second edition.

Chudoba, T. and Richter, F., 2001. Investigation of creep behaviour under load during indentation experiments and its influence on hardness and modulus results. *Surface and Coatings Technology*, **148**(2):191–198.

Ciavarella, M., Demelio, G., Schino, M., and Vlassak, J. J., 2001. The general 3d hertzian contact problem for anisotropic materials. In Key Engineering Materials, volume 221, 281–292. Trans Tech Publ.

Cicero, A. D., Steinhoff, I., McClain, T., Koepke, K. A., and Dezelle, J. D., 2010. Sequence stratigraphy of the Upper Jurassic mixed carbonate/siliciclastic Haynesville and Bossier Shale depositional systems in East Texas and North Louisiana. **60**:133–148.

Cohen, M. H. and Turnbull, D., 1959. Molecular transport in liquids and glasses. *The Journal of Chemical Physics*, **31**(5):1164–1169.

Constantinides, G., Ravi Chandran, K., Ulm, F.-J., and Van Vliet, K. J., 2006. Grid indentation analysis of composite microstructure and mechanics: principles and validation. *Materials Science and Engineering: A*, **430**(1):189–202.

Constantinides, G. and Ulm, F.-J., 2007. The nanogranular nature of C-S-H. *Journal of the Mechanics and Physics of Solids*, **55**(1):64–90.

Cottrell, A. H., 1997. Logarithmic and andrade creep. *Philosophical magazine letters*, **75**(5):301–308.

CSM-Instrument, 2013. Ultra nanoindentation tester user manual.

Curtis, M. E., Ambrose, R. J., Sondergeld, C. H., and Rai, C. S., 2011a. Investigation of the relationship between organic porosity and thermal maturity in the marcellus shale. In North American Unconventional Gas Conference and Exhibition. Society of Petroleum Engineers.

Curtis, M. E., Ambrose, R. J., Sondergeld, C. H., and Rai, C. S., 2011b. Transmission and scanning electron microscopy investigation of pore connectivity of gas shales on the nanoscale. In North American Unconventional Gas Conference and Exhibition. Society of Petroleum Engineers.

Curtis, M. E., Cardott, B. J., Sondergeld, C. H., and Rai, C. S., 2012. Development of organic porosity in the Woodford Shale with increasing thermal maturity. *International Journal of Coal Geology*, **103**:26–31.

Deirieh, A., 2011. Statistical nano-chemo-mechanical assessment of shale by wave dispersive spectroscopy and nanoindentation. Master's project, Civil and Environmental Engineering Department, Massachusetts Institute of Technology, Cambridge, MA.

Deirieh, A., 2016. From clay slurries to mudrocks: a Cryo-SEM investigation of the development of the porosity and microstructure. PhD dissertation, Civil and Environmental Engineering Department, Massachusetts Institute of Technology, Cambridge, MA.

Deirieh, A., Ortega, J. A., Ulm, F.-J., and Abousleiman, Y., 2012. Nanochemomechanical assessment of shale: a coupled wds-indentation analysis. *Acta Geotechnica*, **7**(4):271–295.

Delafargue, A. and Ulm, F.-J., 2004. Explicit approximations of the indentation modulus of elastically orthotropic solids for conical indenters. *International Journal of Solids and Structures*, **41**(26):7351–7360.

Dempster, A. P., Laird, N. M., and Rubin, D. B., 1977. Maximum likelihood from incomplete data via the em algorithm. *Journal of the Royal Statistical Society. Series B (Methodological)*, 1–38.

Doerner, M. F. and Nix, W. D., 1986. A method for interpreting the data from depth-sensing indentation instruments. *Journal of Materials Research*, **1**(04):601–609.

Dormieux, L., Kondo, D., and Ulm, F.-J., 2006. Microporomechanics. John Wiley & Sons.

Dow, W. G., 1977. Kerogen studies and geological interpretations. *Journal of Geochemical Exploration*, **7**:79–99.

Dubes, R. and Jain, A. K., 1976. Clustering techniques: the user's dilemma. *Pattern Recognition*, **8**(4):247–260.

Dyke, P., 2001. An introduction to Laplace transforms and Fourier series. Springer-Verlag, second edition.

Ebrahimi, D., Pellenq, R. J.-M., and Whittle, A. J., 2012. Nanoscale elastic properties of montmorillonite upon water adsorption. *Langmuir*, **28**(49):16855–16863.

EIA, 2013. Technically recoverable shale oil and shale gas resources: An assessment of 137 shale formations in 41 countries outside the United States. Technical report, U.S. Energy Information Administration.

EIA, 2014. U.s. crude oil and natural gas proved reserves, 2013. Technical report, U.S. Energy Information Administration.

Eshelby, J. D., 1957. The determination of the elastic field of an ellipsoidal inclusion, and related problems. In Proceedings of the Royal Society of London A: Mathematical, Physical and Engineering Sciences, volume 241, 376–396. The Royal Society.

Eslinger, E. and Pevear, D. R., 1988. Clay minerals for petroleum geologists and engineers. Society of Economic Paleontologists and Mineralogists.

Espitalié, J., Laporte, J. L., Madec, M., Marquis, F., Leplat, P., Paulet, J., and Boutefeu, A., 1977a. Méthode rapide de caractérisation des roches mères, de leur potentiel pétrolier et de leur degré d'évolution. *Oil & Gas Science and Technology*, **32**(1):23–42.

Espitalié, J., Madec, M., Tissot, B., Mennig, J. J., Leplat, P. et al., 1977b. Source rock characterization method for petroleum exploration. In Offshore Technology Conference. Offshore Technology Conference.

Ewing, T. E., 2001. Review of Late Jurassic depositional systems and potential hydrocarbon plays, northern Gulf of Mexico Basin. **51**:85–96.

Feng, G. and Ngan, A. H. W., 2002. Effects of creep and thermal drift on modulus measurement using depth-sensing indentation. *Journal of Materials Research*, **17**(03):660–668.

Fischer-Cripps, A. C., 2007. Introduction to Contact Mechanics. Springer.

Fischer-Cripps, A. C., 2011. Nanoindentation. Springer.

Fraley, C. and Raftery, A. E., 1998. How many clusters? which clustering method? answers via model-based cluster analysis. *The Computer Journal*, **41**(8):578–588.

Fraley, C. and Raftery, A. E., 1999. MCLUST: Software for model-based cluster analysis. *Journal of Classification*, **16**(2):297–306.

Fraley, C. and Raftery, A. E., 2002a. MCLUST: Software for model-based clustering density estimation and discriminant analysis. Unpublished-Technical Report No. 45, Department of Statistics, University of Washington.

Fraley, C. and Raftery, A. E., 2002b. Model-based clustering, discriminant analysis, and density estimation. *Journal of the American Statistical Association*, **97**(458):611–631.

Fritsch, A., Dormieux, L., Hellmich, C., and Sanahuja, J., 2007. Micromechanics of crystal interfaces in polycrystalline solid phases of porous media: fundamentals and application to strength of hydroxyapatite biomaterials. *Journal of Materials Science*, **42**(21):8824–8837.

Ganneau, F. P., Constantinides, G., and Ulm, F.-J., 2006. Dual-indentation technique for the assessment of strength properties of cohesive-frictional materials. *International Journal of Solids and Structures*, **43**(6):1727–1745.

Garner, D. L. and Turcotte, D. L., 1984. The thermal and mechanical evolution of the Anadarko Basin. *Tectonophysics*, **107**(1):1–24.

Gathier, B., 2008. Multiscale strength and homogenization–application to shale nanoindentation. Master's project, Civil and Environmental Engineering Department, Massachusetts Institute of Technology, Cambridge, MA.

Germaine, J. T. and Germaine, A. V., 2009. Geotechnical laboratory measurements for engineers. John Wiley & Sons.

Gonzalez, J., Lewis, R., Hemingway, J., Grau, J., Rylander, E., and Schmitt, R., 2013. Determination of formation organic carbon content using a new neutron-induced gamma ray spectroscopy service that directly measures carbon. Unconventional Resources Technology Conference (URTEC).

Grim, R. E., 1939. Relation of the composition to the properties of clays. *Journal of the American Ceramic Society*, **22**(1-12):141–151.

Gutschick, R. C. and Sandberg, C. A., 1991. Late Devonian history of Michigan Basin. *Geological Society of America Special Papers*, **256**:181–202.

Handford, C. R., 1986. Facies and bedding sequences in shelf-storm-deposited carbonates–fayetteville shale and pitkin limestone (Mississippian), arkansas. *Journal of Sedimentary Research*, **56**(1):123–137.

Hantal, G., Brochard, L., Laubie, H., Ebrahimi, D., Pellenq, R. J.-M., Ulm, F.-J., and Coasne, B., 2014. Atomic-scale modelling of elastic and failure properties of clays. *Molecular Physics*, **112**(9-10):1294–1305.

Harris, N. B., Miskimins, J. L., and Mnich, C. A., 2011. Mechanical anisotropy in the woodford shale, permian basin: Origin, magnitude, and scale. *The Leading Edge*, **30**(3):284–291.

Hay, J. C., Bolshakov, A., and Pharr, G. M., 1999. A critical examination of the fundamental relations used in the analysis of nanoindentation data. *Journal of Materials Research*, **14**(06):2296–2305.

Hellmich, C., Barthélémy, J.-F., and Dormieux, L., 2004. Mineral–collagen interactions in elasticity of bone ultrastructure – a continuum micromechanics approach. *European Journal of Mechanics-A/Solids*, **23**(5):783–810.

Hershey, A. V. and Dahlgren, V. A., 1954. The elasticity of an isotropic aggregate of anisotropic cubic crystals. *Journal of Applied Mechanics-Transactions of the ASME*, **21**(3):236–240.

Hertz, H., 1882. On the contact of rigid elastic solids and on hardness. chapter 6. Macmillan.

Hill, R., 1965. A self-consistent mechanics of composite materials. *Journal of the Mechanics and Physics of Solids*, **13**(4):213–222.

Ho, N.-C., Peacor, D. R., and Van Der Pluijm, B. A., 1999. Preferred orientation of phyllosilicates in gulf coast mudstones and relation to the smectite-illite transition. *Clays and Clay Minerals*, **47**(4):495–504.

Holt, R. M., Bhuiyan, M. H., Kolstø, M. I., Bakk, A., Stenebraten, J. F., and Fjær, E., 2011. Stress-induced versus lithological anisotropy in compacted claystones and soft shales. *The Leading Edge*, **30**(3):312–317.

Howell, P. D. and Van Der Pluijm, B. A., 1990. Early history of the michigan basin: Subsidence and appalachian tectonics. *Geology*, **18**(12):1195–1198.

Hower, J., Eslinger, E. V., Hower, M. E., and Perry, E. A., 1976. Mechanism of burial metamorphism of argillaceous sediment: 1. mineralogical and chemical evidence. *Geological Society of America Bulletin*, **87**(5):725–737.

Hubler, M. H., Gelb, J., and Ulm, F.-J., submitted. Microtexture analysis of gas shale by xrm imaging. *Acta Geotechnica*.

Hysitron, I., 2011. TI 950 TriboIndenter user manual. Hysitron Incorporated.

Jaeger, H. M., Liu, C.-H., and Nagel, S. R., 1989. Relaxation at the angle of repose. *Physical Review Letters*, **62**(1):40.

Jaeger, J. C., Cook, N. G. W., and Zimmerman, R., 2007. Fundamentals of rock mechanics. Blackwell Publishing Ltd.

Jain, S. K. and Nanda, A., 2010. On the nature of secondary compression in soils.

Jarvie, D. M., Hill, R. J., Ruble, T. E., and Pollastro, R. M., 2007. Unconventional shale-gas systems: The mississippian barnett shale of north-central texas as one model for thermogenic shale-gas assessment. *AAPG bulletin*, **91**(4):475–499.

Jin, L., Rother, G., Cole, D. R., Mildner, D. F. R., Duff, C. J., and Brantley, S. L., 2011. Characterization of deep weathering and nanoporosity development in shale – a neutron study. *American Mineralogist*, **96**(4):498–512.

Jones, L. E. A. and Wang, H. F., 1981. Ultrasonic velocities in cretaceous shales from the williston basin. *Geophysics*, **46**(3):288–297.

Kaliszky, S., 1989. Plasticity: theory and engineering applications, volume 21. Elsevier Science Publishing Company, Inc.

Kass, R. E. and Raftery, A. E., 1995. Bayes factors. *Journal of the American Statistical Association*, **90**(430):773–795.

Katahara, K. W., 1996. Clay mineral elastic properties. In 1996 SEG Annual Meeting. Society of Exploration Geophysicists.

Katz, B. e., 1995. Petroleum Source Rocks. Springer-Verlag.

Keller, G. R., Lidiak, E. G., Hinze, W. J., and Braile, L. W., 1983. The role of rifting in the tectonic development of the midcontinent, usa. *Tectonophysics*, **94**(1):391–412.

Keller, L. M., Holzer, L., Wepf, R., and Gasser, P., 2011. 3d geometry and topology of pore pathways in opalinus clay: Implications for mass transport. *Applied Clay Science*, **52**(1):85–95.

Khursheed, A., 2011. Scanning electron microscope optics and spectrometers. World Scientific Publishing Co. Pte. Ltd.

King, R. B., 1987. Elastic analysis of some punch problems for a layered medium. *International Journal of Solids and Structures*, **23**(12):1657–1664.

Knight, J. B., Fandrich, C. G., Lau, C. N., Jaeger, H. M., and Nagel, S. R., 1995. Density relaxation in a vibrated granular material. *Physical Review E*, **51**(5):3957.

Koesoemadinata, A., El-Kaseeh, G., Banik, N., Dai, J., Egan, M., Gonzalez, A., and Tamulonis, K., 2011. Seismic reservoir characterization in Marcellus Shale. In 2011 SEG Annual Meeting. Society of Exploration Geophysicists.

Kuila, U. and Prasad, M., 2013. Specific surface area and pore-size distribution in clays and shales. *Geophysical Prospecting*, **61**(2):341–362.

Kumar, V., Sondergeld, C., and Rai, C., 2012. Nano to Macro Mechanical Characterization of Shale. *SPE Annual Technical Conference. SPE 159804*.

Lambe, T. W. and Whitman, R. V., 1969. Soil mechanics SI version. John Wiley & Sons.

Lee, E. H., 1955. Stress analysis in visco-elastic bodies. *Quarterly of Applied Mathematics*, **13**:183–190.

Lee, E. H. and Radok, J. R. M., 1960. The contact problem for viscoelastic bodies. *Journal of Applied Mechanics*, **27**(3):438–444.

Lemaître, A., 2002. Rearrangements and dilatancy for sheared dense materials. *Physical Review Letters*, **89**(19):195503.

Leng, Y., 2009. Materials characterization: introduction to microscopic and spectroscopic methods. John Wiley & Sons.

Lonardelli, I., Wenk, H.-R., and Ren, Y., 2007. Preferred orientation and elastic anisotropy in shales. *Geophysics*, **72**(2):D33–D40.

Loucks, R. G., Reed, R. M., Ruppel, S. C., and Jarvie, D. M., 2009. Morphology, genesis, and distribution of nanometer-scale pores in siliceous mudstones of the Mississippian Barnett Shale. *Journal of Sedimentary Research*, **79**(12):848–861.

Loucks, R. G. and Ruppel, S. C., 2007. Mississippian Barnett Shale: Lithofacies and depositional setting of a deep-water shale-gas succession in the Fort Worth Basin, Texas. *AAPG bulletin*, **91**(4):579–601.

Love, A. E. H., 1939. Boussinesq's problem for a rigid cone. *The Quarterly Journal of Mathematics*, (1):161–175.

Lucier, A. M., Hofmann, R., and Bryndzia, L. T., 2011. Evaluation of variable gas saturation on acoustic log data from the Haynesville Shale gas play, NW Louisiana, USA. *The Leading Edge*, **30**(3):300–311.

Martini, A. M., Walter, L. M., Budai, J. M., Ku, T. C. W., Kaiser, C. J., and Schoell, M., 1998. Genetic and temporal relations between formation waters and biogenic methane: Upper Devonian Antrim Shale, Michigan Basin, USA. *Geochimica et Cosmochimica Acta*, **62**(10):1699–1720.

Mavko, G., Mukerji, T., and Dvorkin, J., 1998. The Rock Physics Handbook: Tools for Seismic Analysis in Porous Media, 329 pp. Cambridge University Press, Cambridge.

Mba, K. C., Prasad, M., and Batzle, M. L., 2010. The maturity of organic-rich shales using microimpedance analysis. In SPE Annual Technical Conference and Exhibition. Society of Petroleum Engineers.

McCarthy, K., Rojas, K., Niemann, M., Palmowski, D., Peters, K., and Stankiewicz, A., 2011. Basic petroleum geochemistry for source rock evaluation. *Oilfield Review*, **23**(2):32–43.

McLachlan, G. and Peel, D., 2000. Finite mixture models. John Wiley & Sons.

Mesri, G., 2003. Primary compression and secondary compression. In R. V. Whitman, T. C. Sheahan, and J. T. Germaine (editors), Soil Behavior and Soft Ground Construction. American Society of Civil Engineers, Reston, VA.

Mesri, G. and Castro, A., 1987. C α/c c concept and k 0 during secondary compression. *Journal of Geotechnical Engineering*, **113**(3):230–247.

Meunier, A. and Velde, B., 2004. Illite. Springer-Verlag.

Minear, J. W., 1982. Clay models and acoustic velocities. In SPE Annual Technical Conference and Exhibition. Society of Petroleum Engineers.

Mondol, N. H., Jahren, J., Bjørlykke, K., and Brevik, I., 2008. Elastic properties of clay minerals. *The Leading Edge*, **27**(6):758–770.

Monfared, S. and Ulm, F.-J., 2015. A molecular informed poroelastic model for organic-rich, naturally occurring porous geocomposites. *Journal of the Mechanics and Physics of Solids*.

Montgomery, S. L., Jarvie, D. M., Bowker, K. A., and Pollastro, R. M., 2005. Mississippian Barnett Shale, Fort Worth Basin, north-central Texas: Gas-shale play with multi–trillion cubic foot potential. *AAPG bulletin*, **89**(2):155–175.

Mori, T. and Tanaka, K., 1973. Average stress in matrix and average elastic energy of materials with misfitting inclusions. *Acta Metallurgica*, **21**(5):571–574.

Moseley, H. G. J., 1913. XCIII. The high-frequency spectra of the elements. *The London, Edinburgh, and Dublin Philosophical Magazine and Journal of Science*, **26**(156):1024–1034.

Nabarro, F. R. N., 2001. The time constant of logarithmic creep and relaxation. *Materials Science and Engineering: A*, **309**:227–228.

Nemat-Nasser, S. and Hori, M., 1993. Micromechanics: overall properties of heterogeneous materials. Elsevier.

Nowak, E. R., Knight, J. B., Ben-Naim, E., Jaeger, H. M., and Nagel, S. R., 1998. Density fluctuations in vibrated granular materials. *Physical Review E*, **57**(2):1971–1982.

Oliver, W. C. and Pharr, G. M., 1992. An improved technique for determining hardness and elastic modulus using load and displacement sensing indentation experiments. *Journal of Materials Research*, **7**(06):1564–1583.

Oliver, W. C. and Pharr, G. M., 2004. Measurement of hardness and elastic modulus by instrumented indentation: Advances in understanding and refinements to methodology. *Journal of Materials Research*, **19**(01):3–20.

Ortega, J. A., 2010. Microporomechanical modeling of shale. PhD dissertation, Civil and Environmental Engineering Department, Massachusetts Institute of Technology, Cambridge, MA.

Ortega, J. A., Ulm, F.-J., and Abousleiman, Y., 2007. The effect of the nanogranular nature of shale on their poroelastic behavior. *Acta Geotechnica*, **2**(3):155–182.

Ortega, J. A., Ulm, F.-J., and Abousleiman, Y., 2010. The effect of particle shape and grain-scale properties of shale: A micromechanics approach. *International Journal for Numerical and Analytical Methods in Geomechanics*, **34**(11):1124–1156.

Pei, J., 2008. Strength of Transversely isotropic rocks. PhD dissertation, Civil and Environmental Engineering Department, Massachusetts Institute of Technology, Cambridge, MA.

Pharr, G. M. and Bolshakov, A., 2002. Understanding nanoindentation unloading curves. *Journal of Materials Research*, **17**(10):2660–2671.

Pharr, G. M., Oliver, W. C., and Brotzen, F. R., 1992. On the generality of the relationship among contact stiffness, contact area, and elastic modulus during indentation. *Journal of Materials Research*, **7**(03):613–617.

Ponte Castañeda, P., 1992. New variational principles in plasticity and their application to composite materials. *Journal of the Mechanics and Physics of Solids*, **40**(8):1757–1788.

Ponte Castañeda, P., 2002. Second-order homogenization estimates for nonlinear composites incorporating field fluctuations: I theory. *Journal of the Mechanics and Physics of Solids*, **50**(4):737–757.

Potts, P. J., 1992. A handbook of silicate rock analysis. Springer Science & Business Media.

Prasad, M., Kopycinska, M., Rabe, U., and Arnold, W., 2002a. Measurement of Young's modulus of clay minerals using atomic force acoustic microscopy. *Geophysical Research Letters*, **29**(8).

Prasad, M., Mba, K. C., Sadler, T., and Batzle, M. L., 2011. Maturity and impedance analysis of organic-rich shales. *SPE Reservoir Evaluation & Engineering*, **14**(05):533–543.

Prasad, M. and Mukerji, T., 2003. Analysis of microstructural textures and wave propagation characteristics in shales. In 2003 SEG Annual Meeting. Society of Exploration Geophysicists.

Prasad, M., Mukerji, T., Reinstaedler, M., and Arnold, W., 2009. Acoustic signatures, impedance microstructure, textural scales, and anisotropy of kerogen-rich shales. In SPE Annual Technical Conference and Exhibition, SPE 124840, 1–14. Society of Petroleum Engineers.

Prasad, M., Reinstaedtler, M., Nur, A., and Arnold, W., 2002b. Quantitative acoustic microscopy: Application to petrophysical studies of reservoir rocks. *Acoustical Imaging*, **26**:493–502.

Reed, S. J. B., 2005. Electron microprobe analysis and scanning electron microscopy in geology. Cambridge University Press, Cambridge.

Rogers, H., 2011. Shale gas–the unfolding story. *Oxford Review of Economic Policy*, **27**(1):117–143.

Russ, J. C., 1984. Fundamentals of energy dispersive x-ray analysis. Butterworth-Heinemann.

SA, A. P. T., 2013. Ultra nanoindentation tester user manual.

Sakharova, N. A., Fernandes, J. V., Antunes, J. M., and Oliveira, M. C., 2009. Comparison between berkovich, vickers and conical indentation tests: A three-dimensional numerical simulation study. *International Journal of Solids and Structures*, **46**(5):1095–1104.

Salençon, J., 1983. Calcul à la rupture et analyse limit. *European journal of mechanics. A. Solids.*

Schwarz, G., 1978. Estimating the dimension of a model. *The Annals of Statistics*, **6**(2):461–464.

Schweiger, H. F., 1994. On the use of Drucker-Prager failure criteria for earth pressure problems. *Computers and Geotechnics*, **16**(3):223–246.

Severin, K. P., 2004. Energy dispersive spectrometry of common rock forming minerals. Kluwer Academic Publisher.

Sintubin, M., 1994. Clay fabrics in relation to the burial history of shales. *Sedimentology*, **41**(6):1161–1170.

Sneddon, I. N., 1965. The relation between load and penetration in the axisymmetric boussinesq problem for a punch of arbitrary profile. *International Journal of Engineering Science*, **3**(1):47–57.

Soeder, D. J., Enomoto, C. B., and Chermak, J. A., 2014. The Devonian Marcellus Shale and Millboro Shale. *Field Guides*, **35**:129–160.

Sondergeld, C. H. and Rai, C. S., 2011. Elastic anisotropy of shales. *The Leading Edge*, **30**(3):324–331.

Sone, H., 2012. Mechanical properties of shale gas reservoirs rocks and its relations to the in-situ stress variation observed in shale gas reservoirs. PhD dissertation, Department of Geophysics, Standford University, Palo alto, California.

Sone, H. and Zoback, M. D., 2013. Mechanical properties of shale-gas reservoir rocks – part 2: Ductile creep, brittle strength, and their relation to the elastic modulus. *Geophysics*, **78**(5):D393–D402.

Spaepen, F., 1977. A microscopic mechanism for steady state inhomogeneous flow in metallic glasses. *Acta metallurgica*, **25**(4):407–415.

Stilwell, N. A. and Tabor, D., 1961. Elastic recovery of conical indentations. *Proceedings of the Physical Society*, **78**(2):169.

Sullivan, K. L., 1985. Organic facies variation of the Woodford Shale in western Oklahoma. 185–198.

Suquet, P., 1997. Effective properties of nonlinear composites. In P. Suquet (editor), Continuum Micromechanics, CISM Courses and Lectures No. 377, 197–264. Springer.

Swadener, J. G. and Pharr, G. M., 2001. Indentation of elastically anisotropic half-spaces by cones and parabolae of revolution. *Philosophical Magazine A*, **81**(2):447–466.

Tabor, D., 1948. A simple theory of static and dynamic hardness. In Proceedings of the Royal Society of London A: Mathematical, Physical and Engineering Sciences, volume 192, 247–274. The Royal Society.

Tabor, D., 1951. The hardness of metals, Clarendon. Oxford.

Ting, T. C. T., 1966. The contact stresses between a rigid indenter and a viscoelastic half-space. *Journal of Applied Mechanics*, **33**(4):845–854.

Tissot, B. P. and Welte, D. H., 1984. Petroleum Formation and Occurrence: A New Approach Co Oil and GUS Exploration. Springer-Verlag.

Ulm, F.-J. and Abousleiman, Y., 2006. The nanogranular nature of shale. *Acta Geotechnica*, **1**(2):77–88.

Ulm, F.-J., Constantinides, G., Delafargue, A., Abousleiman, Y., Ewy, R., Duranti, L., and McCarty, D. K., 2005a. Material invariant poromechanics properties of shales. *Poromechanics III. Biot Centennial (1905–2005), AA Balkema Publishers, London*, 637–644.

Ulm, F.-J. and Coussy, O., 2003. Mechanics and Durability of Solids, Volume I, Solid Mechanics. Prentice Hall.

Ulm, F.-J., Delafargue, A., and Constantinides, G., 2005b. Experimental microporomechanics. Springer.

Ulm, F.-J., Vandamme, M., Bobko, C., Ortega, J. A., Tai, K., and Ortiz, C., 2007. Statistical indentation techniques for hydrated nanocomposites: concrete, bone, and shale. *Journal of the American Ceramic Society*, **90**(9):2677–2692.

Ulm, F.-J., Vandamme, M., Jennings, H. M., Vanzo, J., Bentivegna, M., Krakowiak, K. J., Constantinides, G., Bobko, C. P., and Van Vliet, K. J., 2010. Does microstructure matter for statistical nanoindentation techniques? *Cement and Concrete Composites*, **32**(1):92–99.

Van Krevelen, D. W., 1984. Organic geochemistry: old and new. *Organic geochemistry*, **6**:1–10.

Vandamme, M., 2008. The nanogranular origin of concrete creep: A nanoindentation investigation of microstructure and fundamental properties of calcium-silicate-hydrates. PhD dissertation, Civil and Environmental Engineering Department, Massachusetts Institute of Technology, Cambridge, MA.

Vandamme, M., Tweedie, C. A., Constantinides, G., Ulm, F.-J., and Van Vliet, K. J., 2012. Quantifying plasticity-independent creep compliance and relaxation of viscoelastoplastic materials under contact loading. *Journal of Materials Research*, **27**(01):302–312.

Vandamme, M. and Ulm, F.-J., 2006. Viscoelastic solutions for conical indentation. *International Journal of Solids and Structures*, **43**(10):3142–3165.

Vandamme, M. and Ulm, F.-J., 2009. Nanogranular origin of concrete creep. *Proceedings of the National Academy of Sciences*, **106**(26):10552–10557.

Vandamme, M. and Ulm, F.-J., 2013. Nanoindentation investigation of creep properties of calcium silicate hydrates. *Cement and Concrete Research*, **52**:38–52.

Vandamme, M., Ulm, F.-J., and Fonollosa, P., 2010. Nanogranular packing of C-S-H at substochiometric conditions. *Cement and Concrete Research*, **40**(1):14–26.

Vandenbroucke, M. and Largeau, C., 2007. Kerogen origin, evolution and structure. *Organic Geochemistry*, **38**(5):719–833.

Vanorio, T., Prasad, M., and Nur, A., 2003. Elastic properties of dry clay mineral aggregates, suspensions and sandstones. *Geophysical Journal International*, **155**(1):319–326.

Vaughan, M. T. and Guggenheim, S., 1986. Elasticity of muscovite and its relationship to crystal structure. *Journal of Geophysical Research: Solid Earth (1978–2012)*, **91**(B5):4657–4664.

Vernik, L. and Landis, C., 1996. Elastic anisotropy of source rocks: Implications for hydrocarbon generation and primary migration. *AAPG bulletin*, **80**(4):531–544.

Vernik, L. and Liu, X., 1997. Velocity anisotropy in shales: A petrophysical study. *Geophysics*, **62**(2):521–532.

Vernik, L. and Nur, A., 1992. Petrophysical classification of siliciclastics for lithology and porosity prediction from seismic velocities (1). *AAPG Bulletin*, **76**(9):1295–1309.

Vlassak, J. J., Ciavarella, M., Barber, J. R., and Wang, X., 2003. The indentation modulus of elastically anisotropic materials for indenters of arbitrary shape. *Journal of the Mechanics and Physics of Solids*, **51**(9):1701–1721.

Vlassak, J. J. and Nix, W. D., 1993. Indentation modulus of elastically anisotropic half spaces. *Philosophical Magazine A*, **67**(5):1045–1056.

Vlassak, J. J. and Nix, W. D., 1994. Measuring the elastic properties of anisotropic materials by means of indentation experiments. *Journal of the Mechanics and Physics of Solids*, **42**(8):1223–1245.

Wagenmakers, E.-J. and Farrell, S., 2004. AIC model selection using akaike weights. *Psychonomic Bulletin & Review*, **11**(1):192–196.

Walper, J. L., 1977. Paleozoic tectonics of the southern margin of north america: Gulf coast association of geological societies transactions, v. 27. *ndash*, **239**:230p.

Wang, F. P. and Reed, R. M., 2009. Pore networks and fluid flow in gas shales. In SPE Annual Technical Conference and Exhibition. Society of Petroleum Engineers.

Wang, Z., Wang, H., and Cates, M. E., 2001. Effective elastic properties of solid clays. *Geophysics*, **66**(2):428–440.

Weaver, C. E. and Pollard, L. D., 1973. The chemistry of clay minerals. Elsevier Amsterdam.

Weber, C., Heuser, M., Mertens, G., and Stanjek, H., 2014. Determination of clay mineral aspect ratios from conductometric titrations. *Clay Minerals*, **49**(1):17–26.

Willis, J. R., 1966. Hertzian contact of anisotropic bodies. *Journal of the Mechanics and Physics of Solids*, **14**(3):163–176.

Woeber, A. F., Katz, S., and Ahrens, T. J., 1963. Elasticity of selected rocks and minerals. *Geophysics*, **28**(4):658–663.

Wyatt, O. H., 1953. Transient creep in pure metals. *Proceedings of the Physical Society. Section B*, **66**(6):459.

Yang, S., Zhang, Y.-W., and Zeng, K., 2004. Analysis of nanoindentation creep for polymeric materials. *Journal of applied physics*, **95**(7):3655–3666.

Zaoui, A., 2002. Continuum micromechanics: survey. *Journal of Engineering Mechanics*, **128**(8):808–816.

Zargari, S., Prasad, M., Mba, K. C., and Mattson, E. D., 2011. Organic maturity, hydrous pyrolysis, and elastic property in shales. In Canadian Unconventional Resources Conference. Society of Petroleum Engineers.

Zargari, S., Prasad, M., Mba, K. C., and Mattson, E. D., 2013. Organic maturity, elastic properties, and textural characteristics of self resourcing reservoirs. *Geophysics*, **78**(4):D223–D235.

Zeszotarski, J. C., Chromik, R. R., Vinci, R. P., Messmer, M. C., Michels, R., and Larsen, J. W., 2004. Imaging and mechanical property measurements of kerogen via nanoindentation. *Geochimica et cosmochimica acta*, **68**(20):4113–4119.

Zhang, G., Wei, Z., Ferrell, R. E., Guggenheim, S., Cygan, R. T., and Luo, J., 2010. Evaluation of the elasticity normal to the basal plane of non-expandable 2: 1 phyllosilicate minerals by nanoindentation. *American Mineralogist*, **95**(5-6):863–869.